Multi-frequency microwave energy harvesting receivers: Theory and applications

Autora:

Ana López Yela

Tesis doctoral depositada en cumplimiento parcial de los requisitios para el grado de Doctor en Multimedia y Comunicaciones

Universidad Carlos III de Madrid

Directores:

Daniel Segovia Vargas
Catedrático de Universidad
Universidad Carlos III de Madrid

Zoya Popović
Distinguished Professor, Lockheed Martin Endowed Chair
University of Colorado Boulder

Tutor:

Daniel Segovia Vargas

Leganés, Octubre 2020

Y el final por fin llegó ...

Agradecimientos

En este apartado de agradecimientos no puedo comenzar sin agradecer de manera infinita a toda la gente que directa o indirectamente me ha apoyado a lo largo de esta tesis, tanto a aquellos que me han ayudado a resolver mis dudas y a avanzar, como aquellos otros que me han animado siempre a seguir y luchar. Mención especial para el Ministerio de Cultura, Deporte y Educación, por la FPU concedida.

Con esta experiencia he descubierto que soy una persona muy fuerte, que ante las adversidades puedo tropezar pero que me levanto con la cabeza alta, no dejo que me hundan. Por desgracia he tenido muy mala suerte en ciertos aspectos, pero a pesar de eso, mi tesis está aquí y estoy muy orgullosa de ello. He trabajado muy duro para sacarla adelante, menos mal que he tenido compañeros que siempre han estado ahí para resolverme las dudas y guiarme. Gracias a mi director de tesis por la ayuda recibida. Hubo momentos en los que no veía la luz pero mi gran inspiración llegó de la mano de Zoya Popović, mi codirectora, a la que nunca podré parar de agradecer su apoyo. Una gran persona con la que trabajar, además de una gran amiga. Zoya, tu ayuda fue esencial para mí. También en este punto tengo que dar las gracias a mi coautor y hermano, Alberto. Otra persona sin la cual esta tesis ni tendría sentido, ni se hubiese concluido. Mil gracias hermanito, y espero que tengas mucha suerte en tu carrera porque puedo afirmar que eres un genio y como tú hay pocos. Cómo no, agradecer a mi familia, mis padres Ángel y Carmen y a mi otro hermano David, mi cuñada Angélica y mis sobrinitos Darío y Lucía. Ha sido un camino muy

difícil, pero que la gente te apoye y te ayude a seguir es esencial y, sobre todo, cuando el camino tiene piedras que impiden el paso y te quieren hacer tropezar.

Cómo no, recordar a todos aquellos que no están. Tanto mis abuelos Gregorio, Angelita y Estaban, como mi tío Benito.
No me puedo olvidar de mis tíos y primos y en especial de mi tía Paloma y mi abuela Pili, muchas gracias.

Todo aquel que me conoce sabe que estas palabras tenían que salir. Agradezco mi tesis a mi perra, bueno a las dos que me han soportado durante este tiempo. Nala es, y Zara ha sido una gran compañía. Quien tiene animales sabe lo que digo, y por tanto, no podía omitir este párrafo. Mis otros perros ya no pudieron compartir este tiempo conmigo pero su recuerdo siempre sigue.
Muchas gracias a mis amigos del laboratorio, porque no habéis sido sólo compañeros, habéis sido grandes amigos. Hemos pasado momentos increíbles y con eso me quedo. Creo que los mejores momentos vividos fueron cuando eramos una gran piña y todo gracias al maravilloso "team building". Echaré de menos esos momentos porque lo pasamos genial. Todos los vídeos y fotos que tenemos haciendo el payaso son lo mejor. La broma telefónica que me hicisteis ("Ana dice"), el viaje a Suiza y EEUU fueron increíbles, en especial la aventura americana. Anécdotas que no se pueden olvidar. Nuestras comilonas en "El Piratas" y los peligrosos viajes para llegar ahí (recuerdo esa calle en dirección prohibida...). Grandioso equipo de fútbol creasteis, "Los Supremazos", aunque ya sabéis que lo importante es participar. Me encantó el momento en que os metieron en la copa de los buenos y llamasteis al organizador para rogar que queríais ir a la copa de los malos. Allí había más opciones de no ser los últimos. Tampoco se pueden olvidar los "coffee breaks" que hemos tomado prestados o esas comidas en nuestro seminario favorito. Guardo de recuerdo los papeles de esa puja del 2017. Jose ganó una comida a mi costa pero reconozco que fue muy gracioso. Aunque he de decir que ninguno acertó con el final si lo vemos ahora. Hemos pasado ya muchos por esa sala, pero de cada uno guardo recuerdos increíbles. Espero que algún día la vida nos junte de nuevo a todos.

Adri, mil gracias por todo. A pesar de vernos poco seguimos hablando todos los días y es algo de lo que tenemos que estar orgullosos. Eres una magnífica persona y espero que te vaya genial en la vida. Eres un gran currante y te lo mereces. No tengo palabras para agradecerte todo porque siempre que tengo dudas te pregunto a ti antes que a Google. De ti tengo mil momentos vividos, aunque guardo con especial recuerdo la sorpresa que hicimos para tu despedida. La canción fue increíble, y el momento "Star Wars" fue el no va más. Fue difícil de organizar todo eso pero al final todo salió genial. Ahí estoy orgullosa de mi misma (y tú bien lo sabes), porque podía haberla liado mil veces y al final ni una sola vez. Nunca se me escapó nada y eso que sabes que se me da mal mentir y callar. Otro momento grandioso fue cuando te fuiste de estancia a Macao. Ya todos sabemos lo que te pasó con la lata de atún, pero no podía omitirlo. Espero que hayas usado el guante anticorte que te regalamos... Por cierto, mi vídeo favorito es en el que sales montando en bici, ya lo sabes.

Del señor Galindo tengo que recordar ese momento de "Electrokuten". Es algo que no puedo describir de lo surrealista de la situación, pero para los presentes fue de lo mejorcito vivido en Suiza. Todos los que te conocemos sabemos que eres una persona muy seria con un gran sentido del aseo y limpieza de las uñas. Tus selfies eran muy "especiales". Me he reído muchísimo contigo y creo que puedo afirmar que fuiste el alma del laboratorio. Desde que te fuiste se quedó más triste y silencioso.

Qué decir de Josico. Eres un personaje increíble. Me acuerdo cuando celebraste tu primer cumpleaños en el laboratorio. Me gustaron mucho los pasteles aunque la pena es que no venían muchos... Con Gabri formabas un gran equipo investigador. En vuestra especialidad sabíais hacer un buen research. La verdad es que Gabri y tú juntos sois una gran pareja. Me acuerdo de esa noche en la URSI de Cartagena donde se oía a gente cantar en otra planta: ALEEE RABAJO ALE ALE...

Gatuno, mando saludos a Abu Dhabi. Sabes que has sido un gran amigo y compañero de proyecto. Un tío muy cafetero como buen colombiano, forofo de James y del Real Madrid, hasta el punto que te hiciste un selfie con Falcao cuando estaba en el Atleti... Recuerdo el día que fui la jefa en el "team building". ¡Qué gran día! Recuerdo las risas y cuando tenías que irte, que te escribían y tú decías que salías en un rato pero lo ibas posponiendo porque estaba la partida "on fire". Creo que la mejor anécdota que hemos vivido tiene que ver con una mano y unos dientes en una antena. Tú ya sabes...

De Rivera recuerdo su percusión con las baquetas, su capacidad para hacer con los objetos más insospechados la cosa más útil para la mesa de THz. Eres una persona brillante y espero que en el trabajo te expriman al máximo para que des lo mejor. Me encanta tu increíble capacidad para hacer analogías con las cosas más extrañas. Cada vez que oigo "carga adaptada" me acuerdo de tu famosa frase, no puedo evitarlo. Además, es algo que te hace entender perfectamente el concepto. Deberíamos publicarlo en la URSI.

Kerlos, también conocido como Koko, ese gran amante de la cocina de autor, sobre todo cuando el autor es Domino's Pizza. Eres muy buena gente Kerlos y espero que te vaya muy bien junto a Sheeren y Ereeny. Creo que eres la persona más trabajadora que conozco y siempre dispuesto a ayudar, dando igual la hora o la cantidad de trabajo por terminar. Has sido un gran compañero y espero que en el trabajo te valoren igual.

Sergio, espero que en breve acabes y que tu tesis esté genial. Sabes que va a ser duro pero aquí me tienes acabando ya... Compañero de FPU y docencia, estos años han sido muy muy duros pero hay que sacar el lado positivo. Muchas gracias por tu ayuda, en especial este último año. Es una pena no haber tenido nunca un paper en común a pesar de trabajar en bandas parecidas, pero nunca se nos ha dado esa oportunidad. Me quedo con los buenos momentos vividos y esos debates políticos espontáneos que nos hacían filosofar sobre la vida.

Álvaro, aquel estudiante de estancia que vino por dos meses y se quedó siete y porque le echamos... Fue muy bueno tenerte, un aire fresco aunque algo friki. Gran compañero de viaje aunque te aviso que al ritmo que comes pan se te va a poner un culo que ni la Kardashian. Espero que te vaya muy bien en Rennes. Muchas gracias por estar siempre ahí ayudando porque te conozco de hace poco pero puedo decir que eres un gran amigo y de verdad das buenos consejos.

Víctor, nuestro último fichaje y sustituto de Adri. Has sido un gran compañero de debate. Me encantaba comentar la política contigo para ver las cosas desde otra perspectiva. Eres un muy buen matemático y un músico genial. De ti me quedo con esa canción maravillosa del grupo "Los Auténticos Decadentes". Con esta canción la vuelta al trabajo después de la comida se hacía más llevadera.
Porque yo, no quiero trabajar, no quiero ir a estudiar, no me quiero casar, quiero tocar la guitarra todo el día y que la gente se enamore de mi voz ...

Mónica, sabes que te envidio por lo lista que fuiste. Ojalá hubiese hecho lo mismo. Ha sido un placer trabajar contigo. Eres una gran persona. En ti vi mi reflejo del pasado y bien sabes que no dejé que te hundieses en las aguas de ese TFM. Con mucho gusto te he ayudado y sabes que lo seguiré haciendo en cualquier cosa. Con mucho gusto dirigí tu TFM y estoy muy orgullosa del trabajo conseguido: dos artículos de congreso y uno de revista juntas. ¡Bravo!

También me gustaría mencionar, cómo no, a todos los seniors del grupo que han compartido risas con nosotros. Iván, muchas gracias por tu trabajo. Sin Iván esta tesis hubiese estado coja. ¡Magnífico técnico de laboratorio que nos fabrica los circuitos! Súper eficiente además de gran persona. Ugarte, eres un crack. Sigo esperando la canción con el ukelele, pero Adri no me la deja escuchar. Cómo no, Javi Montero. Aquí está tu sucesora con la tesis acabada. ¡Vaya plaza me dejaste! De Nacho heredé la mesa, la mejor del laboratorio. Otro crack del grupo. Tu capacidad para hacer descenso por gradiente es asombrosa. No conozco a nadie igual.

Agradecer a Alejandro Lampérez y Sergio Llorente su ayuda y apoyo en la tesis, sobre todo Alex con la docencia. Mil gracias. Ya sabes que soy tu peor pesadilla... La verdad que en muchas ocasiones tu contribución ha sido esencial y lo agradezco. Siempre dispuesto a resolverme mil dudas.

Mención especial a mis compañeros de la Universidad de Colorado. Jose y Eric, ha sido un placer trabajar con vosotros aunque por la distancia no fue fácil, pero lo hemos conseguido. A Laila, gran viaje por tierras exóticas. Fue increíble conocerte y congeniar tan bien. Espero que te vaya muy bien y consigas sacar adelante tu empresa.

Tengo que agradecer a mis amigos de fuera de la Universidad. Aunque casi hicimos vida en el laboratorio, de vez en cuando salíamos del refugio a ver la vida.

A mis amigos de la UPM (Tamara, Khalid, Sergio, Jean), muchas gracias. Me encanta esa grupo de Whatsapp "FVyA". Con siglas queda más serio. Nunca falta el sentido del humor y las peleas entre Sergi y Calcetín. Sergi, espero que estés cuidando mi plaza, quién sabe si volveré en algún momento, pero mientras tanto sigue con el B2. Khalid, compañero de carrera y máster. Mira que podíamos haber elegido algo más sencillo... Con un poco de suerte, puedo en un futuro dirigir tu TFM. Tamara, gran compañera y amiga de la carrera. Fuimos un gran tándem en el laboratorio. Jean, muchas gracias, me ayudaste muchísimo, junto a Sergi, en el TFG y durante mi máster.

A Leo, Edu, Álex, Javi y Álvaro (y muchos más, que seguro me olvido de gente). Hace mucho que no os veo pero tenemos que organizar un reencuentro. Demasiados momentos en la carrera, menos mal que había humor. Álex, de lo mejorcito fue el primer año. Todavía me acuerdo de las risas con nuestra amiga Nely. Seguro que te acuerdas, y de mil cosas surrealistas que nos han pasado, pero siempre riendo. En la clase donde nos explicaban lo de los tesauros recuerdo mi gran aportación al mundo. Creo que es lo mejor que he podido escribir en mi vida. Fue algo así como "yo soy como el perfume, que vengo en bote pequeño". No podía olvidar a Alberto, mi compañero de máster y de gimnasio. Creo que eres la persona a la que más le gusta hablar. Siempre tienes tema de conversación. Pero desde luego eres una gran persona.

Agradecer a mi Ana, amiga de “TODA LA VIDA”. Es curioso que con la mayoría de amigos puedes definir un momento de cuando les conociste o de hace cuantos años, incluso recordar el día. Puedes conocerlos del cole, del insti. Contigo es imposible. Creo que eramos tan pequeñas que no recuerdo ese momento, solo que nos conocemos de toda la vida. Mil planes juntas. Eres la mejor. Siempre has estado allí escuchando y dando tu opinión, intentando hacer que el mundo sea un poco mejor. Admiro tu capacidad de ayudar a la gente. Yo no sería capaz de irme como médica cooperante a países del tercer mundo y ver el sufrimiento de primera mano. Admiro tu valentía porque no es fácil.

A Belén, mi gran amiga de sincro. Hace más de 15 años que nos conocemos y ahí seguimos. Las vueltas que da la vida pero siempre intentamos estar en contacto. Te aprecio muchísimo. Siempre al pie del cañón cuando se te necesita. Ojalá algún día lleguemos a hacer ese club de sincro que tanto queríamos.

Zineb, ya sabes que te echo de menos, estás muy lejos pero espero ir a visitarte en cuanto pueda. Es una pena que gente tan preparada tenga que irse a trabajar fuera porque no encuentran un trabajo bien remunerado aquí. Eres una persona increíble y muy luchadora. No has tenido las cosas fáciles, pero me encanta tu optimismo y ganas de disfrutar. Creo que de lejos eres la persona con la que más me he reído, sobre todo en el instituto. Hay tantos y tantos momentos de risas que no sé cómo estudiábamos. Fue increíble...

No puedo olvidarme de las chicas de ballet (Claudia, Sheila, Carla, Almu). Gran grupo de baile. Siempre nos quedamos con las ganas de hacer el festival de “El Lago de los Cisnes”, nos hacía mucho ilusión, pero no nos poníamos de acuerdo en los papeles. Todas queríamos ir en la última fila...

Tampoco pueden faltar mis amigos de Liverpool, aunque alguno volvió del destierro antes de tiempo. Ángel, Miguel y Luis. Fue muy bueno conoceros. Lo pasé genial por la tierra de los Beatles y eso que a veces la adaptación no era fácil. Recuerdo esos simulacros de incendio todos los meses y lo divertido que era salir en pijama por la noche cuando sonaba la alarma... Curioso mi compañero en la residencia, Lenny... Espero que

os vaya muy bien con Gargamel aunque ya me dijisteis que cerró el café. ¡Qué pena!. Muchas gracias a mi director de estancia Yi Huang y Chaoyun Song, por su generosidad al haberme acogido en su grupo.

Ellen, fue muy curioso cuando por casualidad estuvimos las dos viviendo en Reino Unido a la vez. Gran viaje lleno de aventuras por las tierras de Robin Hood. El Castillo nos dejó sin palabras... Espero que nos veamos pronto, tengo que ir por Holanda. Muchas gracias por todo, me has ayudado mucho a mejorar mi nivel de inglés. Tú, en cambio, el español lo dominas, ¡eres increíble con los idiomas!

María, aprendí mucho de ti en sincro, primero mi entrenadora y luego compañera. Una pena que te fueses lejos. En ese año y medio aprendí muchísimo de ti, a cómo torear las dificultades y a disfrutar aunque nos lo pusieran difícil. Lo pasamos bien con nuestras niñas. Recuerdo cuando estabas embarazada y me dijeron que si yo había tenido ya el bebé, porque como estaba delgada...
¡Qué bonita es la inocencia! Es una de las cosas más bonitas de la vida.

Muchas gracias a todos y espero que os leáis todos la tesis...

Published and submitted articles and contributions

During the PhD studies, different contributions (journal and conference papers) have been published although not all the work has been included in the thesis. In this section, there is a list of contributions (one journal article and three international conference papers) related to the thesis, where part of the material (data, graphs or even analytical models) has been used. Some work has been done in collaboration with the University of Liverpool (including a three-month research visit) and with the University of Colorado Boulder.

1. J. A. Estrada, E. Kwiatkowski, **A. López-Yela**, M. Borgoñós-García, D. Segovia Vargas, T. Barton, Z. Popovic,“ *An RF-Harvesting Tightly Coupled Rectenna Array Tee-Shirt With Greater Than Octave Bandwidth*,” in IEEE Transactions on Microwave Theory and Techniques, doi: 10.1109/TMTT.2020.2988688.
   Co-author of this journal article. Some material from this contribution is shown in Chapter 5 although most of the work is new.
   This paper was awarded with “the Best Reading Paper of the Issue September 2020”.

2. M. Borgoñós-García, **A. López-Yela**, D. Segovia Vargas, "*Rectenna at 2.45 GHz for Wearable Applications*," 2020 14th European Conference on Antennas and Propagation (EuCAP), Copenhagen, 2020, pp. 1-4.
   Co-author of this conference paper. In this contribution, the Spice model (intermediate approach) developed in Chapter 3 was used for testing different circuits.

3. **Ana López-Yela**, Alberto López-Yela, Z. Popovic, D. Segovia-Vargas, " *Non-Linear Diode Rectifier Analysis for Multi-tone Wireless Power Harvesting*,"2019 IEEE International Conference on Microwaves, Antennas, Communications and Electronic Systems (COMCAS), Tel-Aviv, Israel, 2019, pp. 1-5, doi: 10.1109/COMCAS44984.2019.8957851.
   Author of this conference paper. The material from this contribution is extended in Chapter 2. Indeed, in this chapter, a complete explanation about the development of the analytical model is fully shown, including new results. Moreover, a novel (and unpublished) different approach is presented in the thesis, showing better results than the previous one.

4. J. A. Estrada, E. Kwiatkowski, **A. López-Yela**, M. Borgoñós-García, D. Segovia Vargas, T. Barton, Z. Popovic, " *An Octave Bandwidth RF Harvesting Tee-Shirt*," 2019 IEEE Wireless Power Transfer Conference (WPTC), London, United Kingdom, 2019, pp. 232-235, doi: 10.1109/WPTC45513.2019.9055642.
   Co-author of this conference paper. Some material from this contribution is shown in Chapter 5 although most of the work is new.

Nevertheless, some articles were not included in the thesis. Therefore, the next enumeration shows the rest of contributions, including a co-authored journal paper and six articles in national and international conferences as author.

1. C. Song, **A. López Yela**, Y. Huang , D. Segovia Vargas, Y. Zhuang, Y. Wang, J. Zhou, "*A Novel Quartz Clock With Integrated Wireless Energy Harvesting and Sensing Functions*," in IEEE Transactions on Industrial Electronics, vol. 66, no. 5, pp. 4042-4053, May 2019. doi: 10.1109/TIE.2018.2844848

2. **A. López Yela**, D. Segovia Vargas," *Rectena de banda ancha para la recolección de energía electromagnética ambiental*," XXXIII National Simposium of the International Union of Radio Science, Granada, 2018.

3. **A. López Yela**, D. Segovia Vargas," *A High-efficiency 2.45 GHz Rectenna Design for Electromagnetic Energy Harvesting*," XXXII National Simposium of the International Union of Radio Science, Cartagena, 2017.

4. **A. López-Yela**, F. Albarracín-Vargas and D. Segovia-Vargas, " *An electrically small antenna for potential aircraft applications*," 2017 IEEE International Symposium on Antennas and Propagation and USNC/URSI National Radio Science Meeting, San Diego, CA, 2017, pp. 1993-1994. doi: 10.1109/APUSNCURSINRSM.2017.8073039

5. **A. Lopez-Yela** and D. Segovia-Vargas,"*A triple-band bow-tie rectenna for RF energy harvesting without matching network*," 2017 IEEE Wireless Power Transfer Conference (WPTC), Taipei, 2017, pp. 1-4.doi: 10.1109/WPT.2017.7953809

6. **A. L. Yela**, F. A. Vargas, F. J. H. Martínez, D. S. Vargas and V. G. Posadas, "*Embedded matching networks for electrically small antennas*," 2016 10th European Conference on Antennas and Propagation (EuCAP), Davos, 2016, pp. 1-4. doi: 10.1109/EuCAP.2016.7481537

7. **A. López Yela**, F. Albarracín Vargas, F. J. Herraiz Martínez, D. Segovia Vargas,“ *Passive matching networks for electrically small antenas*,” XXX National Simposium of the International Union of Radio Science, Pamplona, 2015.

Resumen

Las emisiones a lo largo de todo el espectro electromagnético no sólo se pueden utilizar para las comunicaciones, sino que también pueden emplearse para la alimentación de dispositivos electrónicos. Este recurso se ha hecho cada vez más abundante en los últimos años gracias a los recientes despliegues en telefonía móvil de 4G y 5G y a la popularización de las redes inalámbricas de banda ancha (WiFi), sin olvidar las comunicaciones de difusión ya existentes como la radio o televisión. Para poder aprovechar este recurso (actualmente desaprovechado), se utilizan las llamadas rectenas, que son antenas con un elemento rectificador integrado. Esta tesis tiene por objetivo el estudio de estos elementos rectificadores, para desarrollar aplicaciones capaces de reducir o eliminar el uso de baterías en los millones de dispositivos y redes de sensores de bajo consumo existentes hoy día, mediante el autoabastecimiento de energía.

Este proceso podría llevarse a cabo con paneles fotovoltaicos o sistemas piezoeléctricos, pero estos requieren de la presencia continua de la fuente que los origina (vibraciones, horas de sol). Sin embargo, la energía electromagnética producida por las estaciones base, de telefonía o televisión, está presente bajo su zona de cobertura las 24 horas del día, lo cual incluye zonas de difícil acceso, en las que es complicado el recambio o mantenimiento de las baterías. Además, estas emisiones tienen como principal limitación la baja densidad de potencia, obteniéndose valores de eficiencia de conversión RF-DC muy bajos. Esto conlleva que los valores de corriente DC para alimentar al sensor sean muy pequeños, de nA o μA, y por tanto, deben

emplearse técnicas para la mejora del rendimiento.

Esta tesis propone una alternativa para mejorar la eficiencia de conversión, basada en la probada mejora de eficiencia cuando se trabaja con señales con un Peak to Average Power Ratio (PAPR) grande. Esto se da en escenarios multitonales como puede ser el espectro electromagnético. Esta mejora no ha sido abordada teóricamente con resultados precisos en trabajos previos, por lo que en esta tesis se desarrolla un modelo matemático que predice la componente DC de la corriente del diodo, cuando se excita con múltiples tonos. Los resultados obtenidos han sido validados en el laboratorio, demostrándose la mejora en la eficiencia de conversión y el buen comportamiento del modelo teórico. De esta forma, se pueden agilizar los cálculos cuando no se tiene un software de simulación disponible, o cuando éste arroja problemas de convergencia.

Esta tesis consta de seis capítulos y está organizada de la siguiente manera:

En el primer capítulo se expone una breve introducción sobre la evolución de la transferencia inalámbrica de potencia y sobre las diferentes tecnologías que la componen, haciéndose hincapié en la transferencia de potencia no directiva en campo lejano, puesto que se corresponde a la recolección de la energía electromagnética ambiental. Además, se incluye un análisis del estado del arte con los valores más significativos de eficiencia de conversión, así como las principales características de varios diseños (como por ejemplo la potencia o las bandas de trabajo empleadas).

En el segundo capítulo se explora el comportamiento del diodo desde el punto de vista matemático. Bajo densidades de potencia pequeñas, como las presentes en este entorno, el diodo opera en su región no lineal, produciendo un incremento de eficiencia cuando se trabaja con señales con gran PAPR, respecto a un tono con la misma potencia media. Este hecho ha sido probado empíricamente pero ningún modelo teórico preciso ha sido realizado. En este capítulo se incluye un novedoso análisis matemático del funcionamiento del diodo en esa región para múltiples tonos de entrada, variando la amplitud y frecuencia de estos.

En el capítulo 3 se muestra la comparativa entre el modelo teórico, las simulaciones y las medidas en el laboratorio, usando múltiples tonos de

entrada en tres rectificadores. Para comparar adecuadamente todos los resultados, es necesario utilizar un modelo Spice del diodo preciso (incluyendo los parásitos del encapsulado) y un correcto setup de medida. De lo contrario, existirá un error en los resultados debido a una caracterización inadecuada del dispositivo no lineal. Este capítulo aborda esos problemas. El análisis muestra que la frecuencia y amplitud relativa de múltiples señales simultáneas afectan a la eficiencia.

Una vez estudiado el rectificador, el capítulo 4 de la tesis aborda el diseño de la antena. Para ello, se analizan los diferentes criterios de diseño que deben emplearse cuando se trabaja con una transmisión de potencia inalámbrica directiva o no directiva, como es en caso bajo estudio, así como las técnicas de integración entre rectificador y antena. Para concluir, se diseña y mide una rectena tanto en laboratorio como en espacio abierto, usando la energía ambiental, previamente caracterizada con medidas espectrales. Los resultados demuestran que es posible recolectar y rectificar la energía ambiental.

En el capítulo 5 se muestra una posible aplicación al integrarse una rectena impresa en una camiseta para alimentar sensores biológicos o "wearable". Se trata de un diseño de banda ancha que opera en el rango de 2 a 5 GHz, que permite recolectar suficiente energía para alimentar sensores de bajo consumo. Se analiza el funcionamiento de dos tamaños distintos de arrays con diferentes densidades de potencia. Al ser un diseño "wearable", la aplicación ha sido diseñada y probada sobre un maniquí y un cuerpo humano, analizándose el comportamiento de la antena impresa sobre distintas composiciones corporales (personas con más tejido adiposo o por el contrario más fibrosas).

Finalmente, el capítulo 6 recopila las conclusiones del trabajo que se muestra en esta tesis e ideas para trabajos futuros, proponiéndose desde enfoques para reducir más el error en la aproximación del comportamiento no lineal del diodo en el capítulo 2, a posibles mejoras en la antena impresa del capítulo 5, incluyendo la doble polarización lineal.

Abstract

Emissions across the electromagnetic spectrum are not only used for communications, but they can also be used for powering electronic devices. This resource has been made more and more abundant in the last years thanks to the recent deployment of 4G and 5G, and the popularization of broadband wireless networks such as WiFi, including traditional services such as TV and radio broadcasting. In order to take advantage of the energy (currently wasted), rectennas (a rectifier integrated with an antenna) are used. This thesis has the objective of studying these rectifying elements, to reduce or eliminate the use of batteries that are employed in millions of low-power devices and sensor networks planned for deployment in the near future.

To do this, a self-supply system in situ is required. This could be achieved with photovoltaics or piezoelectrics, but they require the presence of light or vibration. However, the electromagnetic energy produced by mobile communications, TV base stations and radar is noticeable inside a large coverage area, 24 hours a day. This includes difficult access areas where it is nearly impossible to provide appropriate maintenance to replace batteries. As explained through the thesis, energy harvesting applications have a severe limitation on the available levels of power density to scavenge, constraining the RF-DC power conversion efficiencies. Therefore, the amount of DC power to feed a sensor is limited and some techniques must be applied to improve the performance.

This thesis proposes an alternative for improving the RF-DC power conversion efficiency based on the multiple-tone scenario (the electromagnetic spectrum). Previous studies have been published about an empirical improvement in the power efficiency when working with high Peak to Average Power Ratio (PAPR) multiple-tone signals, compared to a CW signal with the same average power, although the theoretical proof was not accurate enough. A mathematical model that predicts the expected DC current of the diode when excited with multiple tones is proposed along the thesis, having good agreement with simulations and measurements, demonstrating the good performance of the theoretical model. With this mathematical approach, convergence problems in simulation software can be avoided. This document comprises six chapters and it is organized as follows:

In the first chapter a brief introduction on the evolution of wireless power transfer is presented, including all the different approaches that compose it, emphasizing the far-filed non-directional powering or harvesting, which is the topic of this thesis. In addition, an analysis of the state of the art is presented with the most significant values of conversion efficiency, as well as the main characteristics of various designs.

In the second chapter, the performance of the diode is explored theoretically. For very low incident power densities (those present in the environment), the diode works in a non-linear region, where a power efficiency improvement is obtained when using high PAPR multiple-tone signal instead of a single tone with the same average power. This fact has been empirically tested but an accurate theoretical model has not been accomplished. Therefore, this chapter deals with this issue, showing a novel mathematical analysis of the diode operation in that region for multiple input tones, varying their relative amplitude and frequency.

In Chapter 3, the theoretical analysis is compared with simulations and experiments for multiple input tones with a large resulting PAPR using three different rectifier circuits. To properly compare the results, it is necessary to use an accurate Spice diode model (including parasitics) and an appropriate measurement setup. Otherwise, results will differ due to an inadequate characterization of the non-linear device. This chapter addresses those issues. The analysis shows that the relative frequency and amplitude

of multiple simultaneous signals impacts the amount of efficiency improvement.

Once the rectifier element is studied, Chapter 4 deals with the antenna design, which is part of the rectenna deployment. It is seen that different design criteria must be used when working with a WPT directive beaming application or a non-directive harvesting one, as happens in this thesis. The integration between the antenna and the rectifier is analyzed, showing possible alternatives. Finally, a rectenna design is built and tested through indoor and outdoor measurements. An analysis of the electromagnetic spectrum is included to demonstrate the feasibility of the rectenna model.

In Chapter 5 a wearable rectenna application is shown, with a broadband 2 to 5 GHz rectenna array, implemented on a cotton shirt. This application allows to collect enough energy to power energy-efficient devices. Different rectenna array sizes were tested at different power densities. The single element is a self-complementary tightly-coupled bow-tie. Simulations and measurements were performed over a phantom and over body tissues taking into account the electrical properties of the torso. The thickness of each layer was varied analyzing its influence in the antenna performance, to check what happens under different body compositions (people with more adipose tissue or on the contrary more fibrous).

Finally, Chapter 6 collects the conclusions of the work shown in this thesis and ideas for future work. Some ideas are proposed about Chapter 2 to reduce the error of the mathematical approach when working in the non-linear region. Also, some possible improvements to the printed antenna of Chapter 5 are included such as adding a dual linear polarization.

List of Figures

List of Tables

Contents

Acronyms

AWR Microwave Office. 74, 97, 98, 99, 134, 142, 145, 200

CW Continuous Wave. 9, 55, 58, 76

DTV Digital Television. 35

DUT Device Under Test. 181, 182

EH Energy Harvesting. 33

ESA European Space Agency. 13

EVs Electric Vehicles. 17, 25, 27

FDD Frequency Division Duplexing. 58

GSM Global System Mobile. 35, 54, 194, 197

IC Integrated Circuit. 194, 196

ISM Industrial, Scientific and Medical. 29

ITU International Telecommunication Union. 19

LCM Least Common Multiple. 66

LTE Long Term Evolution. 35, 54, 58

MILAX Microwave Lifted Airplane Experiment. 12

MIT Massachusetts Institute of Technology. 17

NASA National Aeronautics and Space Administration. 9

OFDM Orthogonal Frequency Division Multiplexing. 58

PAE Power Added Efficiency. 182

PAPR Peak to Average Power Ratio. xvi, xx, 33, 36, 37, 55, 58, 59, 91, 161, 167, 169, 176

RFID Radio Frequency Identification. 58

SAR Specific Absorption Rate. 28

SHARP Stationary High Altitude Relay Platform. 10, 12, 29

SP Source-pull. 165

SPS Solar Power Satellite. 9, 10, 13, 29

TEM Transverse Electromagnetic Mode. 136

UAV Unmanned Aerial Vehicle. 29

UHF Ultra High Frequency. 7

UPS Ubiquitous Power Source. 13, 14

UWB Ultra Wide Band. 58

VHF Very High Frequency. 7

VSWR Voltage Standing Wave Ratio. 126, 131

WBLS Multicopter Assisted Wireless Batteryless Sensing System. 17

WCDMA Wideband Code Division Multiple Access. 35, 194

WiFi Wireless Fidelity. 35, 197

Wimax Worldwide Interoperability for Microwave Access. 35

WPC Wireless Power Consortium. 17, 18

WPR wireless power reception. 161

WPT Wireless Power Transfer. 5, 6, 7, 8, 10, 13, 16, 19, 20, 21, 25, 26, 27, 29, 32, 166, 167

WSNs Wireless Sensor Networks. 16, 17

1

Introduction to microwave energy harvesting

In this chapter, a historical perspective on the evolution of the Wireless Power Transfer (WPT) is overviewed to better understand its origins and motivation of the thesis research. Wireless Power Transfer is subdivided into four categories, depending on the type of electromagnetic fields used to store and transfer energy: near-field reactive, near-field over-moded cavity, far-field beaming (directive) and far-field non-directive. Inductive, capacitive and resonant coupling are unified into the same category of near-field WPT due to the similarity in their working principle. Near-field wireless power transfer is typically done over distances much smaller than a wavelength and is sensitive to alignment while far-field powering is done at distances $r > \frac{2D^2}{\lambda}$, where D is the largest dimension of the radiator, and can be directive or non-directive. Power levels vary from kW for, e.g., near-field vehicle charging, to μW for omni-directional RF harvesting.

1.1. Historical perspective

To understand the context of this thesis, this subsection gives a brief overview of the historical development of near and far-field microwave power transfer. WPT is a way to transmit energy without wires taking advantage of electromagnetic fields or waves.

One of the fundamental electromagnetic laws established in 18th century was formulated by André-Marie Ampère (1775 -1836) [1]. He was a mathematician that formulated an electromagnetism theory in 1827. Following to Oersted experiments, Amperè concluded that magnetism and electricity are coupled, as a stationary current creates a static magnetic field with a direction related to the current direction (the right hand law). Shortly afterward, Michael Faraday (1791 - 1867) [2], simultaneously with Joseph Henry, discovered electromagnetic induction in 1831, where a variable magnetic field creates an electric field. This fact was a very first step towards Wireless Power Transfer. Indeed, near-field WPT is based on this concept, using coils or capacitors, taking advantage of the time-varying electric or magnetic fields respectively.

The most important milestone was done by James Clerck Maxwell (1831 - 1879) [3], who unified previously disconnected laws for electric and magnetic fields, resulting in electromagnetic wave propagation. He also showed that light is an electromagnetic wave. He reformulated Ampere's Law for non-stationary fields by adding a term that allows energy transfer through a vacuum (displacement current).

It was not until 1884 when John Henry Poynting (1852-1914) [3] developed a law for the conservation of the electromagnetic field energy (Poynting theorem), describing power carried by an electromagnetic wave. The Poynting vector represents the flux of energy (this is energy transferred per unit area and per unit time) of a wave and is the cross product of the electric and magnetic field vectors, yielding the propagation direction of the wave and the instantaneous energy flux.

Heinrich Rudolf Hertz (1857-1894) [4] demonstrated experimentally the existence of electromagnetic waves eight years after Maxwell's death, between 1886 to 1888. Hertz was the first radio engineer who studied the propagation of electromagnetic waves and possible ways to generate and capture them at frequencies in the Very High Frequency (VHF) and Ultra High Frequency (UHF) range. He also demonstrated the photoelectric effect, although Albert Einstein theoretically contributed to its explanation for which he later received the Nobel prize in 1905.

Oliver Heaviside (1850-1925) introduced the vector calculus, the Heaviside step function (used in circuit analysis to calculate the current when the circuit is switched on) and the transmission line theory, developing the telegrapher's equations.

In 1894, Jagadish Chandra Bose (1858-1937), from British India, continued Hertz's work up to 5 mm radio waves (60 GHz). Two years later, he performed a one-mile wireless transmission.

Nikola Tesla (1856-1943) [5] (Figure 1.1.1) continued Hertz's work on this topic and in 1890 he did some experiments proving the inductive and capacitive coupling, using high voltages (1 million of volts) of alternating current, generated with his famous Tesla Coil. With this setup, he could demonstrate wireless power transfer that powered the lighting system (Geissler tubes) of an enclosure. Later he continued working on this project but no commercial system was presented although he had patents issued in this field in 1902 [6]. In 1893, Tesla gave a talk at the National Electric Light Association. He was confident with his belief that it would be possible to transmit energy, even signals, to remote places without wires. In 1898, an electric exhibition took place at Madison Square Garden where Tesla demonstrated how radio waves carry power and information by controlling a small ship wirelessly. He tried to sell this idea to the American army to develop a radio-controlled torpedo. They refused, and it was not until the Second World War that this concept was incorporated in the military program. Finally, in 1899 Tesla built the Tesla Experimental Station where he did WPT experiments (this research was described and published in the Colorado Springs Notes, 1899-1900) [7], and made the largest Tesla coil ever built.

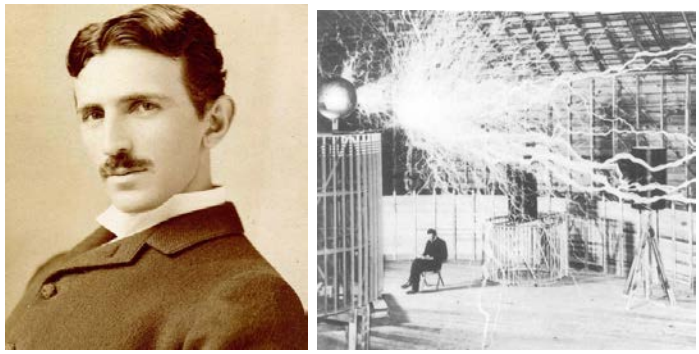

(a) (b)

Figure 1.1.1: Nikola Tesla (1856-1943). a) Nikola Tesla in 1890 (from [8]). b) An experiment in Tesla's laboratory (from [9]).

Later, he built the Wardenclyffe tower for developing transatlantic transmission of power (Figure 1.1.2) to longer distances using the ionosphere, but the project failed. Tesla also developed the synchronous and asynchronous induction motors and generators, the polyphase system based on rotating magnetic fields. He was the president of the first IEEE association, known at that time as the American Institute of Electrical Engineers.

It was not until 1960 that the Wireless Power Transfer concept was revisited with two different approaches, far-field beam WPT and near-field coupling. Both alternatives were proposed years back by Nicola Tesla.

1.1.1. Evolution of wireless power beaming

When plane waves radiated by a tranmitting antenna are used to transfer power directive, we refer to it as wireless power beaming. Receiving this far-field power requires a receiving antenna and associated circuitry. The first rectenna (rectifying antenna) was developed in 1960 by William C. Brown at Raytheon. With the high-frequency sources available at that time and with theoretical studies, demonstrated beaming between 1964 to 1968,

Figure 1.1.2: Wardenclyffe Tower in 1904. It was demolished in 1917 (from [10]).

with a microwave powered small helicopter (drone) (Figure 1.1.3.). For this purpose he designed a rectenna working at 2.45 GHz, receiving 270 W DC from a magnetron transmitter. The time of flight was 10 hours [11].

In 1968, the Solar Power Satellite (SPS) project was conceived to transfer energy harvested from a geostationary satellite solar power station to ground, and this topic is still active today [12]- [14]. The U.S. National Aeronautics and Space Administration (NASA) and Department of Energy showed interest in this project and in 1970, a laboratory experiment was performed with a 50.5 % total efficiency (DC to microwave, to beam propagation, to microwave again, to DC) at 300 kW CW, 3 kHz and a few feet of distance [15] (see Figure 1.1.4).

In 1975 Brown and R. Dickinson succeeded in the largest field experiment to date. They could transmit 30 kW DC at 1.6 km, with 82.5 % of rectification efficiency at JPL-Raytheon [16]. This project was done at the 26 m Goldstone Deep Space network parabolic Antenna (Figure 1.1.5). The experiment succeeded, but it was clear that the size was a limiting factor for commercial applications.

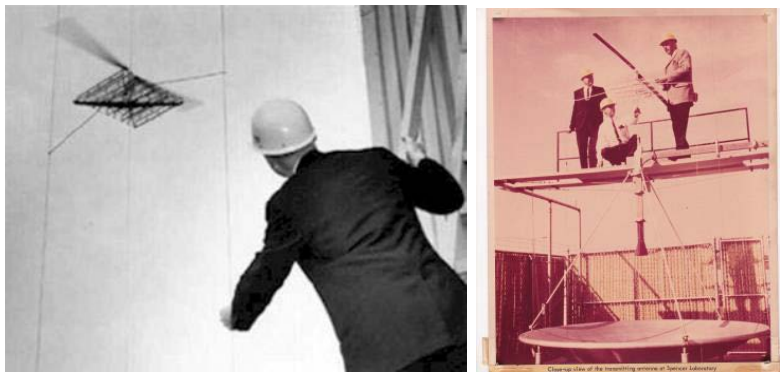

(a) (b)

Figure 1.1.3: First demonstration of a flying drone using microwaves © [2018] IEEE (from [17]). a) Brown and the flying drone. b) Transmitter.

In 1987 a larger WPT field experiment was done in Canada by the Communications Research Centre. They tested the SPS project using a model fuel-less airplane (2.9 m and a wingspan of 4.5 m) at 150 m height, instead of using a satellite [18]. It was named the Stationary High Altitude Relay Platform (SHARP). A thin film array of dipoles with associated rectifying diodes coating the plane were used. This was a prototype for a high altitude flight unmanned airplane, used as a platform for communications and surveillance, covering a 1000 km diameter area. They used a 2.45 GHz parabolic antenna to transmit 10 kW (see Figure 1.1.6).

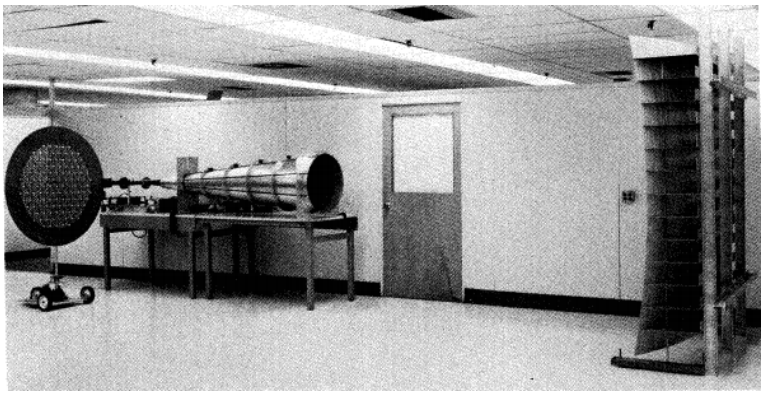

Figure 1.1.4: Laboratory experiment by NASA and Brown © [1973] IEEE (from [15]).

Figure 1.1.5: Venus Site of the JPL Goldstone Facility in California © [2018] IEEE [17]. The dish is used to transmit and the rectenna array is a panel seen in the distance.

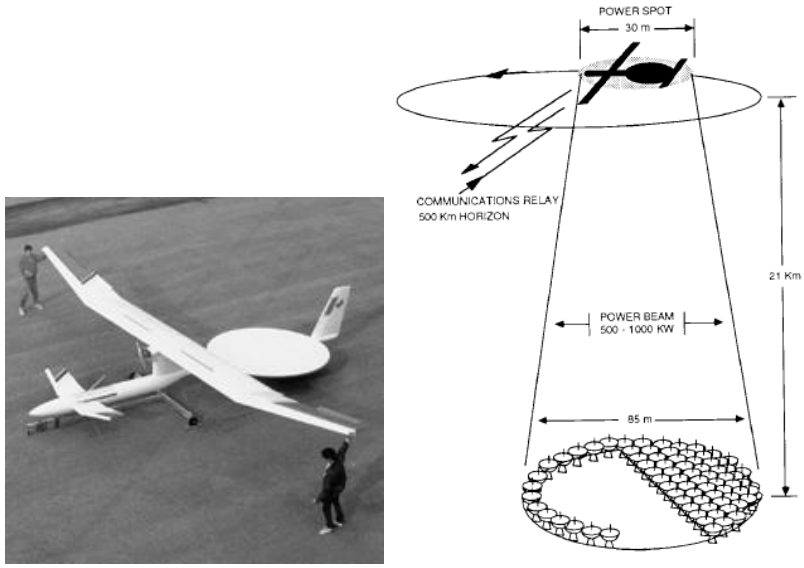

(a) (b)

Figure 1.1.6: SHARP flight project using a 1/8 airplane model © [2018] IEEE (from [17]). a) Miniaturized airplane model drone. b) Transmitter scheme and miniaturized airplane model.

In Japan, the first rectenna was designed in the 1980s and the first rocket experiment was performed in 1983 by Hiroshi Matsumoto (Kyoto University) [19]. In 1992, at Kyoto and Kobe universities, a project similar to SHARP was conducted, the microwave-driven airplane at Microwave Lifted Airplane Experiment (MILAX) project. It was the first phased array antenna used to beam microwaves, and it demonstrated that the beam could be tracked automatically. In 1994, they performed a fixed target experiment to transmit power to an isolated region. A 3 m diameter parabolic antenna and a 5 kW and 2.45 GHz magnetron were used. A rectenna array (3.2 by 3.6 m) was located at 42 m, with a 74 % efficiency [20].

In 1997, a microrobot moving inside a pipe was powered through WPT at 14 GHz, using the pipe as a TE11 mode waveguide [21]. The robot was able to move at a rate of 1 mm/s when 1 W was transmitted, receiving 50 mW. In [22] an observation robot in a 155 mm diameter gas pipe was powered at 2.45 GHz through WPT. Some problems appeared relate to propagation loss in rusty pipes and its complex branching.

Some research has been conducted in Europe over the past years. European Space Agency (ESA) focused in the Solar Power Satellite project, but considered laser power transfer for aperture size reduction. Also, in 2000 a microwave point to point WPT link was designed to provide 10 kW of electricity to the village of Grand-Bassin, in Reunion Island (France), located inside a canyon with difficult access [23,24]. A power density of 5 mW/cm^2 was distributed over a receiving area of 1000 m^2. The transmitting antenna consisted of several parabolic reflectors fed by several microwave sources, forming a phased array. The overall efficiency of 57 % was expected at 700 m distance. A prototype was built and presented in the Wireless Power Transmission conference in 2001 in La Reunion. Due to estimated expenses, the project was cataloged as uneconomic.

Around 2000 the concept of Ubiquitous Power Source (UPS) was established for describing a situation where microwaves are continuously available for charging devices [25], as illustrated in Figure 1.1.7. The idea was to create an uniform microwave power density at 2.45 GHz (ISM band) through slot antennas located at the ceiling around a shielded room. A power density of 1 mW/cm^2 or less was used to prevent problems in the human body under continuous exposure [26]. An improvement to UPS was done in [27] reducing radiation exposure and transmitting power through the use of a phased array design. Total power was reduced from 150 W in the former design to 22 W.

In 2008, in an attempt to improve the SPS project, solar energy was captured from the top of a mountain in Maui, in the Hawaiian Island archipielago, and a 150 km link beamed power to the main island of Hawaii, transmitting 20 W [28]. Although the received signal was very poor, promising results were expected just adjusting the link budget.

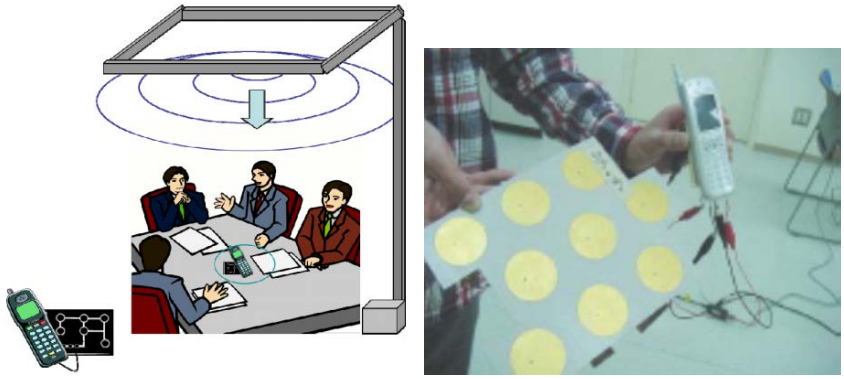

(a) (b)

Figure 1.1.7: Ubiquitous Power Source in a building. a) Concept of ubiquitous power source © [2011] IEEE (from [27]). b) Wireless mobile phone charging experiment using a UPS (from [29]) .

In 2009 a UPS to transmit information and power wirelessly from an airship to ground was designed, at 33 m height (Figure 1.1.8). It was designed for being used in emergencies such as rescues, where no coverage signal is available. Therefore, the mobile phone may be impractical if there is no electricity available or coverage. Measurements were done in Uji ground at Kyoto University. A retrodirective antenna, which transmits the signal in the same direction that incoming waves come, was employed to focus the beam into the target. 200 W CW at 2.45 GHz were transmitted to a cell phone charging system. It was active using a twelve rectenna array in the receiver side [30], while the coverage signal was provided.

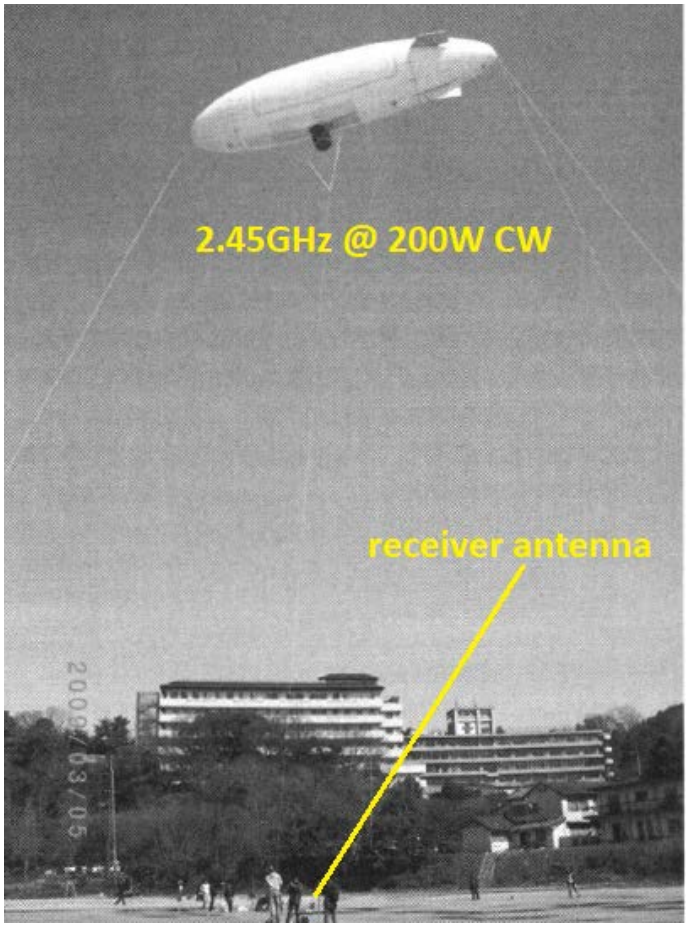

Figure 1.1.8: Microwave power and information transmission from an airship [31].

In 2010, a wireless grid scenario inside a building was developed combining the WPT concept with Wireless Sensor Networks (WSNs), providing reliability to the sensor network and creating a green building, as illustrated in Figure 1.1.9. In this work, solar panels transformed solar energy into DC while it was then converted to RF. Grid nodes with RF transmitters provided RF power around the building where different sensors were located [32], [33]. Sensors were equipped with rectennas to get DC power to interact with its server. Wasted energy was recycled by rectennas installed around the building.

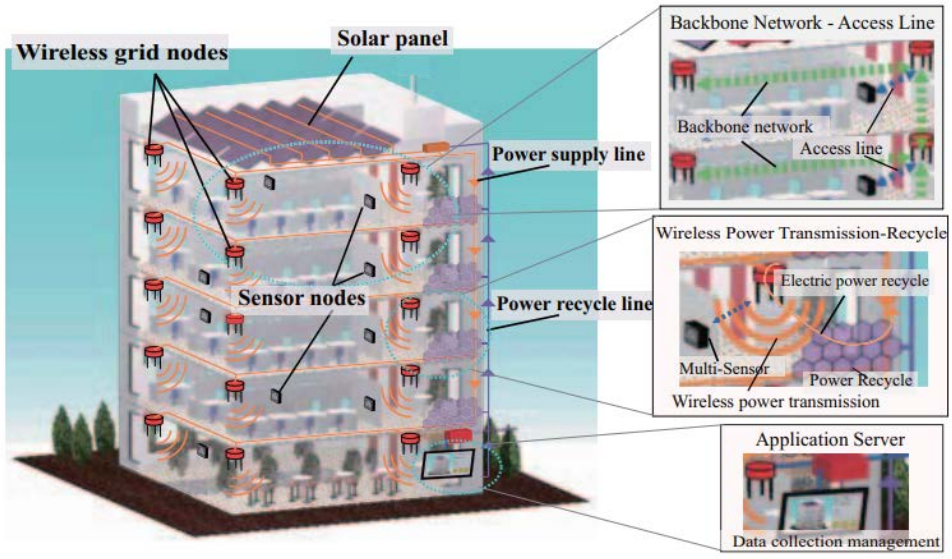

Figure 1.1.9: Wireless grid scenario. Building prototype © [2011] IEEE (from [33]).

A Mars observation microwave driven airplane for continuous surface monitoring was designed by Kyoto University and Kyushu Institute of Technology in 2011. With this prototype the main limitations of the rover were overcome, this is that not bumpy areas can be observed. This is a possible

alternative to the rover, but due to the atmospheric conditions on Mars, the airplane should be as small and light as possible [34, 35].

In 2015 a flying drone was proposed to power a wireless sensor network, to reduce the distance between transmitter and the WSNs, as beam efficiency decreases with distance and antennas can be smaller. It was designed at 5.8 GHz, using an 8 by 8 array (21 dBi) transmitting 8.74 W, resulting in 6.1 mW DC power. The project was named Multicopter Assisted Wireless Batteryless Sensing System (WBLS) and it was developed by WiPoT, Kyoto University, Mini-Surveyor Consortium, and Autonomous Control Systems Laboratory. This drone received readings from sensors, so its application can be extended, for example, to power and monitor sensors close to volcanos or for monitoring critical infrastructures such as tunnels or bridges [36].

1.1.2. Evolution of near-field wireless power

The near-field approach had an important milestone in 1894 when M. Hutin and M. Le-Blanc patented the first method for inductively powering supply lines, at 3 kHz, without mechanical contact for electrically-propelled vehicles [37]. It was not until 1980 and 1990 when new research projects for powering Electric Vehicles (EVs) were started [38]. Also, some commercial devices started using wireless chargers (electric razor, electric toothbrush) through near-field inductive coupling. Wireless chargers are divided into three categories based on the power level, mW for charging phones in coffee shops, W for the household appliance or kW for vehicles.

In 2006, the Massachusetts Institute of Technology (MIT) investigated resonant coupling [39], another non-beam technology for delivering power wirelessly though resonant magnetic coupling, getting efficiencies around 90 %. Nowadays, this technology is available on the market for a variety of applications, for example, charging a car battery in motion. 2010 marked a radical change with the appearance of the first prototypes of wireless chargers for smartphones. This was performed by the Wireless Power Consortium (WPC) [40], formed by more than 600 companies and the Airfuel Alliance [41]. The latter was created in 2015 as a coalition of innovative

companies who developed a common standard for eliminating cords using wireless power (diverse companies are in this consortium: semiconductor, device manufacturers, automotive or infrastructure providers). The WPC developed a wireless charging standard (Qi-Certification [42]) for wireless chargers up to 15 W. More than 3,700 Qi-Certified devices can benefit nowadays from this technology. WPC is working on extending the available power to 60 W, to include laptops. This standard is being extended to other purposes such as cordlees kitchen (Ki standard) where an induction cooktop is hidden beneath the kitchen countertop (Figure 1.1.10) or any other similar surface, delivering up to 2200 W to supply kitchen appliances such as a toaster or a coffee maker [43].

(a) (b)

Figure 1.1.10: Ki Cordless Kitchen prototype (photo Courtesy of the Wireless Power Consortium [44]). a) The induction cooktop is hidden beneath the kitchen countertop. b) Zoom of the inductive cooktop.

At the TechCrunch conference in 2013, a company proposed "Cota", a wireless mobile charger able to remotely charge an iPhone 5 [45]. 1 W of power was delivered at 2.45 GHz at a distance of 10 m. Other companies are introducing devices in the 5.8 GHz ISM band. Higher power standards are also available (robotic vacuum cleaners, e-bikes), where the available power is being extended up to 200 W.

1.2. A general overview of WPT

Wireless Power Transfer is gaining increased interest for a variety of untethered applications ranging from low power levels for unattended sensors to kilowatt levels for vehicle powering. Generally, wireless power transfer can be classified into six approaches as illustrated in Figure 1.2.1: a near-field inductive coupling or capacitive coupling, near-field resonant coupling, near-field over-moded cavity, far-field directional beaming, and far-field non-directive, also known as energy harvesting, although some authors consider the reactive types to be the same (inductive, capacitive and resonant).
The International Telecommunication Union (ITU) has performed reports summarizing all these different alternatives around the world, to deal with the wireless power transfer. Report ITU-R SM.2303 [46] collects information about WPT non-beaming projects such us magnetic induction, magnetic resonance and capacitive coupling technology, whereas Report ITU-R SM.2392-0 [47] focuses on beaming WPT. Therefore, in this section all different alternatives for WPT are shown, being classified concerning the regions where the fields are present (reactive near-field or radiative far-field).

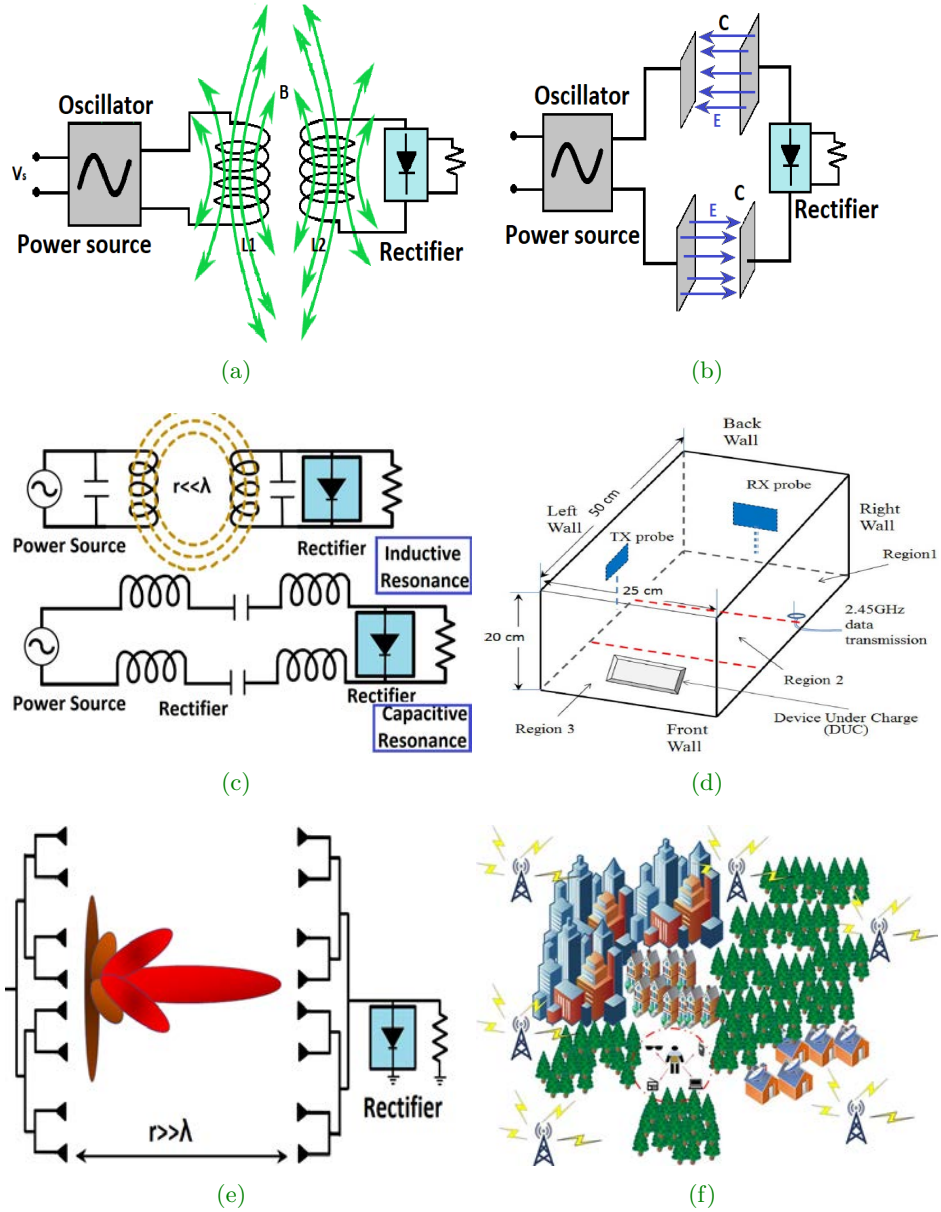

Figure 1.2.1: Different Wireless Power Transfer approaches: a) Near-field inductive coupling. b) Near-field capacitive coupling. c) Near-field resonant coupling. d) Near-field over-moded cavity © [2014] IEEE (from [48]). e) Far-field directional beaming. f) Far-field energy harvesting.

In the near-field region, non-radiative fields are present in the surrounding of the source (one wavelength). Power can be transferred over short distances by electric field taking advantage of the capacitive coupling between two metal electrodes or by magnetic field using the inductive coupling between coils. The transfer is more effective when the L/C are resonated with C/L as in a resonant transformer, increasing the power transfer efficiency. In the far-field (distances beyond $\frac{2D^2}{\lambda_0}$ from the source) electromagnetic waves carry the energy from the transmitter to the receiver. The amount of radiated power by an antenna depends on its electrical size. In electrically small antennas (antenna size $\ll \lambda$) little power is radiated due to the quasi reactance performance of the input impedance of the antenna. Nevertheless, a dipole antenna, with about the same size as the wavelength, radiates electromagnetic waves in almost all directions. Therefore, a receiver antenna will capture a small portion of radiation and if the radiated energy is not captured, it is lost, producing an inefficient transmission. Directive antennas can solve this issue, focusing the radiated power and generating a longer path transmission. As stated by Rayleigh criterion where antenna size must be larger than the wavelength to narrow the beam, high gain antennas can be beneficial (for example, parabolic antennas). Therefore, in far-field two different approaches are developed, depending on the way electromagnetic waves arrive at the receiver. The first approach is the WPT beaming. In this case, a specific source generates EM waves that are transmitted with a specific frequency and power. Narrow beam antennas (very directive) are used on both sides. Long distances can be covered with this technology (km), according to the Friis line of sight formula. Nevertheless, omnidirectional or non-directive antennas can be used to transmit the energy. In this case, instead of using unique purpose sources, available ambient EM energy is employed and a non-directive antenna is used at the receiver. As multipath effects and dispersion can affect the polarization and angle of arrival, non-directive dual polarization antennas (linear or circular) are desired. Non-directive WPT is also known as energy harvesting or scavenging.

1.2.1. Near-field inductive coupling

In this approach, the energy is transferred through the magnetic field using two coupled inductors, where an AC current in the coil at the transmitter (L1) induces electromagnetic forces in the receiver (L2), creating an alternating current through the load of L2, which can be a receiver (see Figure 1.2.2).

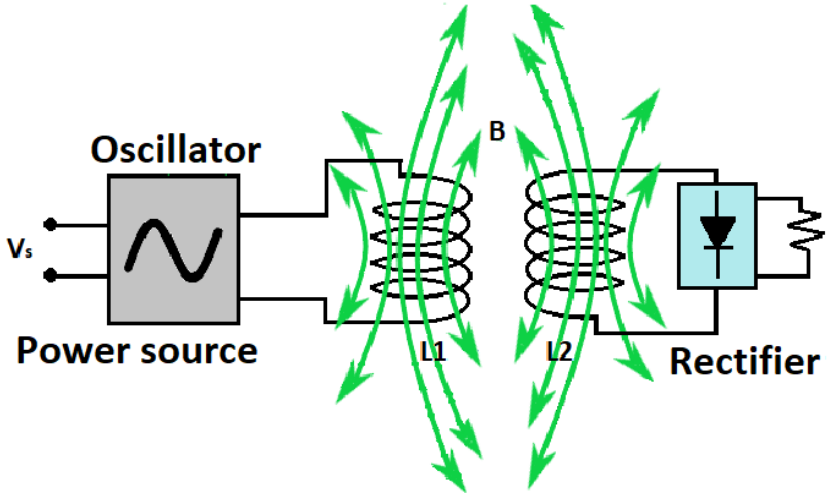

Figure 1.2.2: Near-field inductive coupling scheme.

This is done at specific standardized frequencies ranging from a 100 kHz to 27.12 MHz (6.78, 13.56 and 27.12 MHz). Although high power levels can be transferred with an efficiency above 80 %, the systems are sensitive to alignment and require ferrite materials for focusing the magnetic field at larger distances from the coil, increasing the efficiency.

Inductive coupling is the oldest option that has been available in the market since the 1990s for charging of battery-operated toothbrushes (Figure 1.2.3). Induction cooking and more recently, watt level powers are also inductively transferred (although some capacitors are employed to increase the efficiency, being considered resonant) in some consumer applications

such as phone charging in coffee shops as the ones provided by PowerMat for Starbucks [49,50]. A contactless planar desk-like surface wireless power transfer system has been designed to wirelessly charge a laptop through a coil embedded in the planar surface [51].

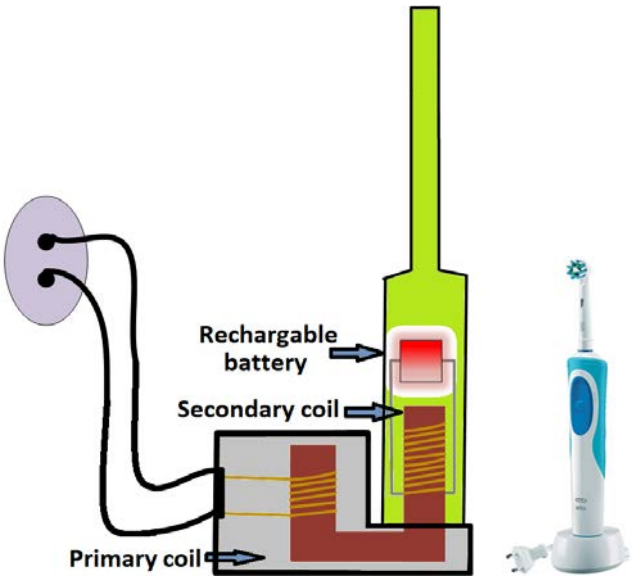

(a) (b)

Figure 1.2.3: Working principle of a electric toothbrush prototype.
a) Circuit schematic. b) Commercial Oral toothbrush courtesy of Oral B (from [52]).

The transcutaneous charging of biomedical implants is powered through inductive coupling such as cardiac pacemakers [53,54] to avoid having wires passing through the skin (Figure 1.2.4). In this case, a primary coil is placed outside the body, over the skin, and the second coil is placed inside, beneath the collarbone, 15 cm below the skin. Although it is announced as inductive, metallic plates are used to increase the efficiency as explained, so it is not easy to distinguish between inductive or resonant coupling as the difference is blurred.

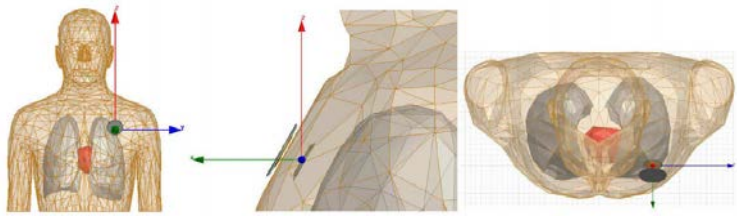

(a)

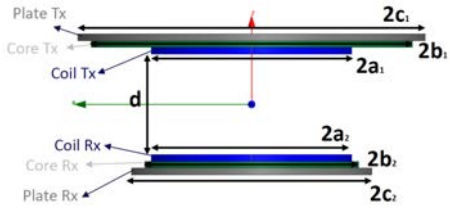

(b)

Figure 1.2.4: The pacemaker charging system. a) Coil L1 is outside the body, and coil L2 is inside the human body. b) Use of ferrite core plates and aluminum plates to improve the coupling [55].

1.2.2. Near-field capacitive coupling

Capacitive coupling is based on the transmission of power between two electrodes using electric fields or displacement current ($\varepsilon \frac{\partial E}{\partial t}$) (see Figure 1.2.5). Murata Manufacturing presented in 2015 the first module for capacitive coupling WPT [56].

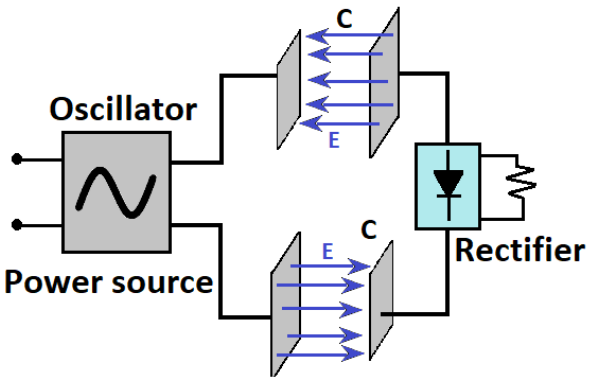

Figure 1.2.5: Near-field capacitive coupling scheme.

The capacitive coupling has recently been applied to charging battery powered portable devices, as well as charging or continuous wireless power transfer in biomedical implants [57]- [59]. EVs have benefited from this technology although just a few limited cases of capacitive power transfer can be found in the literature, as in [60]- [64]. Car powering through WPT capacitive coupling is limited to distances between 12 cm and 20 cm [65]- [67] (see Figure 1.2.6) and frequencies ranging from a kHz to a few MHz. Buses and trains use this technology to power transit vehicles [68]- [70]. Bikes have been tested to recharge the battery on the way [71]. The magnetic field focusing is required to maintain the fields in the surroundings below the levels imposed by safety regulations [72].

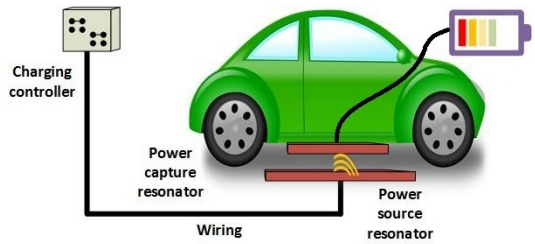

Figure 1.2.6: Capacitive charging of stationary electric vehicles.

1.2.3. Near-field resonant coupling

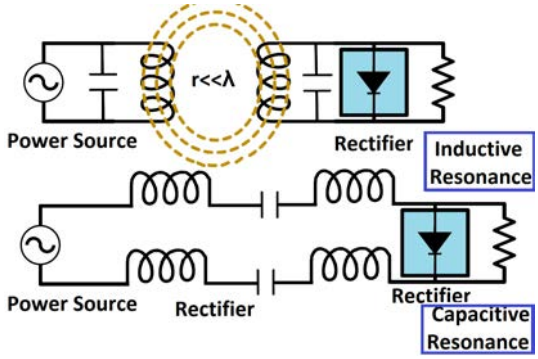

Figure 1.2.7: Near-field resonant coupling scheme.

Some authors consider all the reactive types of near-field WPT to be the same (inductive, capacitive and resonant coupling). Indeed, the difference between them is very small. In this case, an inductor (L) resonates with a capacitor (C) and vice versa to get a better efficiency. Some articles do not specify exactly the model, so the classification can be confusing, but most of them can be considered resonant coupling. Indeed, the main difference is that the highest efficiencies can be obtained with the resonant coupling due to the high Q of the resonator, in some cases achieving up to 90 %.

Electric Vehicles (EVs) have benefited from this technology. Although the percentage of EVs in the market is low (around 1 % in Spain in 2019), it is a well-qualified substitute for internal combustion engine vehicles. Great improvements have been done in the previous years increasing the autonomy of the vehicle through better batteries and charging systems [73, 74]. But it is a still an important limitation as a combustion vehicle has a range of 850 km, while EVs have less than two or three times that (on average 350 km), which is not enough. Electric vehicles with the longest driving range can offer up to 575 km [75]. A possible solution for mitigating this issue is using WPT to charge the vehicle in motion on the road or in parking lots or garages. Indeed, the second alternative is more reliable although 20 kW of power can be transferred at crussing speeds on the road [76]. In [77], a WPT system provides 50 kW over a 12 cm gap with a 90 % efficiency over an area of fewer than 1 m^2.

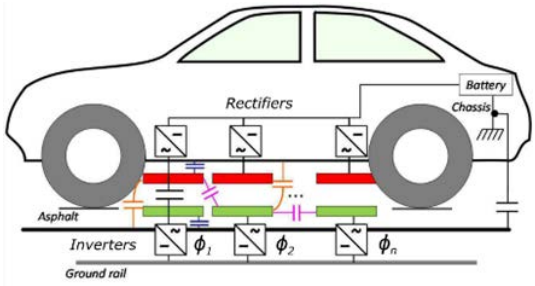

Figure 1.2.8: Near-field resonant coupling used for the charging of electric vehicles on motion © [2017] IEEE (from [77]).

For shorter distances, on the order of millimeters, that are used for example in industrial machinery [78], efficiencies about 90 % at power levels above 20 kW have been reported with inductive transfer by using rotary transformers.

In [79], a resonant inductive link for remote powering of pacemakers at 403 MHz was established, delivering up to 1 mW. It exploits the magnetic coupling interaction between an implanted resonator and an external one, so an implantable device such as a pacemaker can be powered. An average Specific Absorption Rate (SAR) of 1.08 W/kg was measured, being lower than the recommended limit of 2 W/kg.

1.2.4. Near-field over-moded cavity

Another approach is near-field powering with waves in contrast to reactive fields, represented again in Figure 1.2.9 [80, 81]. In this shielded over-moded resonant cavity approach many different modes are superimposed to form a well-distributed electromagnetic field that can power multiple devices simultaneously. Devices are powered by EM waves in a three-dimensional arrangement through rectennas. This has been demonstrated at microwave frequencies between 2 GHz and 10 GHz [48, 82].

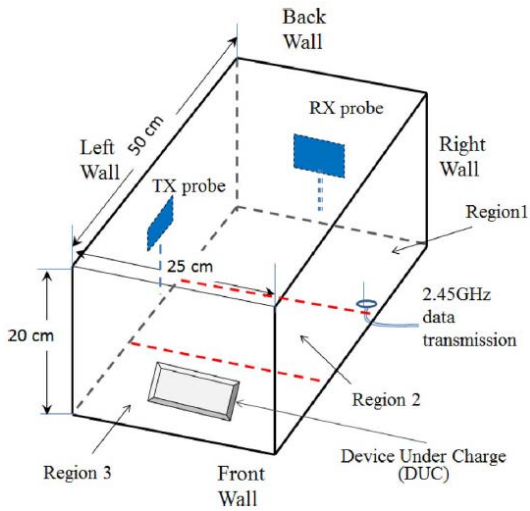

Figure 1.2.9: Near-field over-moded cavity © [2014] IEEE (from [48]).

Besides demonstrating the simultaneous powering of several devices, a statistical analysis was done for obtaining the associated power density distribution inside the multi-mode cavity [83].

1.2.5. Far-field beaming

Some of the earliest demonstrations of wireless power transfer were done by far-field power beaming Figure 1.2.1 (e). In this approach, a directional transmitting antenna beams microwave energy (from a few to tens of GHz) to an array of antennas and rectifiers with high power density, known polarization, range and position. Applications include Solar Power Satellite (SPS), Unmanned Aerial Vehicle (UAV) powering or some biomedical sensor. WPT beaming uses only the carrier of the microwave to transmit the power. In 1968 the SPS project was proposed to transform and deliver solar energy into DC at ground, using microwaves [84]. This project has not been concluded yet but different targets have been achieved through all these years. Other examples include Brown's helicopter [85] as well as the SHARP project detailed in the previous section.

In these applications, the efficiency is very important because of the high power levels and long-range, and it includes the efficiency of the transmitter, beaming efficiency, and rectifier efficiency.

1.2.6. Far-field energy harvesting or scavenging

Non-directive WPT is also known as energy harvesting or scavenging. Here, very low power densities are received from unknown transmitters in the far-field (ambient electromagnetic energy) and the energy is stored over a long time and ultimately rectified (using rectennas, see Figure 1.2.10) to power low duty cycle and low power consumption devices such as wireless maintenance unattended sensors Figure 1.2.1 (f). Different frequency ranges have been studied covering TV [86], mobile base stations [87] or ISM bands [88]. Also, some applications have been designed to use RF signals from the satellite to do satellite health monitoring [89], or side lobe

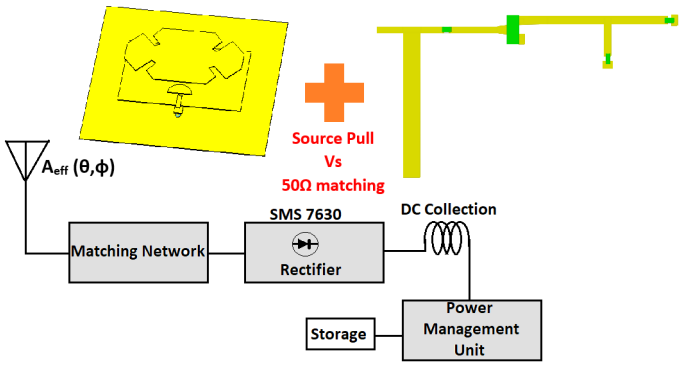

Figure 1.2.10: Rectenna: antenna and rectifier integration from [90].

power from altimeter antennas in airplanes to power up sensors [91]. Different devices have been powered through scavenging ambient power, for example, a common quartz clock antenna [92] used in kitchens. Wearable rectennas [93]- [96] have been implemented to monitor biological parameters or power wearable devices. In [97], a broadband wearable rectenna screen printed over a cotton T-shirt is presented. In Chapter 5 , this work will be addressed, extending the study.

Although scavenged power is low, it can be enough to remove batteries from wireless sensor networks. As stated in [98], thousand of unattended sensors are spatially distribute in remote areas (inaccessible places or even unknown) of many kilometers, decreasing cost associated with battery replacement and making the system more robust (autonomous design) and clean is desirable. Energy harvesting can be an option to power them and ZigBee/IEEE802.15.4 sensors (see Figure 1.2.11) are potential candidates for this technology [99]. Therefore, the main goal here is dealing with the very low power densities (on average on the order of 1-10 μW/cm^2) to collect and rectify enough power to autonomously work with a sensor. To conclude, in Table 1.1, a comparison of all WPT technologies is shown, where N.F stands for Near-field and F.F, Far-field.

Technology	Range	Frequency	Energy transfer element	Application
Inductive Coupling	Short (N.F)	Hz – MHz	Coils	Electric toothbrush, Induction stovetops
Capacitive Coupling	Short (N.F)	kHz – MHz	Metal plates electrodes	Charging portable devices, Biomedical implants
Resonant Coupling	Mid (N.F)	kHz – GHz	Resonators	Charging portable devices (Qi), Biomedical implants, Electric vehicles
Over-moded Cavity	Short (N.F)	GHz	Shielded Cavity	Charging portable devices
Far-field Beaming	Long (F.F)	GHz	Directive antenna	Solar power satellite, Powering drone aircraft
Energy Harvesting	Long (F.F)	GHz	Omnidirectional antenna	Charging WSN

Table 1.1: Comparison of WPT technologies.

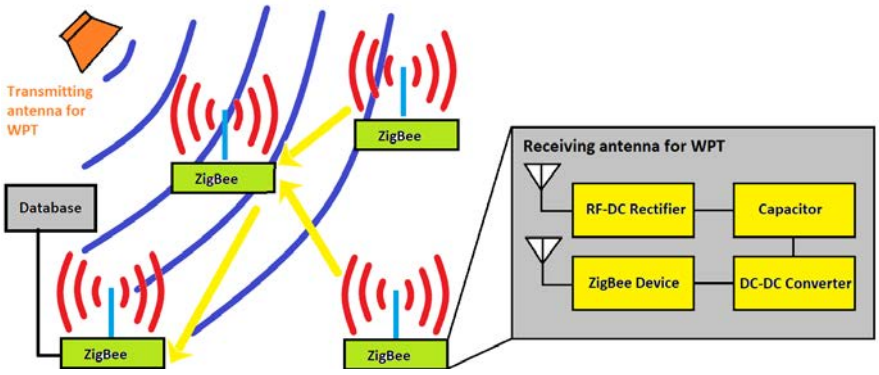

Figure 1.2.11: Wireless powered sensors (ZigBee).

1.3. Scope of the thesis

This thesis focuses on an important extension of this last approach (energy harvesting) for a realistic radio frequency environment that contains multiple stochastic sources, as illustrated in more detail in Figure 1.3.1. As already explained, energy harvesting has a limitation with the very low power density available, on the order of $\mu W/cm^2$. In order to get enough DC power two alternatives can be applied.

The first alternative is to collect more RF power scavenging from more communication bands (use of multiband or broadband antennas). For example, in [100] power was scavenged from 915 MHz and 2.45 GHz getting 11.6 μW and 65.6 μW under 1 $\mu W/cm^2$. Also, in [101] a total of 26 % of power conversion efficiency at -11.4 dBm (averaged power) was obtained at six bands (550, 750, 900, 1850, 2150 and 2450 MHz). In [102] a rectenna working from 1.1 to 2.7 GHz with a maximum of power conversion efficiency ranging from 60 to 85 % was achieved from 0 to 15 dBm. This is a high-efficiency value for energy harvesting. Indeed, those input power values correspond to a WPT beaming application.

The other option is to increase the rectified DC power with different rectification topologies [103]. Most of the works in energy harvesting are

based on Schottky diodes, either in single topology, in series or shunt, or even using multiple diodes such as in a Greinacher (voltage doubler) or a Villard topology. Usually, in EH the output voltage of the rectifier is low due to the low power density limitation. If more bands are used, a cascade of multiplier stages rectifiers can increase the output voltage to power a low consumption IC without using a DC-DC converter. This is just possible when more than one band is used, to overcome the voltage threshold of N diodes, as this means more losses. In [104, 105], different topologies are studied. Just with one band, sometimes is difficult to work with one diode, so a single topology is desired. Just to mention that in [106], heterojunction backward tunnel diodes are proposed as a solution to the maximum efficiency limit reached by Schottky diodes. In this case, the study is based on the electron level, getting promising results, but it is out of the scope of the thesis.

The theory presented in this thesis proposes another alternative for improving the RF-DC power conversion efficiency based on the multiple-tone scenario of the first alternative. Previous studies have been published about an empirical improvement in the RF-DC power conversion efficiency when working with high Peak to Average Power Ratio (PAPR) signals, compared to a CW signal with the same average power [107]- [109]. This is due to the non-linear effects in the diode junction at the exponential region. Some attempts to model this performance were done [110, 111], although an essential parameter of the diode (the series resistance, R_S) was neglected for simplicity, and therefore, not accurate results were presented. This thesis overcomes that limitation taking into account the series resistance of the diode, thus, leading to a more accurate result. A more comprehensive analysis of the rectifying diode IV non-linear characteristic is shown. An improved understanding of the rectification process for multiple-tone signals is presented in a energy harvesting scenario characterized by very low power densities. A mathematical model that predicts the expected DC current of the diode when excited with multiple tones is proposed, having a good agreement with simulations and measurements, and showing an RF-DC power conversion efficiency improvement due to the fact of using multiple tones instead a CW with the same average power. Moreover, this

analytical approach is useful to quickly compute the DC output current of the diode instead of using a harmonic balance simulation, especially when no convergence is achieved. To validate this mathematical model over a rectenna, a broadband antenna was chosen and a prototype was designed and measured, showing an efficiency improvement under multiple-tone signals, for scavenging ambient energy from different bands. Figure 1.3.1 illustrates an example of measured electric field spectrum inside a laboratory at University Charles III of Madrid in July 2019 where multiple wireless applications are present and can be harvested (at that moment 5G had not been deployed yet) so measurements are plotted up to 2.5 GHz.

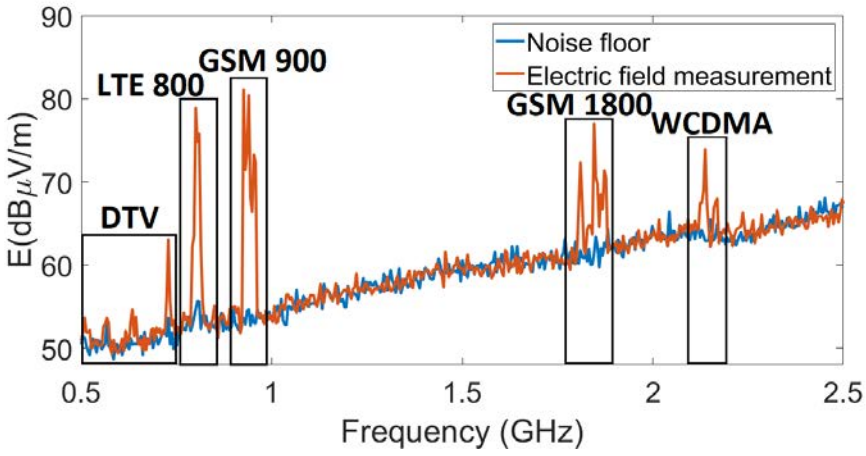

Figure 1.3.1: Measured electric field spectrum at indoor scenario at University Charles III of Madrid.

1.4. Challenges of the thesis

This thesis addresses some challenges that need to be solved for designing a practical wireless power transfer system:

- Sources are at different frequencies covering a wide bandwidth. The radio part of the electromagnetic spectrum is rich in applications, so the energy is spread over a wide bandwidth (DTV (480-780 MHz), GSM 900, GSM 1800, WCDMA 900, WCDMA 2100, LTE 800, LTE 1500, LTE 1800, LTE 2600 and 5G in 700 MHz, 1500 MHz and 3500 MHz approximately. Also, WiFi at 2.45 GHz and 5.8 GHz and Wimax at 3.5 GHz.

- Sources have different carrier frequencies, instantaneous signal bandwidths, power levels and modulations resulting in variations in power density and polarization due to multi-path and increased range.

- Since most of the time power densities are very low, large arrays can be used to receive sufficient power although size can be a problem in some applications.

- For unattended wireless sensors there are often size constraints, limiting the collection area and since the power density is small, a low level of total power is collected. It makes it difficult to turn on a diode rectifier and even more difficult to make it efficient.

- Incident power densities vary significantly, so the non-linear impedance of the rectifier is important and varies versus frequency and power. Due to this variation, rectification varies as well, requiring an efficient power management unit.

- Multiple-tone signals have been proven as an empirical alternative to increase the RF-DC power conversion although not accurate theoretical analysis have been performed.

  This thesis focuses in a mathematical non-linear characterization of the diode under multiple-tone signals.

1.5. Thesis outline

The thesis addresses all of the about challenges and the content has been divided following this outline.

In the first chapter, a brief introduction to the evolution of wireless power transfer is presented. With Maxwell's theory and Hertz's experiments in electromagnetic waves, Tesla was able to perform the first wireless power transfer experiment for the lighting of an exhibition enclosure. It was not until years later, in 1964, that William C. Brown could power a small helicopter at 2.45 GHz using electromagnetic waves and a rectenna.
The wireless power transfer mechanism includes six approaches (although inductive, capacitive and resonant coupling can be unified into the same category due to the similarity in its working principle): i) reactive near-field through magnetic coupling using coils or capacitors; ii) near-field overmoded cavity; iii) far-field directive beaming; iv) far-field non-directional powering /harvesting. All these approaches are explained in the first chapter, emphasizing the last one, which is the topic of this thesis. Besides, an analysis of the state of the art is presented with the most significant values of conversion efficiency, as well as the main characteristics of various designs. A wireless power receiver consists of an antenna, rectifier and DC collection circuit. The rectifier is typically implemented with non-linear devices such as diodes.

In the second chapter, the performance of the diode is explored theoretically. For very low incident power densities (those present in the environment), the diode operates in its non-linear region. Some previous works attempted to perform a mathematical model to predict its performance under multiple-tone excitations, although an essential parameter was neglected for simplicity. In this chapter, all parameters that govern the Schockley diode equation are taken into account, getting an accurate diode modeling. This mathematical analysis for multiple input sinusoidal signals of different powers and frequencies is developed showing an efficiency improvement when working with high PAPR signals.

In Chapter 3, the theoretical model is compared and validated with non-linear harmonic balance simulations of a realistic diode. Quantitative

experimental validation is also provided for multiple input tones with a large resulting Peak to Average Power Ratio as improvements in conversion efficiency can be achieved. To do this, three different rectifier circuits were tested, developing an accurate Spice diode model (including parasitics) and an appropriate measurement setup. Otherwise, results will differ due to an inadequate characterization of the non-linear device. With this mathematical approach, it is not necessary to use a circuit simulator to predict the I_{DC} of the diode, avoiding convergence problems due to the use of a high number of harmonics in a harmonic balance simulator. The analysis shows that the relative frequency and amplitude of multiple simultaneous signals impact the amount of efficiency improvement.

A rectenna prototype for energy harvesting is presented in Chapter 4. This chapter deals with the design of the antenna. It is seen that different design criteria must be used when working with a WPT directive beaming application or a non-directive harvesting one, as happens in this thesis. The integration between the antenna and the rectifier is analyzed, showing possible alternatives. Indoor and outdoor measurements are shown using the rectenna prototype. An analysis of the electromagnetic spectrum is also included to demonstrate the feasibility of the rectenna model.

In Chapter 5 a wearable rectenna application is shown, with a broadband 2 to 5 GHz design, implemented on a cotton T-shirt. This application allows collecting enough energy to power low consumption sensors. Different array sizes are tested (4×4 and 9×9) from 4-130 μW/cm^2 power densities. The single element is a self-complementary tightly-coupled bow-tie array. CST simulations and measurements were performed, over phantom and over a torso. The electrical properties of the body tissues were taken into account and the influence of the thickness of each layer was studied. Moreover, the antenna performance was tested on different physiognomies (people with more adipose tissue or on the contrary more fibrous).

Finally, Chapter 6 collects the conclusions of the work shown in this thesis and ideas for future work. Some ideas are proposed about Chapter 2 to reduce the error of the mathematical approach when working in the non-linear region. Also, some possible improvements to the printed antenna of Chapter 5 are included such as adding a dual linear polarization.

References

[1] J.R. Hofmann. Andre-Marie Ampère: Enlightenment and Electrodynamics. Cambridge Science Biographies. Cambridge University Press,1996. ISBN: 9780521562201.

[2] Hirshfeld, Alan W. (2006). The Electric Life of Michael Faraday. Walker and Company. ISBN 978-0-8027-1470-1.

[3] T. K. Sarkar, Robert Mailloux, Arthur A. Oliner, M. Salazar-Palma, Dipak L. Sengupta - History of Wireless-Wiley-IEEE Press (2006).

[4] Mulligan, J.F, Heinrich Rudolf Hertz (1857-1894), Routledge Library Editions: Science and Technology in the Nineteenth Century Series, 2018.

[5] Cheney, M. Man Out of Time, Simon and Schuster Press.

[6] Glenn, J. (1994). The Complete Patents of Nikola Tesla Paperback, Dorset Press.

[7] Tesla, N. Marinčić, A. Popović, V. (1986.) Colorado Springs Notes, 1899–1900, Angriff Press.

[8] Nikola Tesla biography from Wikimedia Commons, the free media repository.
https://es.wikipedia.org/wiki/Nikola_Tesla.

[9] Rudinska, Iwona. Editor "The Tesla Collection." Original Article Author, "Article Title." Publication Publication Date: Page(s). http://www.teslacollection.com.

[10] Wardenclyffe Tower history from Wikimedia Commons, the free media repository. https://en.wikipedia.org/wiki/Wardenclyffe_Tower.

[11] W. C. Brown, "Experiments Involving a Microwave Beam to Power and Position a Helicopter," in IEEE Transactions on Aerospace and Electronic Systems, vol. AES-5, no. 5, pp. 692-702, Sept. 1969.

[12] N. Shinohara and S. Kawasaki, "Recent Wireless Power Transmission technologies in Japan for space solar power station/satellite," 2009 IEEE Radio and Wireless Symposium, San Diego, CA, 2009, pp. 13-15.

[13] K. Maki et al., "Microwave characteristics of a wireless power transmission panel toward the orbital experiment of a solar power satellite," 2012 IEEE MTT-S International Microwave Workshop Series on Innovative Wireless Power Transmission: Technologies, Systems, and Applications, Kyoto, 2012, pp. 131-134.

[14] S. Sasaki, K. Tanaka and K. Maki, "Microwave Power Transmission Technologies for Solar Power Satellites," in Proceedings of the IEEE, vol. 101, no. 6, pp. 1438-1447, June 2013.

[15] W. C. Brown, "Adapting Microwave Techniques to Help Solve Future Energy Problems," in IEEE Transactions on Microwave Theory and Techniques, vol. 21, no. 12, pp. 753-763, Dec. 1973.

[16] R. M. Dickinson, "Performance of a High-Power, 2.388-GHz Receiving Array in Wireless Power Transmission Over 1.54 km," 1976 IEEE-MTT-S International Microwave Symposium, Cherry Hill, NJ, USA, 1976, pp. 139-141.

[17] N. Shinohara, "History of Research and Development of Beam Wireless Power Transfer," 2018 IEEE Wireless Power Transfer Conference (WPTC), Montreal, QC, Canada, 2018, pp. 1-4.

[18] J. J. Schlesak, A. Alden and T. Ohno, "A microwave powered high altitude platform," 1988., IEEE MTT-S International Microwave Symposium Digest, New York, NY, USA, 1988, pp. 283-286 vol.1.

[19] H. Matsumoto, "Research on Solar Power Station and Microwave Power Transmission in Japan : Review and Perspectives", IEEE Microwave Magazine, pp.36-45, Dec. 2002.

[20] Shinohara N. and H. Matsumoto, "Dependence of dc Output of a Rectenna Array on the Method of Interconnection of Its Array Element", Electrical Engineering in Japan, Vol. 125, No. 1, pp. 9-17, 1998.

[21] T. Shibata, T. Sasaya and N. Kawahara, "Microwave energy supply system for in-pipe micromachine," MHA'98. Proceedings of the 1998 International Symposium on Micromechatronics and Human Science. - Creation of New Industry - (Cat. No.98TH8388), Nagoya, Japan, 1998, pp. 237-242.

[22] Hirayama, K., N. Shinohara, K. Hashimoto, H. Matsumoto, T. Nakauchi, and Y. Yoshida, "Fundamental Study of Microwave Power Transmission to a Robot Moving in Gas Pipes (in Japanese)", Proc. of IEICE Comm., p. 116, March 1997.

[23] A. Celeste, P. Jeanty, and G Pignolet, "Case study in Reunion island", Acta Astronautica, vol. 54, pp. 253-258, 2004.

[24] Celeste, A., J-D. L.S. Luk, J.P. Chabriat, and G. Pignolet, "The Grand-Bassin Case Study: Technical Aspects", Proc. of SPS'97, pp. 255-258, 1997.

[25] Shinohara, N., T. Mitani, and H. Matsumoto, "Study on Ubiquitous Power Source with Microwave Power Transmission", Proc. of International Union of Radio Science (URSI) General Assembly 2005. http://www.ursi.org/proceedings/procGA05/pdf/C07.5(01145).pdf.

[26] Requirements for support of ubiquitous sensor network (USN) applications and services in the NGN environment: Recommendation ITU-T Y.2221 (2010). https://www.itu.int/rec/T-REC-Y.2221/en.

[27] K. Hashimoto, T. Ishikawa, T. Mitani and N. Shinohara, "Improvement of a ubiquitous power source," 2011 XXXth URSI General Assembly and Scientific Symposium, Istanbul, 2011, pp. 1-4.

[28] Beam 'Space' Solar Power in Hawaii. https://www.wired.com/2008/09/visionary-beams/.

[29] N. Shinohara, T. Mitani, and H. Matsumoto, "Study on Ubiquitous Power Source with Microwave Power Transmission", Proc. of International Union of Radio Science (URSI) General Assembly 2005, C07.5(01145).pdf, 2005.

[30] Mitani, T., H. Yamakawa, N. Shinohara, K. Hashimoto, S. Kawasaki, F. Takahashi, H. Yonekura, T. Hirano, T. Fujiwara, K. Nagano, H. Ueda, and M. Ando, "Demonstration Experiment of Microwave Power and Information Transmission from an Airship", Proc. of 2nd International Symposium on Radio System and Space Plasma 2010, pp. 157-160, 2010.

[31] Bulleting of Research Institute for Sustainable Humanosphere Kyoto University (2009), 5: 12-12.

[32] D. Maehara et al., "Experiment on battery-less sensor activation via multi-point wireless energy transmission," 2013 IEEE 24th Annual International Symposium on Personal, Indoor, and Mobile Radio Communications (PIMRC), London, 2013, pp. 2336-2340.

[33] SR. P. Wicaksono, G. K. Tran, K. Sakaguchi and K. Araki, "Wireless Grid: Enabling Ubiquitous Sensor Networks with Wireless Energy Supply," 2011 IEEE 73rd Vehicular Technology Conference (VTC Spring), Yokohama, 2011, pp. 1-5.

[34] A. Nagahama et al., "Study on a microwave power transmitting system for Mars observation airplane," 2011 IEEE MTT-S International Microwave Workshop Series on Innovative Wireless Power Transmission: Technologies, Systems, and Applications, Uji, Kyoto, 2011, pp. 63-66.

[35] A. Nagahama, T. Mitani, N. Shinohara, K. Fukuda, K. Hiraoka and K. Yonemoto, "Auto tracking and power control experiments of a magnetron-based phased array power transmitting system for a Mars observation airplane," 2012 IEEE MTT-S International Microwave Workshop Series on Innovative Wireless Power Transmission: Technologies, Systems, and Applications, Kyoto, 2012, pp. 29-32.

[36] Multicopter Asisted Wireless Bateryless Sensing System. https://www.kyoto-u.ac.jp/en/about/events_news/department/seizonken/news/2015/150716_1.html.

[37] M. Hutin and M. Le-Blanc, "Transformer System for Electric Railways", US Patent Number 527,875, 1894.

[38] Shinohara, N., "Wireless Power Transfer via Radiowaves (Wave Series)", ISTE Ltd. and John Wiley and Sons, Inc., Great Britain and United States, 2014.1.

[39] Kurs, A., A. Karalis, R. Moffatt, J.D. Joannopoulos, P. Fisher and M. Soljačić, "Wireless power transfer via strongly coupled magnetic resonances", Science, Vol. 317, pp. 83-86, 2007.

[40] Wireless Power Consortium. https://www.wirelesspowerconsortium.com.

[41] AirFuel.
https://www.airfuel.org.

[42] Qi Certification.
https://www.wirelesspowerconsortium.com/knowledge-base/testing-and-certification/qi-certified-products.html.

[43] WPC Ki Cordless Kitchen Video.
https://www.youtube.com/watch?v=1CXDmgv9ws8&feature=youtu.be.

[44] Ki Cordless Kitchen Standard.
https://www.wirelesspowerconsortium.com/kitchen/.

[45] Aol Tech.
http://techcrunch.com/2013/09/09/cota-by-ossia-wireless-power/.

[46] Wireless power transmission using technologies other than radio frequency beam: Report ITU-R SMS.2303.
https://www.itu.int/pub/R-REP-SM.2303.

[47] Applications of wireless power transmission via radio frequency beam: Report ITU-R SMS.2392-0.
https://www.itu.int/pub/R-REP-SM.2392.

[48] S. Korhummel, A. Rosen and Z. Popović, "Over-Moded Cavity for Multiple-Electronic-Device Wireless Charging," in IEEE Transactions on Microwave Theory and Techniques, vol. 62, no. 4, pp. 1074-1079, April 2014.

[49] Starbucks: Powermat Wireless Charging.
https://www.starbucks.co.uk/coffeehouse/powermat.

[50] Powermat.
https://powermat.com/.

[51] J. A. Taylor, Z. N. Low, J. Casanova and J. Lin, "A wireless power station for laptop computers," 2010 IEEE Radio and Wireless Symposium (RWS), New Orleans, LA, 2010, pp. 625-628.

[52] Electric toothbrush Oral B from:
https://www.oralb.es/es-es/.

[53] Puers, R. (2008). Omnidirectional Inductive Powering for Biomedical Implants. Springer Science and Business Media. pp. 4–5. ISBN 978-1402090752.

[54] Sun, Tianjia; Xie, Xiang; Zhihua, Wang (2013). Wireless Power Transfer for Medical Micr2osystems. Springer Science and Business Media. ISBN 978-1461477020.

[55] Vulfin, Vladimir, Sayfan-Altman, Shai and Ianconescu, Reuven. (2017). Wireless power transfer for a pacemaker application. Journal of medical engineering and technology. 41. 1-8. 10.1080/03091902.2017.1299232.

[56] Production starts for Capacitive Coupling Wireless Power Transmission Module.
https://corporate.murata.com/en-eu/about/newsroom/techmag/metamorphosis16/productsmarket/wireless?intcid5=com_xxx_xxx_cmn_hd_xxx

[57] Erfani, R.; Marefat, F.; Sodagar, A. M.; Mohseni, P. (May 2017). Transcutaneous capacitive wireless power transfer (C–WPT) for biomedical implants. Proc. IEEE Int. Symp. Circuits and Systems (ISCAS), May 2017. pp. 2561–2564.

[58] Erfani, R.; Marefat, F.; Sodagar, A. M.; Mohseni, P. (April 2018). "Modeling and Characterization of Capacitive Elements With Tissue as Dielectric Material for Wireless Powering of Neural Implants". IEEE Trans. Neural Syst. Rehabil. Eng. 26 (5): 1093–1099. doi:10.1109/TNSRE.2018.2824281. ISSN 1534-4320. PMID 29752245.

[59] Erfani, R.; Marefat, F.; Sodagar, A. M.; Mohseni, P. (August 2017). "Modeling and experimental validation of a capacitive link for wireless power transfer to biomedical implants". IEEE Transactions on Circuits and Systems II: Express Briefs. 65 (7): 923–927. doi:10.1109/TCSII.2017.2737140. ISSN 1558-3791.

[60] H. Zhang, F. Lu, H. Hofmann, W. Liu, and C. C. Mi, "A four-plate compact capacitive coupler design and lcl-compensated topology for capacitive power transfer in electric vehicle charging application," IEEE Transactions on Power Electronics, vol. 31, no. 12, pp. 8541–8551, Dec 2016.

[61] J. Dai and D. C. Ludois, "Capacitive power transfer through a conformal bumper for electric vehicle charging," IEEE Journal of Emerging and Selected Topics in Power Electronics, vol. 4, no. 3, pp. 1015–1025, Sept 2016.

[62] F. Lu, H. Zhang, H. Hofmann and C. Mi, "A Double-SidedLCLC-Compensated Capacitive Power Transfer System for Electric Vehicle Charging," in IEEE Transactions on Power Electronics, vol. 30, no. 11, pp. 6011-6014, Nov. 2015.

[63] J. Deng, W. Li, T. D. Nguyen, S. Li and C. C. Mi, "Compact and Efficient Bipolar Coupler for Wireless Power Chargers: Design and Analysis," in IEEE Transactions on Power Electronics, vol. 30, no. 11, pp. 6130-6140, Nov. 2015.

[64] W. Li, H. Zhao, S. Li, J. Deng, T. Kan and C. C. Mi, "Integrated *LCC* Compensation Topology for Wireless Charger in Electric and Plug-in Electric Vehicles," in IEEE Transactions on Industrial Electronics, vol. 62, no. 7, pp. 4215-4225, July 2015.

[65] A. Zaheer, M. Neath, H. Z. Z. Beh and G. A. Covic, "A Dynamic EV Charging System for Slow Moving Traffic Applications," in IEEE Transactions on Transportation Electrification, vol. 3, no. 2, pp. 354-369, June 2017.

[66] A. Tejeda, G. A. Covic and J. T. Boys, "Novel single-sided ferriteless magnetic coupler for roadway EV charging," 2015 IEEE Energy Conversion Congress and Exposition (ECCE), Montreal, QC, 2015, pp. 3148-3153.

[67] A. Kamineni, G. A. Covic and J. T. Boys, "Self-Tuning Power Supply for Inductive Charging," in IEEE Transactions on Power Electronics, vol. 32, no. 5, pp. 3467-3479, May 2017.

[68] Valtchev, Stanimir S.; Baikova, Elena N.; Jorge, Luis R. (December 2012). "Electromagnetic Field as the Wireless Transporter of Energy" (PDF). Facta Universitatis Ser. Electrical Engineering. 25 (3): 171–181. CiteSeerX 10.1.1.693.1938. doi:10.2298/FUEE1203171V. Retrieved 15 December 2014.

[69] Ashley, Steven (20 November 2012). "Wireless recharging: Pulling the plug on electric cars". BBC website. British Broadcasting Corp. Retrieved 10 December 2014.

[70] Tomar, Anuradha; Gupta, Sunil (July 2012). "Wireless power Transmission: Applications and Components". International Journal of Engineering Research and Technology. 1 (5). ISSN 2278-0181. Retrieved 9 November 2014.

[71] H. Z. Z. Beh, G. A. Covic and J. T. Boys, "Wireless Fleet Charging System for Electric Bicycles," in IEEE Journal of Emerging and Selected Topics in Power Electronics, vol. 3, no. 1, pp. 75-86, March 2015.

[72] I. C. on Non-Ionizing Radiation Protection (ICNIRP), "Guidelines for limiting exposure to time-varying electric, magnetic and electromagnetic fields (up to 300 GHz)," Health Physics, vol. 74, no. 4, pp. 494 – 522, 1998.

[73] S. S. Williamson, A. K. Rathore, and F. Musavi, "Industrial electronics for electric transportation: Current state-of-the-art and future

challenges," IEEE Transactions on Industrial Electronics, vol. 62, no. 5, pp. 3021–3032, May 2015.

[74] P. Miller, "Automotive lithium-ion batteries: State of the art and future developments in lithium-ion battery packs for passenger car applications," Platinum Metals Review, vol. 59, no. 1, pp. 4 – 13, 2015.

[75] Electric cars with the longest range.
https://newmotion/electric-cars-with-the-longest-range.

[76] G. A. Covic and J. T. Boys, "Modern trends in inductive power transfer for transportation applications," IEEE Journal of Emerging and Selected Topics in Power Electronics, vol. 1, no. 1, pp. 28–41, March 2013.

[77] J. Estrada, S. Sinha, B. Regensburger, K. Afridi and Z. Popović, "Capacitive wireless powering for electric vehicles with near-field phased arrays," 2017 47th European Microwave Conference (EuMC), Nuremberg, 2017, pp. 196-199.

[78] R. Trevisan and A. Costanzo, "A 1-kW contactless energy transfer system based on a rotary transformer for sealing rollers," IEEE Trans. Ind. Electron., vol. 61, pp. 6337–6345, Nov 2014.

[79] G. Monti, P. Arcuti and L. Tarricone, "Resonant Inductive Link for Remote Powering of Pacemakers," in IEEE Transactions on Microwave Theory and Techniques, vol. 63, no. 11, pp. 3814-3822, Nov. 2015.

[80] E. G. Kilinc, B. Canovas, F. Maloberti, and C. Dehollaini, "Intelligent cage for remotely powered freely moving animal telemetry systems," in Proc. IEEE Int. Symp. Circuits Syst., May 20–23, 2012, pp. 2207–2210.

[81] C-L Liou, C-G Kuo, M-L Lee, S-G Mao, "Wireless charging system of mobile handset using metamaterial-based cavity resonator," IEEE MTT IMS Digest 2012, pp.1-3.

[82] S. Rahimizadeh, S. Korhummel, B. Kaslon and Z. Popovic, "Scalable adaptive wireless powering of multiple electronic devices in an over-moded cavity," 2013 IEEE Wireless Power Transfer (WPT), Perugia, 2013, pp. 84-87.

[83] A. G. Zajić and Z. Popović, "Statistical modeling of a shielded wireless charging device," 2015 9th European Conference on Antennas and Propagation (EuCAP), Lisbon, 2015, pp. 1-5.

[84] P. E. Glaser,, "Power from the Sun: Its future", Science, No.162, pp.857 - 886, 1968.

[85] W.C. Brown, "The Microwave Powered Helicopter", Proc. symp. Microw. Power, Canada, 24, Mar., 1966.

[86] T. Furuta, M. Ito, N. Nambo, K. Itoh, K. Noguchi and J. Ida, "The 500MHz band low power rectenna for DTV in the Tokyo area," 2016 IEEE Wireless Power Transfer Conference (WPTC), Aveiro, 2016, pp. 1-3.

[87] M. Piñuela, P. D. Mitcheson and S. Lucyszyn, "Ambient RF Energy Harvesting in Urban and Semi-Urban Environments," in IEEE Transactions on Microwave Theory and Techniques, vol. 61, no. 7, pp. 2715-2726, July 2013.

[88] V. Palazzi et al., "Design of a ultra-compact low-power rectenna in paper substrate for energy harvesting in the Wi-Fi band," 2016 IEEE Wireless Power Transfer Conference (WPTC), Aveiro, 2016, pp. 1-4.

[89] A. Takacs, H. Aubert, S. Fredon, L. Despoisse and H. Blondeaux, "Microwave Power Harvesting for Satellite Health Monitoring," in IEEE Transactions on Microwave Theory and Techniques, vol. 62, no. 4, pp. 1090-1098, April 2014.

[90] A. López-Yela et al." Rectena de banda ancha para la recolección de energía electromagnética ambiental," XXXIII National Simposium of the International Union of Radio Science, Granada, 2018.

[91] J. Estrada, P. Zurek and Z. Popović, "Harvesting of aircraft radar altimeter sidelobes for low-power sensors," 2018 International Applied Computational Electromagnetics Society Symposium (ACES), Denver, CO, 2018, pp. 1-2.

[92] C. Song et al., "A Novel Quartz Clock With Integrated Wireless Energy Harvesting and Sensing Functions," in IEEE Transactions on Industrial Electronics, vol. 66, no. 5, pp. 4042-4053, May 2019.

[93] H. Lee, J. Tak and J. Choi, "Wearable Antenna Integrated into Military Berets for Indoor/Outdoor Positioning System," in IEEE Antennas and Wireless Propagation Letters, vol. 16, pp. 1919-1922, 2017.

[94] S. Gorgutsa, S. Bellemare-Rousseau, P. Guay, A. Miled and Y. Messaddeq, "Smart T-shirt with wireless respiration sensor," 2017 IEEE SENSORS, Glasgow, 2017, pp. 1-3.

[95] J. Wang, M. Leach, E. G. Lim, Z. Wang, R. Pei and Y. Huang, "An Implantable and Conformal Antenna for Wireless Capsule Endoscopy," in IEEE Antennas and Wireless Propagation Letters, vol. 17, no. 7, pp. 1153-1157, July 2018.Arrays of rectennas.

[96] S. Li and J. Li, "Smart patch wearable antenna on Jeans textile for body wireless communication," 2018 12th International Symposium on Antennas, Propagation and EM Theory (ISAPE), Hangzhou, China, 2018, pp. 1-4.

[97] Jose Estrada, Eric Kwiatkowski, Ana López-Yela, Mónica Borgoñós-García, Daniel Segovia-Vargas, Taylor Barton, and Zoya Popovic, "An Octave Bandwidth RF Harvesting Tee-Shirt," 2019 IEEE Wireless Power Transfer Conference (WPTC), London, 2019.

[98] "Applications of Wireless Sensor Networks in Next Generation Networks," ITU-T Technical Paper Y.2000 (2014).

[99] Ichihara, T., T. Mitani, and N. Shinohara, "Study on Intermittent Microwave Power Transmission to a ZigBee Device", Proc. of 2012

IEEE MTT-S International Microwave Workshop Series on Innovative Wireless Power Transmission: Technologies, Systems, and Applications (IMWS-IWPT2012), pp. 209-212, 2012.

[100] R. Scheeler, S. Korhummel and Z. Popovic, "A Dual-Frequency Ultralow-Power Efficient 0.5-g Rectenna," in IEEE Microwave Magazine, vol. 15, no. 1, pp. 109-114, Jan.-Feb. 2014.

[101] C. Song et al., "A Novel Six-Band Dual CP Rectenna Using Improved Impedance Matching Technique for Ambient RF Energy Harvesting," in IEEE Transactions on Antennas and Propagation, vol. 64, no. 7, pp. 3160-3171, July 2016.

[102] C. Song, Y. Huang, P. Carter, J. Zhou, S. D. Joseph and G. Li, "Novel Compact and Broadband Frequency-Selectable Rectennas for a Wide Input-Power and Load Impedance Range," in IEEE Transactions on Antennas and Propagation, vol. 66, no. 7, pp. 3306-3316, July 2018.

[103] Kuhn, V., Seguin, F., Lahuec, C., and Person, C. (2016). Enhancing RF-to-DC conversion efficiency of wideband RF energy harvesters using multi-tone optimization technique. International Journal of Microwave and Wireless Technologies, 8(2), 143-153. doi:10.1017/S1759078714001457.

[104] E. Falkenstein, M. Roberg and Z. Popovic, "Low-power wireless power delivery," IEEE Trans. Microwave Theory Techn., vol. 60, no. 7, pp. 2277–2286, July 2012.

[105] T. Soyata, L. Copeland and W. Heinzelman, "RF Energy Harvesting for Embedded Systems: A Survey of Tradeoffs and Methodology," in IEEE Circuits and Systems Magazine, vol. 16, no. 1, pp. 22-57, Firstquarter 2016.

[106] C. H. P. Lorenz et al., "Breaking the Efficiency Barrier for Ambient Microwave Power Harvesting With Heterojunction Backward Tunnel Diodes," in IEEE Transactions on Microwave Theory and Techniques, vol. 63, no. 12, pp. 4544-4555, Dec. 2015.

[107] J. A. Hagerty, F. B. Helmbrecht, W. H. McCalpin, R. Zane, Z. Popovic, "Recycling ambient microwave energy with broad-band rectenna arrays," in IEEE Transactions on Microwave Theory and Techniques, vol. 52, no. 3, pp. 1014-1024, March 2004.

[108] Z. Liu, Z. Zhong and Y. Guo, "Intermodulation harvesting rectifier design for high efficiency multi-sine wireless power transfer," 2016 IEEE MTT-S International Microwave Symposium (IMS), San Francisco, CA, 2016, pp. 1-3.

[109] A. Collado and A. Georgiadis, "Improving wireless power transmission efficiency using chaotic waveforms," 2012 IEEE/MTT-S International Microwave Symposium Digest, Montreal, QC, 2012, pp. 1-3.

[110] A. S. Boaventura and N. B. Carvalho, "Maximizing DC power in energy harvesting circuits using multisine excitation," 2011 IEEE MTT-S International Microwave Symposium, Baltimore, MD, 2011, pp. 1-4.

[111] D. Belo and N. B. Carvalho, "Harmonic spaced multisines for efficient wireless power transmission," 2015 IEEE Wireless Power Transfer Conference (WPTC), Boulder, CO, 2015, pp. 1-4.

2

Non-linear diode analysis for multiple-tone wireless power harvesting

Electromagnetic waves from mobile communications, radar and TV broadcasting can be harvested to use low-power electronics. To this end, an antenna coupled to a rectifier circuit can be used. The rectifier circuit transforms the RF signal into DC, but at low input power levels the conversion efficiency is low. The aim of this chapter is to study the diode non-linearity with multiple-tone input signals to research a possible increase in the conversion efficiency in these scenarios. A theoretical multi-signal analysis with two different approaches is developed. The first approach characterizes the non-linear region of the diode, where very low input voltages can be used to verify the model. The second approach is valid over low and high input voltages, modeling also the linear region, through an expansion of Legendre polynomials.

2.1. Introduction

In RF energy harvesting, the available incident power densities are low and the power is radiated from sources in unknown locations that can cover a broad bandwidth and can be arbitrarily modulated. The values of power density vary both: in space and across the spectrum. In [1], a measurement survey was performed from 0.3 to 3 GHz over more than 270 underground stations over street levels in London, from 10 AM to 3 PM on weekdays from March 5 to April 4, 2012. The average values of power density varied from 12 nW/cm^2 for 3G to 84 nW/cm^2 for GSM 1800. In addition to the survey data, an own study was carried out in July 2019 to characterize the power densities in the working area, the university in Leganés (details of measurements are presented in Section 4.3). Spectrum measurements were carried out from 0.5 to 5 GHz recording data every 30 second for 3 hours at different locations during two weeks, to compare the information and get more accurate data from the work environment. On average, power densities around 19 nW/m^2 for GSM 1800 and 25 nW/m^2 for 3G in an outdoor location were measured. For indoor scenarios, values increased up to 310 and 370 nW/m^2 for GSM 1800 and 3G. However, these values are low but it is due to the distance to base stations. Leganés is a small city (a population of less than 190.000 people while London is a huge city with thousands of base station, therefore, the coverage level must be higher in London). In France [2], power density values for different services were measured at 200 m distance from the base station showing values around 200 $\mu W/m^2$. The power measurements showed that the average power level is 30 % higher in urban environments than in the countryside.

The relative position between power transmitters and receivers can vary over time requiring non-directive antennas and power reception circuits that can maintain the efficiency over variable power levels. In a low-power time-varying environment, the received power from one service (GSM 900 or LTE) by an antenna is possibly not even sufficient to always turn on a rectifying device such as a Schottky diode, being limited by the threshold voltage. This limits the usefulness of RF energy harvesting. Different approaches have been done to overcome this limitation. From the circuital

point of view [3], different topologies were analyzed. Single-diode topologies reduce losses (power efficient) when compared to other topologies and are good candidates for low input power scenarios, although with charge pumps the voltage level is increased, being possible to power up a microcontroller, depending on the input level. Nevertheless, some studies paid attention to the waveform of the excitation signal, comparing the rectifier performance when different waveforms are applied (multisines, chaotic or white noise signals). This approach is possible as ambient electromagnetic energy from base stations is scavenged and their signals have different waveforms. This alternative is known as power-optimized waveform [4]. Multiple-tone carriers and different modulations are used to provide a higher Peak to Average Power Ratio (PAPR) than a Continuous Wave (CW) with the same average power, therefore higher peak levels appear, overcoming the threshold barrier more efficiency, charging the capacitor at a larger value (see Figure 2.1.1). The Peak to Average Power Ratio shows the ratio of the peak power (peak amplitude squared) compared to average power (RMS amplitude squared) as can be seen in (2.1.1). For a CW signal, the PAPR is 3 dB and for a N-multiple-tone signal is $10 \log 2N$.

$$PAPR = \frac{x_{peak}^2}{x_{rms}^2}. \tag{2.1.1}$$

In [5] early work has shown experimental results on a wideband rectenna array with two arbitrarily spaced signals of varying power level and frequency spacing in the 1-8 GHz range. With 10,000 different power-frequency combinations for the two tones, it was shown that in all cases the rectified power increased relatively to the sum of the same two individual signals. This is due to the non-linear diode characteristics.

Subsequent work with high peak to average power ratio modulated signals [6], chaotic signals [7]- [8] and multiple-tone signals [9, 10] have shown similar effects. In [9, 10] a limited theoretical treatment is shown about the efficiency improvement but unfortunately, most of the works are empirical, that through a bunch of measurements certify that some waveforms are more power-efficient.

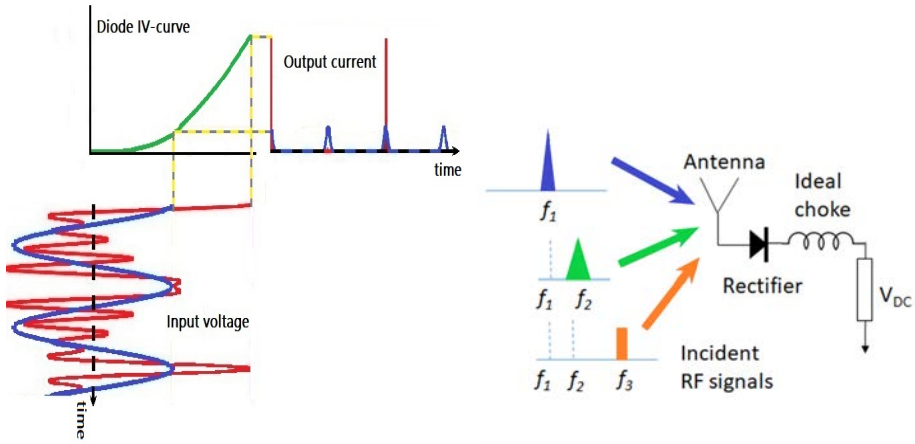

(a) (b)

Figure 2.1.1: a) IV curve with a CW and a multiple-tone signal (high PAPR) with the same average power. b) RF wireless power harvesting scenario with multiple input signals with unequal frequency spacing, of unequal powers and with different modulations.

2.1.1. Background

Diode performance in the forward mode is governed by the IV relationship known as Shockley diode equation [11]:

$$I = I_s(e^{(\frac{V_j}{nV_T})} - 1), \tag{2.1.2}$$

where I_s is the saturation current, R_s is the series resistance, V_j is the built-in junction voltage, n the ideality factor and $V_T = kT/e$ the thermal voltage, being k the Boltzmann constant, T the temperature and e the electron charge. As seen in the simple diode equivalent circuit in Figure 2.1.2, if V is the voltage drop across the diode terminals then,

$$V_j = V - IR_s. \tag{2.1.3}$$

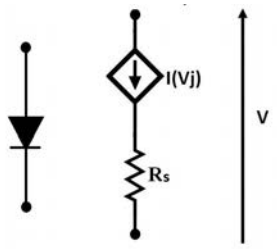

Figure 2.1.2: Simplified equivalent circuit of a diode with series resistance R_S and a dependent current source $I(V_j)$ given by (2.1.2).

The expression (2.1.3) relates the current in the diode to the junction voltage. Two different trends can be seen when (2.1.2) is plotted (see Figure 2.1.1 (a)). At very low current values, and as R_s is small [12] and nV_T is not negligible, the IV curve is dominated by the exponential term (non-linear region) where $I \approx I_s(e^{(\frac{V}{nV_T})} - 1)$. Nevertheless, for higher current values, if we express $V(I)$, then $I \gg \log(1 + \frac{I}{I_s})$ and therefore $V \approx IR_s$.

Energy harvesting scenarios are characterized by a variable low power density over time and space, so the non-linear region is important for the diode performance. The efficiency improvement when working with multiple-tone signals has been tested experimentally, but just a few attempts have been done to provide an analytical explanation of the performance. In [9, 10] a Taylor expansion is used to approximate the IV curve. The resistance R_s was neglected to obtain a simple theoretical relation for the DC term. Two cases were considered: first when the input $x(t)$ is a signal with $\Delta\omega << \omega_0$, where $\Delta\omega$ is the spacing between tones and second when harmonically-spaced multi-sine signals are used. In both cases, the DC term is shown to be higher for the multiple-tone signal in comparison with individual CW with the same average power. For the second case, due to the harmonic relationship, some terms will further increase the DC component, and reduce the ripple across the DC load, thus increasing efficiency. This approach is not complete since it is only available for a reduce set of frequencies and where R_s is small enough to neglect its contribution.

In [13], intermittent transmission, also known as ICW, is used to experimentally extend the reading range of an RFID tag by increasing rectification efficiency while reducing the power consumption by three-quarters, with a duty cycle of 40 %. Nevertheless, in [14, 15], multi-sine signals are used. Although the application is different, the theoretical concept behind is the same, to increase the RF to DC power conversion efficiency. These waveforms can be used to increase the efficiency of diode rectifiers through high PAPR signals.

In [16], the effect of the bandwidth and number of tones is investigated but the analytical approximations are not stated. A CW signal in [7] and [17] is compared in terms of conversion efficiency to three signals with different PAPR: a chaotic signal, white noise, and an OFDM LTE FDD signal, however, again, no theoretical analysis is presented. In [18], Ultra Wide Band (UWB) signals through a train of short duration pulses are studied as they exhibit a high PAPR. An efficiency of 50 % is obtained at 7.5 dBm input power using a voltage doubler rectifier topology. UWB designs require more complexity than multisine approaches, as the working band is enlarged, and the non-linear rectifier impedance varies with frequency, input power and load conditions. In [3], pros and cons of each approach are summarized and Table 2.1 shows some collected results at -15 dBm and 433 MHz.

In summary, although multiple simultaneous signal rectification has been shown and limited analysis results presented, to the best of the author's knowledge, a theoretical treatment of multisine diode rectification is missing in the literature. In this chapter, an analytical development to estimate the I_{DC} current for simultaneous low input multiple-tone signals, including all parameters that govern the direct mode of the diode is presented. The analytical model can be applied to any diode with the IV curve satisfying (2.1.2). To show the accuracy of the model, the analytical expression is applied to a Skyworks SMS7630 Schottky diode. It provides a small relative error compared to the harmonic balance simulations in NI/AWR at low input voltages, giving an accurate prediction with insight into the physical operation.

Waveform	PAPR (dB)	Power Efficiency (%)
CW	3.0	34
OFDM	12.0	38
White noise	13.7	47
Chaotic	14.8	49

Table 2.1: Maximum power efficiency improvement using different waveforms with the same average power at -15 dBm and 433 MHz [17].

2.2. Analytical approximation of diode IV curve with series resistance

Different input tones result in different DC output across a non-linear diode, depending on the input amplitudes, frequency spacings, and relative phases. The non-linearity of the diode was studied in [9] using (2.1.2) with $V_j = V$ to see how an N-tone low input voltage can produce a higher DC output than a single tone with the same total average power. Then, this equation describes an ideal diode model with no series resistance. In this chapter, a more realistic intrinsic diode model is considered, so it is necessary to take into account the voltage drop across the series resistance in Figure 2.1.2. The series resistance can only be neglected for very low input voltages when the diode is off, below threshold. In the non-linear region, with low input RF voltage, the diode switches between ON and OFF states, and, for an accurate model, R_s needs to be taken into account since it affects the slope of the IV curve. As the non-linear effects, such as rectification, are due to the non-linear region, the slope of the curve will critically affect the RF-DC conversion efficiency for multiple-tone signals.

To include the series resistance, (2.1.2) and (2.1.3) are combined to give:

$$I = I_s(e^{(\frac{V-IR_s}{nV_T})} - 1). \tag{2.2.1}$$

As already explained, previous studies approximated this curve through a Taylor expansion centered at the origin, neglecting the R_s parameter. The DC term was obtained after filtering out the RF and baseband components

[9], where four tones were used as excitation at the input, repeated here for completeness:

$$x(t) = A \sum_{n=1}^{4} \cos(\omega_n t + \phi_n). \tag{2.2.2}$$

The value of the DC component obtained in [9] through a Taylor expansion of order 4 was:

$$I_{DC} = \frac{4A^2k_2}{2} + \frac{21A^4k_4}{2} + \frac{3A^4k_4}{2}\cos(2\phi_3 - \phi_2 - \phi_4) + \frac{3A^4k_4}{2}\cos(-2\phi_2 + \phi_1 + \phi_3) + 3A^4k_4\cos(\phi_1 - \phi_2 - \phi_3 + \phi_4), \tag{2.2.3}$$

where k_n are the Taylor coefficients [9] and $\Delta\omega << \omega_0$. In the case in which the frequencies are harmonically spaced, this value is increased due to the intermodulation products contribution (see [10]). Nevertheless these approximations are non-longer accurate when the input voltage increases (see Figure 2.3.4 (b)).

In this thesis, the series resistance is included, so the Taylor expansion cannot be directly computed as above since the current also appears in the exponential term [19]. Nevertheless, if we invert the current-voltage dependence of (2.2.1), from the author's point of view there are alternatives to perform this task:

$$V = R_s I + nV_T \log\left(1 + \frac{I}{I_s}\right). \tag{2.2.4}$$

Along this chapter two possible solutions are shown. The first approach tries to solve the problem using the Wright Omega function and the Taylor series. The accuracy of this model is very good, but reduced to the convergence region of the function (for very low input voltages). Nevertheless, a second alternative is presented using Legendre polynomials. In this case, the problems with the convergence region are avoided, as these polynomials provide a good estimation, minimizing the L^2-norm, in the interval $[V_0, V_1]$ (exponential and linear region). It is worth mentioning that in both cases

a resistive rectifier is considered for the analysis (see Figure 2.1.2). The non-linearity of the junction capacitance is not used for rectification as the model follows the Shockley diode (2.1.2). The non-linear capacitance will be included in the future in analogy to the analysis of reactive mixers, see e.g., [20] as its performance will improve the analytical approach as shown in Figure 2.2.1.

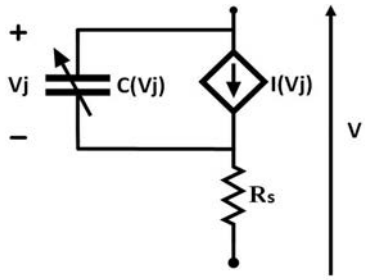

Figure 2.2.1: Complete equivalent circuit of a diode with a voltage-variable capacitor $C(V_j)$, a series resistance R_s and a dependent current source $I(V_j)$.

2.3. Non-linear diode rectifier analysis for multiple-tone excitation: Taylor series

It is noticeable that by applying some transformations, this expression (2.2.4) resembles to (2.3.1). In this way, it is possible to relate the $I(V)$ expression in terms of the Wright Omega function:

$$\omega(x) = \{x \in \mathbb{R} \,|\, x = \omega(x) + \log \omega(x)\}. \tag{2.3.1}$$

The Wright Omega function [21] is a very useful expression as it models the Shockley equation. It is defined in terms of the Lambert W function as follows:

$$\omega(x) = W(e^x), \tag{2.3.2}$$

where the Lambert W is defined as:

$$W(x) = \{x \in \mathbb{R} \,|\, x = W(x)e^{W(x)}\}. \tag{2.3.3}$$

We will only be interested in the case in which $x \in \mathbb{R}$. In that case, it is easy to see that the function is injective (and therefore, invertible) for $x \geqslant 0$.

In [22], it was not possible to formulate an analytical expression for defining the current of the diode in terms of the input voltage when the series resistance is different than zero, using elementary functions. Therefore, the Lambert function was employed, being possible to extract R_s through simple measurements of the $I(V)$ curve. However, this chapter shows a possible way to theoretically solve the problem through the Wright Omega function. In this case, it is necessary to perform the following transformations to (2.2.4), where the process is divided into five steps. First, the currents are normalized and later the voltages.

Step 1: Current normalization $\bar{I} = \dfrac{I}{I_s}$ ***, results in:***

$$V = R_s I_s \bar{I} + nV_T \log(1 + \bar{I}). \tag{2.3.4}$$

Step 2: Define $I' = 1 + \bar{I}$ ***, which gives:***

$$\begin{aligned} V &= R_s I_s \left(I' - 1\right) + nV_T \log(I') \\ &= R_s I_s I' - R_s I_s + nV_T \log(I'). \end{aligned} \tag{2.3.5}$$

Step 3: Set $I'' = \dfrac{I'}{\alpha}$***, as:***

$$V = R_s I_s I''\alpha - R_s I_s + nV_T \log(I'') + nV_T \log(\alpha). \tag{2.3.6}$$

Now, it is necessary to transform the voltages to analytically compare this expression to the Wright Omega function in (2.3.1).

Step 4: Voltage normalization $V' = \dfrac{V}{\beta}$ ***leads to:***

$$V' = \frac{R_s I_s I'' \alpha}{\beta} + \frac{nV_T}{\beta}\log(I'') + \frac{1}{\beta}\left(nV_T \log(\alpha) - R_s I_s\right). \tag{2.3.7}$$

Step 5: Set $V'' = V' - \gamma$***, which results in:***

$$V'' = \frac{R_s I_s I'' \alpha}{\beta} + \frac{nV_T}{\beta}\log(I'') + \frac{1}{\beta}\left(nV_T \log(\alpha) - R_s I_s\right) - \gamma. \tag{2.3.8}$$

Then, α, β and γ must fulfill the following equalities:

$$\begin{aligned} &\frac{nV_T}{\beta} = 1, \\ &\frac{R_s I_s \alpha}{\beta} = 1, \\ &\frac{1}{\beta}\left(nV_T \log(\alpha) - R_s I_s\right) - \gamma = 0. \end{aligned} \tag{2.3.9}$$

In this way, we thus obtain $V'' = I'' + \log I''$ that is similar to the expression $x = \omega(x) + \log \omega(x)$, where $x = V''$ and $\omega(x) = I''$. Therefore, $I'' = \omega(V'')$ where α, β and γ are given by:

$$\alpha = \frac{nV_T}{R_s I_s}, \quad \beta = nV_T, \quad \text{and} \quad \gamma = \log(\alpha) - \frac{R_s I_s}{nV_T}. \tag{2.3.10}$$

If we formulate I'' and V'' as a function of I and V, then, $V'' = V' - \gamma = \dfrac{V}{\beta} - \gamma$ and $I'' = \dfrac{I'}{\alpha} = \dfrac{1 + \bar{I}}{\alpha} = \dfrac{I_s + I}{\alpha I_s}$. Now, the diode current can be written in terms of the Wright Omega function and its derivatives used for the Taylor expansion.

$$I(V) = I_s\left[\alpha\omega\left(\frac{V}{\beta} - \gamma\right) - 1\right]. \tag{2.3.11}$$

If we start computing the first three derivatives for the Wright Omega function in (2.3.1), we get:

$$1 = \omega^{(1)}(x) + \frac{\omega^{(1)}(x)}{\omega(x)} = \omega^{(1)}(x)\left(1 + \frac{1}{\omega(x)}\right), \tag{2.3.12}$$

hence,

$$\omega^{(1)}(x) = \frac{\omega(x)}{1+\omega(x)}, \tag{2.3.13}$$

and following the recurrence:

$$\begin{aligned} \omega^{(2)}(x) &= \frac{\omega^{(1)}(x)}{(1+\omega(x))^2} = \frac{\omega(x)}{(1+\omega(x))^3}, \\ \omega^{(3)}(x) &= \frac{1-2\omega(x)}{(1+\omega(x))^5}\omega(x). \end{aligned} \tag{2.3.14}$$

By induction it can be seen that the n^{th} derivative can be expressed:

$$\omega^{(n)}(x) = \frac{a_{n,n-1}\cdot\omega^{n-1}(x) + \ldots + a_{n,2}\cdot\omega^2(x) + a_{n,1}\cdot\omega(x)}{(1+\omega(x))^{2n-1}}, \tag{2.3.15}$$

and the coefficients satisfy the following recursive relation:

$$a_{n,n-k} = (n-k)a_{n-1,n-k} - (n+k-2)a_{n-1,n-1-k}, \qquad k = 1,\ldots,n-2, \tag{2.3.16}$$

where $a_{n,1} = 1$, $a_{1,1} = 1$, $a_{n,n} = 0$ and,

$$a_{n,n-1} = (-1)^n\,(n-1)! \qquad \text{for} \qquad n \geqslant 2. \tag{2.3.17}$$

The Taylor series of $\omega(x)$ centered at x_0 is given by:

$$\omega(x) \approx \sum_{k=0}^{\infty} \frac{\omega^{(k)}(x_0)\,(x-x_0)^k}{k!}, \tag{2.3.18}$$

where this approximation is valid for $|x - x_0| < \rho$, where ρ is the convergence radius of this series.

Substituting the Taylor series of the Wright Omega function in (2.3.11) yields:

$$I = I_s \left[\alpha \sum_{k=0}^{\infty} \frac{1}{k!} \omega^{(k)} \left(\frac{V_0}{\beta} - \gamma \right) \left(\frac{V - V_0}{\beta} \right)^k - 1 \right]. \tag{2.3.19}$$

The diode current can be analytically expressed as a truncated power series in the convergence region, $I_M(V)$, with order M, as:

$$I_M(V) = \sum_{k=0}^{M} C_k \left(V - V_0 \right)^k, \tag{2.3.20}$$

where $(V - V_0)^k$ is defined as:

$$(V - V_0)^k = \sum_{m=0}^{k} \binom{k}{m} V^m \left(-1 \right)^{k-m} V_0^{k-m}, \tag{2.3.21}$$

and where C_k represents the coefficients:

$$\begin{aligned} C_0 =& I_s \left[\alpha\omega \left(\frac{V_0}{\beta} - \gamma \right) - 1 \right], \\ C_k =& \frac{I_s \alpha}{k! \beta^k} \omega^{(k)} \left(\frac{V_0}{\beta} - \gamma \right), \qquad k = 1, 2, \ldots. \end{aligned} \tag{2.3.22}$$

The Taylor series is point-wise convergent inside the convergent region of $\omega \left(\frac{V}{\beta} - \gamma \right)$, this is:

$$\lim_{M \to \infty} \left(I_M(V) - I(V) \right) = 0. \tag{2.3.23}$$

Thus, (2.3.20) can be rewritten into (2.3.24) for a general excitation:

$$\begin{aligned} \sum_{k=0}^{M} C_k \left(V - V_0 \right)^k &= \sum_{k=0}^{M} \sum_{m=0}^{k} C_k \binom{k}{m} \left(-V_0 \right)^{k-m} V^m \\ &= \sum_{k=0}^{M} \left[\sum_{m=k}^{M} C_m \binom{m}{k} \left(-V_0 \right)^{m-k} \right] V^k = \sum_{k=0}^{M} D_{M,k} V^k, \end{aligned} \tag{2.3.24}$$

with,

$$D_{M,k} = \sum_{m=k}^{M} C_m \binom{m}{k} (-V_0)^{m-k}. \tag{2.3.25}$$

This expression is valid for whatever DC bias value applied to the Taylor expansion. As this study is focused on energy harvesting scenarios, this expression can be reduced to the case where no bias is used ($V_0 = 0$).

$$I_M(V) = \sum_{k=0}^{M} C_k V^k, \tag{2.3.26}$$

With the above formulation, multiple-tone input signals can be applied and therefore, the output current can be analytically calculated.

2.3.1. Multiple-tone excitation for the analytical approximation of the diode IV curve

Now that the analytical expression for the non-linear IV characteristic is developed, multiple RF tones can be used as excitation. We are interested in finding the DC component which, for a periodic signal, is computed as the first coefficient of its Fourier series:

$$I_{DC} = \frac{1}{T} \int_0^T I(V(t)) \mathrm{d}t, \tag{2.3.27}$$

where T is the period of the signal.
Let us consider the following N-tone signal:

$$V(t) = A \sum_{r=1}^{N} \cos(\omega_r t) = \frac{A}{2} \sum_{r=1}^{N} \left(\mathrm{e}^{j\omega_r t} + \mathrm{e}^{-j\omega_r t} \right), \tag{2.3.28}$$

with $\omega_r = \dfrac{2\pi}{T_r}$ for $r = 1, 2, \ldots, N$.

The period of this signal will be the Least Common Multiple (LCM) of the periods of every tone: $T = \mathrm{LCM}(T_1, T_2, \ldots, T_N)$, this is, $T = n_1 T_1 =$

$n_2T_2 = \cdots = n_NT_N$, with $n_r \in \mathbb{N}$, such that its greatest common division is 1. By substituting (2.3.26) in (2.3.27), we have:

$$I_{DC} \simeq \frac{1}{T}\sum_{k=0}^{M} C_k \int_0^T V(t)^k \mathrm{d}t = \frac{1}{T}\sum_{k=0}^{M} C_k \frac{A^k}{2^k} \int_0^T \left[\sum_{r=1}^{N}\left(\mathrm{e}^{j\omega_r t} + \mathrm{e}^{-j\omega_r t}\right)\right]^k \mathrm{d}t$$
$$= \sum_{k=0}^{M} C_k \frac{A^k}{2^k} B_{N,k}, \tag{2.3.29}$$

where,

$$B_{N,k}(\omega_1 \ldots \omega_N) = \frac{1}{T}\int_0^T \left[\sum_{r=1}^{N}\left(\mathrm{e}^{j\omega_r t} + \mathrm{e}^{-j\omega_r t}\right)\right]^k \mathrm{d}t \qquad \omega_1, \ldots, \omega_N. \tag{2.3.30}$$

At this point, it is necessary to use the multinomial theorem, which is a generalization of the binomial theorem when more than two variables are applied [23] to expand the sum of exponentials, which results in:

$$\sum_{r=1}^{N}\left[\left(\mathrm{e}^{j\omega_r t} + \mathrm{e}^{-j\omega_r t}\right)\right]^k = \sum_{\substack{p_{-N}+\cdots \\ +p_N=k}} \binom{k}{p_{-N}, \ldots, p_N} \prod_{q=-N}^{N} \mathrm{e}^{j\omega_q p_q t}$$
$$= \sum_{\substack{p_{-N}+\cdots \\ +p_N=k}} \binom{k}{p_{-N}, \ldots, p_N} \prod_{q=1}^{N} \mathrm{e}^{j\omega_q (p_q - p_{-q})t} = \tag{2.3.31}$$
$$\sum_{\substack{p_{-N}+\cdots \\ +p_N=k}} \binom{k}{p_{-N}, \ldots, p_N} \mathrm{e}^{j\omega t \sum_{q=1}^{N}(p_q - p_{-q})n_q},$$

where $p_{-N} + \ldots + p_N = k$ indicates the partitions in which k can be divided into $2N$ non-negative integers and $\omega_q = 2\pi/T_q = n_q 2\pi/T = n_q\omega$. We will consider the general case for wireless power harvesting, where the incident signal frequencies ω_r (e.g., signals f_1, f_2 and f_3 in Figure 2.1.1) are non-

harmonically spaced and satisfy that:

$$\sum_{q=1}^{N}(p_q - p_{-q})n_q = 0, \qquad \text{only} \qquad p_{-q} = p_q, \qquad \forall q. \tag{2.3.32}$$

Notice that $B_{N,k}$ in (2.3.30) is going to be different from zero only in that case. Moreover, this condition only holds for a certain subset of even partitions, this is, $\int_0^T V(t)^k \mathrm{d}t = 0$, if k is odd.

Let us consider the example where a four-tone signal (N) is used and an 8th order (M) Taylor expansion approximation is developed. In this general scenario, $\sum_{q=1}^{N}(p_q - p_{-q})n_q = 0$ only for a small set of even partitions. For these cases, the DC term can be approximate as:

$$\begin{aligned} I_{DC} &\approx \sum_{k=0}^{M} C_k \frac{A^k}{2^k} B_{N,k} = \\ &C_0 + C_2\frac{A^2}{2^2}B_{4,2} + C_4\frac{A^4}{2^4}B_{4,4} + C_6\frac{A^6}{2^6}B_{4,6} + C_8\frac{A^8}{2^8}B_{4,8}. \end{aligned} \tag{2.3.33}$$

A matrix representation is used to plot all the different partitions. The first row represents the number of the partition (a total of eight, as four tones are replaced by eight exponentials), while the following rows represent the value associated to that specific partition (p_q).

- For $k = 0$ there are no partitions, so $B_{4,0} = 1$.
- For $k = 2$, just partitions where $p_1 + \ldots + p_N = \frac{k}{2} = 1$ as $p_q = p_{-q}$ (see Table 2.2). The integral from (2.3.34) comes from (2.3.30) to compute the $B_{4,2}$ coefficient.

p_{-4}	p_{-3}	p_{-2}	p_{-1}	p_4	p_3	p_2	p_1
1	0	0	0	1	0	0	0
0	1	0	0	0	1	0	0
0	0	1	0	0	0	1	0
0	0	0	1	0	0	0	1

Table 2.2: Partitions for $k = 2$.

$$B_{4,2} = \frac{1}{T}\int_0^T \sum_{r=1}^{4} \left(\mathrm{e}^{j\omega_r t} + \mathrm{e}^{-j\omega_r t}\right)^2 \mathrm{d}t = \binom{4}{1,3} \cdot \binom{2}{1,0,0,0,1,0,0,0}$$
$$= 4 \cdot 2 = 8. \tag{2.3.34}$$

- For $k = 4$, we can have two different partitions of the elements (see Table 2.3), and the $B_{4,4}$ coefficient becomes:

p_{-4}	p_{-3}	p_{-2}	p_{-1}	p_4	p_3	p_2	p_1
2	0	0	0	2	0	0	0
0	2	0	0	0	2	0	0
0	0	2	0	0	0	2	0
0	0	0	2	0	0	0	2
1	1	0	0	1	1	0	0
1	0	1	0	1	0	1	0
1	0	0	1	1	0	0	1
0	1	1	0	0	1	1	0
0	1	0	1	0	1	0	1
0	0	1	1	0	0	1	1

Table 2.3: Partitions for $k = 4$.

$$B_{4,4} = \binom{4}{1,3} \cdot \binom{4}{2,0,0,0,2,0,0,0} + \binom{4}{2,2} \cdot \binom{4}{1,1,0,0,1,1,0,0}$$
$$= 4 \cdot 6 + 6 \cdot 24 = 168. \tag{2.3.35}$$

- For $k = 6$, we can have three different partitions (see Table 2.4).

p_{-4}	p_{-3}	p_{-2}	p_{-1}	p_4	p_3	p_2	p_1
3	0	0	0	3	0	0	0
0	3	0	0	0	3	0	0
0	0	3	0	0	0	3	0
0	0	0	3	0	0	0	3
2	1	0	0	2	1	0	0
2	0	1	0	2	0	1	0
2	0	0	1	2	0	0	1
0	2	1	0	0	2	1	0
0	2	0	1	0	2	0	1
1	2	0	0	1	2	0	0
1	0	2	0	1	0	2	0
1	0	0	2	1	0	0	2
0	1	2	0	0	1	2	0
0	1	0	2	0	1	0	2
0	0	2	1	0	0	2	1
0	0	1	2	0	0	1	2
1	0	1	1	1	0	1	1
1	1	0	1	1	1	0	1
1	1	1	0	1	1	1	0
0	1	1	1	0	1	1	1

Table 2.4: Partitions for $k = 6$.

The $B_{4,6}$ coefficient is computed as:

$$B_{4,6} = \binom{4}{1,3} \cdot \binom{6}{3,0,0,0,3,0,0,0} + \binom{4}{1,1,2} \cdot \binom{6}{2,1,0,0,2,1,0,0} + \binom{4}{3,1} \cdot \binom{6}{1,1,1,0,1,1,1,0} = 4 \cdot 20 + 12 \cdot 180 + 4 \cdot 720 = 5120. \tag{2.3.36}$$

- To conclude, for $k = 8$, four different partitions must be computed. Table 2.5 represents the partitions and (2.3.37) shows the coefficient $B_{4,8}$ when $k = M$.

p_{-4}	p_{-3}	p_{-2}	p_{-1}	p_4	p_3	p_2	p_1
4	0	0	0	4	0	0	0
0	4	0	0	0	4	0	0
0	0	4	0	0	0	4	0
0	0	0	4	0	0	0	4
3	1	0	0	3	1	0	0
3	0	1	0	3	0	1	0
3	0	0	1	3	0	0	1
1	3	0	0	1	3	0	0
0	3	1	0	0	3	1	0
0	3	0	1	0	3	0	1
1	0	3	0	1	0	3	0
0	1	3	0	0	1	3	0
0	0	3	1	0	0	3	1
1	0	0	3	1	0	0	3
0	1	0	3	0	1	0	3
0	0	1	3	0	0	1	3
2	2	0	0	2	2	0	0
2	0	2	0	2	0	2	0
2	0	0	2	2	0	0	2
0	2	2	0	0	2	2	0
0	2	0	2	0	2	0	2
0	0	2	2	0	0	2	2
2	1	1	0	2	1	1	0

p_{-4}	p_{-3}	p_{-2}	p_{-1}	p_4	p_3	p_2	p_1
2	1	0	1	2	1	0	1
2	0	1	1	2	0	1	1
1	2	1	0	1	2	1	0
1	2	0	1	1	2	0	1
0	2	1	1	0	2	1	1
1	1	2	0	1	1	2	0
1	0	2	1	1	0	2	1
0	1	2	1	0	1	2	1
0	1	1	2	0	1	1	2
1	0	1	2	1	0	1	2
1	1	0	2	1	1	0	2
1	1	1	1	1	1	1	1

Table 2.5: Partitions for $k = 8$.

$$B_{4,8} = \binom{4}{1,3} \cdot \binom{8}{4,0,0,0,4,0,0,0} + \binom{4}{1,1,2} \cdot \binom{8}{3,1,0,0,3,1,0,0} + \binom{4}{2,2} \cdot \binom{8}{2,2,0,0,2,2,0,0} + \binom{4}{1,2,1} \cdot \binom{8}{2,1,1,0,2,1,1,0} + \binom{4}{4,0} \cdot \binom{8}{1,1,1,1,1,1,1,1} = 4 \cdot 70 + 12 \cdot 1120 + 6 \cdot 2520 + 12 \cdot 10080 + 40320 = 190120. \quad (2.3.37)$$

To summarize, the analytical truncated formula to order 8, that fits the real performance of the diode for a four-tone input excitation, where the frequencies satisfy (2.3.32), is shown:

$$I_{DC} \approx C_0 + A^2 \frac{C_2}{2^2} \cdot 8 + A^4 \frac{C_4}{2^4} \cdot 168 + A^6 \frac{C_6}{2^6} \cdot 5120 + A^8 \frac{C_8}{2^8} \cdot 190120. \quad (2.3.38)$$

where C_k coefficients are obtained from (2.3.22).

2.3.2. Analysis example

As an example of the derived analytical method, we choose a zero-bias Schottky diode manufactured by Skyworks (SMS7630) for which a non-linear Spice model is provided, with parameters: $I_s = 5\,\mu$A, $n = 1.05$ and $R_s = 20\,\Omega$. The results are plotted in Figure 2.3.3.

In Figure 2.3.1, a comparison is shown between the IV curve, based on the non-linear model from the manufacturer (red solid line), the proposed analytical model (yellow dashed line) and the model when no series resistance is included (blue dotted line). This approximation holds for V close to 0 as it is a Taylor series. If we consider the expansion to order 8 and V in the interval $(0, 0.1)$, the maximum relative error is lower than 6%. So, in that interval the approximation is good. If V is larger, the error will increase dramatically.

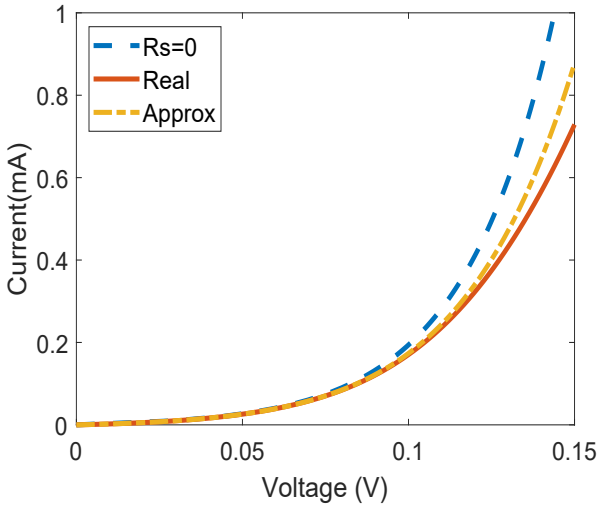

Figure 2.3.1: Comparison of the approximated analytical IV curve till order 8th (dotted yellow line) with the one obtained from the manufacturer (solid red line) and for a model with no series resistance (dashed blue line).

The model was tested using tones with equal amplitudes and randomly spaced in the frequency domain corresponding to some standard wireless bands that would be appropriate for energy harvesting: 0.85, 1.85, 2.1 and 2.45 GHz. The predicted DC value of the output current obtained by the approximate theory was then compared with Microwave Office (AWR) non-linear harmonic balance simulations with the Spice diode model. Independent sources were employed for the simulation (see Figure 2.3.2).

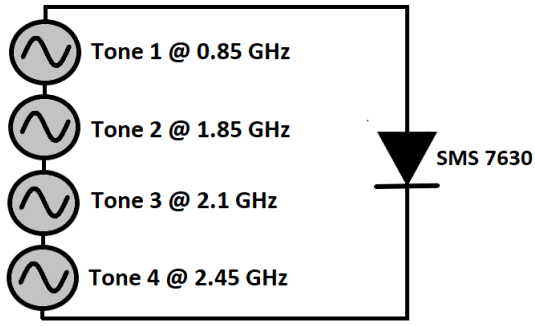

Figure 2.3.2: Diode Spice model in Microwave Office (AWR) excited with a four-tone signal with equal amplitudes at 0.85, 1.85, 2.1 and 2.45 GHz.

In Table 2.6, four equal-amplitude tones and a single tone are compared at different input amplitude cases, but with the same average power. Thus, if let A_1 be the amplitude of the one-tone signal and A_N the amplitude for each of the N-tones signal, then if the same average power is used $A_N = A_1/\sqrt{N}$. For this specific example, as $N = 4$, $A_1 = 2A_4$. In this table, the first column represents the number of tones in the excitation. The second column shows the amplitude for each tone and the third one the average power level. The predicted output DC current is shown in the fourth column. The fifth column shows the DC term obtained with the manufacturer-provided non-linear model and harmonic balance simulations in Microwave office. Finally, the last column shows the relative error between theory and simulations.

N	Tone Amplitude (mV)	Input Power (dBm)	Predicted I_{DC} (μA)	Simulated I_{DC} (μA)	Maximum Relative Error (%)
4	10.00	-24.0	$71.03{\cdot}10^{-2}$	$71.96{\cdot}10^{-2}$	1.29
1	20.00	-24.0	$69.32{\cdot}10^{-2}$	$70.20{\cdot}10^{-2}$	1.25
4	12.50	-22.0	$11.46{\cdot}10^{-1}$	$11.61{\cdot}10^{-1}$	1.32
1	25.00	-22.0	$11.03{\cdot}10^{-1}$	$11.17{\cdot}10^{-1}$	1.28
4	15.00	-20.5	$17.16{\cdot}10^{-1}$	$17.39{\cdot}10^{-1}$	1.37
1	30.00	-20.5	$16.23{\cdot}10^{-1}$	$16.44{\cdot}10^{-1}$	1.25
4	17.50	-19.1	$24.44{\cdot}10^{-1}$	$24.8{\cdot}10^{-1}$	1.45
1	35.00	-19.1	$22.68{\cdot}10^{-1}$	$22.98{\cdot}10^{-1}$	1.34
4	20.00	-18.0	$33.65{\cdot}10^{-1}$	$34.15{\cdot}10^{-1}$	1.46
1	40.00	-18.0	$30.51{\cdot}10^{-1}$	$30.90{\cdot}10^{-1}$	1.27
4	22.50	-17.0	$45.19{\cdot}10^{-1}$	$45.90{\cdot}10^{-1}$	1.56
1	45.00	-17.0	$39.91{\cdot}10^{-1}$	$40.48{\cdot}10^{-1}$	1.41
4	25.00	-16.0	$59.57{\cdot}10^{-1}$	$60.48{\cdot}10^{-1}$	1.50
1	50.00	-16.0	$51.12{\cdot}10^{-1}$	$51.87{\cdot}10^{-1}$	1.45
4	27.50	-15.1	$77.43{\cdot}10^{-1}$	$78.56{\cdot}10^{-1}$	1.44
1	55.00	-15.1	$64.39{\cdot}10^{-1}$	65.37E-1	1.50
4	30.00	-14.5	$99.55{\cdot}10^{-1}$	10.08	1.24
1	60.00	-14.5	$80.04{\cdot}10^{-1}$	$81.29{\cdot}10^{-1}$	1.54
4	32.50	-13.8	12.69	12.81	0.94
1	65.00	-13.8	$98.41{\cdot}10^{-1}$	9.99	1.59
4	35.00	-13.0	16.06	16.11	0.31
1	70.00	-13.0	11.99	12.19	1.64
4	37.50	-12.5	20.21	20.09	0.60
1	75.00	-12.5	14.50	14.75	1.69
4	40.00	-12.0	25.30	24.83	1.90
1	80.00	-12.0	17.43	17.73	1.72
4	42.50	-11.5	31.54	30.41	3.72
1	85.00	-11.5	20.82	21.20	1.79

Table 2.6: Predicted and simulated DC output current versus average input power for a single tone and four-tone excitation.

The predicted value for the DC current is higher when using a multiple-tone signal when compared to a CW signal with the same total power. Figure 2.3.3 (a) shows the predicted and simulated DC output current for a single tone and a four-tone excitation at different input power levels. The DC current improvement is represented on Figure 2.3.3 (b). In Figure 2.3.4, the relative error of the theoretical approximation using a four-tone excitation is shown. At A=100 mV an error of 13 % is obtained. This is a very high value so the model is appropriated for lower input voltages values up to 90 mV (6 % of error). For simplicity, just a few amplitude scenarios are shown in Table 2.6, although in the Chapter 7 the extended version is included in Table 7.1. In Figure 2.3.4 (b) a comparison of the IV curve is presented for the model developed in this chapter, and for the work presented in [9] where $R_s = 0$. Besides, NI/AWR simulations are included for completeness.

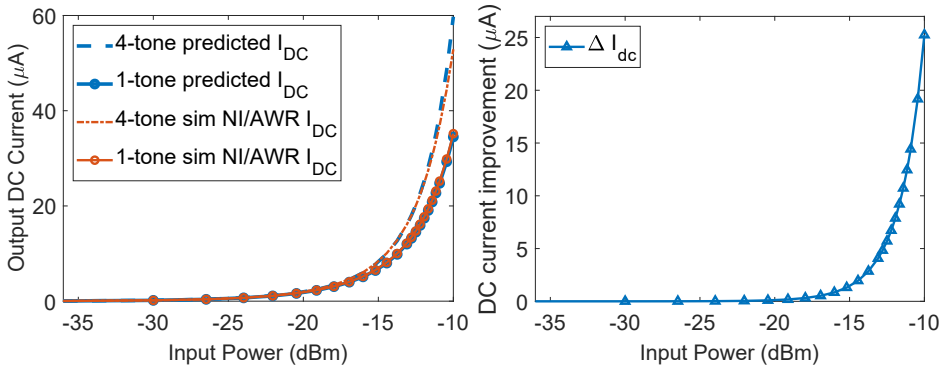

(a) (b)

Figure 2.3.3: a) Predicted DC output current versus average input power for a single tone and four-tone excitation. b) DC current improvement using a four-tone excitation.

A small relative error compared to harmonic balance non-linear simulations is obtained with this approximation, which gives a more intuitive and very fast estimate of multiple-tone behavior. Thus, we conclude that this expression is valid for approximating diode non-linear performance under multiple-tone signal excitation with low input power levels. In Section 2.4, a new model is developed to overcome this limitation, being able to work from very low to larger input voltage values in the same scenario.

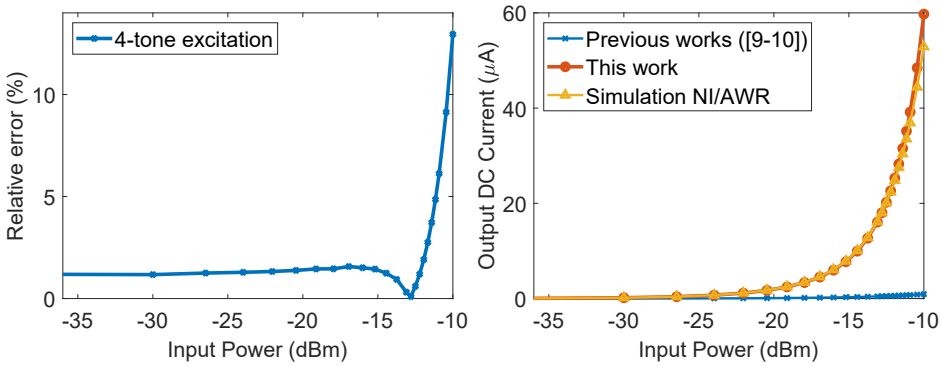

Figure 2.3.4: Predicted DC output current versus average input power for a four-tone excitation. a) Relative error. b) Comparison with previous studies and NI/AWR simulations.

2.4. Non-linear diode rectifier analysis for multiple-tone excitation: Legendre polynomials

The previous analysis is valid for a multiple-tone scenario with low input power levels ($A < 90\,mV$), being accurate enough (less than 6% relative error). This is due to the convergence radius of the Taylor expansion.

It is desirable to have a another approximation for higher voltage scenarios. The difficult task is how to get a valid approach with the smallest error for this specific situation. In this section, an interesting analysis has been done approximating the diode IV curve by means of Legendre Polynomials. In this way, it is possible to accurately characterize using the same model, low and high voltage input tones, which corresponds to the non-linear and linear regions. Therefore, this mathematical analysis can be very interesting to predict the DC rectified current component, when a rectifier is used to transform a multiple-tone RF excitation into DC, for whatever voltage level, while a good estimation is obtained.

Along this section, an explanation about how it is possible to approximate the IV curve of the diode to a set of polynomials is shown. In order to start solving this problem, let us introduce f, which is a function that belongs to $L^2[-1,1]$, this is the space of square integrable functions on the interval $[-1,1]$, i.e:

$$\int_{-1}^{1} |f(x)|^2 \cdot dx < \infty. \tag{2.4.1}$$

From orthogonal polynomials theory (see any text of orthogonal polynomials, for example [24]) any function $f \in L^2[-1,1]$ can be approximated by a convergent expansion in Legendre polynomials:

$$f(x) = \sum_{k=0}^{\infty} A_k L_k(x), \tag{2.4.2}$$

where $\left\{L_k(x)\right\}_{k=0}^{\infty}$ represents the set of Legendre polynomials.

An important property about approximating a function f with orthogonal polynomials is that the mean quadratic error is minimized, this is:

$$\left\{A_k\right\}_{k=0}^{M} = \underset{B_0,\ldots,B_M}{\operatorname{argmin}} \int_{-1}^{1} \left(f(x) - \sum_{k=0}^{M} B_k L_k(x) \right)^2 dx, \tag{2.4.3}$$

where M is the approximation order. Legendre polynomials satisfy the following orthogonality relation:

$$\int_{-1}^{1} L_m(x) L_k(x) dx = \frac{2}{2k+1} \delta_{mk}, \tag{2.4.4}$$

where δ_{mk} denotes the Kronecker delta. Therefore, using the orthogonality relation in (2.4.4), it can be seen that the solution of the minimazation problem in (2.4.3) is given by:

$$A_k = \frac{2k+1}{2} \int_{-1}^{1} f(x) L_k(x) dx. \tag{2.4.5}$$

It is important to notice that the interval $[-1, 1]$ is being considered. Nevertheless, different intervals are of interest for the analysis (depending on the voltage excitation). Therefore, a change of variable is applied, and the expression (2.4.4) can be rewritten, to be orthogonal in the interval $[x_0, x_1]$:

$$\int_{x_0}^{x_1} L_m\left(\frac{x' - \sigma}{\lambda}\right) L_k\left(\frac{x' - \sigma}{\lambda}\right) dx' = \frac{2\lambda}{2k+1} \delta_{mk}, \tag{2.4.6}$$

where $x' = \lambda x + \sigma$ and therefore, $\lambda = \dfrac{x_1 - x_0}{2}$ and $\sigma = \dfrac{x_1 + x_0}{2}$. Thus, for any function $f \in L^2[x_0, x_1]$, its expansion in Legendre polynomials is given by:

$$f(x') = \sum_{k=0}^{\infty} A'_k L_k\left(\frac{x' - \sigma}{\lambda}\right), \tag{2.4.7}$$

where A'_k is defined as:

$$A'_k = \frac{2k+1}{2\lambda} \int_{x_0}^{x_1} f(x') L_k\left(\frac{x' - \sigma}{\lambda}\right) dx. \tag{2.4.8}$$

In the following pages, this concept is applied to the function under study, which is the $I(V)$ relationship $\big($replacing $f(x)\big)$ in (2.3.11), that represents the current of the diode versus the voltage. $I(V)$ it is shown again:

$$I(V) = I_s \left[\alpha\omega \left(\frac{V}{\beta} - \gamma \right) - 1 \right]. \tag{2.4.9}$$

As it was explained in (2.3.1), the Wrigth Omega function was used as it models the Shockley equation and some transformations were applied (2.3.4).

The objective is to get an analytical expression, similar to the one we obtained in previous sections in (2.3.29) $\big($where the complete expression is shown in (2.3.38)$\big)$, to characterize the diode under a multiple-tone excitation at higher voltage levels with the minimum error. Thus, $I(V)$ can be formulated as a sum of Legendre polynomials:

$$I(V) = \sum_{k=0}^{\infty} A'_k L_k \left(\frac{V - \sigma}{\lambda} \right), \tag{2.4.10}$$

where the coefficients A'_k are the weights that multiply at each polynomial order. In order to get this approximation, it is necessary to solve the following analytical expression for these integrals (2.4.8), and therefore for:

$$\int_{V_0}^{V_1} I(V) \left(\frac{V - \sigma}{\lambda} \right)^k dV \qquad \text{for any} \qquad k = 0, 1 \ldots . \tag{2.4.11}$$

In principle, that may seems very cumbersome but, in this section it will be shown that it is possible. The fact is that if it can be proved that there exists an analytical solution for the integral, it is possible to approximate $I(V)$ through a combination of Legendre polynomials of order M. Hence, let us first try to solve the integral for whatever polynomial V^k multiply by the Wright Omega function:

$$\int V^k \omega(V) dV \qquad \text{for any} \qquad k = 0, 1 \ldots . \tag{2.4.12}$$

This process is shown along this chapter. First, notice that the Omega Wright function satisfies (2.3.12). Therefore, when approximating the function to different polynomials:

$$\int V^k \omega(V) dV = \int V^k \left(1 + \omega(V)\right) \omega^{(1)}(V) dV. \tag{2.4.13}$$

If this expression is integrated by parts, then:

$$\begin{aligned} \int V^k \omega(V) dV &= V^k \left[\frac{\omega^2(V)}{2} + \omega(V)\right] \\ &- k \int V^{k-1} \left[\frac{\omega^2(V)}{2} + \frac{3\omega(V)}{2} + 1\right] \omega^{(1)}(V) dV. \end{aligned} \tag{2.4.14}$$

At this point, if the integration by parts is applied recursively, it is easy to see that in every iteration the power of V is decreased, but the order of the polynomial $\omega(V)$ (by which is multiplied) is increased, in such a way, that its coefficients only depend on the coefficients of the polynomial in the previous step. Thus, by induction, it can be proven that:

$$\int V^k \omega(V) dV = k! \sum_{m=0}^{k} (-1)^m \frac{V^{k-m}}{(k-m)!} \sum_{j=1}^{m+2} a_{m+2,j} \omega^j(V) + cte, \tag{2.4.15}$$

where the coefficients $a_{m+1,j}$ satisfy the following recurrence relation:

$$\begin{aligned} &a_{m+1,j} = \frac{a_{m,j} + a_{m,j-1}}{j} \qquad \text{when} \qquad j \geqslant 2, \qquad m \geqslant 0, \\ &a_{m,1} = 1, \\ &a_{m,m+1} = 0. \end{aligned} \tag{2.4.16}$$

As the goal is to solve the integral from (2.4.11), a change of variable is required to substitute V by $V - \mu$:

$$\int (V-\mu)^k \omega(V) dV = k! \sum_{m=0}^{k} (-1)^m \frac{(V-\mu)^{k-m}}{(k-m)!} \sum_{j=1}^{m+2} a_{m+2,j} \omega^j(V) + cte. \tag{2.4.17}$$

Finally, if (2.4.17) and (2.4.9) are combined and the integral is evaluated in its limits (V_0 and V_1), then:

$$\int_{V_0}^{V_1} I(V)\left(\frac{V-\sigma}{\lambda}\right)^k dV = \frac{I_s}{\lambda^n}\left[\alpha\beta^{k+1}k!\sum_{m=0}^{k}\frac{(-1)^m}{(k-m)!}\sum_{j=1}^{m+2}a_{m+2,j}\right.$$
$$\cdot\left[(V_1'-\mu)^{k-m}\omega(V_1')^j-(V_0'-\mu)^{k-m}\omega(V_0')^j\right]-\frac{1}{k+1}\left[(V_1-\sigma)^{k+1}\right.$$
$$\left.\left.-(V_0-\sigma)^{k+1}\right]\right], \tag{2.4.18}$$

recalling (2.3.10) and,

$$\lambda=\frac{V_1-V_0}{2},\quad \sigma=\frac{V_1+V_0}{2},$$
$$V_0'=\frac{V_0}{\beta}-\gamma,\quad V_1'=\frac{V_1}{\beta}-\gamma. \tag{2.4.19}$$

This previous result together with the following expansion for Legendre polynomials [25]:

$$L_k\left(\frac{V-\sigma}{\lambda}\right)=\frac{1}{2^k}\sum_{m=0}^{[k/2]}\frac{(-1)^m(2(k-m)!)}{m!(k-2m)!(k-m)!}\left(\frac{V-\sigma}{\lambda}\right)^{k-2m}, \tag{2.4.20}$$

where $[\cdot]$ denotes the integer part, carry us to compute the coefficient A_k' in (2.4.21) for the $I(V)$ function.

$$A_k'=\frac{2k+1}{2\lambda}\int_{V_0}^{V_1}I(V)L_k\left(\frac{V-\sigma}{\lambda}\right)dV=\frac{2k+1}{2\lambda}\frac{I_s}{2^k}\sum_{m=0}^{[k/2]}\frac{(-1)^m\,(2\,(k-m))!}{m!\,(k-m)!\lambda^{k-2m}}$$
$$\cdot\left[\alpha\sigma^{k-2m+1}\sum_{l=0}^{k-2m}\frac{(-1)^l}{(k-2m-l)!}\sum_{j=1}^{l+2}a_{l+2,j}\left[\left(V_1'-\mu\right)^{k-2m-l}\omega(V_1')^j\right.\right.$$
$$\left.\left.-\left(V_0'-\mu\right)^{k-2m-l}\omega(V_0')^j\right]-\frac{(V_1-\sigma)^{k-2m+1}-(V_0-\sigma)^{k-2m+1}}{(k-2m+1)!}\right], \tag{2.4.21}$$

and thus, the $I(V)$ function can be expresses as a sum of Legendre polynomials.

$$I(V) = \sum_{k=0}^{\infty} A'_k L_k \left(\frac{V-\sigma}{\lambda}\right) = \sum_{k=0}^{\infty} \frac{A'_k}{2^k} \sum_{m=0}^{[k/2]} \frac{(-1)^m (2(k-m)!)}{m!\,(k-2m)!\,(k-m)!} \cdot \left(\frac{V-\sigma}{\lambda}\right)^{k-2m} = \sum_{k=0}^{\infty} A'_k \sum_{m=0}^{[k/2]} C_{k,m} (V-\sigma)^{k-2m}, \tag{2.4.22}$$

where,

$$C_{k,m} = \frac{(-1)^m (2(k-m)!)}{2^k \lambda^{k-2m} (k-2m)!\,(k-m)!m!}. \tag{2.4.23}$$

This expression can be rewritten in a power series with respect to V, and truncated to order M. Thus, it is necessary to reorganized the coefficients for simplifying the following expression:

$$I_M(V) = \sum_{k=0}^{M} D_{N,k} V^k. \tag{2.4.24}$$

After reordering the coefficients of (2.4.24) and using the binomial theorem (2.3.21), it can be seen that this coefficients can be written as:

$$D_{N,k} = \sum_{s=0}^{N-k} E_{N,k+s} \binom{k+s}{k} (-\sigma)^s, \tag{2.4.25}$$

where $E_{N,k}$ is defined as:

$$E_{N,k} = \sum_{s=0}^{[n-k/2]} A'_{k+2s} C_{k+2s,s}. \tag{2.4.26}$$

In this way, $I_M(V)$ converges to $I(V)$, minimizing $L^2[V_0, V_1]$ norm as:

$$\lim_{M\to\infty} \int_{V_0}^{V_1} (I_M(V) - I(V))^2 \frac{1}{2k+1} = 0. \tag{2.4.27}$$

The main difference between this approach (2.4.27) with Legendre polynomials and the previous one (2.3.23) with the Taylor series lies in the convergence region. In the Taylor series the convergence is point-wise, as already explained, in an specific interval denoted by the Wright Omega function. Nevertheless, the Legendre polynomial approximation has the advantage that it converges in the orthogonality region, in our case, $[V_0, V_1]$. The disadvantage of this approximation is that the convergence is weaker since it converges in L2-norm although we will see in the experiments (see Figure 2.4.1) that the approximation is pretty good.

2.4.1. Multiple-tone excitation for the analytical approximation of the diode IV curve

In this case, (2.4.24) represents the truncated version of $I(V)$ to order M. To compute the I_{DC}, let us proceed as in previous section with the Taylor series (2.3.27).

$$\begin{aligned} I_{DC} &\simeq \frac{1}{T}\sum_{k=0}^{M} D_{N,k}\int_0^T V(t)^k \mathrm{d}t \\ &= \sum_{k=0}^{M} D_{N,k}\frac{A^k}{2^k}B_{N,k}. \end{aligned} \tag{2.4.28}$$

It is similar to (2.3.29) where C_k is replaced by $D_{N,k}$. The $B_{N,k}$ coefficients remains the same, as the number of tones and the truncated order are not varied. Nevertheless, for simplicity its values can be checked in the previous section (from (2.3.34) to (2.3.37)). As in the previous study, the DC contribution is obtained calculating the first term of the Fourier series, defined as (2.4.28): Then,

$$I_{DC} \simeq D_{4,0} + 2A^2 D_{4,2} + \frac{21}{2}A^4 D_{4,4} + 80A^6 D_{4,6} + \frac{23765}{32}A^8 D_{4,8}. \tag{2.4.29}$$

In a non-general scenario $\sum_{q=1}^{N}(p_q - p_{-q})\,n_q = 0$, even for some partitions where $p_q \neq p_{-q}$. To show that, let us consider a harmonic spaced four-tone signal, this is, $\omega_i = i\omega_i + \phi_i$, $i = 1, \ldots, 4$, where ϕ_i is the phase of tone i. It is important to notice that phase terms (ϕ_i) do not contribute in the computation of the DC current if $p_q = p_{-q}$ as occurs in the general scenario shown in previous section. In this case, for a truncation of order 8, our procedure gives the following formula for the DC current:

$$
\begin{aligned}
I_{DC} \simeq\ & D_{4,0} + 2A^2 D_{4,2} + A^4 D_{4,4}\left[\frac{21}{2} + \frac{3}{2}\cos(\phi_2 - 2\phi_3 + \phi_4) + \frac{3}{2}\cos(\phi_1\right. \\
& \left. -2\phi_2 + \phi_3) + 3\cos(\phi_1 - \phi_2 - \phi_3 + \phi_4)\right] + A^6 D_{4,6}\left[80 + \frac{105}{4}\cos(\phi_2 - 2\phi_3\right. \\
& \left. +\phi_4) + \frac{105}{4}\cos(\phi_1 + -2\phi_2 + \phi_3) + 45\cos(\phi_1 - \phi_2 - \phi_3 + \phi_4) + \frac{15}{8}\cos(\phi_1\right. \\
& \left. -3\phi_3 + 2\phi_4) + \frac{15}{8}\cos(2\phi_1 - 3\phi_2 + \phi_4)\right] + A^8 D_{4,8}\left[\frac{23765}{32} + \frac{5985}{16}\cos(\phi_2\right. \\
& \left. -2\phi_3 + \phi_4) + \frac{105}{32}\cos(2\phi_2 - 4\phi_3 + 2\phi_4) + \frac{35}{4}\cos(\phi_1 - 3\phi_2 + 3\phi_3 - \phi_4)\right. \\
& \left. + \frac{5985}{16}\cos(\phi_1 - 2\phi_2 + \phi_3) + \frac{1155}{2}\cos(\phi_1 - \phi_2 - \phi_3 + \phi_4) + \frac{875}{16}\cos(\phi_1\right. \\
& \left. -3\phi_3 + 2\phi_4) + \frac{105}{32}\cos(2\phi_1 - 4\phi_2 + 2\phi_3) + \frac{875}{16}\cos(2\phi_1 - 3\phi_2 + \phi_4)\right. \\
& \left. + \frac{315}{16}\cos(2\phi_1 - 2\phi_2 - 2\phi_3 + 2\phi_4)\right]. \qquad (2.4.30)
\end{aligned}
$$

Notice that the contributions such that $p_q \neq p_{-q}$ produce terms depending on the cosines of linear combinations of phases. These factors are obtained as in the general case by finding the number of combinations. For example, to see how to get these terms, let us show how we have obtained the term $3/2\cos(\phi_2 - 2\phi_3 + \phi_4)$ in the first row of 2.4.30, where its partition and the complementary one are shown in Table 2.7. These partitions are considered complementary because they only differ in the sign. That is why the cosine appears, because two complex exponentials with different sign are added.

p_{-4}	p_{-3}	p_{-2}	p_{-1}	p_4	p_3	p_2	p_1
0	2	0	0	1	0	1	0
1	0	1	0	0	2	0	0

Table 2.7: Complemetary partitions for a harmonic spaced example.

The number of combinations are obtained as in (2.3.35), in this case:

$$\binom{4}{0,2,0,0,1,0,1,0} = 12,$$

then, the number 3/2 comes from:

$$\frac{1}{2^4} \cdot 2 \cdot \binom{4}{0,2,0,0,1,0,1,0} = \frac{3}{2}.$$

Moreover, it is interesting to check that both odd and even values of k can contribute in this case to the DC component.

2.4.2. Analysis example

As in the previous analysis, four equal amplitude tones are compared with two equal amplitude tones and a single tone with the same average power, using this new approach. The main difference is that this model is valid for larger input voltage values (a few volts), getting less than a 6 % in the relative error. The previous analytical approach was very accurate up to 90 mV. The amplitude for each tone is varied from 0.005 V to 1V. It is noticeable that the four-tone improvement happens only in the non-linear region of the diode (exponential term). At low input power levels, as long as the number of tones is increased, more DC current is obtained at the output, therefore increasing the conversion efficiency (see Figure 2.4.1(a-b)). This is due to the non-linear region of the IV curve of the diode. If we continue pushing the voltage upwards, there is a point where the diode enters in the linear region and a single tone starts to get a better performance (see Figure 2.4.1(c)). This means that the efficiency improvement when working with

multiple-tone signals is just useful at low input power densities, as happens with the ambient spectrum. In Table 2.8 and Table 2.9, the simulated and predicted DC output current are summarized. The error of the analytical model is included, showing a good approximation for high voltage levels (a maximum error of 6 % when the amplitude of each tone is 0.95 V).

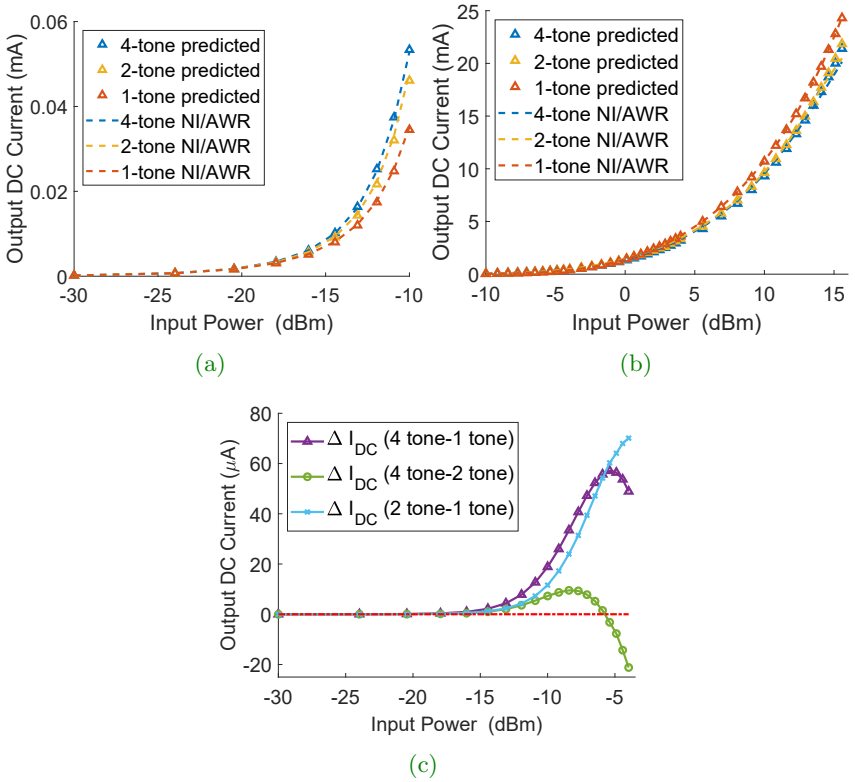

Figure 2.4.1: Predicted DC output current versus average input power. a) Small signal excitation below 0.05 V. b) Large signal excitation up to 0.95 V. c) ΔI_{DC} for a four-tone excitation compared with a CW.

N	Tone Amplitude (mV)	Input Power (dBm)	Predicted I_{DC} (mA)	Simulated I_{DC} (mA)	Maximum Relative Error (%)
4	5.00	-30.0	$1.702{\cdot}10^{-4}$	$1.722{\cdot}10^{-4}$	1.16
2	7.07	-30.0	$1.697{\cdot}10^{-4}$	$1.718{\cdot}10^{-4}$	1.22
1	10.00	-30.0	$1.691{\cdot}10^{-4}$	$1.712{\cdot}10^{-4}$	1.23
4	10.00	-24.0	$7.113{\cdot}10^{-4}$	$7.196{\cdot}10^{-4}$	1.15
2	14.14	-24.0	$7.042{\cdot}10^{-4}$	$7.134{\cdot}10^{-4}$	1.29
1	20.00	-24.0	$6.932{\cdot}10^{-4}$	$7.020{\cdot}10^{-4}$	1.25
4	20.00	-18.0	$3.399{\cdot}10^{-3}$	$3.415{\cdot}10^{-3}$	0.47
2	28.28	-18.0	$3.228{\cdot}10^{-3}$	$3.227{\cdot}10^{-3}$	0.03
1	40.00	-18.0	$3.050{\cdot}10^{-3}$	$3.090{\cdot}10^{-3}$	1.30
4	30.00	-14.5	$10.170{\cdot}10^{-3}$	$10.080{\cdot}10^{-3}$	0.89
2	42.42	-14.5	$9.164{\cdot}10^{-3}$	$9.344{\cdot}10^{-3}$	1.92
1	60.00	-14.5	$8.004{\cdot}10^{-3}$	$8.129{\cdot}10^{-3}$	1.54
4	40.00	-12.0	$2.524{\cdot}10^{-2}$	$2.483{\cdot}10^{-2}$	1.67
2	56.56	-12.0	$2.166{\cdot}10^{-2}$	$2.220{\cdot}10^{-2}$	2.43
1	80.00	-12.0	$1.743{\cdot}10^{-2}$	$1.773{\cdot}10^{-2}$	1.69
4	50.00	-10.0	$5.336{\cdot}10^{-2}$	$5.289{\cdot}10^{-2}$	0.89
2	70.71	-10.0	$4.609{\cdot}10^{-2}$	$4.800{\cdot}10^{-2}$	3.96
1	100	-10.0	$3.451{\cdot}10^{-2}$	$3.518{\cdot}10^{-2}$	1.90
4	60.00	-8.5	$9.732{\cdot}10^{-2}$	$9.840{\cdot}10^{-2}$	1.10
2	84.85	-8.5	$8.781{\cdot}10^{-2}$	$9.275{\cdot}10^{-2}$	5.33
1	120.00	-8.5	$6.386{\cdot}10^{-2}$	$6.519{\cdot}10^{-2}$	2.04
4	70.00	-7.0	$1.580{\cdot}10^{-1}$	$1.620{\cdot}10^{-1}$	2.47
2	98.99	-7.0	$1.502{\cdot}10^{-1}$	$1.601{\cdot}10^{-1}$	6.18
1	140.00	-7.0	$1.108{\cdot}10^{-1}$	$1.131{\cdot}10^{-1}$	2.03
4	80.00	-6.0	$2.352{\cdot}10^{-1}$	$2.460{\cdot}10^{-1}$	4.39
2	113.13	-6.0	$2.337{\cdot}10^{-1}$	$2.498{\cdot}10^{-1}$	6.45
1	160.00	-6.0	$1.795{\cdot}10^{-1}$	$1.831{\cdot}10^{-1}$	1.97
4	90.00	-5.0	$3.283{\cdot}10^{-1}$	$3.470{\cdot}10^{-1}$	5.39
2	127.27	-5.0	$3.360{\cdot}10^{-1}$	$3.591{\cdot}10^{-1}$	6.43
1	180.00	-5.0	$2.719{\cdot}10^{-1}$	$2.771{\cdot}10^{-1}$	1.88

Table 2.8: Predicted and simulated DC output current vs average input power for one, two and four tones. Small signal excitation.

N	Tone Amplitude (V)	Input Power (dBm)	Predicted I_{DC} (mA)	Simulated I_{DC} (mA)	Maximum Relative Error (%)
4	0.1000	-4.0	$4.36{\cdot}10^{-1}$	$4.64{\cdot}10^{-1}$	6.03
2	0.1414	-4.0	$4.57{\cdot}10^{-1}$	$4.86{\cdot}10^{-1}$	5.96
1	0.2000	-4.0	$3.87{\cdot}10^{-1}$	$3.95{\cdot}10^{-1}$	2.02
4	0.2000	2.0	2.10	2.22	5.41
2	0.2828	2.0	2.25	2.31	2.60
1	0.4000	2.0	2.40	2.37	1.27
4	0.3000	5.5	4.30	4.49	4.23
2	0.4242	5.5	4.53	4.56	0.66
1	0.6000	5.5	5.00	4.99	0.20
4	0.4000	8.0	6.70	6.96	3.74
2	0.5656	8.0	7.02	7.04	0.28
1	0.8000	8.0	7.80	7.82	0.26
4	0.5000	10.0	9.30	9.54	2.52
2	0.7071	10.0	9.62	9.63	0.10
1	1.0000	10.0	10.70	10.75	0.47
4	0.6000	11.5	11.90	12.11	1.73
2	0.8485	11.5	12.27	12.30	0.24
1	1.2000	11.5	13.70	13.73	0.22
4	0.7000	13.0	14.60	14.61	0.07
2	0.9899	13.0	14.98	15.09	0.73
1	1.4000	13.0	16.70	16.74	0.24
4	0.8000	14.0	17.30	16.93	2.18
2	1.1313	14.0	17.71	17.50	1.20
1	1.6000	14.0	19.70	19.77	0.35
4	0.9000	15.0	20.00	19.07	4.87
2	1.2727	15.0	20.46	19.50	4.92
1	1.8000	15.0	22.80	22.82	0.09
4	0.9500	15.5	21.40	20.07	6.63
2	1.3435	15.5	21.85	20.37	7.27
1	1.9000	15.5	24.30	24.33	0.12

Table 2.9: Predicted and simulated DC output current vs average input power for one, two and four tones. Large signal excitation.

2.5. Conclusions

A theoretical analysis in the diode has been performed to predict the amount of DC current obtained when multiple-tone input signals are used at the same time. Some previous studies were limited to a very simplified model where $R_s = 0$. This assumption is no longer valid as that parameter affects the IV curve slope, especially in the exponential region where the non-linear rectifying process happens. Therefore, this thesis tries to give a comprehensive answer to that problem. Two different approaches to estimate the I_{DC} contribution are shown, one that can be used only for low input voltage and other that can be used to any voltage. In the first approach, the Wright Omega function and its finite derivatives are used to approximate the IV curve using a Taylor series. This approach is good (less than 6 %) in its convergence region (estimated empirically) below 0.1 V. Nevertheless, for higher input voltages the error is high. The other approach is implemented for working with low and high voltage excitations when Legendre polynomials are used. The Legendre polynomial approximation has the advantage that it converges in the orthogonality region, in our case, $[V_0, V_1]$. The disadvantage of this approximation is that the convergence is weaker since it converges in L2-norm although it is pretty good, as observed in the experiements. Both models have been tested over the Spice parameters published in the datasheet for the SMS7630 zero-bias Schottky diode. Next chapter deals with the accuracy of these parameters, developing a more precise Spice (and parasitic) model.

The diode analysis presented here is focused on a general four-tone scenario where tones are not equally spaced, although the harmonic separation is analyzed in one section. In this case, the DC current component is increased as the harmonic relation between tones contributes to more DC current.

It is theoretically proven that a DC output current improvement is achieved when high PAPR signals are applied, when compared to a single tone excitation with the same average power, but in the non-linear region (low input voltage levels). As long as the input voltage is increased, the efficiency improvement decays. The mathematical model is tested and compared to simulations for one, two and four tones when the amplitude of each tone is varied from 0.005 to 0.95 V. By default in the harmonic balance simulation in NI/AWR [26] the number of harmonics is limited (see Figure 2.5.1). Nevertheless, the harmonics and intermodulation products affect. Therefore, the accuracy of this simulator is compared using different number of harmonics (Table 2.10).

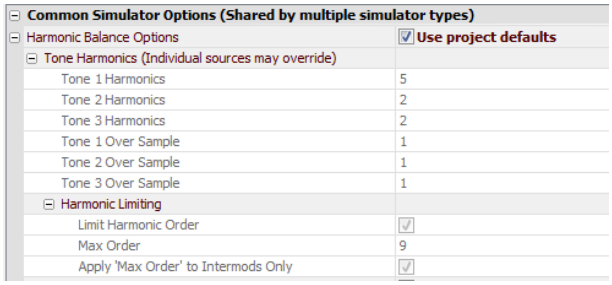

Figure 2.5.1: Default values for the harmonic balance simulator of NI/AWR.

First, each tone had one harmonic and later, each tone provided up to eight harmonics (the maximum value). The maximum order of the intermodulation products was not varied. This was tested for a four-tone scenario, when the amplitude of each tone was 0.8 V. As it can be seen, as long as the number of harmonics is increased, more accuracy can be obtained at the expenses of a higher simulation time. Nevertheless, the default properties of the simulator provide an accurate result. In this way, it is possible to compare the non-linear region where the multiple-tone approach is valid, and the linear regions where no longer improvement is obtained, with a lower simulation time.

Harmonic Order	I_{DC} (mA)	Simulation Time (s)
1	17.14	0.67
8	16.92	13.21
Default	16.93	1.69

Table 2.10: I_{DC} value and simulation time for different harmonic orders.

It is worth mentioning that in both mathematical approaches a resistive rectifier is considered for the analysis. Nevertheless, the junction capacitance can be included in the future studies in analogy to the analysis of reactive mixers, see e.g., [20]. Also, the parasitic influence of the package can be analized for a future improvement. Although this theoretical prediction is good (good accuracy over low and high voltage levels and for four tones), this idea would improve estimation at the expense of adding great complexity.

The approximation using the Taylor expansion was presented in the 2019 IEEE International Conference on Microwaves, Antennas, Communications and Electronic Systems (COMCAS) in Tel Aviv. A deeper study is presented in the thesis, with a new approach using Legendre polynomials. This contribution was done in collaboration with Alberto López Yela, a researcher from University Charles III of Madrid.

Conference contribution:
Ana López-Yela, Alberto López-Yela, D. Segovia-Vargas and Z. Popović, "Non-Linear Diode Rectifier Analysis for Multi-Tone Wireless Power Harvesting," 2019 IEEE International Conference on Microwaves, Antennas, Communications and Electronic Systems (COMCAS), Tel-Aviv, Israel, 2019, pp. 1-5, doi: 10.1109/COMCAS44984.2019.8957851.

References

[1] M. Piñuela, P. D. Mitcheson and S. Lucyszyn, "Ambient RF Energy Harvesting in Urban and Semi-Urban Environments," in IEEE Transactions on Microwave Theory and Techniques, vol. 61, no. 7, pp. 2715-2726, July 2013.

[2] Kuhn, V., Seguin, F., Lahuec, C., and Person, C. (2016). Enhancing RF-to-DC conversion efficiency of wideband RF energy harvesters using multi-tone optimization technique. International Journal of Microwave and Wireless Technologies, 8(2), 143-153. doi:10.1017/S1759078714001457

[3] A. Boaventura, D. Belo, R. Fernandes, A. Collado, A. Georgiadis and N. B. Carvalho, "Boosting the Efficiency: Unconventional Waveform Design for Efficient Wireless Power Transfer," in IEEE Microwave Magazine, vol. 16, no. 3, pp. 87-96, April 2015. doi: 10.1109/MMM.2014.2388332

[4] M. S. Trotter, J. D. Griffin, and G. D. Durgin, "Power-optimized waveforms for improving the range and reliability of RFID systems," in Proc. IEEE Int. Conf. RFID, 2009, pp. 80–87.

[5] J. A. Hagerty, F. B. Helmbrecht, W. H. McCalpin, R. Zane, Z. Popovic, "Recycling ambient microwave energy with broad-band rectenna arrays," in IEEE Transactions on Microwave Theory and Techniques, vol. 52, no. 3, pp. 1014-1024, March 2004.

[6] Z. Liu, Z. Zhong and Y. Guo, "Intermodulation harvesting rectifier design for high efficiency multi-sine wireless power transfer," 2016 IEEE MTT-S International Microwave Symposium (IMS), San Francisco, CA, 2016, pp. 1-3.

[7] A. Collado and A. Georgiadis, "Improving wireless power transmission efficiency using chaotic waveforms," 2012 IEEE/MTT-S International Microwave Symposium Digest, Montreal, QC, 2012, pp. 1-3.

[8] A. Collado and A. Georgiadis, "Optimal waveforms for efficient wireless power transmission," IEEE Microwave Wireless Compon. Lett., vol. 24, no. 5, pp. 354–356, May 2014.

[9] A. S. Boaventura and N. B. Carvalho, "Maximizing DC power in energy harvesting circuits using multisine excitation," 2011 IEEE MTT-S International Microwave Symposium, Baltimore, MD, 2011, pp. 1-4.

[10] D. Belo and N. B. Carvalho, "Harmonic spaced multisines for efficient wireless power transmission," 2015 IEEE Wireless Power Transfer Conference (WPTC), Boulder, CO, 2015, pp. 1-4.

[11] The Shockley diode equation:
https://en.wikipedia.org/wiki/Shockley_diode_equation

[12] SMS7630 Series Surface Mount Mixer and Detector Schottky Diodes from Skyworks.
http://www.skyworksinc.com/Product/511/SMS7630_Series#four

[13] H. Matsumoto and K. Takei, "An experimental study of passive UHF RFID system with longer communication range," in Proc. Asia-Pacific Microwave Conf., 2007, pp. 1–4.

[14] A. S. Boaventura and Nuno Borges Carvalho, "Enhanced front-end to extend reading range of commercial RFID readers using efficient multisine signals," 2012 IEEE/MTT-S International Microwave Symposium Digest, Montreal, QC, 2012, pp. 1-3.

[15] A. S. Boaventura and N. B. Carvalho, "Extending reading range of commercial RFID readers," IEEE Trans. Microwave Theory Tech., vol. 61, no. 1, pp. 633–640, Jan. 2013.

[16] N. Pan, A. S. Boaventura, M. Rajabi, D. Schreurs, N. B. Carvalho and S. Pollin, "Amplitude and frequency analysis of multi-sine wireless power transfer," 2015 Integrated Nonlinear Microwave and Millimetre-wave Circuits Workshop (INMMiC), Taormina, 2015, pp. 1-3.

[17] A. Collado and A. Georgiadis, "Optimal Waveforms for Efficient Wireless Power Transmission," in IEEE Microwave and Wireless Components Letters, vol. 24, no. 5, pp. 354-356, May 2014.

[18] L. Chun-Chih, Y. Yu-Lin, T. Chi-Lin, L. Chieh-Sen, and Y. Chin-Lung, "Novel wireless impulsive power transmission to enhance the conversion efficiency for low input power," in Proc. Microwave Workshop Series Innovative Wireless Power Transmission, 2011, pp. 55–58.

[19] Ana López-Yela, Alberto López-Yela, Z. Popovic, D. Segovia-Vargas, " *Non-Linear Diode Rectifier Analysis for Multi-tone Wireless Power Harvesting*," 2019 IEEE International Conference on Microwaves, Antennas, Communications and Electronic Systems (COMCAS), Tel-Aviv, 2019.

[20] D. N. Held and A. R. Kerr, "Conversion Loss and Noise of Microwave and Millimeterwave Mixers: Part 1 - Theory," in IEEE Transactions on Microwave Theory and Techniques, vol. 26, no. 2, pp. 49-55, Feb. 1978.

[21] Corless, R. M. and D. J. Jeffrey. "The Wright omega Function." Artificial Intelligence, Automated Reasoning, and Symbolic Computation (J. Calmet, B. Benhamou, O. Caprotti, L. Henocque, and V. Sorge, eds.). Berlin: Springer-Verlag, 2002, pp. 76-89.

[22] T. C. Banwell and A. Jayakumar, "Exact analytical solution for current flow through diode with series resistance," in Electronics Letters, vol. 36, no. 4, pp. 291-292, 17 Feb. 2000. doi: 10.1049/el:20000301

[23] Multinomial Theorem.
https://www.britannica.com/science/multinomial-theorem

[24] T.S. Chihara. *An introduction to Orthogonal Polynomials*. Dover. New York (2011).

[25] S. B. Yuste, Métodos Matemáticos Avanzados para Cientficos e Ingenieros, Universidad de Extremadura, 2006.

[26] Harmonic Balance Analysis in NI/AWR.
https://awrcorp.com/download/faq/english/docs/Simulation/hb_analysis.html

3

Non-Linear rectifier analysis for multiple-tone wireless power harvesting: verification of the analytical approach

To validate the analytical model presented in Chapter 2, multiple-tone measurements have been performed for the non-linear diode rectifier, comparing them to simulations with an RF microwave design software, AWR. To properly compare these three results, it is necessary to use an accurate Spice diode model (including parasitics) and an appropriate measurement setup. Otherwise, results will differ due to an inadequate characterization of the non-linear device. This chapter addresses those issues in addition to measurements.

3.1. Introduction

In the previous chapter, an analytical expression for an ideal diode was developed to theoretically characterize its non-linearity under multiple-tone input signals (2.4.28). As already explained, the Shockley equation governs the diode performance in the direct mode, using some of its Spice parameters (such as the saturation current, the ideality factor or the series resistance). Thus, this general expression (2.4.28) is valid for whatever device fulfilling the Shockley equation and that it is excited with a multiple-tone signal. In this way, it is possible to accurately estimate the DC current in a multiple-tone scenario for an ideal diode, avoiding convergence problems of simulators.

The Spice model provided by the manufacturer [1] was used to perform the analysis in the previous chapter although, in this case, neither the input power levels nor the frequency range were specified in the datasheet. Nevertheless, those values were used to validate the theoretical approach of the diode, getting a good accuracy (see Table 2.9). This chapter deals with multiple-tone simulations and measurements in a rectifier. The goal is to compare both results with the trend obtained from the theoretical approach, to verify the efficiency improvement when working with multiple-tone excitations. Thus, it is necessary to guarantee the accuracy of the Spice model and include the package parasitics of the diode to simulate the RF performance of a real rectifier. Otherwise, simulations and measurements will differ due to an inaccurate modeling of the Spice definition and therefore, it would not be possible to compare them with the theoretical analysis.

In Figure 3.1.1 a comparison between the IV curve provided by the manufacturer and the simulated IV curve in AWR using the Spice parameters from the datasheet [1] is shown. A significant difference is appreciated and at first glance this difference denotes some inaccuracies in the extracted model. It may be because the frequency and power range where the model works is not specified. Indeed, the operational point may be different from the one used for energy harvesting and even at another frequency range. Then, a new Spice definition of the diode is required.

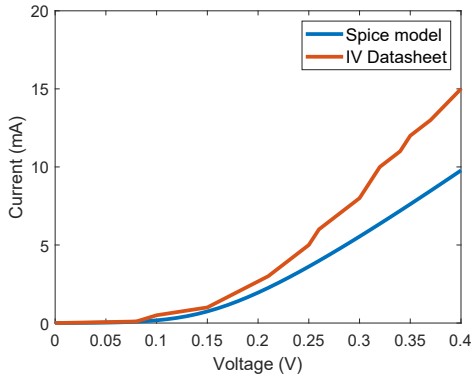

Figure 3.1.1: IV curve. Spice model simulated in AWR vs datasheet data from [1].

To do this, different rectifier circuits are tested to extract an accurate model for the diode in the simulations in AWR. Once the model is validated, it is possible to perform the multiple-tone analysis comparing the trend of the ideal mathematical approach (where no-parasitics are included but with the corrected Spice parameters), with simulations and the real rectifier performance. A simulation and measurement setup has been designed to perform the analysis where up to four tones with different voltage amplitudes are used to excite the circuit.

3.2. Development of the parasitical and intrinsic circuit diode model

When working with non-linear devices (in this case a diode), it is necessary to check if the Spice model is accurate enough and the parasitics associated with the package are included. Otherwise, a comparison between simulations and measurements cannot be established. In this section, the Spice model and its associated package parasitics are revised to obtain a complete diode modeling for simulations. In this way, it is possible to get accurate results when doing measurements.

For this purpose, the SMS7630 Zero Bias Schottky diode from Skyworks [1] is chosen due to its good characteristics under low input power levels (low threshold voltage) and fast switching response at high frequencies (low junction capacitance). Besides, as it is a zero bias diode, no bias is required to use the diode, which is a good choice for using this device in an energy harvesting application. A series pair configuration with a SOT-23 package is used through these chapters in order to benefit from a voltage doubler topology. The most significant values from the Spice model of the diode are shown in Table 3.1.

Parameter	I_S	R_S	B_V	C_{jo}	I_{BV}	V_j	N
Datasheet value	5 μA	20 Ω	2 V	0.14 pF	100 μA	0.34 V	1.05

Table 3.1: SMS7630 Spice parameters from datasheet [1].

A circuital model including the Spice parameters and the diode package parasitics is required. Thus, a rectifier is designed, where the SOT-23 package from Skyworks [2] (see Figure 3.2.1) is used to model the package and the Spice model from the datasheet [1] is inserted in the diode chip. In Figure 3.2.2, this circuit under test is shown. It is designed at 2.23 GHz, being simulated and measured from -25 to -10 dBm in the 0.1-3.6 GHz range. This prototype is composed of a voltage doubler rectifier, a fixed 3.9 kΩ load and a matching network with an open stub. It is built on a Duroid 5880 substrate (H=0.787 mm, ϵ_r=2.2 and tan δ=0.0009).

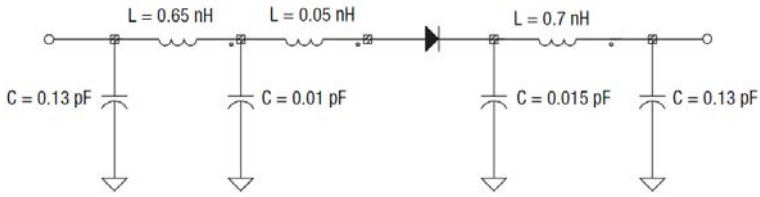

Figure 3.2.1: Parasitic circuital model courtesy of Skyworks [2].

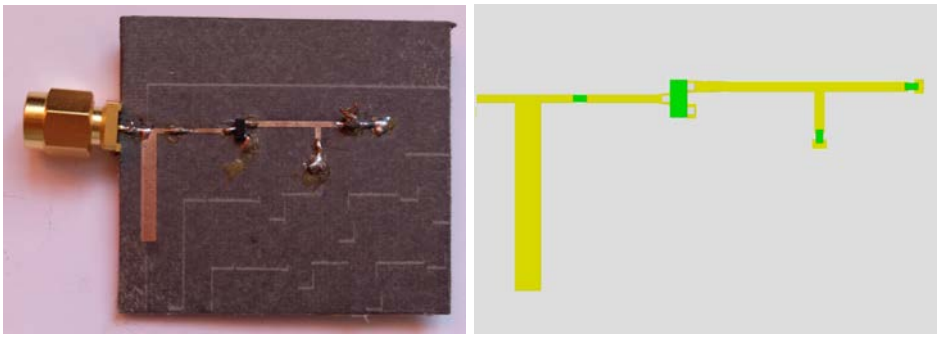

(a) (b)

Figure 3.2.2: Diode rectifier circuit under test, used for extraction of the circuital model, with an open stub in the matching network. a) Prototype circuit. b) Layout.

The comparison between simulations and measurements is established through the absolute error of the S-parameters (magnitude and phase) and the RF-DC power conversion efficiency to quantify the deviation of the circuital model. In this way the measurements are used as the target or real value:

$$\text{Absolute Error} = \text{Simulated Value} - \text{Measured Value}.$$

S-parameters measurements are performed using the handheld network analyzer (N9918A FieldFox Handheld Microwave Analyzer working up to 26.5 GHz [3]) from 0.1 to 3.6 GHz, using the large signal S-parameters (LS_{xx}) as it is a non-linear measurement [4]. When working with non-linear devices, small-signal S-parameters are not suitable for characterization. A non-linear device, such as a diode, produces a different response attending to the bias point, input power level, frequency and loading conditions. Moreover, superposition assumption is no longer valid under large signals conditions as strong non-linearities can appear and a linear approximation is not applicable. Therefore, the use of large signal S-parameter is required.

Measurements are performed varying the excitation power level from -25 to -10 dBm. For the power efficiency measurements, the DC voltage component is measured through a voltage-meter connected to the fixed load. Power and frequency are varied in this case from -25 to -10 dBm and from 0.1 to 3 GHz. The conversion efficiency relates the percentage of DC power to RF input power.

$$\eta = \frac{P_{DC}}{P_{RF}} = \frac{V_{DC}/R_L}{P_{RF}}. \tag{3.2.1}$$

In this case, the frequency limit (3 GHz) is imposed by the characteristics of the signal generator (N5181A-503 from Keysight [5]). In both cases, a 30 cm coaxial cable from Rosenberger is employed to connect the network analyzer or signal generator to the circuit itself. The S-parameter measurements are not affected by the cable losses as a previous calibration was done of the complete setup. Nevertheless, efficiency measurements are affected, so the S_{21} parameter of the cable was measured to calculate its losses, and it was also included in simulations.

Frequency-dependent results are obtained so the maximum value of the absolute error helps us to quantify deviations although it is not a significant parameter. Frequency deviations can affect the error providing very high values, as the error is computed for each frequency point, between the simulation and the measurement. In RF circuit simulation is common to suffer from frequency shifts due to different factors, ranging from bad treatment of inaccuracies or even due to fabrication tolerances. Therefore a frequency shift is expected as a common error and its presence sometimes is unavoidable. Nevertheless, a possible way to mitigate this fact it to work with the mean error. The mean value provides a good estimation of the model as it is a sum of errors of order 1, analyzing the precision. Whatever mean estimation of error is valid (for order 2, getting the mean square error). Attending to the relative error, for this case it is not relevant. Frequency deviations will produce very large relative errors that in other scenarios can imply a bad estimation. In this case, this parameter does not give significant information about the model.

3.2.1. Skyworks parasitic model

Once the procedure for analyzing the model is established, the Skyworks model is tested, showing a disagreement with the measurements and a large absolute error (see Figure 3.2.3). In Table 3.2, a compilation of the maximum and mean value for the absolute error for the S_{11} (magnitude and phase) and efficiency are listed, showing very large values.

Input power / Error	-10 dBm	-15 dBm	-20 dBm	-25 dBm
Max Error $\lvert S_{11}\rvert$	0.76	0.79	0.82	0.83
Mean Error $\lvert S_{11}\rvert$	0.21	0.21	0.20	0.20
Max Error $\measuredangle S_{11}$ (°)	316.70	318.74	321.04	329.09
Mean Error $\measuredangle S_{11}$ (°)	146.97	147.42	146.22	145.67
Max Error η_{RF-DC} (%)	28.80	23.54	15.73	8.20
Mean Error η_{RF-DC} (%)	5.59	3.72	1.96	0.87

Table 3.2: Maximum and mean absolute error of the Skyworks model: analysis of the magnitude and phase of the S-parameter and the RF-DC power conversion efficiency.

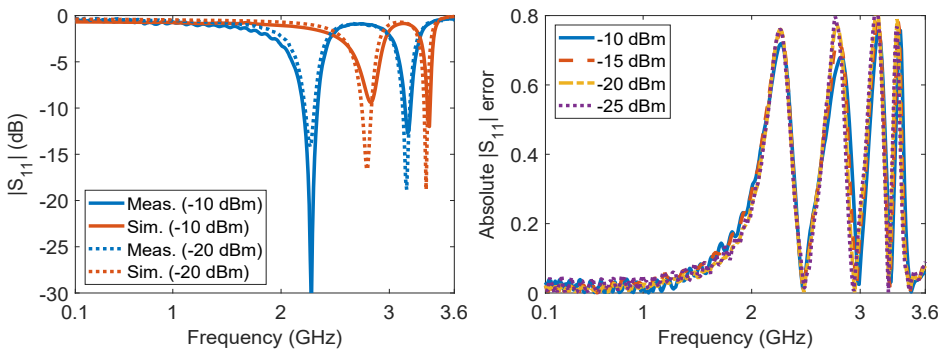

(a) (b)

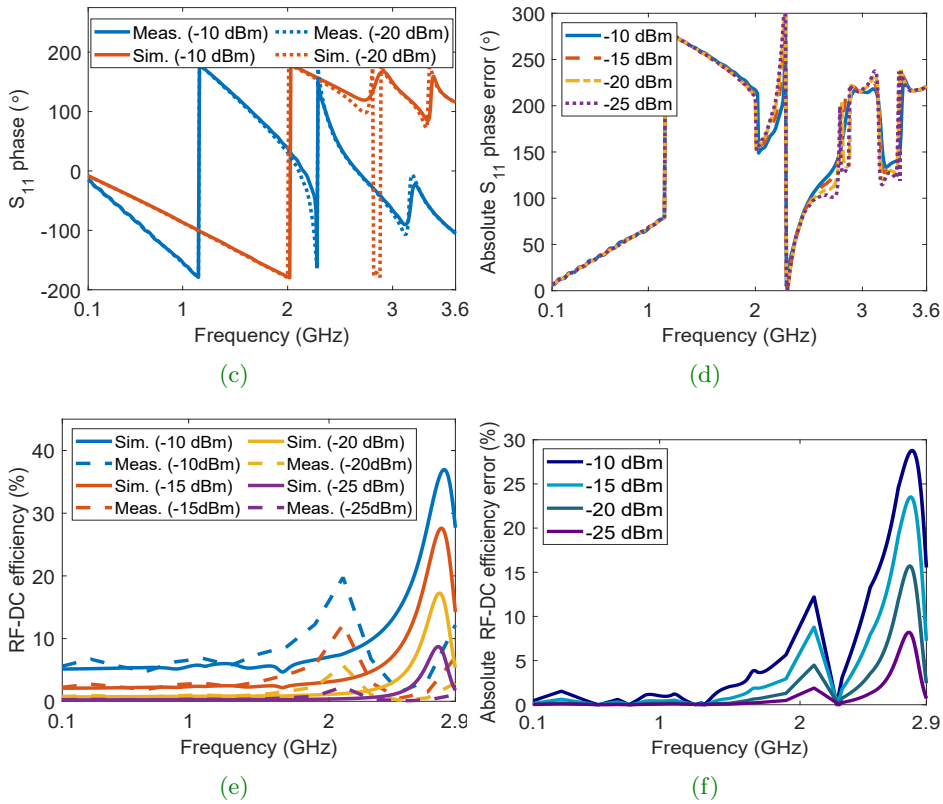

Figure 3.2.3: Circuit under test with the Skyworks model. a) $|S_{11}|(dB)$. b) Absolute $|S_{11}|$ error. c) Phase of S_{11}. d) Absolute phase error of S_{11}. e) $\eta_{RF-DC}(\%)$. f) Absolute efficiency error.

Both $|S_{11}|$ and efficiency provide an unacceptable mean absolute error for a proper characterization of the device, larger than 0.2 for the $|S_{11}|$, and with peaks greater than 23.5 % and 29 % for the efficiency at both -15 dBm and -10 dBm (see Figure 3.2.3), using the parasitic modeling from Skyworks [2]. The S_{11} phase shows a complete different performance over the frequency range, and the magnitude suffers a huge frequency shift. Therefore, it can be concluded that this model is not appropriate for an accurate simulation of the diode rectifier. Then, a different model is going to be tested.

3.2.2. Broadcom parasitic model

In this case, the Broadcom [6] parasitic modeling for a SOT-23 package is going to be tested in order to know if this model can give a better estimation with a lower error. The parasitic circuit modeling from Broadcom is shown in Figure 3.2.4, where the diode chip remains being the same Spice model from the datasheet in [1].

Input power / Error	-10 dBm	-15 dBm	-20 dBm	-25 dBm
Max Error $\|S_{11}\|$	0.89	0.92	0.94	0.94
Mean Error $\|S_{11}\|$	0.20	0.21	0.20	0.20
Max Error $\measuredangle S_{11}$ (°)	318.90	319.87	321.40	329.04
Mean Error $\measuredangle S_{11}$ (°)	148.38	147.70	146.57	145.58
Max Error η_{RF-DC} (%)	37.82	28.95	18.15	9.10
Mean Error η_{RF-DC} (%)	6.10	4.07	2.18	0.96

Table 3.3: Maximum and mean absolute error of the Broadcom model: analysis of the magnitude and phase of the S-parameter and the RF-DC power conversion efficiency.

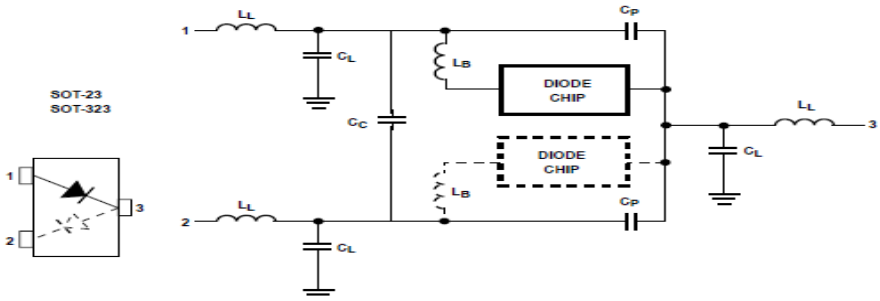

(a)

	Element:	L_L	C_L	C_P	C_C	L_B
	Description:	Leadframe Inductance	Leadframe Capacitance	Package Capacitance	Coupling Capacitance	Bondwire Inductance
	Units:	nH	pF	pF	pF	nH
SOT-23/SOT-143	to 3 GHz	0.50	0	0.080	0.060	1.0

(b)

Figure 3.2.4: Parasitic circuital diode model courtesy of Broadcom [6]. a) Parasitic circuit. b) Table of parameters.

In Figure 3.2.5 and in Table 3.3 the mean and maximum absolute error values are shown at different power levels. For this model, the error is very large and in the same order of magnitude than with the Skyworks model. Therefore, it can be concluded that neither this model nor the previous one provides an appropriate estimation of the diode rectifier performance. Moreover, this model shows just one resonance in the S_{11} magnitude while two resonances should appear. The phase response is completely different and the efficiency provides a large error. To overcome this issue, a new model is going to be designed, starting from the Broadcom scheme as from the author's point of view, its circuit model (not the values) better exemplifies the behavior of the parasitic elements. This new model will be iterated till reduce as much as possible the errors, to get a good accuracy.

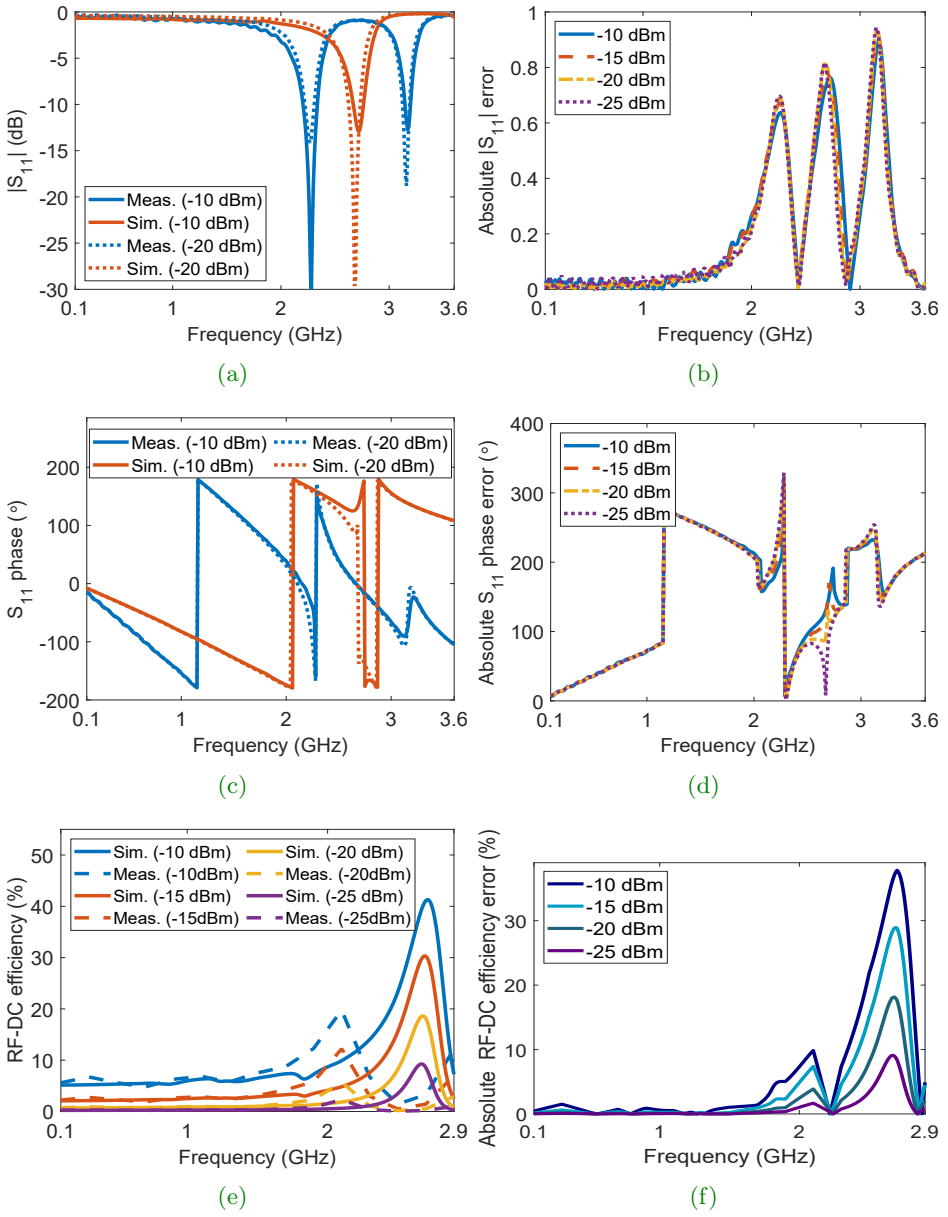

Figure 3.2.5: Circuit under test with the Broadcom model. a) $|S_{11}|\,(dB)$. b) Absolute $|S_{11}|$ error. c) Phase of S_{11}. d) Absolute phase error of S_{11}. e) $\eta_{RF-DC}(\%)$. f) Absolute efficiency error.

3.2.3. Design of a parasitic model for SMS7630 diode

A new model is going to be designed based on [6], tuning the parasitics and some Spice parameters to match the simulations to measurements for low input power levels (from -25 to -10 dBm) around 0.1 to 3.6 GHz. The new model is based on Broadcom parasitic circuital model (see Figure 3.2.4), instead of Skyworks one, as it can be easily identified the effect of each parasitic. As both models result in larger errors, it cannot be said that neither model is better than the other.

Analyzing the circuital model, the lead effect is included by adding an inductor, L_L. C_C represents the coupling between both diode chips. To conclude, L_B models the bondwire inductance and C_P represents the package parasitic. In order to tune the model, an iterative process adjusting the values of the different parameters has been undertaken, analyzing the influence of each parameter. For simplicity just two approaches are presented. The first one shows an intermediate designed model with a good performance for the $|S_{11}|$ and efficiency but not the S_{11} phase. The second scheme has a phase correction applied that reduces the error of the model providing a good estimation. Moreover, the efficiency error is improved.

Not all parameters are changed, just some of them are varied considering the influence of each parameter in the simulation when compared with measurements. For example, the saturation current I_S varies the level of the magnitude of the S_{11}, affecting the efficiency. If I_S is reduced the $|S_{11}|$ is increased, lowering the V_{DC} and the efficiency. The opposite occurs if it is increased. The phase of the S_{11} is not affected. The series resistance affects the efficiency very significantly. If the value is lowered (R_S=20 Ω) the efficiency peak gets 40 % for -10 dBm, what is quite far from current measurements. Nevertheless, if the value is higher, the magnitude of the $|S_{11}|$ is increased, leading to a drop in efficiency, and also for the V_{DC}. It affects the phase of the S_{11} at higher frequencies (around 3.2 GHz). If the value is lowered, it favors an abrupt variation of the phase at that point. C_P and L_L produce frequency shifts. If C_P or L_L are increased (0.25 pF and 1.3 nH), the $|S_{11}|$, V_{DC} and efficiency are shifted in frequency downwards. The opposite occurs if they are decreased. In both cases,

the efficiency values are affected. These parameters are varied according to this explanation, to approximate the simulations performance to the measurements for each power level under study. An illustrative variation with arrows is shown in Table 3.4.

	Variation	$\|S_{11}\|$	η_{RF-DC}	V_{DC}
I_S	↓	↑	↓	↓
I_S	↑	↓	↑	↑
R_S	↓	↓	↑	↑
R_S	↑	↑	↓	↓
C_p	↓	→	↕	↕
C_p	↑	←	↕	↕
L_L	↓	→	↕	↕
L_L	↑	←	↕	↕

Table 3.4: Influence in the variation of intrinsic and parasitic parameters for SMS7630 diode model.

For the final model, a phase correction is needed to approximate the RF impedance simulation to the measurement as the previous parameters did not varied significantly its performance. Therefore, a phase correction has been implemented through a phase shifter element, introducing a phase correction of 112 °. This model has been adjusted till get a good accuracy, reducing the errors. The values for the parasitic and experimental Spice parameters for both approaches are shown in Table 3.5 and Table 3.6 .

Name	Intermediate approach	Final approach	Description
L_L	1.15 nH	0.50 nH	Leadframe inductance
C_C	0.25 pF	0.25 pF	Coupling capacitance
L_B	0.08 nH	0.08 nH	Bondwire inductance
C_P	0.12 pF	0.19 pF	Package capacitance

Table 3.5: SMS7630 diode parasitic values for SOT-23 packaging.

Parameter	Datasheet Value	Experimental Value (intermediate model)	Experimental Value (final model)
I_s	5 μA	1 μA	4 μA
R_s	20 Ω	100 Ω	100 Ω
B_V	2 V	2 V	2 V
C_{jo}	0.14 pF	0.14 pF	0.14 pF
I_{BV}	1.0E-4 A	1.0E-4 A	1.0E-4 A
V_J	0.34 V	0.34 V	0.34 V
N	1.05	1.05	1.05

Table 3.6: SMS-7630 Spice parameters: datasheet [1] vs experimental parameters.

As it can be seen, the new model provides a lower error and, therefore, it is a better approximation for low input power levels in the specific frequency range (see Table 3.7, Table 3.8 and Figure 3.2.6). The performance in the range from 0.1-3.6 GHz is quite good taking into account the non-linear dependence of the diode with frequency and input power. In this range, multiple-tone measurements will be performed. The model can be extended upwards in frequency. Impedance measurements were extended in frequency till 6 GHz (see Figure 3.2.7), showing a good agreement below 4 GHz for the S_{11} (both magnitude and phase), but the efficiency was tested up to the maximum frequency point available by the source generator, 3 GHz (N5181A-503 from Keysight).

Apart from this, it is important to remark that the model is not so accurate for high input power levels (higher than -10 dBm). At higher power the performance dramatically changes so for those cases, a new model with some variations in the parameters should be sketched. The intermediate approach of this model was used by a Master's student to test the performance of a rectifier at 2.4 GHz, getting satisfactory results for the $|S_{11}|$ and efficiency, although not for the phase, as already explained [7, 8].

Input power / Error	-10 dBm	-15 dBm	-20 dBm	-25 dBm
Max Error $\lvert S_{11}\rvert$	0.26	0.23	0.23	0.23
Mean Error $\lvert S_{11}\rvert$	0.06	0.07	0.06	0.06
Max Error $\measuredangle S_{11}$ (°)	303.50	331.00	280.60	280.72
Mean Error $\measuredangle S_{11}$ (°)	156.27	156.83	155.63	155.38
Max Error η_{RF-DC} (%)	11.71	8.56	4.85	2.09
Mean Error η_{RF-DC} (%)	4.80	2.66	1.14	0.44

Table 3.7: Maximum and mean absolute error of an intermediate approach of the new design parasitic and intrinsic model: analysis of the magnitude and phase of the S-parameter and the RF-DC power conversion efficiency.

Input power / Error	-10 dBm	-15 dBm	-20 dBm	-25 dBm
Max Error $\lvert S_{11}\rvert$	0.39	0.39	0.40	0.40
Mean Error $\lvert S_{11}\rvert$	0.06	0.07	0.07	0.07
Max Error $\measuredangle S_{11}$ (°)	331.28	323.34	319.30	322.74
Mean Error $\measuredangle S_{11}$ (°)	92.86	93.77	95.42	95.73
Max Error η_{RF-DC} (%)	13.83	7.56	3.37	1.27
Mean Error η_{RF-DC} (%)	2.93	1.47	0.62	0.24

Table 3.8: Maximum and mean absolute error of the final design parasitic and intrinsic model: analysis of the magnitude and phase of the S-parameter and the RF-DC power conversion efficiency.

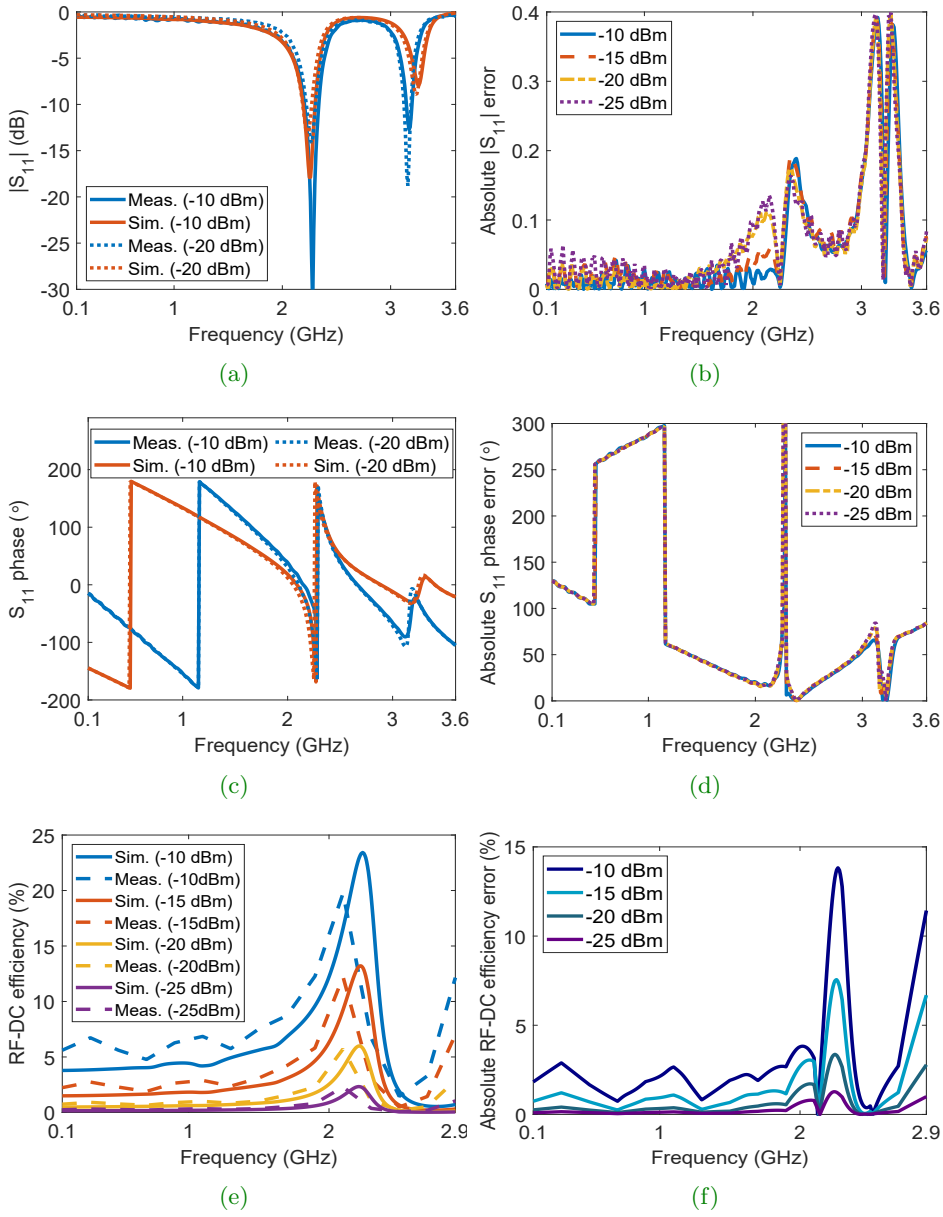

Figure 3.2.6: Circuit under test with the final designed model. a) $|S_{11}|\,(dB)$. b) Absolute $|S_{11}|$ error. c) Phase of S_{11}. d) Absolute phase error of S_{11}. e) $\eta_{RF-DC}(\%)$. f) Absolute efficiency error.

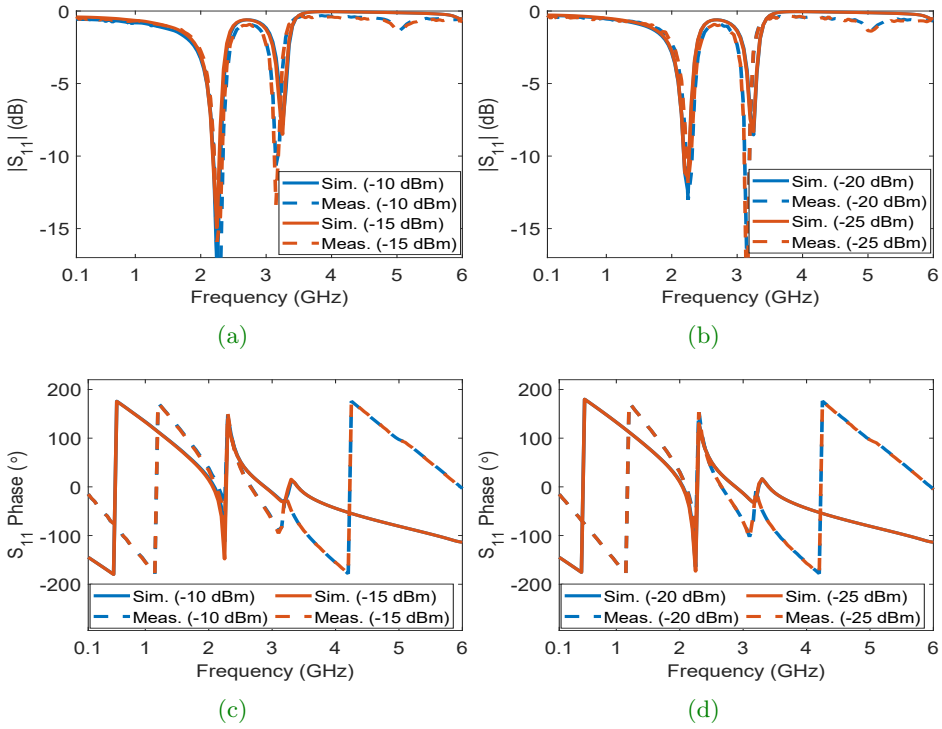

Figure 3.2.7: Comparison of the rectifier circuit under test with the final model. Performance up to 6 GHz. a) $|S_{11}|\,(dB)$ at -10 and -15 dBm and b) at -20 and -25 dBm. c) Phase of the S_{11} at -10 and -15 dBm and d) at -20 and -25 dBm.)

In [9] a similar analysis was performed with a gallium arsenide Schottky barrier diode from Macom (MA4E2038). Its Spice model was modified due to its inaccuracy in the characterization. Besides, some parasitics were included in the model. Nevertheless, the analysis and characterization provided in this chapter for the diode SMS7630 is more complete and accurate, as the model is compared with measurements for the S_{11} (magnitude and phase) and RF-DC power conversion efficiency. To conclude with the model extraction, in Figure 3.2.8, the DC output voltage is compared and the similarity between simulations and measurements is clearly visible.

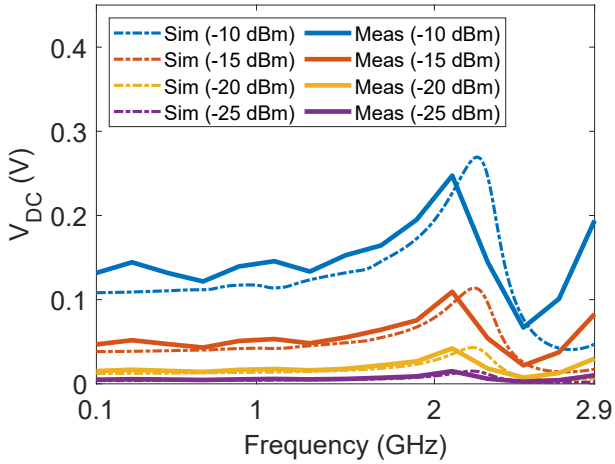

Figure 3.2.8: Diode rectifier circuit under test. DC voltage at different input power levels.

The RF to DC power conversion efficiency can be computed into different ways attending to the RF power concept employed. The most common case is to define $P_{RF} = P_{IN} = P_{Ava}$, this is, taking into account an ideal case where the input power is the available power as in a perfect conjugate match situation as shown in Figure 3.2.9. Previous plots showed this assumption where cable losses were included. This is the desired case where the maximum power transfer concept is defined but in reality, a few power

is reflected. The reflected power depends on the circuit design and this power is reduced as much as possible although it is not zero. Therefore, the other way to compute the efficiency is taking into account the accepted power (P_{Acc}), this means, the power transmitted to the circuit, different from P_{IN}.

$$P_{Acc} = P_{IN} - P_{Refl} = P_{IN}(1 - |S_{11}|^2). \tag{3.2.2}$$

The second case is more realistic to analyze the efficiency conversion of the rectifier, as the reflected power is not included as a loss of the diode itself. It is not something intrinsic to the diode, it is something variable from one rectifier to another so it should not be included and therefore, it shows a more realistic power conversion efficiency. In Figure 3.2.9, a representation of the V_{DC} measurement setup is sketched, where the incident and reflected power waves are displayed with a green a red arrows, and the orange arrow represents the transmitted (or accepted) power wave.

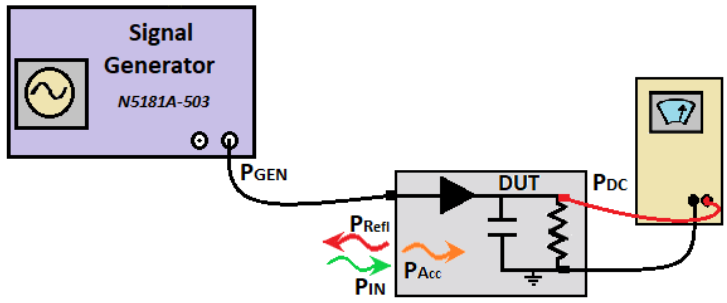

Figure 3.2.9: V_{DC} measurement setup for the rectifier.

In Table 3.9 the mean and maximum absolute efficiency error values are listed when the accepted power is employed and in Figure 3.2.10, the available power (left) and the accepted power (right) are used to compute the power conversion efficiency. At -10 dBm the model is more inaccurate, as explained above, but for lower input powers the approach is good.

Error \ Input power	-10 dBm	-15 dBm	-20 dBm	-25 dBm
Max Error η_{RF-DC} (%)	23.53	12.90	5.52	1.91
Mean Error η_{RF-DC} (%)	6.09	3.76	1.37	0.52

Table 3.9: Mean and maximum absolute error of the efficiency using the accepted power.

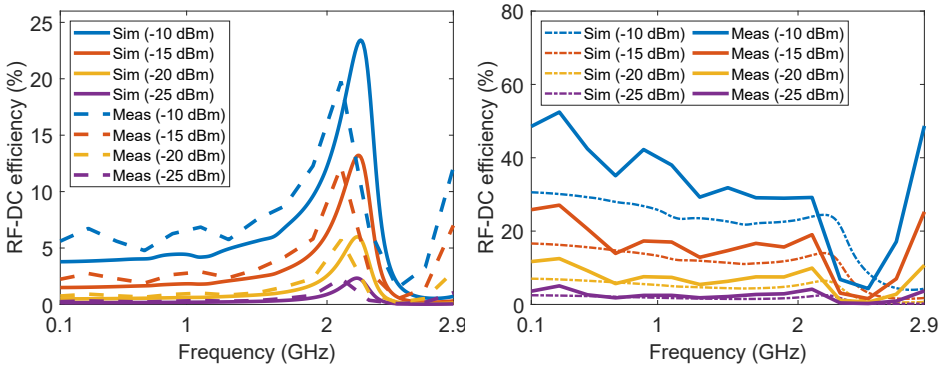

Figure 3.2.10: Diode rectifier circuit under test. Efficiency simulations vs measurements at different input power levels using the a) available power and b) the accepted power.

3.2.4. Validation of the circuit Spice model

The model is going to be validated using two different circuits shown in Figure 3.2.11 (a) and (c). All circuit rectifiers have the same voltage doubler topology, built over the same Duroid 5880 substrate to reduce losses (H=0.787 mm, ϵ_r=2.2 and $\tan\delta$=0.0009) and a fixed load of 3.9 kΩ. A different matching network is chosen, working at slightly different frequencies, to check if the model is properly designed in that frequency range. In (a-b) "circuit 2" or "c2" has a short-circuited stub in the matching network working in a dual band at 1.8 and 2.7 GHz. Nevertheless, in (c-d) "circuit 3" or "c3" has a radial stub working at 2 GHz. .

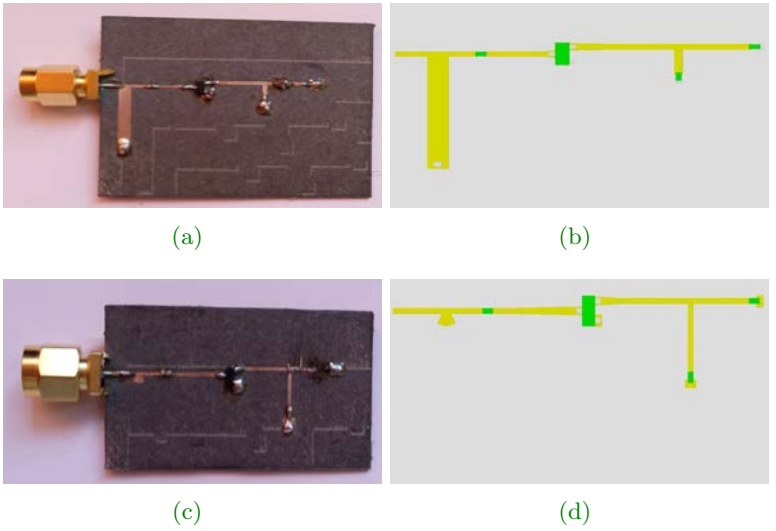

(a) (b)

(c) (d)

Figure 3.2.11: Rectifier circuits for validation of the model. a, b) Prototype and layout for circuit 2. c, d) Prototype and layout for circuit 3.

The maximum and mean values of the absolute error for S_{11} (magnitude and phase) and conversion efficiency of these circuits at different input power levels are summarized in Table 3.10 and Table 3.11. As can be seen, a low error is made for low input power levels (-15 to -25 dBm). At -10 dBm the error is higher although it is assumable. In Figure 3.2.12 and Figure 3.2.13 the magnitude and phase of the input reflection coefficient are shown for different power levels ranging from -25 to -10 dBm, comparing the performance between simulations (with extracted model) and measurements for both circuits.

Input power / Error	-10 dBm	-15 dBm	-20 dBm	-25 dBm
Max Error $\lvert S_{11}\rvert$	0.22	0.21	0.21	0.20
Mean Error $\lvert S_{11}\rvert$	0.06	0.06	0.06	0.06
Max Error $\measuredangle S_{11}$ (°)	331.28	323.34	319.30	322.74
Mean Error $\measuredangle S_{11}$ (°)	41.66	42.89	44.86	44.75
Max Error η_{RF-DC} (%)	6.48	3.92	2.70	1.31
Mean Error η_{RF-DC} (%)	1.67	1.07	0.56	0.23

Table 3.10: Maximum and mean absolute error of the circuit 2.

Input power / Error	-10 dBm	-15 dBm	-20 dBm	-25 dBm
Max Error $\lvert S_{11}\rvert$	0.23	0.22	0.19	0.18
Mean Error $\lvert S_{11}\rvert$	0.04	0.04	0.04	0.04
Max Error $\measuredangle S_{11}$ (°)	331.28	323.34	319.30	322.74
Mean Error $\measuredangle S_{11}$ (°)	41.66	42.89	44.86	44.75
Max Error η_{RF-DC} (%)	3.70	1.85	1.23	0.43
Mean Error η_{RF-DC} (%)	1.32	0.67	0.30	0.10

Table 3.11: Maximum and mean absolute error of the circuit 3.

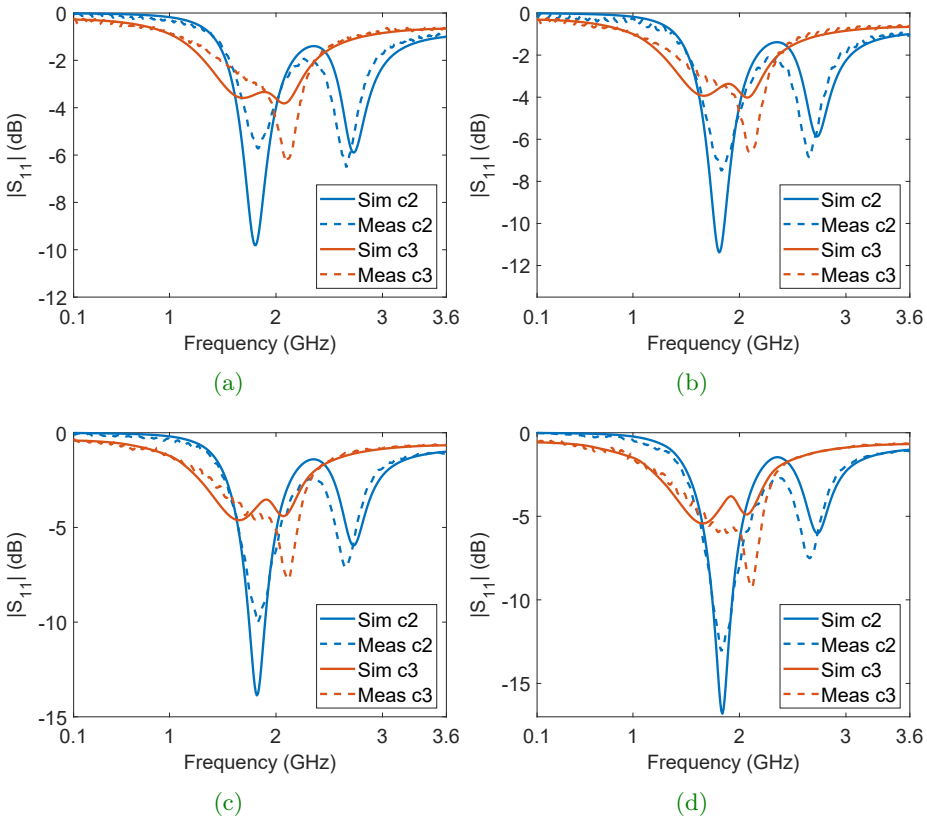

Figure 3.2.12: Magnitude of the input reflection coefficient for circuit 2 (c2) and Circuit 3 (c3). Comparison between the extracted model and measurements for different input power levels. a) -25 dBm. b) -20 dBm. c) -15 dBm. d) -10 dBm.

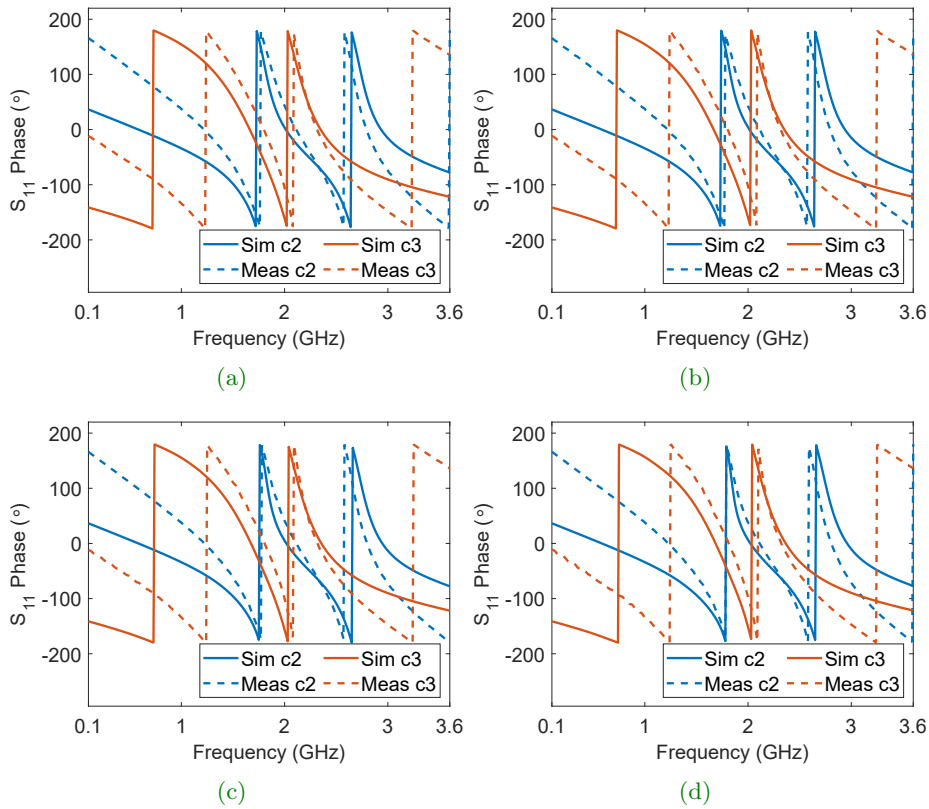

Figure 3.2.13: Phase of the input reflection coefficient for circuit 2 (c2) and Circuit 3 (c3). Comparison between the extracted model and measurements for different input power levels. a) -25 dBm. b) -20 dBm. c) -15 dBm. d) -10 dBm.

In Figure 3.2.14, the DC voltage measured in circuit 2 and circuit 3 is compared with the simulations and as expected, simulations are in agreement with the measurements with a low error.

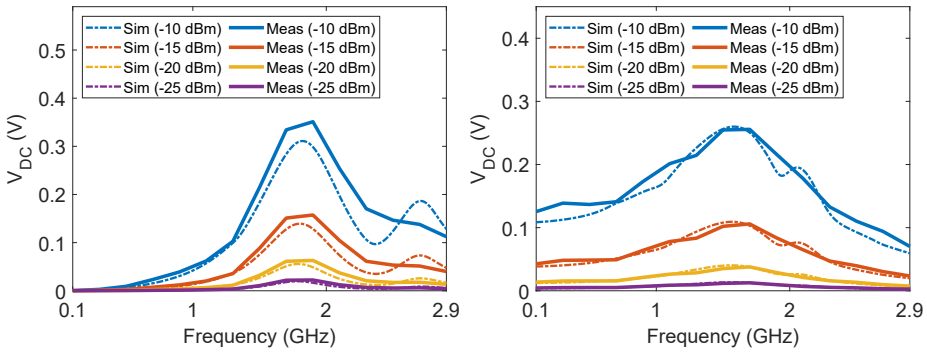

(a) (b)

Figure 3.2.14: Diode rectifier circuit under test. DC voltage simulations vs measurements at different input power levels. a) Circuit c2. b) Circuit c3.

In Figure 3.2.15 the RF to DC power conversion efficiency is shown for the case when the available and the accepted power are used. For Figure 3.2.15 (a,b) the model outperforms for the circuit 3, although for circuit 2 it has some errors in the peak of the efficiency estimation for -10 dBm. For lower powers the prediction is better. In Figure 3.2.15 (c,d) some discrepancies appear in the lower band and at high input power, but as can be seen in Table 3.12 and 3.13, the mean error is low in both circuits.

Input power / Error	-10 dBm	-15 dBm	-20 dBm	-25 dBm
Max Error η_{RF-DC} (%)	12.61	6.49	2.36	0.96
Mean Error η_{RF-DC} (%)	5.04	2.25	0.85	0.31

Table 3.12: Mean and maximum absolute error of the efficiency using the accepted power for circuit 2.

Error \ Input power	-10 dBm	-15 dBm	-20 dBm	-25 dBm
Max Error η_{RF-DC} (%)	13.58	8.96	4.56	1.64
Mean Error η_{RF-DC} (%)	5.69	3.90	2.08	0.72

Table 3.13: Mean and maximum absolute error of the efficiency using the accepted power for circuit 3.

After all these comparisons, it can be concluded that the designed model (parasitic and Spice model) is a good candidate to estimate the performance of the SMS7630 diode rectifier in simulations. The diode model works for input powers ranging from -25 to -10 dBm and frequencies in the range 0.1-3.6 GHz (even 4 GHz), with a low error. Although, the approximation is really good from 0.9 GHz upwards.

It is noticeable that the accepted efficiency in Figure 3.2.15 d) shows high levels, despite the fact the $|S_{11}|$ is bad in some regions (see Figure 3.2.12 for circuit 3, from 0.1 to 1 GHz). This means that although the accepted power is low, the efficiency conversion in that region is high. So, both the $|S_{11}|$ and the accepted efficiency cannot be dissociated when designing. Otherwise, lot of power can be transmitted to the circuit, having a bad conversion efficiency or just a few power can be accepted with good efficiency values. Thus, a compromise should be established.

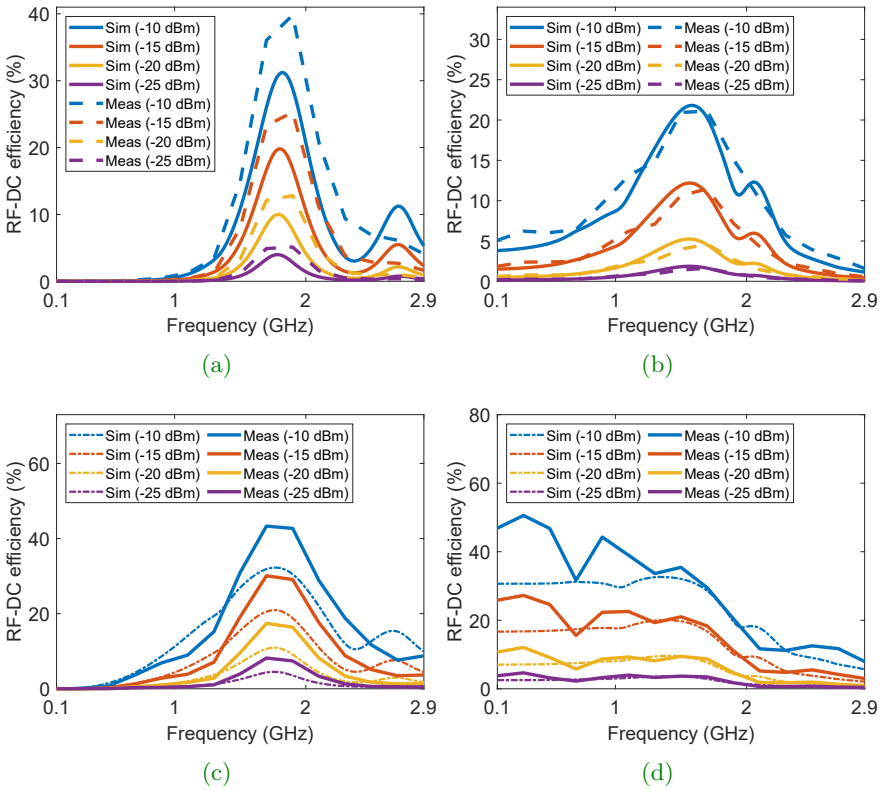

Figure 3.2.15: RF-DC efficiency comparison between the simulated extracted model and measurements for different power levels using the available power for a) Circuit 2 (c2). b) Circuit 2 (c3). And using the accepted power for c) Circuit 2 (c2). d) Circuit 3 (c3).

3.2.5. Verification of the analytical approximation of the diode with the designed Spice model

The theoretical model from (2.4.29) is used again with the new Spice model. In Figure 3.2.16 the diode output DC current is shown, where predicted and simulated results are in agreement from low to high voltage levels. All data are summarized in the Appendix (see Table 7.3 and 7.4).

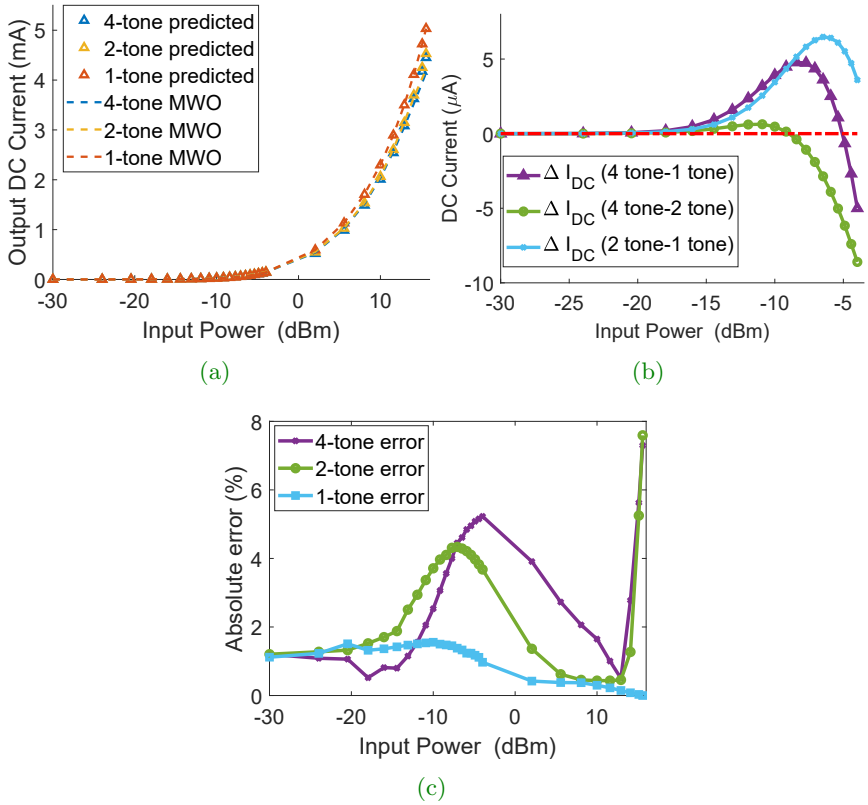

Figure 3.2.16: DC output current versus average input power for a multiple-tone excitation. a) SMS7630 final verification. b) DC current improvement. c) Absolute error between theory and simulations.

3.3. Measurement Setup

Once the circuital model has been validated, it is necessary to design the measurement setup. No multiple-tone sources were available at the laboratory so an alternative setup has been configured in order to establish an accurate process to characterize the rectifier performance under multiple-tone signals. In this case, a four-tone scenario is needed so, four different single-sources are used, in the frequency range from 0.9 to 3.5 GHz, and a broadband 4-to-1 Wilkinson power combiner is designed for summing all different tones at one port. Then, a 20 dB coupler is introduced between the combiner and the rectifier, to quantify the accepted power to the diode circuit, through the connection of a spectrum analyzer. It is necessary to know the amount of accepted power at each tone to compare the setup with the simulations. The complete measurement setup is shown in Figure 3.3.1. The goal is to excite the rectifier with different tones at the same time (from 0.9 to 3.5 GHz), varying the input power and compare it to a single-tone excitation with the same average power, quantifying if there is any RF-DC efficiency improvement. Therefore, the setup specifications will be extended to cover that frequency range. As independent sources are used, no correlation appears between tones. The correlation is not studied in this thesis, although it would be interesting to take that fact into account, measuring the influence of the phase difference between tones (multipath effects should also be included).

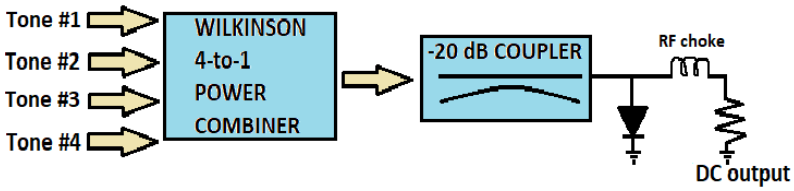

Figure 3.3.1: Measurement setup for validating the theoretical multiple-tone approach presented in the Chapter 2.

3.3.1. Multi-section matching transformers

A broadband Wilkinson and 20 dB coupler are required in this measurement setup for covering the 0.9 to 3.5 GHz frequency range. It is desirable to enhance that frequency range to avoid problems (for example to cover between 0.7 to 3.7 GHz). Some requirements must be fulfilled in that operational bandwidth. The return losses must be greater than 10 dB and the isolation level between some specific ports must be at least 20 dB. The coupling factor for the coupler is set to 20 dB. Both circuits must show reduced dimensions and low losses. Otherwise, the complete setup will be very larger and losses will increase. Assuming that all these requirements must be satisfied and as both circuits are well known, standard designs with a single section are analyzed. The working bandwidth can not be covered, fulfilling the matching and isolation criteria, with the standard designs (single section). For the Wilkinson power combiner, with just one section, nearly $\frac{f_2}{f_1} = 1.44:1$, a Voltage Standing Wave Ratio (VSWR)< 1.2 is assumable.

Multistage transformers have been widely used to overcome these issues, increasing the working bandwidth but enlarging the number of sections. Small discontinuities between sections are created where a partial reflection is produced. From theory, it is well known the possibility of synthesizing whatever reflection coefficient shape, as a function of frequency, by properly choosing the reflection coefficient of each section, Γ_n (see Figure 3.3.2), in a multisection transformer. This technique is known as "the theory of small reflections" (section 5.5 in [10]). The input reflection coefficient of a general multistage transformer, as the one shown in Figure 3.3.2 is defined as:

$$\Gamma(\theta) = \Gamma_0 + \Gamma_1 e^{-j2\theta} + \Gamma_2 e^{-j4\theta} + \Gamma_N e^{-j2N\theta}, \tag{3.3.1}$$

Any smooth variation can be approximate through a Fourier series when enough terms are used. The *binomial* and the *Chebyshev* transformation are the most common bandpass responses. Both options have been widely studied and used in different filter prototype for so long. As a general case, a load Z_L can be matched to Z_0 using these approaches.

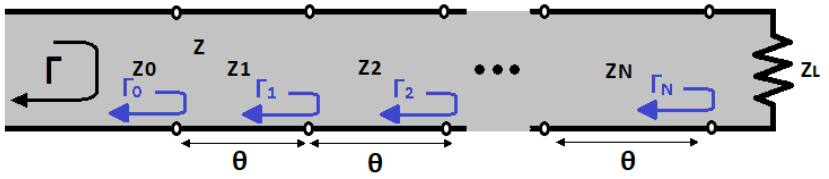

Figure 3.3.2: N-section transformer showing the partial reflection coefficient for each section.

3.3.2. Binomial multi-section transformer

The binomial transformation offers a maximally flat response of the bandpass at f_0 and surroundings (section 5.6 in [10]). It is an optimum solution as it provides the flatness response for an N-section design. This solution sets $|\Gamma(\theta)| = 0$ at f_0 where:

$$\Gamma(\theta)_{Bin} = K(1 + e^{-2j\theta})^N, \tag{3.3.2}$$

and its magnitude can be reduced to:

$$|\Gamma(\theta)|_{Bin} = 2^N |K| |cos\theta|^N. \tag{3.3.3}$$

Also for the N-1 derivatives, $d^n|\Gamma(\theta)|/d\theta^n = 0$, when $\theta = \pi/2$ which corresponds to a transmission line distance of $l = \lambda/4$ at f_0. K is a constant and can be determined at $f = 0$ ($\theta = \beta l = 0$), where all commensurate transmission lines are of zero length and, therefore, Γ is determined just by the relation between the load Z_L and the characteristic impedance (Z_0).

$$\Gamma(0)_{Bin} = 2^N K = \frac{Z_L - Z_0}{Z_L + Z_0}. \tag{3.3.4}$$

Then, the binomial term in (3.3.2) is expanded as previously used in Chapter 2 in (2.3.21) as:

$$(V + 1)^N = \sum_{n=0}^{N} \binom{N}{n} V^n. \tag{3.3.5}$$

$\Gamma(\theta)$ can be reformulated merging (3.3.2) and (3.3.5) and being equated to the small reflection theory of broadband transformers (3.3.1), which leads to (3.3.6).

$$\Gamma(\theta) = K \sum_{n=0}^{N} \binom{N}{n} e^{-2j\theta n} = \Gamma_0 + \Gamma_1 e^{-2j\theta} + \Gamma_2 e^{-4j\theta} + \Gamma_N e^{-2Nj\theta}. \quad (3.3.6)$$

The exponential term in (3.3.6) represents the displacement (or phase delay) of the incoming wave that excites the circuit, and its movement back and forth through all the transmission lines of θ length. In this way, it is possible to obtain the reflection coefficient for each section as $\Gamma_n = K \sum_{n=0}^{N} \binom{N}{n}$.

Last, the characteristic impedance of each section (Z_n) can be computed as:

$$\Gamma_n = \frac{Z_{n+1} - Z_n}{Z_{n+1} + Z_n}, \quad (3.3.7)$$

although there exits some tables where it is possible to find that information attending to the number of sections and the ratio of Z_L/Z_0.

In Section 3.3.5, the binomial transformation is used for implementing a coupler although in this case the coupling factor is used to be maximally flat, not the reflection coefficient (or bandpass).

3.3.3. Chebyshev multi-section transformer

For the Chebyshev or equal ripple response, the main difference lies in the shape of the bandpass. The Chebyshev transformer optimizes the bandwidth at the expense of increasing the bandpass ripple (section 5.7 in [10]). For a given number of sections (N), the bandwidth optimization in this design outperforms the binomial multistage transformer performance with the ripple cost. If some ripple is possible, this alternative can be more efficient reducing the number of sections, as the circuit size is reduced.

The Chebyshev transformer is designed by equating $|\Gamma(\theta)|$ to a Chebyshev polynomial, which has the following form, where n means the polynomial order:

$$T_n(x) = 2xT_{n-1}(x) - T_{n-2}(x), \tag{3.3.8}$$

where $T_1(x) = x$ and $T_2(x) = 2x^2 - 1$.

The main properties of $T_n(x)$ polynomials are summarized as follows:

1. In the $-1 \leqslant x \leqslant 1$ range, the polynomial oscillates between ± 1 as $|T_n(x)| \leqslant 1$. This is the equal ripple property as this region is mapped to the bandpass.

2. The outer region ($|x| > 1$) is mapped with the stopband an the slope of the polynomial increases faster as long as the order is increased.

A Chebyshev polynomial representation with different orders is shown in Figure 3.3.3 (a), where the equal ripple region is delimited between dashed lines. In the $|x| < 1$ region, the polynomial performance can be approximate to $T_n(\cos\theta) = \cos n\theta$ where $x = \cos\theta$, as shown in Figure 3.3.3 (b).

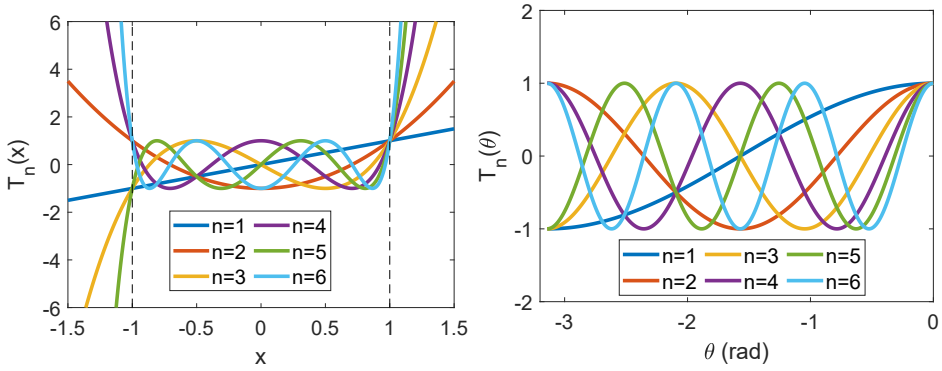

(a) (b)

Figure 3.3.3: a) Chebyshev polynomial representation, $T_n(x)$. b) Approximation to Chebyshev polynomials in $-1 < x < 1$ region when $x = \cos\theta$.

Generally, this expression can be reformulated for covering also the outbounded region where $|x| > 1$ as:

$$\begin{cases} T_n(x) = \cos\left(n \cos^{-1} x\right) & |x| \leqslant 1, \\ T_n(x) = \cosh\left(n \cosh^{-1} x\right) & |x| > 1. \end{cases} \tag{3.3.9}$$

The bandpass operation must be mapped inside the $-1 \leqslant x \leqslant 1$ region, where $x = 1$ transforms in θ_1 and $x = -1$ in $\theta_{-1} = \pi - \theta_1$, being these points the limit of the bandpass. If $x = \cos\theta$ is normalized to $x = \cos\theta / cos\theta_1$, then the polynomials can be defined as:

$$T_1(\sec\theta_1 \cos\theta) = \sec\theta_1 \cos\theta, \tag{3.3.10}$$

$$T_2(\sec\theta_1 \cos\theta) = \sec^2\theta_1(1 + \cos 2\theta) - 1, \tag{3.3.11}$$

$$T_3(\sec\theta_1 \cos\theta) = \sec^3\theta_1(\cos 3\theta + 3\cos\theta) - 3\sec\theta_1 \cos\theta. \tag{3.3.12}$$

The $\Gamma(\theta)$ for a Chebychev transformation must be equated to the corresponding polynomial order. In a general way, (3.3.13) must be equalize to (3.3.1) (see Figure 3.3.2).

$$\Gamma(\theta)_{Cheby} = Ke^{-jN\theta} T_N(\sec\theta_1 \cos\theta). \tag{3.3.13}$$

The K constant represents the maximum value for the reflection coefficient in the passband, and as the maximum value of the Chebyshev polynomial in the bandpass is 1 in (3.3.13), therefore $\Gamma_{max} = |K|$. Γ_{max} limits the maximum allowable ripple (a_{rip}) as $|a_{rip}|^2 + |\Gamma_{max}|^2 = 1$. For $f = 0$, and as $\Gamma(\theta)$ is equated to $\Gamma(\theta)_{Cheby}$, it leads to:

$$T_N(\sec\theta_1) = \frac{1}{\Gamma_{max}} \left(\left| \frac{Z_L - Z_0}{Z_L + Z_0} \right| \right), \tag{3.3.14}$$

where $\sec\theta_1$ is:

$$\sec\theta_1 = cosh\left[\frac{1}{N} cosh^{-1} \left(\frac{1}{\Gamma_{max}} \left| \frac{Z_L - Z_0}{Z_L + Z_0} \right| \right) \right]. \tag{3.3.15}$$

In this way it is possible to compute the reflection coefficient and, therefore, the characteristic impedance for N-sections. There exists some normalized

tables where these values can be obtained. Nevertheless this is just useful for some Z_L/Z_0 ratios, a few ripple scenarios and some specific number of sections. Otherwise, the solution must be manually extracted through the formulas presented here.

3.3.4. Broadband 4-to-1 Wilkinson power combiner

For combining different sources into one port, a Wilkinson power combiner has been chosen as a possible alternative. This microwave circuit was an evolution of previous T-junctions and resistive dividers. It was developed in 1960s by E.J. Wilkinson [12]. Lossless T-junctions could not matched at all ports, an the isolation was not possible between the ports. The resistive divider could be matched at all ports but still no isolation was achieved despite not being lossless. Nevertheless, the Wilkinson was designed with the property of appearing lossless when the output ports are matched, being reciprocal, and with isolation between the outputs [13]. This is possible as only the reflected power from the output ports is dissipated.
A common single section Wilkinson power combiner provides a fractional bandwidth of $\frac{f_2}{f_1} = 1.44 : 1$, a Voltage Standing Wave Ratio (VSWR)$<$ 1.22 and an isolation level larger than 20 dB. This single section design is not enough to fulfill the setup specifications. As happens with broadband matching transformers, the number of sections increases the operational bandwidth. Therefore, different strategies have been studied, including the binomial and Chebyshev approaches. In [14] some multistage designs have been tested using the binomial approach. Also, in [15, 16] broadband multisection Wilkinson were analyzed using the Chebyshev polynomials to equate the reflection coefficient, including unequal split power ratios [17].

In this design, the Chebyshev technique is chosen to reduce the circuit size, as it optimizes the bandwidth to the number of sections. As a trade-off some ripple is tolerated. In this specific case, a three-cascade double section Wilkinson is designed as an alternative to cover the frequency range from 0.9-3.5 GHz, with four input ports and one output, fulfilling specifications, as two sections provide a good performance.

In order to design a Wilkinson employing a two-section chebyshev trans-

former, the reflection coefficient from a general step transformer (3.3.16) (see Figure 3.3.2) is equated to a second order chebyshev polinomial. $\Gamma(\theta)$ in (3.3.1) can be rewritten as a sum of cosines, assuming that the circuit is going to be symmetric for an even number of sections ($N = 2$).

$$\Gamma(\theta) = 2e^{-j2N\theta}\left[\Gamma_0 \cos N\theta + \Gamma_1 \cos(N-2)\theta + \Gamma_n \cos(N-2n)\theta + \frac{1}{2}\Gamma_{N/2}\right]. \tag{3.3.16}$$

Then, equating (3.3.16) to (3.3.13) for $N = 2$, it produces:

$$\begin{aligned}\Gamma(\theta) &= 2e^{-j2\theta}(\Gamma_0 \cos 2\theta + \frac{\Gamma_1}{2}) = Ke^{-j2\theta}T_2(\sec\theta_1 \cos\theta) = \\ &Ke^{-j2\theta}\left(\sec^2\theta_1\,(1+\cos 2\theta) - 1\right).\end{aligned} \tag{3.3.17}$$

Leading to:

$$\Gamma_0 = K\frac{\sec^2\theta_1}{2}, \tag{3.3.18}$$

$$\Gamma_1 = K(\sec^2\theta_1 - 1), \tag{3.3.19}$$

where Γ_0 and Γ_1 represent the reflection coefficients for the two sections. This design has 0.06 dB of ripple in the passband therefore, the maximum reflection coefficient ($|\Gamma_{max}|$) is limited to -18.6 dB. From [15], it is possible to determine the isolation resistors, where θ_1 and θ_{-1} represent the band-pass edges and, θ_2 and θ_3 the ripple zero points for $N = 2$, where $\sec\theta_1$ can be approximate to:

$$\sec\theta_1 = cosh\left[\frac{1}{2}cosh^{-1}\left(\frac{1}{\Gamma_{max}}\left|\frac{Z_L - Z_0}{Z_L + Z_0}\right|\right)\right], \tag{3.3.20}$$

and θ_2 (by symmetry θ_3):

$$\theta_2 = 90^\circ - \frac{1}{\sqrt{2}}(90^\circ - \theta_1). \tag{3.3.21}$$

Thus, the the isolation resistors (R_1 and R_2) are:

$$R_2 = \frac{2Z_1Z_2}{\sqrt{(Z_1+Z_2)(Z_2-Z_1\cot^2\theta_3)}}, \tag{3.3.22}$$

$$R_1 = \frac{2R_2(Z_1+Z_2)}{R_2(Z_1+Z_2)-2Z_2}, \tag{3.3.23}$$

where from (3.3.20) $\theta_1 = 44.7^\circ$ as $Z_L = 100\,\Omega$ and $Z_0 = 50\,\Omega$. A representation of the magnitude of $\Gamma(x)$ is shown in Figure 3.3.4, where for clarity θ_1 and θ_{-1} are equated to the $x = \pm 1$ (passband limit).

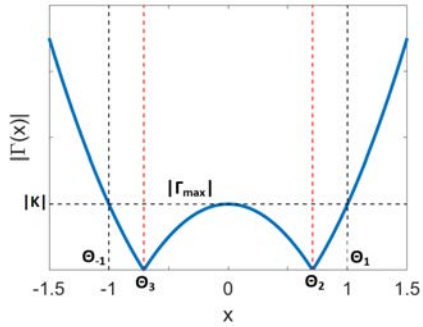

Figure 3.3.4: Magnitude of $\Gamma(x)$ for $N = 2$.

In Table 3.14, the theoretical values of the characteristic impedance for both sections, and the shunt resistances are shown. Prime values denote the real parameter value after optimization.

Section number	$Z_n(\Omega)$	R_n (Ω)	$Z'_n(\Omega)$	R'_n (Ω)
1	63	197	63	180
2	79	113	79	130

Table 3.14: Two-section Wilkinson power combiner. Shunt resistance and characteristic impedance for each section.

Arlon 600 has been chosen as substrate due to its good compromise between low losses and small circuit dimensions (high permittivity and thin substrate). Its main parameters are: $\epsilon_r = 6.15$, $\tan\delta = 0.0035$ and H=0.6 mm.

For getting the characteristic impedances in Table 3.14, the following dimensions were used: L_{Z_1}=18.42 mm, W_{Z_1}=0.53 mm, L_{Z_2}=18.86 mm and W_{Z_2}=0.29 mm. The performance and the layout of the two-section Wilkinson combiner is shown in Figure 3.3.5.

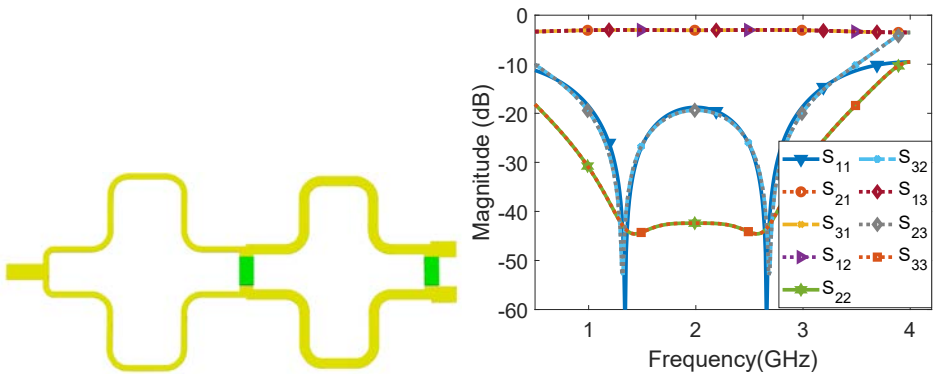

(a) (b)

Figure 3.3.5: Two-section Wilkinson power combiner. a) Layout with two sections. b) Simulation performance in MWO.

The final prototype and the layout are shown in Figure 3.3.6, where three Wilkinsons are connected in cascade to generate a 4-to-1 Wilkinson, as four input ports are required. Its performance has been tested first in AWR and then using a full wave simulator (CST), getting similar results. But for brevity reasons just CST simulations are compared with the measurements (see Figure 3.3.7). An algorithm provided by [18] was used to compare the results for the characteristic impedance and the shunt resistance for each section. The values provided by the theoretical study were similar although the algorithm was not the same.

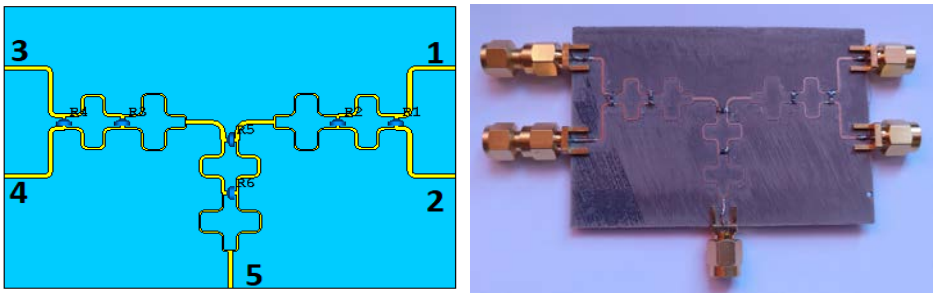

(a) (b)

Figure 3.3.6: Wideband 4-to-1 Wilkinson power combiner. a) Layout. b) Prototype.

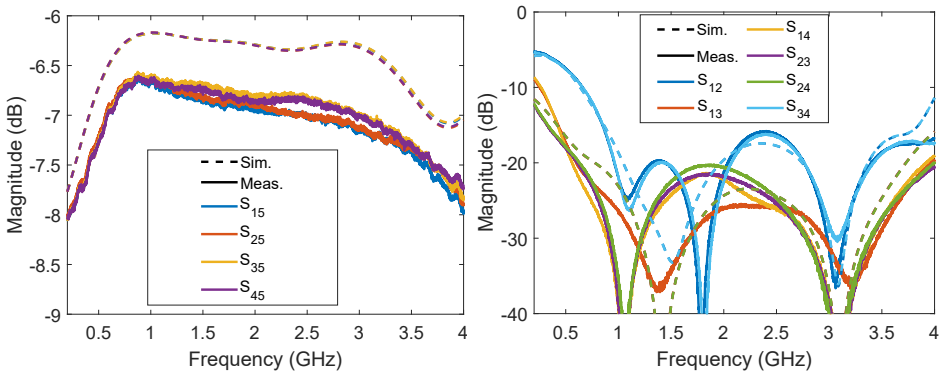

(a) (b)

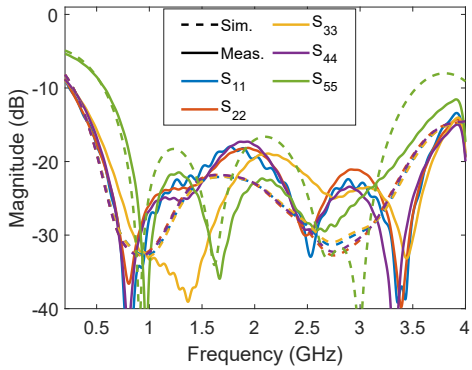

(c)

Figure 3.3.7: 4-to-1 Wilkinson power combiner. Full-wave CST simulation vs measurement. a) Through ports. b) Isolation. c) Matching.

3.3.5. Broadband 20 dB coupled line coupler

We can benefit from the electromagnetic interaction of two close and unshielded transmission lines to develop power couplers [10], [19], [20]. For a stripline design, a Transverse Electromagnetic Mode (TEM) propagation can be assumed. This implies that electrical characteristic of the coupled lines can be defined through the velocity of propagation in the line and the effective capacitance between the lines. An arbitrary excitation can be modeled as a superposition of amplitudes of an even and odd mode excitation. In the even mode, two currents with the same amplitude and direction are applied through the strips conductors. For the odd mode, the direction is the opposite. In this way, whatever excitation can be decomposed into them. Here, both strip lines are identical and symmetric with the same propagation constant ($\beta = \omega/v_p$) and phase velocity ($v_p = c/\sqrt{\epsilon_r}$) in both modes. The following equations are extracted from [10].

$$Z_{0e} = \frac{1}{v_p c_e}, \tag{3.3.24}$$

$$Z_{0o} = \frac{1}{v_p c_o}. \tag{3.3.25}$$

The characteristic impedance for even and odd mode are shown in (3.3.24) and (3.3.25) , being c_e and c_o the effective capacitance for the even and odd mode. If we apply the even-odd mode analysis to a specific length of coupled line (θ), we get the even and odd input impedance for a single-section coupled lines coupler (3.3.26) and (3.3.27).

$$Z_{\text{in}}^{e} = Z_{0e}\frac{\sqrt{Z_{0o}} + j\sqrt{Z_{0e}}\tan\theta}{\sqrt{Z_{0e}} + j\sqrt{Z_{0o}}\tan\theta}, \tag{3.3.26}$$

$$Z_{\text{in}}^{o} = Z_{0o}\frac{\sqrt{Z_{0e}} + j\sqrt{Z_{0o}}\tan\theta}{\sqrt{Z_{0o}} + j\sqrt{Z_{0e}}\tan\theta}. \tag{3.3.27}$$

If $Z_0 = \sqrt{Z_{0e} \cdot Z_{0o}}$, then by symmetry all ports are matched. In this case, a binomial multi-section transformer is employed to enlarge the bandwidth, as a one-section coupler is bandwidth limited. The flatness response for the coupled port is preferred for designing a broadband 20 dB coupled line coupler. To do that, the theory presented in the Subsection 3.3.2 is applicable, but making maximally flat the coupling coefficient (C), which is defined as (3.3.29), instead of the reflection coefficient.

$$\frac{V_2}{V_1} \approx jC\sin\theta \cdot e^{-j\theta} \qquad \text{for} \qquad \theta = \pi/2, \tag{3.3.28}$$

being V_1 and V_2 the voltages on the line at port 1 and 2, when port 1 is excited and port 2 is coupled. It can be rewritten as:

$$C = \frac{V_2}{V_1} = \frac{Z_{0e} - Z_{0o}}{Z_{0e} + Z_{0o}}, \tag{3.3.29}$$

where the even and odd characteristic impedances can be reformulated with respect to C as:

$$Z_{0e} = Z_0\sqrt{\frac{1+C}{1-C}},$$
$$Z_{0o} = Z_0\sqrt{\frac{1-C}{1+C}}. \tag{3.3.30}$$

A single section coupled line coupler is bandwidth constrained due to the $\lambda/4$ lines, so an specific coupling level cannot be fulfilled all over the desired bandwidth [21]. In this case, multiple sections are used, as it happens with broadband matching transformers [22] with the theory of the small reflections (3.3.1). A symmetric design with respect to the center, with an odd number of sections (N), is going to be assume due to the better phase characteristics. Taking into account the coupling coefficient of each section,

$$\begin{aligned} V_2 = {} & (jC_1 \sin\theta e^{-j\theta})V_1 + (jC_2 \sin\theta e^{-j\theta})V_1 e^{-2j\theta} + ... \\ & + (jC_N \sin\theta e^{-j\theta})V_1 e^{-2j(N-1)\theta} \end{aligned} \tag{3.3.31}$$

where C_n corresponds to the coupling of each section. As a symmetric odd design in employed, $M = (N+1)/2$ different sections are included.

For a maximally flat response it is necessary to solve:

$$\frac{\mathrm{d}}{\mathrm{d}\theta^n} C(\theta)\bigg|_{\theta=\pi/2} = 0, \qquad \text{for} \qquad n = 0, 1, ..., N-1. \tag{3.3.32}$$

while C is the coupling factor of the completed design. In a microstrip design, coupled lines have a different phase velocity at each mode due to the different field configurations in the air-dielectric interface. For the even mode, a lower fringing field appears so the phase velocity is lower. This fact degrades the coupling factor. Some techniques can be applied to solve this issue such as dielectric overlays and anisotropic substrates, to have equal phase velocities. In this case, the microstrip coupler is an option for weak coupling. Larger coupling factor can imply a non-feasible set of even-odd characteristic impedance. For this design, different number of odd sections (N) are studied (Figure 3.3.8) and Arlon 600 is chosen as a substrate.

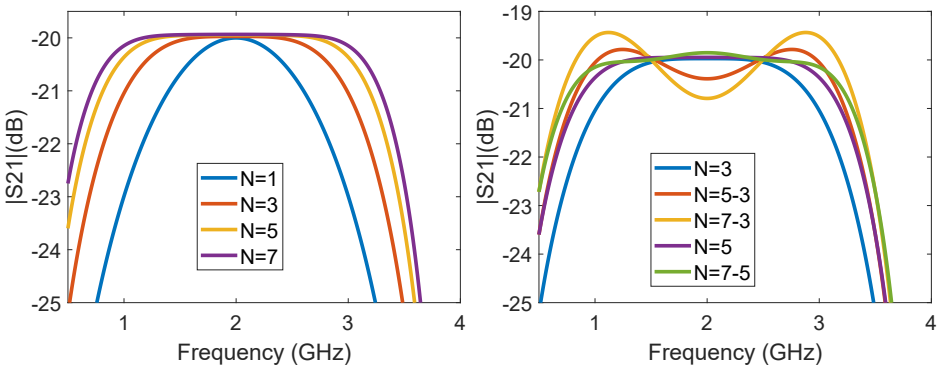

Figure 3.3.8: Coupled coefficient for multistage 20 dB coupler with different number of sections. a) Odd number of sections. b) Reducing the number of sections removing uncoupled lines.

C_n coefficients are extracted when N is varied from 1 to 7. For a maximally flat response (3.3.32) is solved, where C is the 20 dB coupling factor of the complete coupled line coupler, and C_n represents the coupling level for each M different section. As long as the number of sections is increased, the bandwidth is bigger for the ideal case (see Figure 3.3.8 (a)), but the circuit length is a problem. The pair of even/odd characteristic impedance for each M different section (3.3.30) is summarized in Table 3.15. The pair of characteristic impedances is closer to 50 Ω for the outer sections as long as N increases, which means that the coupled lines at the edges are more separated, so less coupled. Indeed, when designing the microstrip layout, some pairs may not couple so can be removed, decreasing the circuit size. For example, in Figure 3.3.8 (b) this fact can be observed in the nomenclature "7-5", as it means $N = 7$ where the four different sections can be reduced to three, as the outer sections are not coupled, so its effect can be considered negligible from the coupled lines point of view. This effect is tested, reducing the number of sections, where some ripple appear.

N	$Z_{0e}/Z_{0o}(\Omega)$ 1st section	$Z_{0e}/Z_{0o}(\Omega)$ 2nd section	$Z_{0e}/Z_{0o}(\Omega)$ 3rd section	$Z_{0e}/Z_{0o}(\Omega)$ 4th section
1	55.28/45.23	-	-	-
3	50.62 / 49.37	56.69/ 44.09	-	
5	50.12 / 49.87	51.13 / 48.88	57.56 / 43.42	-
7	50.02 / 49.97	50.26 / 49.73	51.48 / 48.56	58.08 / 43.03

Table 3.15: Multi-section 20 dB coupler: even-odd characteristic impedance for each section.

In Table 3.16, a multi-section comparison is established, analyzing the coupled level (S_{21} in Figure 3.3.9) and the ripple for each case. The ripple appears when an uncoupled section is removed. Some ripple can be tolerated as the bandwidth remains the same while the circuit size is reduced, being beneficial for the design. The five-section coupler, reduced to three-sections "5-3", is the chosen option because of the important size reduction, low ripple at f_o and good bandwidth. The seventh-section option is feasible but provides a larger size and therefore more losses appear.

From $N = 1$ to 7 (odd values), the system equation for solving (3.3.32) is shown, for this especific coupling level ($C = 0.1$). C_n represents the coupling level for each M different section.

- For $N = 1$, with (3.3.30), $C = 0.1$.

- For $N = 3$:

$$\begin{aligned} C_1 &= \frac{C}{8}, \\ C_2 &= 10C_1. \end{aligned} \tag{3.3.33}$$

- For $N = 5$:

$$\begin{aligned} C &= 2C_1 - 2C_2 + C_3 = 0.1, \\ &- 34C_1 + 10C_2 - C_3 = 0, \\ 682C_1 &- 82C_2 + C_3 = 0. \end{aligned} \tag{3.3.34}$$

- For $N = 7$:

$$\begin{aligned} &- 2C_1 + 2C_2 - 2C_3 + C_4 = 0.1, \\ 74C_1 &- 34C_2 + 10C_3 - C_4 = 0, \\ &- 3026C_1 + 706C_2 - 82C_3 + C_4 = 0, \\ 133274C_1 &- 16354C_2 + 730C_3 - C_4 = 0. \end{aligned} \tag{3.3.35}$$

N	$\lvert S21\rvert$(dB) at 0.9 GHz	$\lvert S21\rvert$(dB) at 3.5 GHz	Ripple (dB) at 2 GHz
1	23.7	28.3	-
3	21.5	25.2	-
5-3	20.4	23.6	0.39
7-3	19.7	22.7	0.79
5	20.6	23.6	-
7-5	20.3	22.7	0.15
7	20.3	22.7	-

Figure 3.16: Multi-section 20 dB coupler comparison.

In Figure 3.3.9 the final layout in CST and the prototype circuit are shown. Some curved transmission lines have been added between sections as transitions to adjust the coupled lines between different sections.

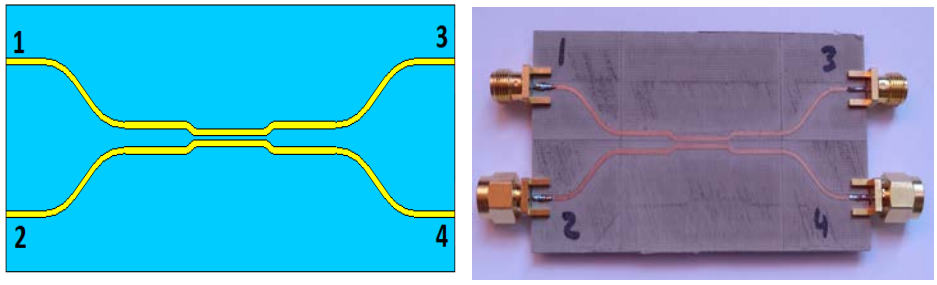

(a) (b)

Figure 3.3.9: Broadband 20 dB RF coupler. a) Layout. b) Prototype.

The size of the SMA connectors has been taken into account, as the input ports must be far enough to avoid connection problems. The prototype performance has been tested first in AWR and then using a full wave simulation in CST, getting similar results. But for brevity just CST simulations are compared to the measurements (see Figure 3.3.10). A good agreement between simulations and measurements is shown, fulfilling the required specifications.

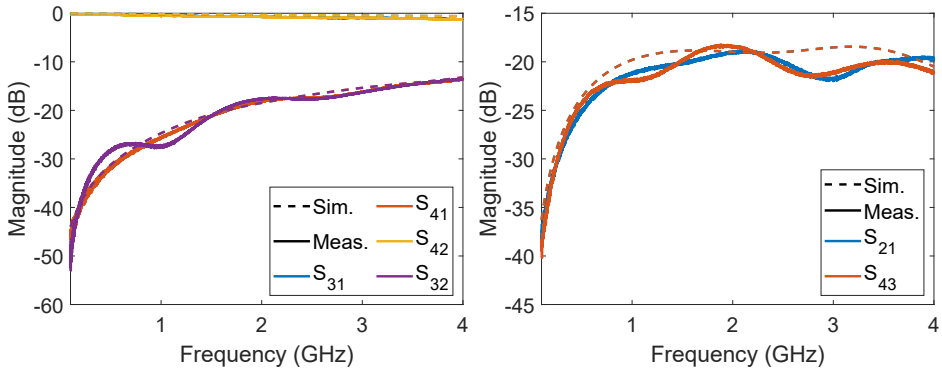

(a) (b)

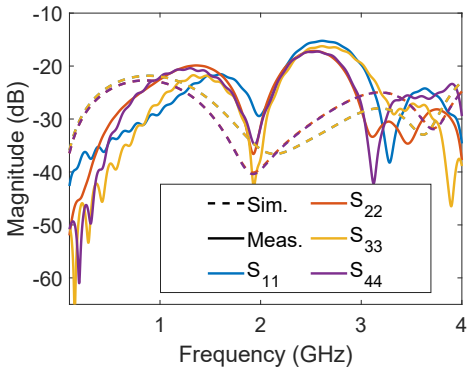

(c)

Figure 3.3.10: Broadband coupled lines coupler S-parameters. Full-wave CST simulation vs measurement. a) Isolation (S_{41} and S_{32}) and direct transmission between input and through ports (S_{31} and S_{42}) . b) Coupling. c) Matching.

3.4. Rectifier performance in a multiple-tone scenario

The circuital model of the diode was extracted and validated in the previous subsection. Moreover, the setup measurement has been designed and established. Now, it is possible to analyze the diode performance under a multiple-tone excitation using the rectifier circuits shown along this chapter (see Figure 3.2.2 and Figure 3.2.11). Thus, multiple-tone simulations and measurements are summarized, to analyzed the RF-DC power conversion efficiency improvement. The layout of the complete design, including the 4-to-1 Wilkinson power combiner, the 20 dB coupled lines coupler and the rectifier, is shown in Figure 3.4.1.

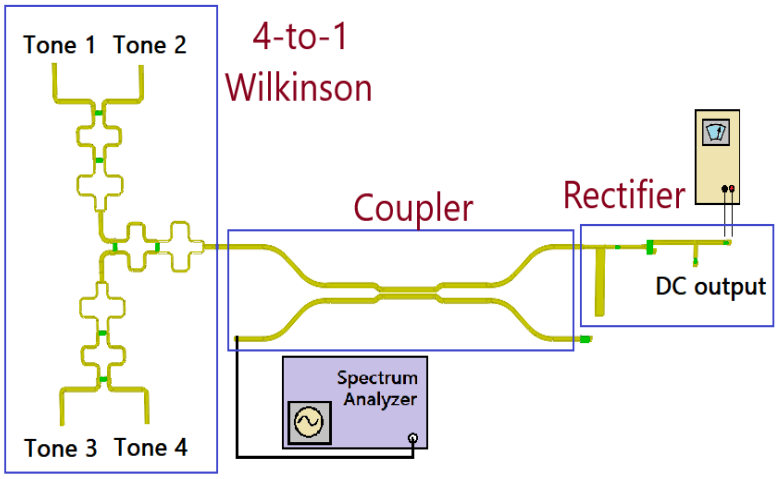

Figure 3.4.1: Complete layout of the measurement setup.

3.4.1. Multiple-tone simulations in a rectifier

Simulations using up to 4 tones have been performed, varying the frequency spacing from 0.9 to 3.25 GHz. The input power has been varied from -21 to 20 dBm (each tone) in the four-tone scenario, +3 dB for the two-tone case, and +6 dB more when just one tone is used, for a comparison to the CW case with the same average power. The goal is to compare the rectified DC power for an N-tone with a CW signal. The RF-DC power efficiency improvement has been computed and a comparison has been established using plots, to quantify the efficiency improvement of the multiple-tone technique.

For the characterization of the multiple-tone process is necessary to use different circuits in order to work in different frequency bands (different matching networks). Then, a fully characterization of the diode along frequency and input power can be done. In this case, the three rectifiers shown in this chapter have been used. Each circuit has been excited with different sets of tones. All simulations and measurements data are shown

in the appendix (Section 7.2). From Figure 3.4.2 to Figure 3.4.6, the simulated DC power vs average input power (to the rectifier) and the RF-DC power conversion efficiency improvement are plotted at different frequencies, comparing the CW signal with different multiple-tone cases in AWR. The multiple-tone improvement is noticeable as published in [5]- [9]. But, as stated in Chapter 2, it is just valid under a low power excitation where as long as the number of tones increases, the efficiency improvement is larger. This has been tested with one, two and four tones. Nevertheless, the slope begins decay quicker for large N when the input power is increased.

In Figure 3.4.2, the rectified DC power (and efficiency improvement) for a CW and for a four-tone excitation, with the same average power and at different frequencies, are shown for circuit 1. Three different subsets of four tones have been tested for the four-tone scenario: (0.9+1.85+2.1+2.45) GHz, (1.85+2.1+2.25+3.25) GHz and (2.15+2.2+2.25+2.3) GHz. The efficiency improvement is done comparing each 4-tone substet with its corresponding CW signal. In Figure 3.4.2 (b), markers with different shapes are used to show the values of each subsets.

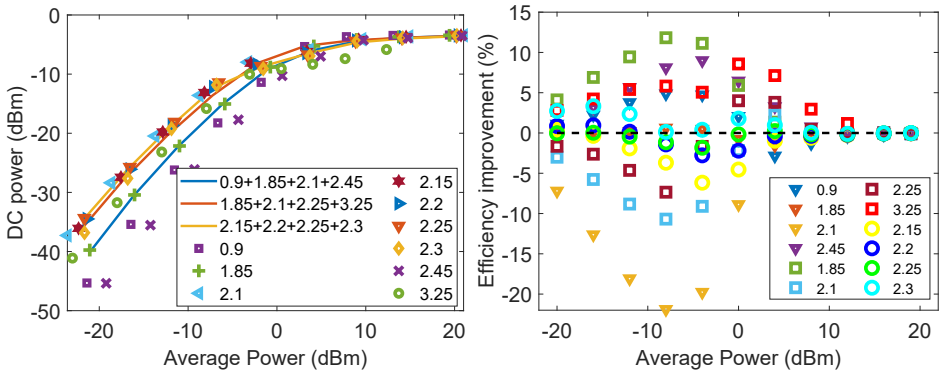

(a) (b)

Figure 3.4.2: Simulated DC power for a CW and four tones at different frequencies for circuit 1. a) DC power and b) efficiency improvement.

In Figure 3.4.3 the two-tone case is compared to a CW excitation, where three different subsets of two tone are used: (1.85+2.1) GHz, (2.25+3.25) GHz, and (2.15+2.3) GHz. Then, each single tone, with the same average power of the N-tone excitation, is compared to its corresponding subset of frequencies (e.g., 0.9 GHz is tested in the first subset of four tones, while 2.25 GHz appears in the second and third subsets).

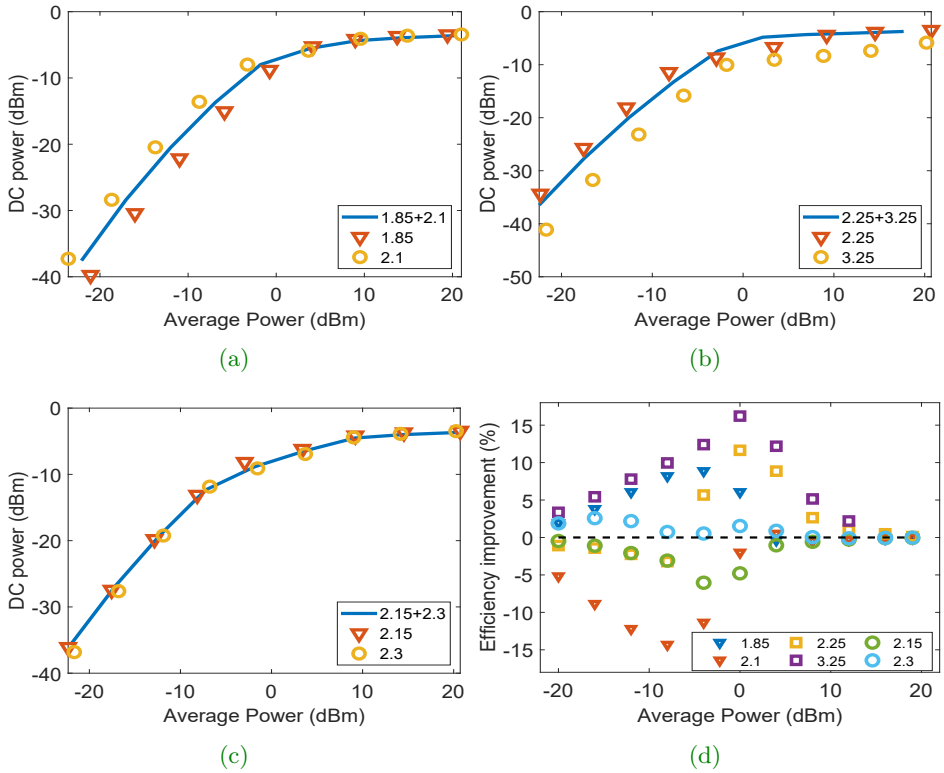

Figure 3.4.3: Simulated rectified DC power for a CW and for a two-tone excitation at different frequencies for circuit 1. DC power at a) 1.85+2.1 GHz, b) 2.25+3.25 GHz and c) 2.15+2.3 GHz. d) Efficiency improvement.

For circuit 2 (see Figure 3.4.4 and Figure 3.4.5) the following frequency subsets are used: (0.9+1.85+2.1+2.45) GHz, (1.7+1.9+2.+2.1) GHz, (1.7+1.75 +1.8+1.85) GHz, (0.9+2.45) GHz, (1.7+2) GHz and (1.75+1.85) GHz .

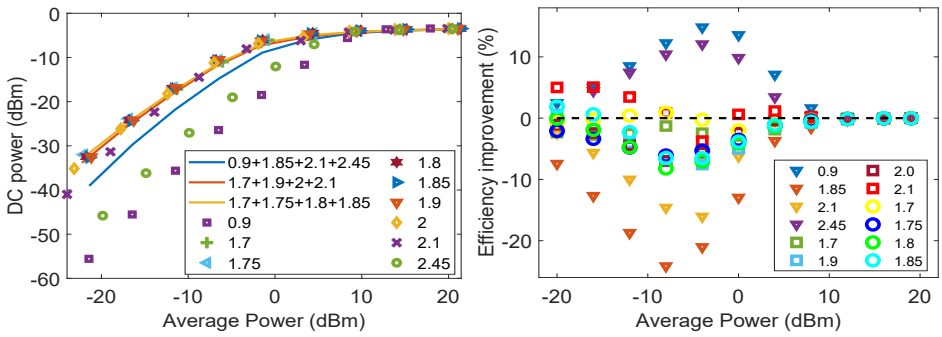

(a) (b)

Figure 3.4.4: Simulated DC power for a CW and four tone at different frequencies for circuit 2. a) DC power and b) efficiency improvement.

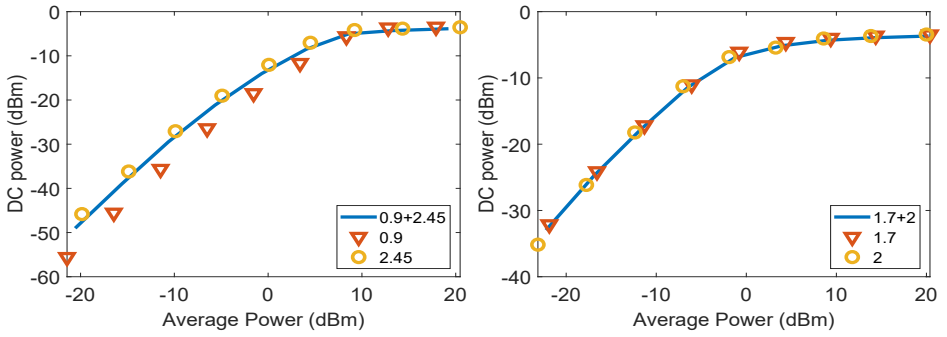

(a) (b)

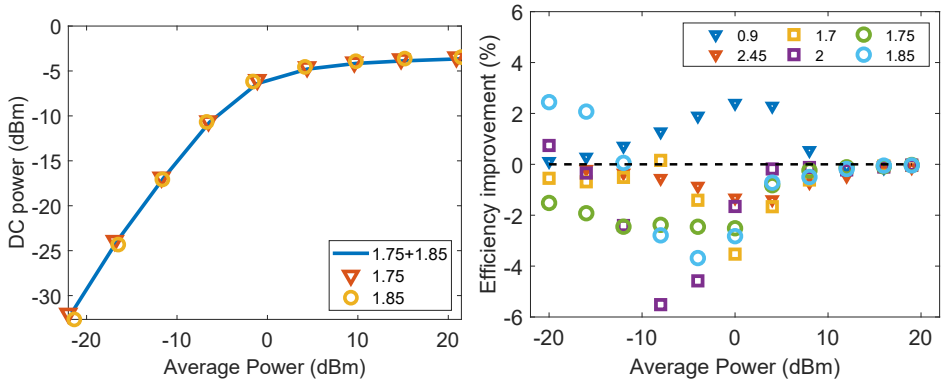

(c) (d)

Figure 3.4.5: Simulated rectified DC power for a CW and for a two-tone excitation at different frequencies for circuit 2. DC power at a) 0.9+2.45 GHz b) 1.7+2.0 GHz and c) 1.75+1.85 GHz. d) Efficiency improvement.

For the circuit 3 (see Figure 3.4.6), the following frequency subsets are used for the four-tone approach: (0.9+1.85+2.1+2.45) GHz, (1.4+1.55 +1.75.+2.1) GHz and (1.5+1.55+1.6+1.65) GHz.
To conclude, (0.9+2.45) GHz, (1.4+1.75) GHz and (1.55+1.65) GHz are used for the two tone approach.

It is important to remark that for the efficiency improvement plot an interpolation has been performed at the post-processing stage, over the simulated data (also over measurements), with the aim to compare all cases with the same average power, not similar values, to get an accurate result.

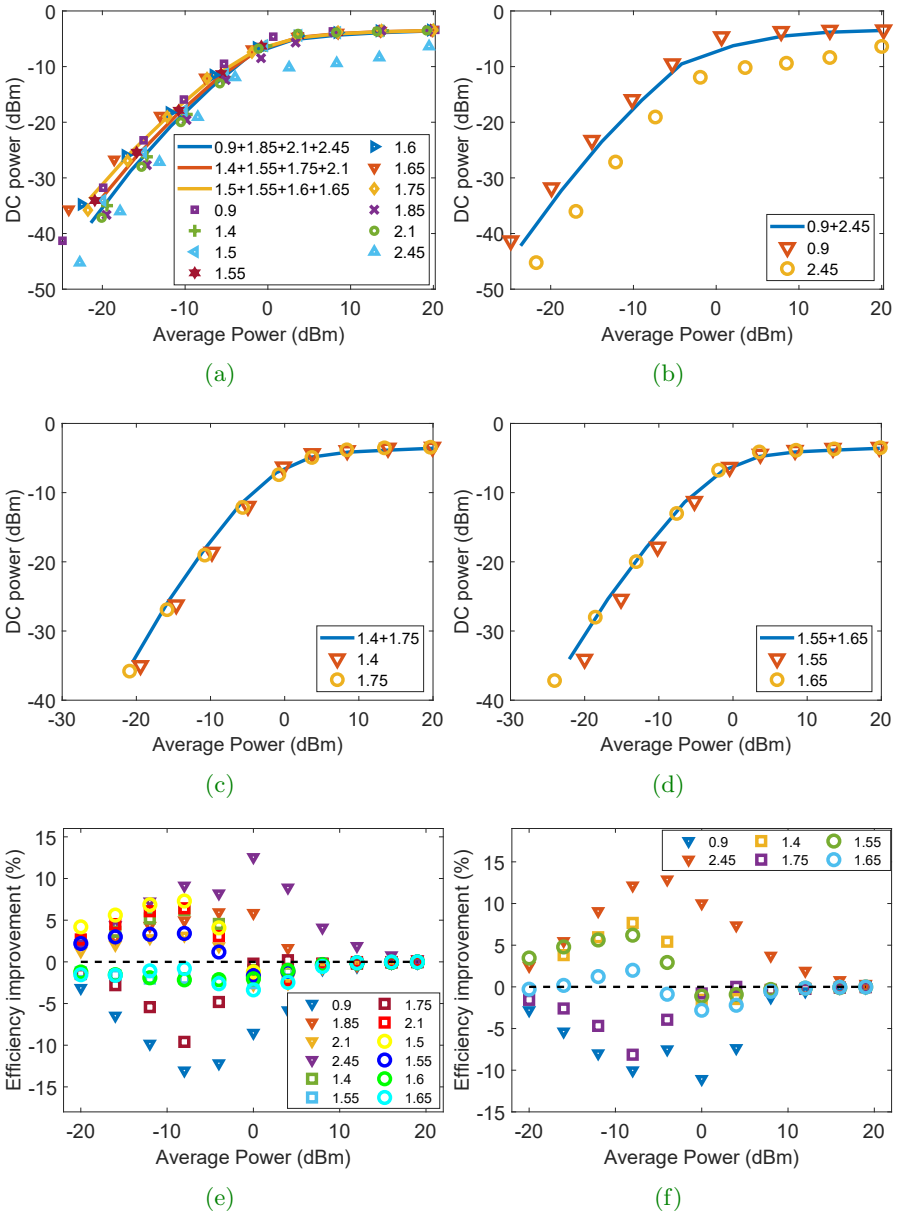

Figure 3.4.6: a) DC power for a CW and a four-tone excitation. b),c),d) for a CW and a two-tone excitation. Efficiency improvement for e) four tones and f) two tones over a CW signal.

3.4.2. Multiple-tone measurements in a rectifier

Multiple-tone and CW measurements have been performed in the lab, varying the frequency and amplitude of each tone. To do this, the measurement setup developed in the previous sections has been used, as can be seen in Figure 3.4.7, where the four independent sources appear. All data have been collected and summarized in the appendix (Section 7.2). During the measurement process, there were some issues, summarized in the following points.

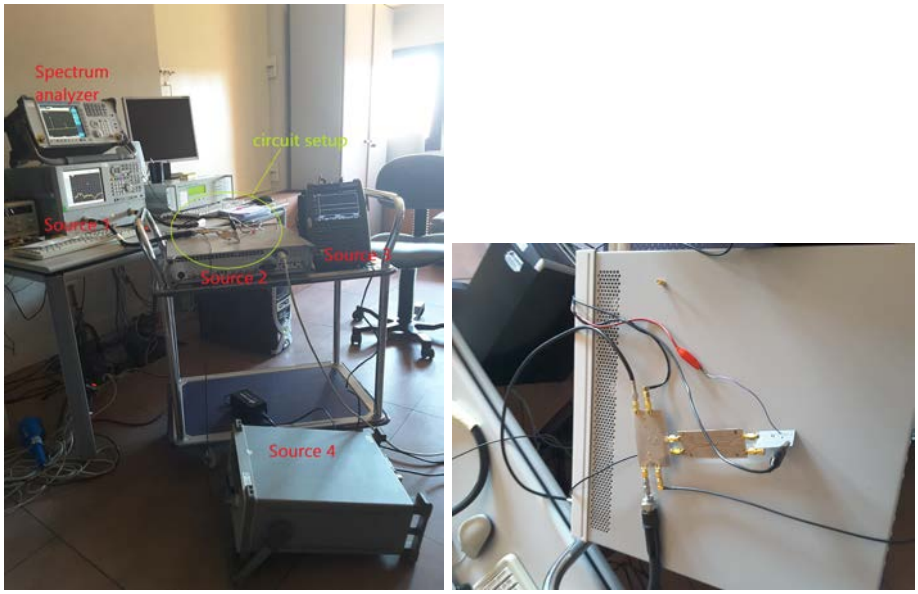

(a) (b)

Figure 3.4.7: Measurement setup with four independent sources.

- Although multiple-tone simulations have been performed for one, two and four tones, three-tone measurements have also been included. Four independent sources were used, as a multiple-tone generator was

not available. This fact created some problems, as an special measurement setup was required (power combiner and coupler). Moreover, two sources limited the variation of the power levels. One source could provide 3 dBm in its top limit, and another source could provide -10 dBm in its bottom limit. Measurements were performed from -25 to 2 dBm (each tone) up to three tones. The fourth tone was limited from -10 to 2 dBm.

- The connector of circuit 3 was damaged. Therefore, and due to the lack of time and problems to access the laboratory, this circuit was not measured using the multiple-tone approach. Nevertheless, the other circuits were used, providing more than enough measurements to characterize the non-linear effect under the multiple-tone scenario.

- The RF and DC power in the rectifier must be measured to get the power conversion efficiency values. However, it is not possible to quantify directly the input power to the rectifier, in the lab measurement, using the proposed setup. To do this, the simulation of the setup and its good modeling is crucial. The coupler has a port which is connected to a spectrum analyzer, where part (around -20 dB) of the input power is measured. Through simulations it is possible to quantify the power difference between the input and coupled ports. The coupler is not loaded exactly with 50 Ω (a Wilkinson and different rectifiers are connected to it), thus, the coupled port is not exactly 20dB lower that the direct transmission (see S-parameters of the coupler in Figure 3.3.10). The simulated difference between ports (ports 1-2 and ports 3-4) when connected to the setup is used to compute the input power at the rectifier. Once the RF power is obtained, the DC power is monitored with a voltage meter when the amplitude and spacing of the tones is varied.

In spite of these limitations, multiple-tone measurements were performed (see Appendix 7.2 for a recapitulation of measured data), showing the existence of an RF-DC power conversion improvement when multiple tones were used. This improvement involves a non-linear process, as the

excitation of N tones at the same time produce a larger DC component than when individually used, with the same average power. This process is non-linear and, therefore, depends on the relative frequency and amplitude of each tone. Once the non-linear region is overpassed, the process decays as the diode starts working in a linear region. In Figure 3.4.8, the measured DC power is compared using different number of tones, varying their amplitude and frequency spacing for circuit 1 and circuit 2.

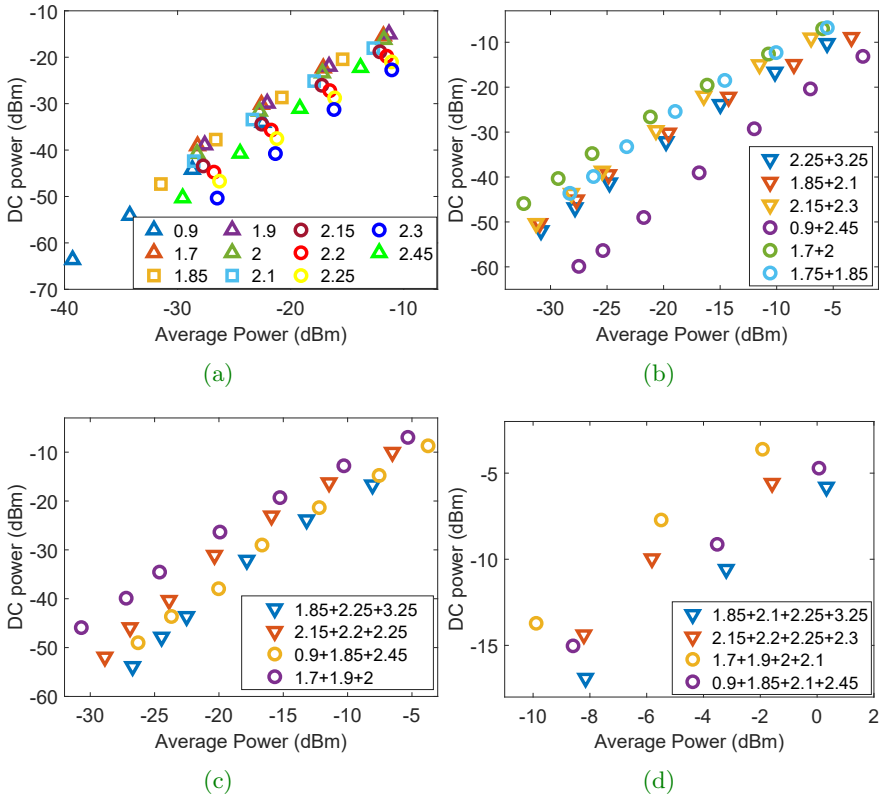

Figure 3.4.8: Rectified DC power for a multiple-tone excitation. a) one-tone, b) two-tone, b) three-tone and c) four-tone excitation.

In Figure 3.4.9, the DC power contribution is shown when multiple-tones and CW excitation are used. Each plot corresponds to a different frequency subset. Thus, inside a plot it is easy to see that sometimes the N-tone approach outperforms to the CW excitation as in Figure 3.4.9(c,d). Other times, the opposite happens, where a CW works more efficiently as in Figure 3.4.9 (a,b), outperforming the N-tone approach. This happens because the efficiency is not constant with frequency. At some frequencies the efficiency is higher than in others. Thus, if two tones are used ($T_1 + T_2$), T_1 with a good efficiency and T_2 with bad efficiency, the contribution can be smaller than the case where T_1 is used with the same average power (this means $A_{1-Tone} = \sqrt{2} \cdot A_{2-Tones}$). Thus, in this last case the rectifier is being excited with a higher amplitude in a region where the efficiency is higher and therefore, $\eta_{T1} > \eta_{T1+T2}$. As conclusion, the power conversion efficiency improvement in a rectifier can be understood as a non-linear process, respect to the frequency and input power. Some frequency tones produce a higher efficiency than others. And also, low input power levels make the diode to work in the exponential region, where the threshold limit can be overpassed more efficiently, getting higher current peaks. The same effect can be observed in the simulations.

Finally, in Figure 3.4.10 the efficiency improvement is shown, for a two-tone and three-tone excitation. The four-tone excitation was not included as their measured values were done in a different input power range due to the sources limitations (-10 to 3 dBm). As already explained, in some subsets an efficiency improvement is obtained when a multiple-tone excitation is used, and this depends on the individual efficiency at each frequency. The available power conversion efficiency using a CW, for circuit 1 and circuit 2, can be seen in Figure 3.2.10 and Figure 3.2.15.

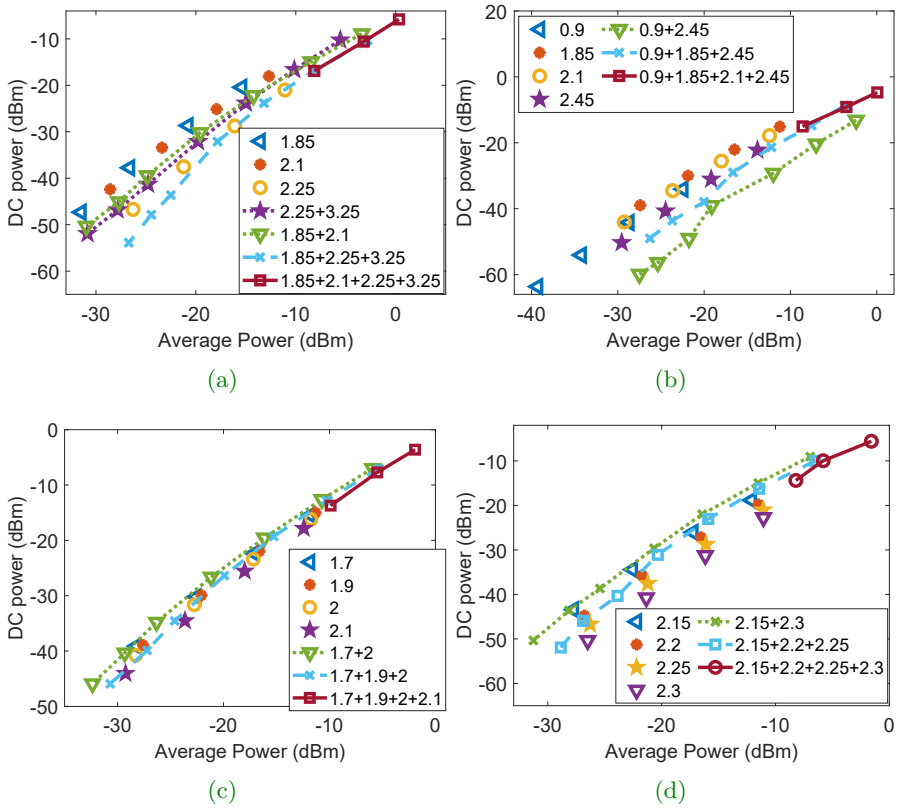

Figure 3.4.9: Comparison of the rectified DC power for an N-tone excitation vs a CW signal from its corresponding frequency subset. a,d) Using circuit 1 and b,c) using circuit 2.

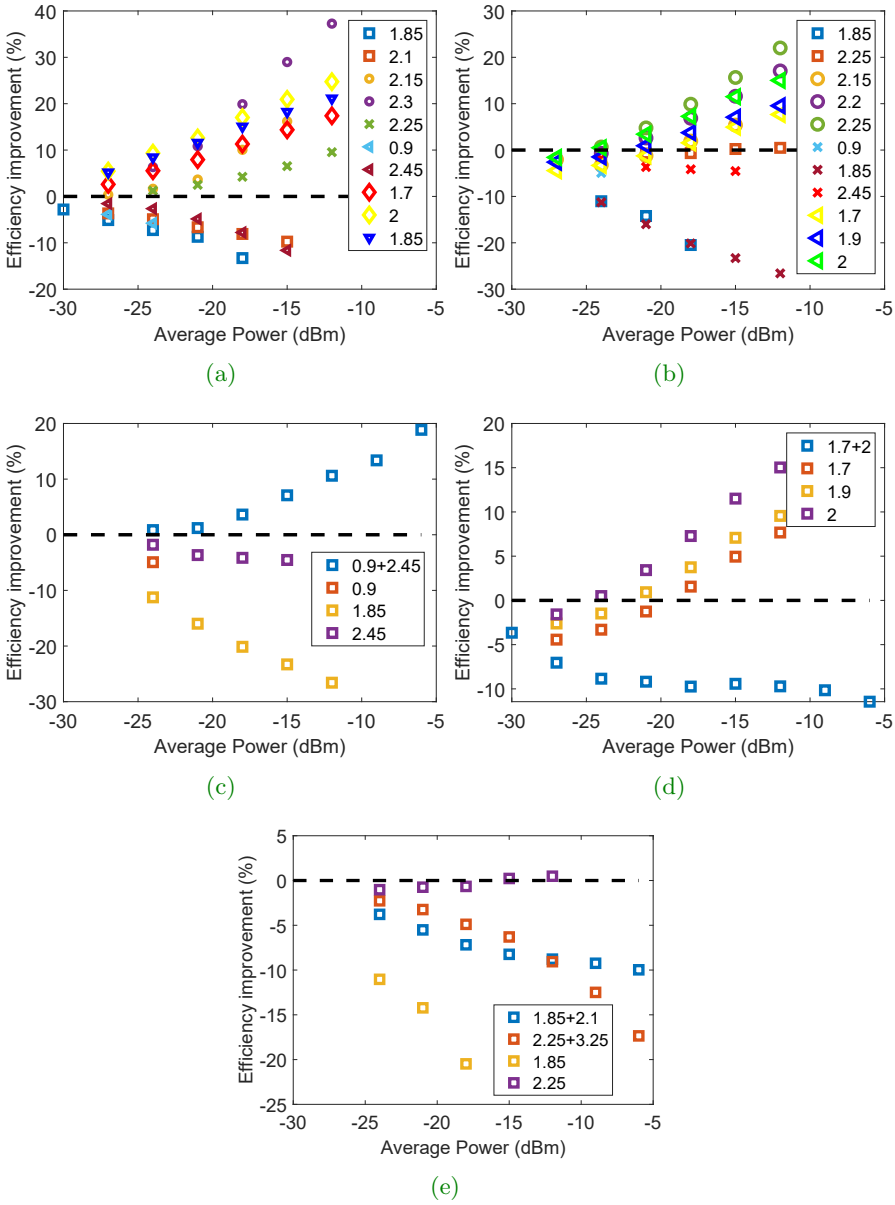

Figure 3.4.10: Efficiency improvement under a multi-tone scenario. a) Two-tone signal vs CW. b) Three-tone signal vs CW. c,d,e) Three-tone signal vs a two-tone and CW excitation at different frequency subsets.

3.5. Conclusions

The diode is a non-linear device that when it is excited with a multiple-tone signal in its non-linear region, an RF-DC power conversion efficiency improvement can be obtained, attending to the relative frequency and amplitude of each tone. This mechanism can be used in energy harvesting to increase the amount of the rectified DC power. This chapter deals with the multiple-tone simulations and measurement of a rectifier. For that purpose, an accurate simulation and experimental setup have been designed. The diode Spice model was analyzed, showing poor agreement between simulation and measurements. Therefore, a new Spice and parasitic model is presented along this chapter, where a very good characterization of the diode is shown from -10 to -25 dBm and from 0.9 to 4 GHz. In this way, it has been possible to verify the RF-DC efficiency improvement under a multiple-tone scenario. Measurements were not carried out at high power levels due to some limitations of the available sources. To summarize, the power conversion efficiency improvement in a rectifier can be understood as a non-linear process, respect to the frequency and input power. Some frequency tones produce a higher efficiency than others. And also, low input power levels make the diode to work in the exponential region, where the threshold limit can be overpassed more efficiently, getting higher current peaks under multiple-tone excitations. Nevertheless, at higher power levels this efficiency improvement disappears, as the diode starts working in a linear region.

References

[1] SMS7630 Series Surface Mount Mixer and Detector Schottky Diodes from Skyworks.
http://www.skyworksinc.com/Product/511/SMS7630_Series#four

[2] APN1001: Circuit Models for Plastic Packaged Microwave Diodes.
https://www.digikey.be/de/pdf/s/skyworks-solutions/skyworks-plastic-packaged-microwave-diodes.

[3] N9918A FieldFox Handheld Microwave Analyzer
https://www.keysight.com/en/pdx-x201927-pn-N9918A/fieldfox-handheld-microwave-analyzer-265-ghz?nid=-32495.1150498&cc=US&lc=eng&pm=ov

[4] Large Signal S-Parameters Simulation from Keysight
http://literature.cdn.keysight.com/litweb/pdf/ads2003a/pdf/cktsimlssp.pdf

[5] Keysight N5181A-503 RF Signal Generator
https://www.keysight.com/us/en/assets/7018-02282/product-fact-sheets/5990-4534.pdf

[6] Linear Models for Diode Surface Mount Packages. Application Note 1124.
https://docs.broadcom.com/wcs-public/products/

application-notes/application-note/829/290/
av02-0038en-an_1124-21jul10.pdf

[7] Borgoñós García, M. (2019). Development of Narrowband Rectennas for Biomedical Applications (master's thesis). Universidad Carlos III de Madrid.

[8] M. Borgoñós-García, A. López-Yela, D. Segovia Vargas, "Rectenna at 2.45 GHz for Wearable Applications," 2020 14th European Conference on Antennas and Propagation (EuCAP), Copenhagen, 2020, pp. 1-4.

[9] J. Bito et al., "Millimeter-wave ink-jet printed RF energy harvester for next generation flexible electronics," 2017 IEEE Wireless Power Transfer Conference (WPTC), Taipei, 2017, pp. 1-4.

[10] Pozar, D.M. (2012), "Microwave Engineering". 4th Edition. Wiley, New York.

[11] Boyd, John and Petschek, Rolfe. (2014). The Relationships Between Chebyshev, Legendre and Jacobi Polynomials: The Generic Superiority of Chebyshev Polynomials and Three Important Exceptions. Journal of Scientific Computing. 59. 10.1007/s10915-013-9751-7.

[12] E. J. Wilkinson, "An N-way hybrid power divider", IRE Trans. Microwave Theory and Techniques, vol. MTT-8, pp. 116-118, January 1960.

[13] R. Sorrentino and G. Bianchi. "Microwave and RF engineering".John Wiley and Sons ldt, Chichester, 1st edition, 2010.

[14] B. Mishra, A. Rahman, S. Shaw, M. Mohd, S. Mondal and P. P. Sarkar, "Design of an ultra-wideband Wilkinson power divider," 2014 First International Conference on Automation, Control, Energy and Systems (ACES), Hooghy, 2014, pp. 1-4.

[15] S. B. Cohn, "A Class of Broadband Three-Port TEM-Mode Hybrids", in IEEE Transactions on Microwave Theory and Techniques, vol. 16, no. 2, pp. 110-116, February 1968.

[16] Kasar, Ömer, Gözel, Mahmut, kahriman, mesud. (2018). Broadband Wilkinson power divider based on chebyshev impedance transform method. Journal of Advanced Medical Sciences and Applied Technologies. 2. 299-303.

[17] Salimi, Puria. "A Design Procedure for Multi-Section Micro-Strip Wilkinson Power Divider with Arbitrary Dividing Ratio." International Journal of New Technology and Research, vol. 3, no. 12, Dec. 2017.

[18] Designing Wilkinsons in Excel. Microwaves101 encyclopedia. http://www.microwaves101.com/encyclopedia/wilkinson_Excel.cfm

[19] G.L. Matthaei, "Microwave filters, impedance-matching networks, and coupling structures" v. 1. McGraw-Hill, 1964.

[20] E. M. T. Jones,"Coupled-Strip-Transmission-Line Filters and Directional Couplers," in IRE Transactions on Microwave Theory and Techniques, vol. 4, no. 2, pp. 75-81, April 1956

[21] Collin, R. E. (2001), "Foundations for microwave engineering",2nd Edition. Wiley-IEEE Press44

[22] L. Young, "The analytical equivalence of TEM-mode directional couplers and transmission-line stepped-impedance filters", in Proceedings of the Institution of Electrical Engineers, vol. 110, no. 2, pp. 275-281, February 1963.

4

The wireless power reception unit: multiband vs broadband analysis

An energy harvester prototype is composed of different parts, the wireless power reception (WPR) unit and the DC management unit. The WPR unit deals with EM waves to get DC power while the DC management unit manages the DC power side, in order to properly interact with the sensor (microcontroller, storage devices, DC-DC converter). The WPR unit is composed of a rectenna which corresponds to the integration of an antenna and a rectifying circuit. This chapter deals with its integration, with a common $50\,\Omega$ match design while in Chapter 5 a source-pull integration is developed, although the source-pull technique is introduced here. As explained in previous chapters, high PAPR signals improve the RF to DC power conversion efficiency in the rectifier, therefore, indoor and outdoor multiple-tone measurements are included. When designing an antenna for energy harvesting, different questions arise. Is it better a single band, multiband or a broadband rectenna? Should the antenna present a directional beam or an onmidirectional radiation pattern? All this questions are addressed throughout this chapter.

4.1. Introduction to energy harvesters

An energy harvester transform EM power in waves into DC power to feed an autonomous low duty cycle sensor. Thus, the sensor can monitor significant parameters such as temperature [1], blood pressure level or water level in rivers [2], without using batteries. Also, it is possible to transmit information to the main node of a network when a wireless sensor network is established (e.g fire detection nodes in the forest). Energy harvesters have been designed for powering sensors at different scenarios. In [3], an energy harvester was designed to scavenge energy from a radar sidelobes to power unattended sensors on an aircraft. Moreover, sometimes it is possible to benefit from everyday objects to integrate them in the design. For example, in [4], the kitchen clock functionality was extended using the clock hands as an antenna. A rectenna was designed, scavenging ambient EM from mobile base stations using the clock to power an environmental sensor.

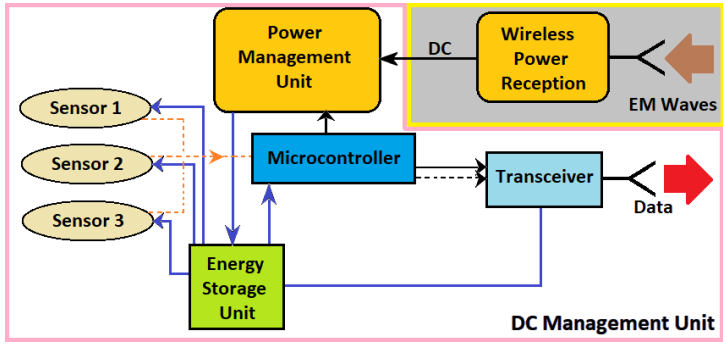

Figure 4.1.1: Complete power management circuit for an electromagnetic energy harvester.

The energy harvester is composed of different parts, the wireless power reception unit and the DC management unit (see Figure 4.1.1). The first part extracts the power from EM waves through the antenna. Depending on the antenna topology and design, different frequency bands (single band, multiband), polarization (linear, circular, dual polarization) and beam di-

rection are used. Later, that RF power is rectified and converted into DC through Schottky diodes or whatever rectifying devices (N-P-N or P-N-P junctions in transistors). In literature, different rectification schemes have been analyzed [5].

The DC management unit distributes and controls the DC part, in order to autonomously power a sensor. In this unit, a DC-DC boost converter and a microcontroller are integrated. The DC-DC boost converter can be used to step up very low DC voltage levels to those levels that can power up a microcontroller (3.3V). A storage supercapacitor must be included to store excess of harvested energy between burst periods. In this way, it is possible to power up low duty cycle devices. An example of a DC-DC converter is shown in Figure 4.1.2. A low input power DC-DC converter (LTC 3107 [6]) is used to step up harvested voltage up to 3.6 V (V_{OUT}) when V_{IN} is higher than 20 mV. In this way, a microcontroller can be powered autonomously without including batteries. This DC-DC converter stores energy during long periods of time to enable short power burst to power up a microcontroller. The burst must occur at low duty cycle to control that the required power during burst periods does not exceed the stored power integrated over the time between burst. It consumes 80 nA when there is harvested energy and 6 μA when there is no harvested energy. Top and bottom faces are plotted in the blue and green ink, as seen in Figure 4.1.2.

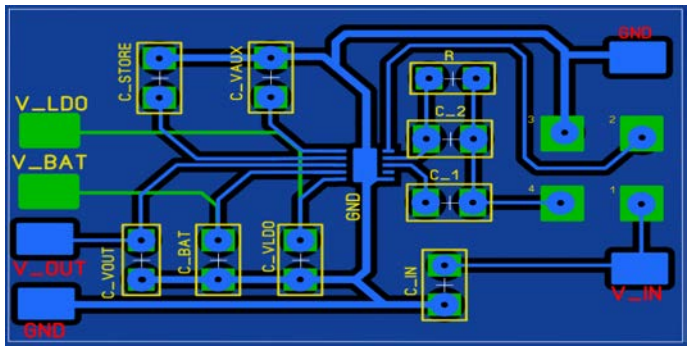

(a)

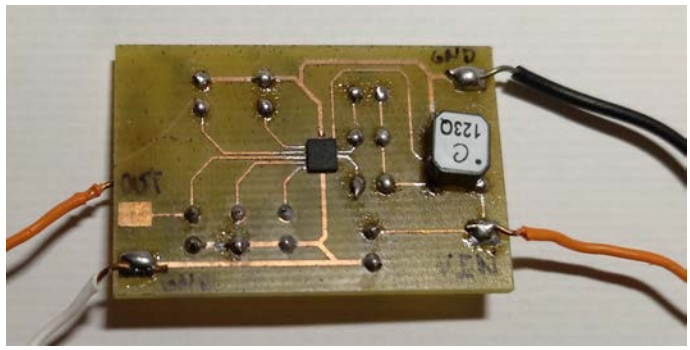

(b)

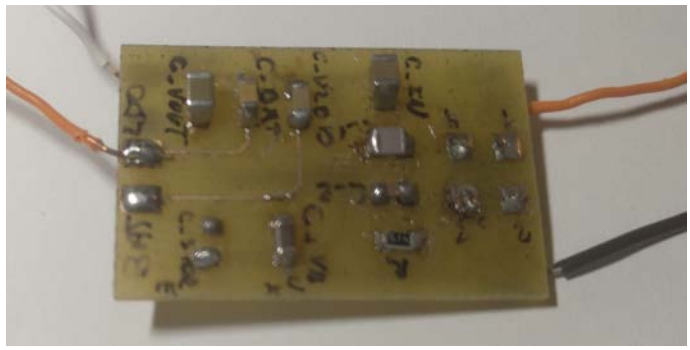

(c)

Figure 4.1.2: DC-DC converter.a) Layout and circuit prototype. b) Top face. c) Bottom face.

Then, the microcontroller interacts with the power management unit and the energy storage unit, delivering power to the sensor when it is possible, or sending information to the transceiver when desired [7]. The transceiver part is highly influenced by the application, as some applications are just focused on the autonomously power of a device, information delivery is not required. This chapter deals with the wireless power reception part, focusing on different aspects to take into account in the rectenna design. As the diode has a non-linear performance, the rectenna integration

must be analyzed. Two different strategies can be followed for the integration: a common 50 Ω matching or the use of a Source-pull (SP) technique. In a 50 Ω design, a matching network is required, fulfilling the RF maximum power transfer theorem, where Γ_L=Γ^*_{OUT} and Γ_S=Γ^*_{IN}. In this case, the circuit dimensions are enlarged and losses are increased. Nevertheless, for non-linear systems the solution is significantly different. It is necessary to assess optimal values for the reflection coefficients Γ_S and Γ_L using load and source-pull techniques to maximize the DC power transfer (not RF). Usually Γ_{SPmax} is closer to Γ^*_{IN}. So, for single band schemes, it can be easy to get a good design in both cases. Nevertheless, with the source-pull technique the matching network is removed, simplifying the rectifier design, modifying the antenna configuration and reducing losses. For broadband designs, source-pull is a better option as the design complexity is reduced. All this is explained throughout this chapter. The multiple-tone theory from Chapters 2 and 3 is validated through a rectenna prototype. Indoor and outdoor spectrum measurements are carried out to analyzed the working environment. Therefore, a multiband or broadband design is desired to scavenge power from different bands. In this case, the design procedure for the integration is analyzed, attending to the application: energy harvesting or directional beaming.

4.2. Wireless power reception unit: Antenna

As already mentioned in Chapter 1, there exists two different approaches to wirelessly power transfer: directional beaming and energy harvesting. Both options provide the same result (cordless power transfer) but the background of the idea is different. Directional beaming implies the use of sources in a single link, so some parameters can be controlled (power density, polarization and beam direction). Therefore, it is possible to get enough DC power at a fixed distance just configuring the link budget, fulfilling the regulation. The position of the receiver must be aligned with the transmitter to minimize mismatches. Nevertheless, energy harvesting is based on the opposite requirements. No sources are available, just ambient

electromagnetic energy from mobile communications (also TV [8], radar [3], etc). The position, polarization and angle of arrival of the waves are unknown. Two facts should be highlighted: the power density is variable at the harvester due to multipath fading, being very low (on the order of μ W/m^2) and the polarization is affected, varying with time.

With these assumptions, an appropriate polarization scheme and antenna topology must be chosen, to get the best performance for the application.

4.2.1. Polarization schemes and antenna topology

For a linear polarized source, the electric field at a linearly polarized receiving antenna will be proportional to the cosine of the angle formed by the polarization vectors of the transmitting and receiving antenna [9]. Nevertheless, multipath propagation makes, over a vertically polarized antenna, the receiving electric field to be contained on average equal power in the two orthogonal polarizations. Therefore, for a line of sight scenario, single linear (or circular) polarized antennas can be used, but if multipath propagation is produced, dual linear (or dual circular) polarization is recommended to improve the received power.

Concerning the antenna topology, for a WPT beaming application, directional antennas are desired while in an energy harvesting application, omnidirectional or non-directive antennas are preferred.

Antennas with a ground plane can be a good option since it is possible to isolate the antenna radiation from the rectifier. It avoids undesired couplings, although in general, whatever topology can be chosen attending to the application.

4.2.2. DC power combining vs RF power combining

Due to the low power density values for EM ambient energy, the rectenna performance is limited by the RF to DC power conversion efficiency. The power conversion efficiency for a single element is defined as:

$$\eta = \frac{P_{DC}}{S(\theta, \phi) \cdot A_g}, \tag{4.2.1}$$

where $S(\theta, \phi)$ is the spatial power density from one or more plane waves and A_g is the geometric area of the antenna. It results in a conservative efficiency estimate (as seen in [10]) as the geometric area is always larger than the effective area for any passive antenna. The total incident power can be computed through the integral in a sphere that surrounds the antenna. This definition does not include a possible mismatch between the antenna and the rectifier, or ohmic losses.

In order to increase RF to DC power conversion, multiple-tone signals have been studied in Chapter 2 and 3. It has been analytically shown that high PAPR signals improve the conversion efficiency when tones are present in the same rectifier. The theoretical analysis is in agreement with rectifier measurements and simulations. This is due to the non-linear performance of the diode and its exponential performance under low input power levels. This is at the rectifier level to increase the conversion efficiency. Nevertheless, at the antenna level is possible to improve the DC power collected through two different ways: RF combining or DC combining (see Figure 4.2.1).

RF combining is obtained through antenna arrays, designed to narrow the beamwidth. This is an important strategy in WPT beaming. Nevertheless, DC combining through rectenna arrays is convenient for energy harvesting applications, to multiply the harvested power at the expense of increasing the prototype size. The difference to quantify the harvested DC power for both options is explained in [11]. In RF combining, the total harvested DC power is influenced by the RF input power level, the gain of the antenna array (G_{ar}) and by the efficiency of the rectifier (η_r) and the combining circuit (η_c).

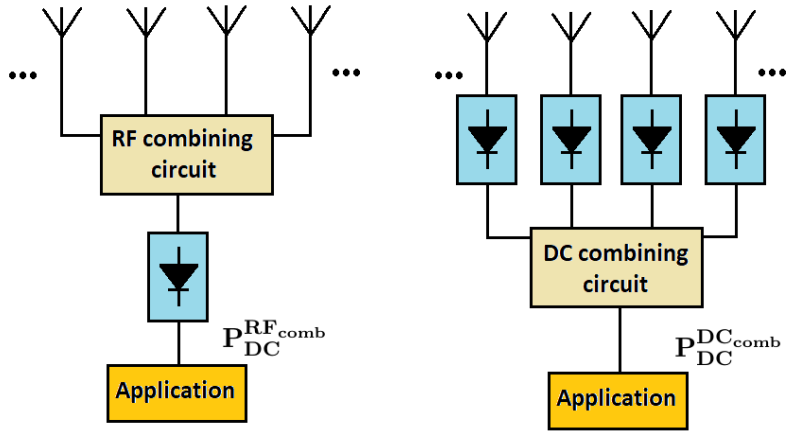

(a) (b)

Figure 4.2.1: Combining circuit schemes. a) RF combining circuit b) DC combining circuit.

$$P_{DC}^{RF_{comb}} = P_{RF_{IN}} G_{ar} \eta_r \eta_c, \tag{4.2.2}$$

where $\eta_r(P_{RF_{IN}}, G_{ar}, \eta_c)$. Nevertheless, for DC combining, instead of using the gain of the array, it depends on the gain of the antenna element(G_a) and the number of elements (N).

$$P_{DC}^{DC_{comb}} = P_{RF_{IN}} N G_a \eta_r \eta_c, \tag{4.2.3}$$

but η_r depends on $\eta_r(P_{RF_{IN}}, G_a)$.

In an RF combiner topology, an antenna array is formed. As long as we increase the number of elements, the beamwidth is reduced, so more energy is scavenged at boresight but less in other angles. In this case, the rectifier can be used more efficiently as the input power is increased. Nevertheless, with a DC combiner, power can be harvested at different angles and the design forms an array of rectennas. Each element works independently and later, DC power is added. In this case, as long as the number of elements is

increased (antennas or rectennas), the DC power combiner outperforms the RF combiner [11]. The beamwidth reduction of the antenna array in the RF combiner reduces the harvested power at some angles. In both cases, the power density will not be constant over all the elements. Also, there is a limit in the maximum number of elements, due to size limitations and losses.

Some examples of a single element and with a rectenna array using a DC combiner topology are shown in [12] and [13]. Two different interconnection can be established for elements in the DC combiner, depending on the position of the rectennas, in series or parallel. RF combining is convenient in WPT directive beaming scenarios as a well characterized source is employed. Therefore, as the link direction is known, the beamwidth is reduced and usually single band (or double band) antennas are employed to transmit power. Broadband antennas are not common in these applicactions. For energy harvesting, the RF combining approach, forming an antenna array is not valid as electromagnetic signals comes from unknown directions. In this case, DC combining is useful, where an array of rectennas is employed at different bands (even in a broadband design).

A triple band [14] at 0.9, 1.8 and 2.45 GHz and a dual band [15] at 2.45 and 5.8 GHz schemes were designed, where the rectennas were stacked in parallel, connected to different filters (low pass and band pass) in each band, adding the circuit for collecting the DC output. In [16], multiple services were scavenged to increase the amount of harvested power, although one antenna and more than one rectifier were used, using a cascaded rectifying stages with different filters in each branch, summing DC contributions in the load. In all cases, more power is scavenged at three bands when compare with one band. Nevertheless, other alternatives can be analyzed to increase the DC power. This thesis focuses on the RF to DC power conversion improvement when multiple-tone signals are exciting at the same time a rectifier. This means that over one rectifier, two or more tones can produce a DC current improvement, because the PAPR is larger, when compare to the DC output at each tone:

$$P_{DC}^{2-Tones} \geqslant P_{DC}^{Tone1} + P_{DC}^{Tone2}. \tag{4.2.4}$$

At a glance, this can be done through: i) using multiple single band antennas (at different bands) and summing the RF contribution through an RF power combiner; ii) a multiband antenna; iii) and a broadband antenna. These approaches are explained in following sections.

4.3. Indoor and outdoor ambient spectrum measurements

Indoor and outdoor electric field measurements were performed at the University Carlos III in Leganés, Madrid. The aim was to characterize the spectrum, to see expected levels and which bands were the most significant ones to perform some rectenna measurements. The spectrum analysis was taken at different scenarios, two laboratory rooms at the second and third floor of the building and the rooftop. The measurements were performed using a Keysight N6850A broadband Omnidirectional antenna working from 0.5 to 6GHz and a N9918A FieldFox Handheld Microwave Analyzer working up to 26.5GHz. It was necessary to calibrate the system in order to ensure a fully working setup. So, the antenna factor correction was applied [17]. This parameter is employed to correct possible deviations in spectrum or field measurement. It is provided by the antenna's manufacturer and relates the ratio between the magnitude of the electric field incident on the antenna and the voltage at the antenna's connector. It is expressed in dB/m. The antenna factor parameter, shown in (4.3.1), can be applied before or after the measurement. If applied before, electric field is measured at the antenna's connector. If applied later, voltage is measured. In both cases it is necessary to change the units in the spectrum analyzer to $dB\mu V$. Otherwise, the scaling factor is wrongly used.

$$F(dB/m) = \frac{E(dB\mu V/m)}{V(dB\mu V)}. \tag{4.3.1}$$

Measurements were taken between the first and second week on July 2019, for vertical and horizontal polarization, so the 5G standard had not been deployed yet. The spectrum analyzer was configured with 1004 frequency points, resolution bandwidth of 10 kHz, recording measurements every 30 second for 3 hours. In Figure 4.3.1, electric field measurements are plotted. The noise floor of Keysight N9918A Analyzer is also included to check that the slope is due to the device.

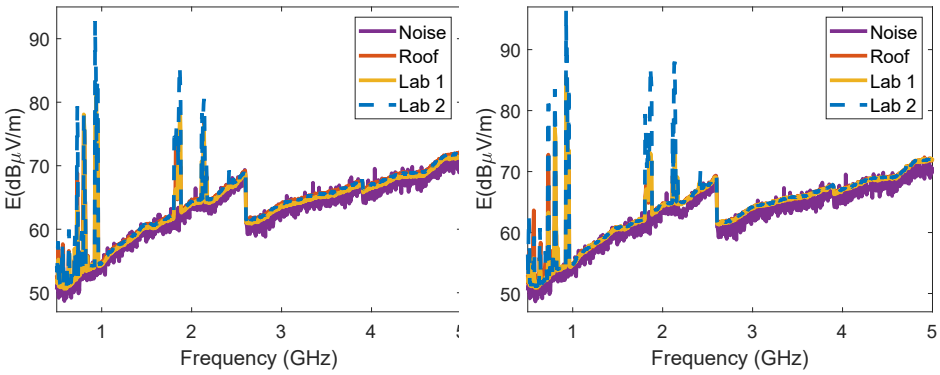

Figure 4.3.1: Electric field measurement at three different scenarios: outdoors (at the roof of the building) and indoors (at two different laboratories) for a) vertical polarization, b) horizontal polarization.

From Table 4.1 to Table 4.3, on average and maximum power density values (S) (4.3.2) are summarized, dividing the spectrum into different communications services, in uplink (UL) and downlink (DL) contributions, although from 3.5 GHz upwards, no significant peaks appear in the spectrum.

$$S = \frac{E_{RMS}^2}{\eta_0} \tag{4.3.2}$$

being η_0 the characteristic impedance of the medium, in this case 377 Ω.

Name	Band (MHz)	Average Density Power V-pol	Maximum Density Power (V-pol)	Average Density Power (H-pol)	Maximum Density Power (H-pol)
DTV	470-782	1.05	20.37	2.34	50.26
LTE-800 (DL)	791-821	42.86	100.74	10.95	23.90
LTE-800 (UL)	832-862	0.71	1.02	0.67	0.70
GSM-900 (DL)	925-960	55.24	131.00	39.87	122.62
GSM-900 (UL)	880-915	0.71	0.72	0.72	0.75
GSM-1800 (DL)	1805-1880	18.67	54.5	13.49	21.17
GSM-1800 (UL)	1710-1785	4.02	4.28	4.13	4.54
WCDMA (DL)	2110-2170	24.4	125.23	13.74	31.41
WCDMA (UL)	1920-1980	6.39	7.33	6.56	7.01
WiFi	2400-2500	13.63	14.77	14.02	15.80
Wimax (DL)	3500-3600	10.13	11.07	10.26	10.89
Wimax (UL)	3400-3500	9.61	9.99	9.84	10.49

Table 4.1: Power density measurements in Madrid (July 2019). Outdoor power density values in nW/m^2 at different bands, measured in the roof of the building.

Name	Band (MHz)	Average Density Power (V-pol)	Maximum Density Power (V-pol)	Average Density Power (H-pol)	Maximum Density Power (H-pol)
DTV	470-782	6.30	227.20	13.63	344.00
LTE-800 (DL)	791-821	61.40	166.00	129.41	596.00
LTE-800 (UL)	832-862	0.66	0.69	0.68	0.71
GSM-900 (DL)	925-960	1134.30	4990.50	2242.40	11530.00
GSM-900 (UL)	880-915	0.70	0.72	0.72	0.76
GSM-1800 (DL)	1805-1880	236.70	973.90	311.40	1399.00
GSM-1800 (UL)	1710-1785	4.10	4.40	4.14	4.32
WCDMA (DL)	2110-2170	105.60	299.30	373.00	1682.50
WCDMA (UL)	1920-1980	6.40	7.10	6.69	7.00
WiFi	2400-2500	15.30	22.30	16.40	28.12
Wimax (DL)	3500-3600	10.10	10.90	10.40	10.90
Wimax (UL)	3400-3500	9.60	10.30	10.10	10.48

Table 4.2: Power density measurements in Madrid (July 2019). Indoor power density values in nW/m^2 at different bands, measured in the lab of the second floor of the building (Lab 1).

Name	Band (MHz)	Average Density Power (V-pol)	Maximum Density Power (V-pol)	Average Density Power (H-pol)	Maximum Density Power (H-pol)
DTV	470-782	0.65	6.02	0.62	5.67
LTE-800 (DL)	791-821	57.71	170.72	51.46	137.68
LTE-800 (UL)	832-862	0.67	0.98	0.80	1.48
GSM-900 (DL)	925-960	153.56	491.96	227.36	1001.03
GSM-900 (UL)	880-915	0.67	0.75	0.71	0.75
GSM-1800 (DL)	1805-1880	45.03	184.50	25.84	54.71
GSM-1800 (UL)	1710-1785	3.74	4.08	4.11	4.49
WCDMA (DL)	2110-2170	27.74	114.00	21.54	84.74
WCDMA (UL)	1920-1980	5.81	6.43	6.42	7.19
WiFi	2400-2500	12.65	13.75	14.84	18.13
Wimax (DL)	3500-3600	9.05	9.55	10.27	10.97
Wimax (UL)	3400-3500	8.62	8.91	9.76	10.26

Table 4.3: Power density measurements in Madrid (July 2019). Indoor power density values in nW/m^2 at different bands, measured in the lab of the third floor of the building (Lab 2).

The maximum, average and minimum power density values are shown in Figure 4.3.2 at the different bands, in a bar plot, to see deviations as values vary over time and space. Vertical polarization measurements are on the left and horizontal polarization results are on the right. Variable incident power densities are crucial at the rectifier element, as they produce a significant change in the impedance. As it is a non-linear element, its performance in an energy harvesting scenario is dramatically affected. Moreover, power density values are low, therefore, to power a sensor it is necessary to scavenge energy from different bands, also getting benefit from the multiple-tone scenario as seen in Chapter 2.

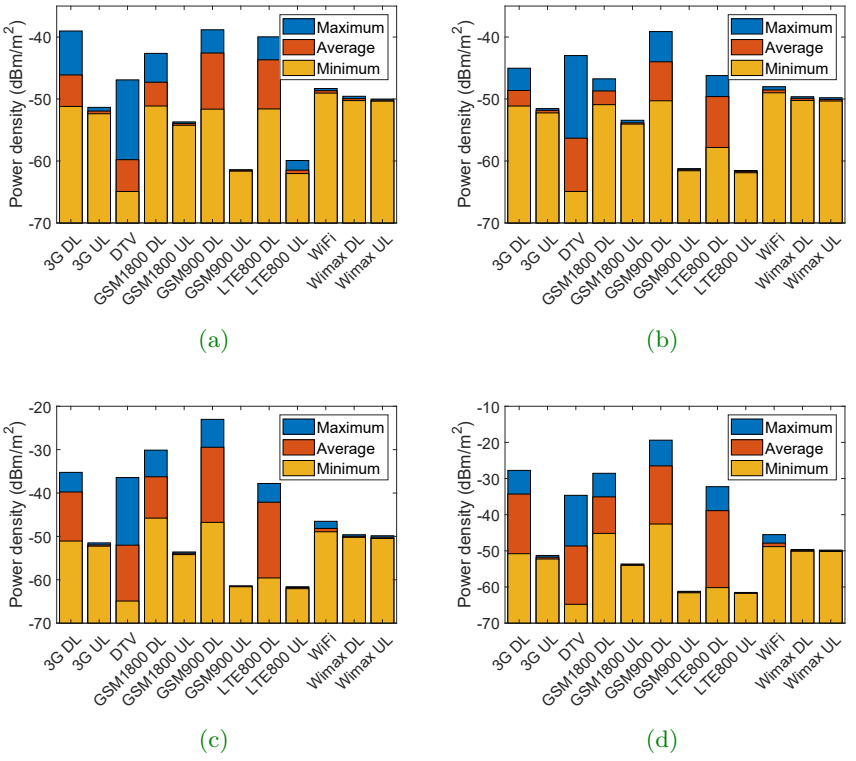

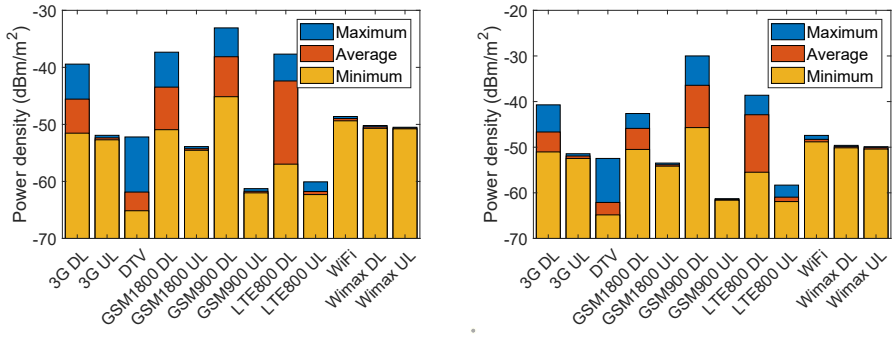

Figure 4.3.2: Bar plot showing power density values at each band at different scenarios for vertical (left) and horizontal polarization (right).
a,b) In the roof of the building. c,d) In the "Lab 1". e,f) In the "Lab 2".

4.4. Rectenna design and considerations

The ambient electromagnetic spectrum is populated with different services as shown in Figure 4.3.1, although energy harvesting applications suffer from very low power density values. In Chapter 3, the rectifier performance has been analyzed under multiple tones, getting an RF to DC power conversion improvement when high PAPR signals excite the circuit. In this way, the peak voltage at the capacitor is increased, overcoming the threshold level of the diode IV curve more efficiency, although this approach is just possible when tones are present in the same rectifier. Therefore, different options are analyzed to benefit from the multiple-tone scenario for energy harvesting: i) using single band antennas at each band and later summing the RF signals at the rectifier input, through a wilkinson power combiner (RF combiner avoiding the use of an antenna array), ii) multiband antennas and iii) broadband antennas. All these alternatives are analyzed throughout this chapter giving an answer with an empirical bunch of measurement under the real ambient spectrum.

4.4.1. Single band antennas

The design of a broadband antenna and a broadband rectifier is a very difficult task. Especially the rectifier part as it is a non-linear circuit that varies its input impedance with frequency, input power and load. Moreover, the rectifier and antenna integration into a rectenna is complex task. Sometimes source-pull techniques (see Section 4.5) must be used for this purpose, because a 50 Ω matching design maybe it is not the best option to maximize the RF-DC conversion efficiency. Therefore, it can be an option to try to simplify all this design into several resonant antennas and several resonant rectifiers. This example can be easily modeled. Then, each rectifier can provide a DC voltage that can be added all together increasing the efficiency. This solution can be a valid approximation for high input power scenarios, but for energy harvesting the interesting point is to work with a multiple-tone signal in the rectifier to benefit from the power efficiency improvement studied in Chapter 2. Therefore, using four antennas and a single rectifier can be a solution for this example as a first approximation.

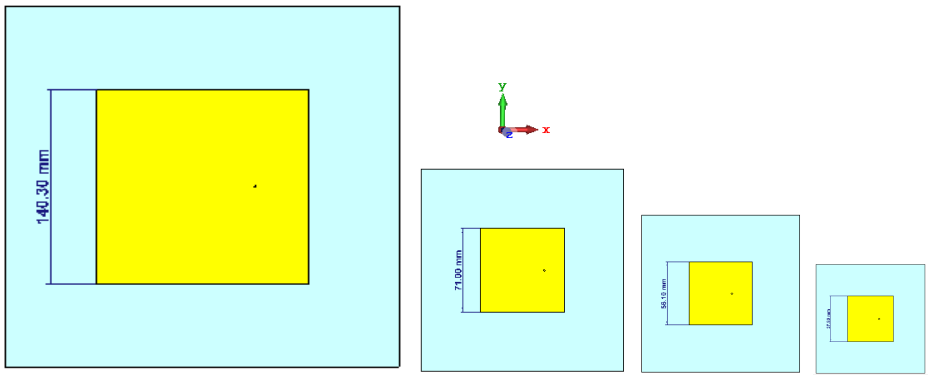

Figure 4.4.1: Single patch design at different frequencies. a) At 0.9 GHz. b) At 1.8 GHz. c) At 2.4 GHz. d) At 3.5 GHz.

A patch antenna has been chosen as the antenna topology due to its broadside radiation pattern. Moreover, the ground plane isolates possible coupling between the antenna an the rectifier. In Figure 4.4.1, four different narrow band patch antennas centered at 0.9, 1.8, 2.45 and 3.5 GHz are shown. In Figure 4.4.2 and Figure 4.4.3, the input reflection coefficient and radiation pattern at the operational point are shown for each patch. The 4-to-1 Wilkinson power combiner (already presented in Chapter 3) is used with the purpose of summing all the signals in one output port, in order to work with just one rectifier. This solution is ideally valid if we consider that the Wilkinson is matched at all ports and at all frequencies. But this is not the real situation, as when the antenna is resonant, a 50 Ω load is provided to that Wilkinson port, but at the rest of the frequencies its impedance is reactive. The Wilkinson power combiner cannot deal with this fact, so as each antenna is resonant at one specific band, the design is not working and the power cannot be added at the output port, as can be seen in Figure 4.4.4, where the reflection coefficient at the the output port is poor, especially at 0.9 GHz. Therefore, just a multiband or broadband antenna can be possible solutions for this work.

E-plane and H-plane for realized gain pattern are shown in Figure 4.4.3. In Table 4.4, the design parameters of each patch antenna are shown.

Center Frequency (MHz)	Bandwidth (MHz)	Realized Gain (dBi)	Patch/ Ground Size (mm)
900	918-962	9.98	140.3/350.0
1800	1797-1896	9.83	71.0/170.0
2450	2400-2480	9.85	56.1/140.0
3500	3500-3600	9.89	37.8/90.0

Table 4.4: Patch antenna: design parameters and characteristics.

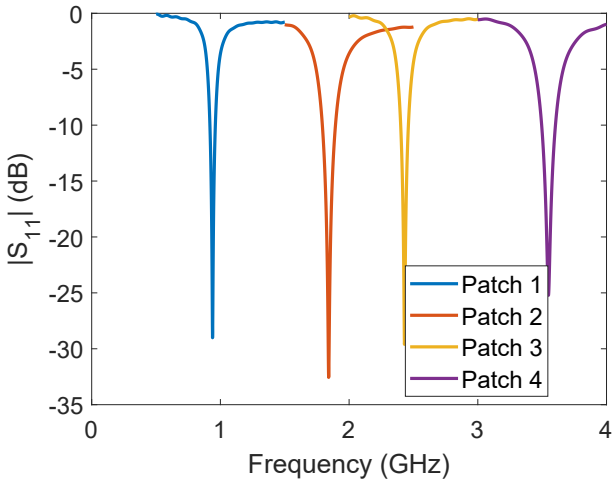

Figure 4.4.2: Input reflection coefficient of each patch.

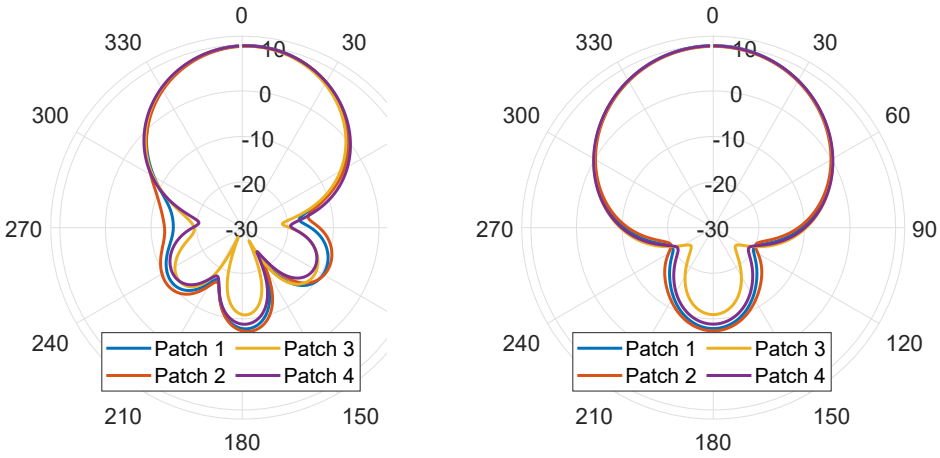

(a) E plane (b) H plane

Figure 4.4.3: 2-D radiation pattern for each antenna.

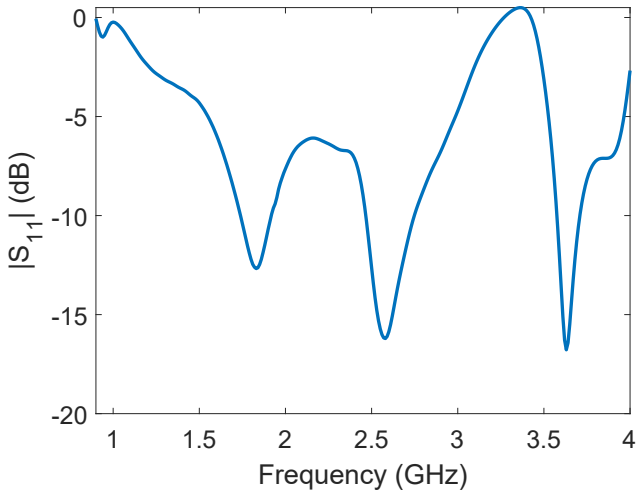

Figure 4.4.4: Input reflection coefficient in the output port of 4-1 Wilkinson combiner connected to four patch antennas.

In conclusion, this approach is not valid for the thesis purpose as it is not possible to sum RF signals from each patch in one port to feed the rectifier, and therefore, it would not be possible to evaluate the multiple-tone analysis proposed as novelty in the thesis.

4.4.2. Broadband or multiband antennas

Multiband or broadband antennas are required to perform the analysis with the complete rectenna. The operational bandwidth of an antenna is the frequency region where some characteristics remain steady, although a possible oscillations can occur. This means that along the operational bandwidth, the reflection coefficient must be small, the polarization must be as constant as possible and the beamwidth not to change dramatically.

By analyzing exclusively its characteristics (without taking into account the complexity of the design), the main difference between both options lies in the operating frequency range. A multiband antenna works over a

very limited frequency range, while a broadband design has a very large bandwidth. In addition, it is important to see that a broadband antenna has a smoother impedance variation, making its integration with a rectifier easier. It also allows to collect energy from all bands present in the range. Thus, from the author's point of view, a broadband antenna is the best choice for working in a energy harvesting scenario. Nevertheless, both multiband [18, 19] and broadband [20] topologies are quite extended in the literature for energy harvesting.

For the integration, a matching network must be included, so losses are increased and the circuit size is enlarged. The design follows the maximum RF power transfer theorem and the matching network transforms a $50\,\Omega$ load to the complex conjugate match of the rectifier. Nevertheless, as the rectifier is a non-linear circuit, sometimes it is tricky to present a $50\,\Omega$ input impedance over a broad bandwidth. Source-pull technique is employed in non-linear designs to overcome this issues, removing the matching network and maximizing in this case the DC output power and then, the RF to DC power conversion efficiency.

4.5. Source-pull non-linear analysis

When working with non-linear devices, small signal S-parameters are not suitable for the characterization. A non-linear device produces a different response depending on the bias point, input power lever, frequency of the excitation and loading conditions, and this cannot be characterized with a linear model such as small signal S-parameters. The load/source-pull technique is a method to empirically perform nonlinear device characterization. In load-pull, the load seen by the device under test is systematically varied through a tuner, while the performance of the Device Under Test (DUT) is assessed. In source-pull the same concept is applied but varying the source impedance and therefore, synthesizing different source reflection coefficients presented to the device [21]. In this way, the DUT can be characterized at different operating conditions (frequency, input power or load conditions). The source-pull setup is shown in Figure 4.5.1.

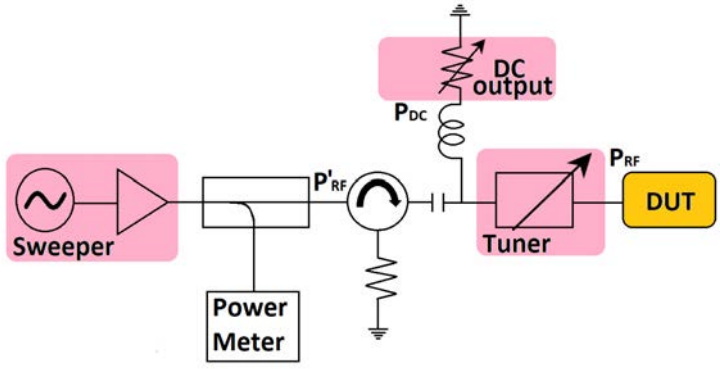

Figure 4.5.1: Source-pull setup.

It is possible to quantify the RF impedance that should be presented to the DUT (for the source and/or the load) to maximize or produce an specific output (output DC power, Power Added Efficiency (PAE)). This is done through the Smith Chart by plotting constant frequency and constant power plots. Source or load impedance tuners are swept at different frequencies, power levels and loads, measuring the output response of the system. The contours over the Smith Chart are not usually circular, different shapes can appear, specially if the device is close to oscillation.

Source and load-pull systems appeared in the 1970s although such an improvement has been done today as it is possible to quickly characterize microwave devices through simulations. Indeed CAD tools such as AWR provide load and source-pull simulations, reducing complexity when designing amplifiers.

In conclusion, the objective of using source or load-pull is to find the proper values for the reflection coefficients Γ_S and Γ_L that must be presented to a DUT, using constant frequency and constant power plots in the Smith Chart. For linear cases it has a very simple solution. For maximum RF power transfer, in a general case the matching network has to be designed to fulfill that $\Gamma_L{=}\Gamma^*_{OUT}$ and $\Gamma_S{=}\Gamma^*_{IN}$. Nevertheless, for non-linear

systems the solution is significantly different. It is an iterative process, varying the reflection coefficient (source and/or load) at each frequency and power level, until an optimum loading condition is found, generating non-uniform circles. In this way, the output DC power is maximized and therefore the RF to DC conversion efficiency.

Next section shows a rectenna integration over 50 Ω, while Chapter 5 presents a wearable rectenna array using the source-pull technique.

4.6. Rectenna measurements

Rectenna measurements over a broadband design have been performed to conclude with the multiple-tone characterization of the diode. An antipodal bow-tie antenna has been chosen as a possible alternative. As already explained, an omnidirectional antenna is desired for energy harvesting applications, and its impedance variation along the bandwidth is smooth, which ease the design. Moreover, the testing process is performed using a linearly polarized horn antenna, so a bow-tie topology is a good candidate for the rectenna measurements. A matching network is used for the integration, while next chapter deals with the source-pull, to see that both techniques can be used to design a rectenna.

The antenna has been fabricated over a FR4 substrate (ϵ=4.5 and $\tan\delta$=0.025), for working from 0.5 to 4 GHz. Its dimmsions are 18×16 cm. The rectifiers from the previous chapters are used at two different frequency subset of four tones to cover different bands.

In Figure 4.6.1, the bow-tie layout and the input reflecion coefficient (simulation and measurement) are shown, getting a good agreement. The 2-D radiation patterns (realized gain) are shown for phi=0 ° and phi=90 ° (E-plane and H-plane) in Figure 4.6.2. The metallic holder (used for the measurement process in the anechoic chamber) behind the antenna and the SMA connector were included in the simulation for an accurate characterization. The radiation pattern is distorted due to the ground plane effect of the metallic holder, especially in the back radiation, when the antenna is rotated in the RF anechoic chamber, hindering the line of sight.

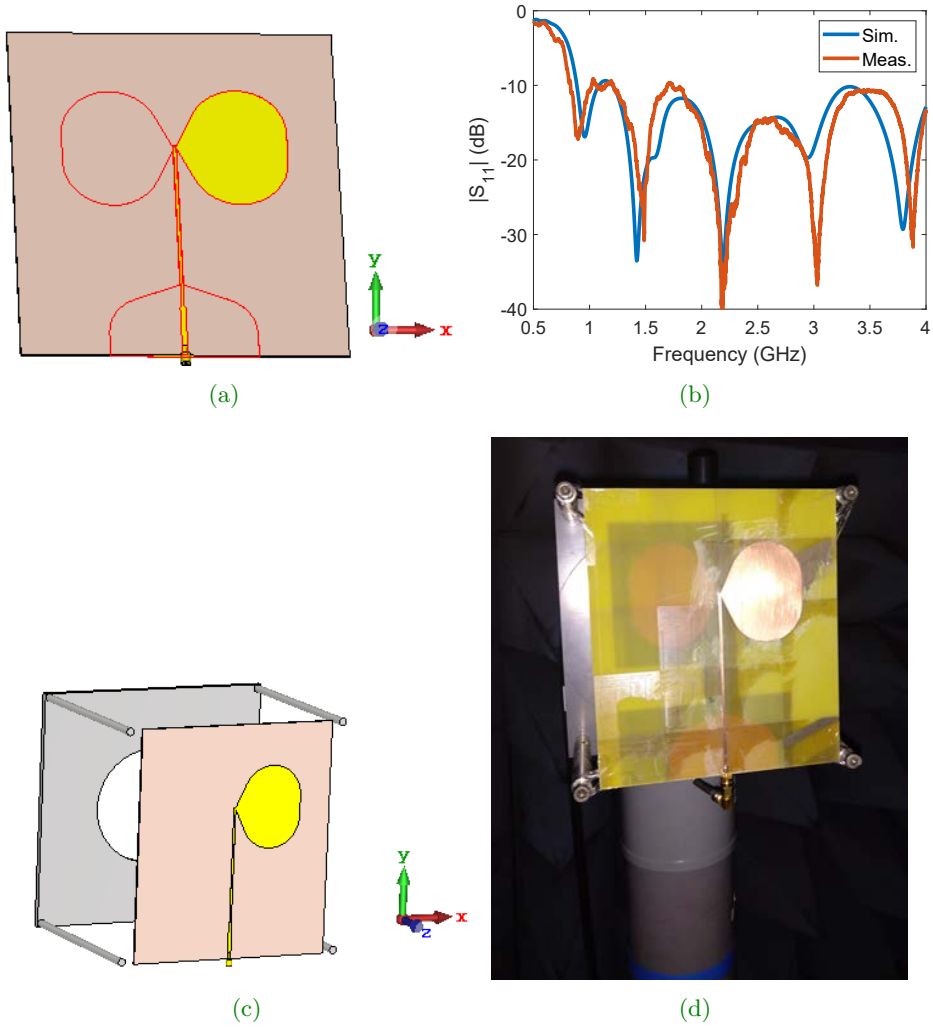

Figure 4.6.1: Bow-tie antenna prototype. a) Antenna layout. b) Input reflection coefficient. c) Antenna layout, including the metallic holder and SMA connector. d) Measured prototype in RF the anechoic chamber.

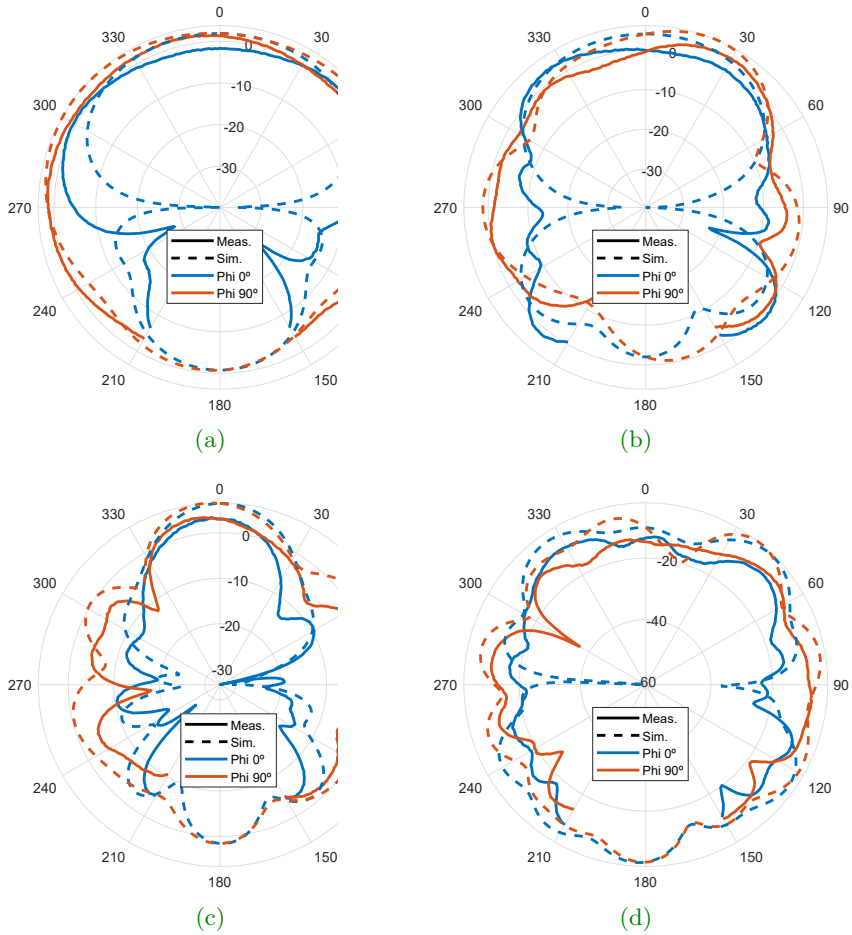

Figure 4.6.2: Realized gain patterns for the bow-tie antenna prototype. a) 0.9 GHz. b)1.85 GHz. c) 2.45 GHz. d) 3.25 GHz.

4.6.1. Indoor measurements inside the RF anechoic chamber

Indoor multiple-tone measurements inside the RF anechoic chamber were carried out. Two different frequency subset of four-tone excitation were used, getting 14 (Table 4.5) and 21 mV (Table 4.6) over a 3.9 kΩ load, this is, -43 and -39.5 dBm of DC power. Each transmitter delivered 3 dBm, although a power amplifier was included. The rectenna was placed at 3 m, aligned and in perfect line of sight with the transmitted horn antenna. The data for each measurement is shown, including the received RF power for each tone at the rectenna. A comparison with a single tone is not interesting in this case due to the power limitation from the sources. In that case, with just one tone is impossible to even turn on the diode, but with the multiple-tone approach a small amount of DC power is achieved.

$P_{TX}(dBm)$	$V_{DC}(mV)$	Tone 1 1.85 GHz	Tone 2 2.10 GHz	Tone 3 2.25 GHz	Tone 4 3.25 GHz
3	14	-29.17	-33.52	-30.88	-51.59

Table 4.5: Received RF power inside the anechoic chamber using a four-tone excitation (1/2).

$P_{TX}(dBm)$	$V_{DC}(mV)$	Tone 1 2.15 GHz	Tone 2 2.20 GHz	Tone 3 2.25 GHz	Tone 4 2.30 GHz
3	21	-32.97	-31.97	-29.87	-29.53

Table 4.6: Received RF power inside the anechoic chamber using a four-tone excitation (2/2).

4.6.2. Outdoor measurements: ambient spectrum

To conclude, outdoor measurements were carried out, harvesting the ambient spectrum from the window of a third floor in Leganés. A maximum of 20 mV were obtained, although some photos were taken at different DC output power (see Figure 4.6.3). The ambient energy is variable, so the DC voltage varies. The maximum value corresponds to -40 dBm of DC power, which is approximately the same value obtained in the indoor measurements. These results belong to an individual broadband rectenna. Taking into account the effective area, the power density and the number of elements, this value can be enlarge to power a low duty cycle sensor.

4.7. Conclusions

This chapter is focused on the wireless reception unit. The integration of the antenna and the rectifier is studied, explaining two different alternatives, a common 50 Ω design and using the source-pull technique. Also, the antenna topology is analyzed, explaining the different alternatives that are constrained to the application: energy harvesting design and WPT beaming scenario. Indoor and outdoor multiple-tone measurements have been carried out using a single rectenna element. A bow-tie antenna has been chosen as the antenna prototype due to its good characteristics for an energy harvesting scenario (broadband and omnidirectional). With this antenna and the rectifiers designed in previous chapters, a maximum of 20 mV (-40 dBm) were scavenged from the ambient spectrum. Future steps will include working with a dual linear polarized antenna to scavenge energy from both polarizations, and adding a DC-DC boost converter to produce a steady DC output. Different number of elements can be included to increase the rectified DC power. Indeed, in Chapter 5 some of above aspects are shown. Also, different studies can be performed comparing multiband and broadband designs, and its integration with the rectifier and efficiencies.

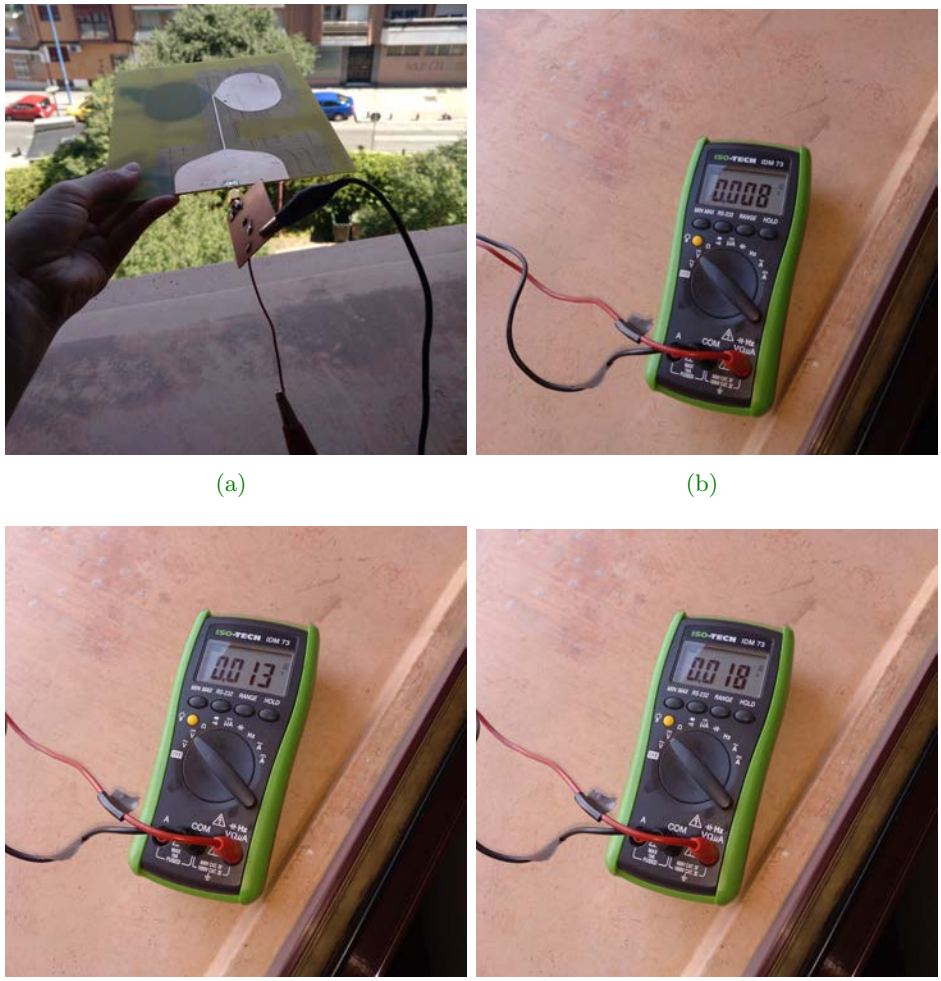

(a) (b)

(c) (d)

Figure 4.6.3: Measured DC output voltage (mV) from the ambient spectrum in Leganés.

References

[1] H. Takhedmit, "Ambient RF power harvesting: Application to remote supply of a batteryless temperature sensor," 2016 IEEE International Smart Cities Conference (ISC2), Trento, 2016, pp. 1-4. doi: 10.1109/ISC2.2016.7580800

[2] Z. Mihajlovic, A. Joza, V. Milosavljevic, V. Rajs and M. Zivanov, "Energy harvesting wireless sensor node for monitoring of surface water," 2015 21st International Conference on Automation and Computing (ICAC), Glasgow, 2015, pp. 1-6. doi: 10.1109/IConAC.2015.7313997

[3] J. Estrada, P. Zurek and Z. Popović, "Harvesting of aircraft radar altimeter sidelobes for low-power sensors," 2018 International Applied Computational Electromagnetics Society Symposium (ACES), Denver, CO, 2018, pp. 1-2. doi: 10.23919/ROPACES.2018.8364265

[4] C. Song et al., "A Novel Quartz Clock With Integrated Wireless Energy Harvesting and Sensing Functions," in IEEE Transactions on Industrial Electronics, vol. 66, no. 5, pp. 4042-4053, May 2019. doi: 10.1109/TIE.2018.2844848

[5] E. Falkenstein, M. Roberg and Z. Popovic, "Low-power wireless power delivery," IEEE Trans. Microwave Theory Techn., vol. 60, no. 7, pp. 2277–2286, July 2012.

[6] Datasheet LTC-3107
https://www.analog.com/media/en/technical-documentation/data-sheets/3107f.pdf

[7] Z. Popović, E. A. Falkenstein, D. Costinett and R. Zane, "Low-Power Far-Field Wireless Powering for Wireless Sensors," in Proceedings of the IEEE, vol. 101, no. 6, pp. 1397-1409, June 2013. doi: 10.1109/JPROC.2013.2244053

[8] T. Furuta, M. Ito, N. Nambo, K. Itoh, K. Noguchi and J. Ida, "The 500MHz band low power rectenna for DTV in the Tokyo area," 2016 IEEE Wireless Power Transfer Conference (WPTC), Aveiro, 2016, pp. 1-3. doi: 10.1109/WPT.2016.7498819

[9] D. Costinett, E. Falkenstein, R. Zane and Z. Popovic, "RF-powered variable duty cycle wireless sensor," The 40th European Microwave Conference, Paris, 2010, pp. 41-44. doi: 10.23919/EUMC.2010.5616367

[10] Z. Popović, E. A. Falkenstein, D. Costinett and R. Zane, "Low-Power Far-Field Wireless Powering for Wireless Sensors," in Proceedings of the IEEE, vol. 101, no. 6, pp. 1397-1409, June 2013.

[11] U. Olgun, C. Chen and J. L. Volakis, "Investigation of Rectenna Array Configurations for Enhanced RF Power Harvesting," in IEEE Antennas and Wireless Propagation Letters, vol. 10, pp. 262-265, 2011. doi: 10.1109/LAWP.2011.2136371

[12] Z. Popović et al., "Scalable RF Energy Harvesting," in IEEE Transactions on Microwave Theory and Techniques, vol. 62, no. 4, pp. 1046-1056, April 2014. doi: 10.1109/TMTT.2014.2300840

[13] J. A. Hagerty, F. B. Helmbrecht, W. H. McCalpin, R. Zane and Z. B. Popovic, "Recycling ambient microwave energy with broad-band rectenna arrays," in IEEE Transactions on Microwave Theory and Techniques, vol. 52, no. 3, pp. 1014-1024, March 2004. doi: 10.1109/TMTT.2004.823585

[14] S. Keyrouz, H. J. Visser and A. G. Tijhuis, "Multi-band simultaneous radio frequency energy harvesting,"7th European Conference on Antennas and Propagation (EuCAP), Gothenburg, 2013 pp.3058-3061.

[15] Young-Ho Suh and Kai Chang, "A high-efficiency dual-frequency rectenna for 2.45- and 5.8-GHz wireless power transmission," in IEEE Transactions on Microwave Theory and Techniques, vol. 50, no. 7, pp. 1784-1789, July 2002. doi: 10.1109/TMTT.2002.800430

[16] Kuhn, V., Seguin, F., Lahuec, C., and Person, C. (2016). Enhancing RF-to-DC conversion efficiency of wideband RF energy harvesters using multi-tone optimization technique. International Journal of Microwave and Wireless Technologies, 8(2), 143-153. doi:10.1017/S1759078714001457

[17] Antenna factor definition by Com-Power Corporation. https://www.com-power.com/uploads/technote/AN-106%20Antenna%20Factor.pdf

[18] V. Kuhn, C. Lahuec, F. Seguin and C. Person, "A Multi-Band Stacked RF Energy Harvester With RF-to-DC Efficiency Up to 84%," in IEEE Transactions on Microwave Theory and Techniques, vol. 63, no. 5, pp. 1768-1778, May 2015. doi: 10.1109/TMTT.2015.2416233

[19] D. Masotti, A. Costanzo, M. D. Prete, and V. Rizzoli, "Genetic-based design of a tetra-band high-efficiency radio-frequency energy system," Microw. Antennas Propag., vol. 7, no. 15, pp. 1254–1263, Jun. 2013.

[20] C. Song, Y. Huang, J. Zhou, J. Zhang, S. Yuan and P. Carter, "A High-Efficiency Broadband Rectenna for Ambient Wireless Energy Harvesting," in IEEE Transactions on Antennas and Propagation, vol. 63, no. 8, pp. 3486-3495, Aug. 2015, doi: 10.1109/TAP.2015.2431719.

[21] Teppati, V., Ferrero, A., and Sayed, M. (Eds.). (2013). Modern RF and Microwave Measurement Techniques (The Cambridge RF and Microwave Engineering Series). Cambridge: Cambridge University Press. doi:10.1017/CBO9781139567626

5

A wearable rectenna array over a cotton T-shirt

This chapter shows a wearable design for energy harvesting, focused on a broadband self-complementary tightly coupled bow-tie rectenna array. The antenna is screen printed on a cotton T-shirt, for scavenging power densities from 4 to 130 μW/cm^2 between 2 to 5 GHz. The cotton fabric is placed on top of a specific tissue layer stack-up, for a body phantom and a human torso. Full-wave simulations in CST are carried out to check the performance variations when non-standard tissue thicknesses are involved in the human torso, e.g., overweight people, or taking into account different bending conditions. Zero bias Schottky diodes (SMS7630-079LF) are attached across the feed points for different rectenna array sizes (4×4 and 9×9), where their impedance variation (over frequency and input power) is analyzed using source-pull harmonic-balance simulations. Rectenna measurements show up to 20 μW of DC power for incident power densities of 4 μW/cm^2 at 2.2 GHz over a water-filled phantom, with a DC load of R_{DC} = 2 kΩ. For higher incident power density levels of 72 μW/cm^2, up to 62 % efficiency is measured at 2.2 GHz.

5.1. Introduction

Rectennas for ambient RF energy harvesting have been of interest for powering energy-efficient devices and low duty-cycle sensors for several decades [1]. The average values of power density available range from 12 nW/cm^2 for 3G (WCDMA) to 84 nW/cm^2 for GSM 1800, as it was experimentally demonstrated in an urban outdoor spectrum characterization in 2012 [2], around London underground stations. Nevertheless, in July 2019, spectrum measurements were carried out at University Charles III of Madrid (see Chapter 4), from 0.5 to 5 GHz recording measurements every 30 seconds for 3 hours at different scenarios during two weeks, showing much lower power densities.

The conclusion drawn is that ambient power densities vary significantly and it is fundamental to integrate a rectenna with a power management circuit to increase the output voltage, and stabilize the signal, to be able to power a low duty-cycle sensor with the highest possible efficiency [3]. This is a difficult task because a diode rectifier is a non-linear element with a variable input impedance [1], [4]. In [5], high efficiencies were presented while adapting the Integrated Circuit (IC) to this variable load.

With the aim of improving the RF to DC power conversion efficiency, different rectenna designs were studied such as using low mass substrate (2-gram design on a flexible substrate [6]), unconventional reflector topologies [7] or dual-polarized rectenna topologies such the one presented in [8] where a 2 GHz narrow band rectenna was designed or in [1] where a 2-18 GHz bandwidth broadband spiral array was integrated with a rectifier, presenting difficulties in the design.

For wearable applications, the antenna design has evolved rapidly adapting to the demands and needs to cover. Existing and new applications are being incorporated on and on into the wearable world. Textile clothes are being used as substrates to lower costs and reduce the size, increasing the functionalities available until this moment. In this way, low power sensors can be powered through wearable antennas attached to our clothing (or even to complements). For example, an implantable antenna (284 to 825 MHz) on a wireless capsule endoscopy [9] was designed for body telemetry. In [10] an eyewear frame was designed on a 3D printer with two antennas at 2.4 GHz, strategically located. The eyewear communicates with the laptop on the front, in the side direction with a fixed hotspot access point, and downwards with a smartphone inside the user's pocket.

The characterization of different textile materials for wearable antennas was described in [11], and in [12], a review of different techniques to integrate the antenna on clothing was accomplished (e.g., using copper coated fabric, screen print or conducting nylon), where challenges associated with soldering electronic devices to conductive textile patterns were highlighted.

Different antenna topologies were studied. For example, in [13], a silver fabric patch antenna with detachable radiating elements was designed, where different geometric configurations were available varying the polarization and resonance frequency moving/replacing snap-on buttons. For example, interchangeable left-hand and right-hand circular polarization could be obtained just hanging out the radiating element with a diagonal slot. These prototypes were tested over a torso and phantom, taking into account bending conditions.

Jeans textile was used as a substrate for a dual-band [14] and for a circularly-polarized slotted patch antenna [15]. When the antenna was folded, it experienced a frequency shift from 2.44 to 2.9 GHz, degrading the return losses. The axial ratio became worse, as the slots were affected by the curvature. The beamwidth got smaller and the directivity decreased a bit. Therefore, bending effects are important and can be a problem depending on the application. The polarization purity (circularly-polarized) was degraded, as under low curvature radiuses the antenna became linearly-polarized.

Wearable antennas are designed to be worn on different parts of the body: back, chest, head, wrist or even feet. A dual-band indoor/outdoor global positioning system (GPS) antenna attached to a military beret was presented in [16]. The antenna was fabricated on a conductive metalized nylon fabric over a felt substrate. The human head and bending effects were studied as the antenna is folded on the beret. In [17], an antenna was integrated into an insole for on body telemetry, which seems very practical. A flexible 2.45 GHz wireless power harvesting wristband was presented in [18], where a low sensitivity was obtained. Energy could be harvested from -24.3 dBm RF input, although a maximum conversion efficiency of 28.7 % was obtained at -7 dBm. A dual band version using a 2×2 MIMO antenna for 5G was shown in [19], where the antennas were placed on the top and bottom sides of the watch. This idea gives a good fit for smart watches. Over the torso, a UHF RFID tag [20] attached to a T-shirt was designed using silver ink and a conductive thread. The tag and the IC were coated with an encapsulant. The performance of the tag was tested under different conditions (washing drying cycled, over human body).

The integration of the antenna and rectifier and its placement on the clothing and human body is a major design challenge. Human electrical characteristics degrade the antenna performance. Therefore, placing it on the outermost layer of clothing can be beneficial to reduce the coupling between the antenna and the human body. It is also possible to mitigate this problem by introducing a ground plane between the antenna and the body as in a microstrip patch, which can reduce the effect of the body. However, some designs can become impractical with a ground plane and these antennas are narrowband, [21], limiting the application usefulness. Single band and broadband antennas offer different possibilities depending on the application. The broadband arrays described in this chapter are therefore designed without a ground plane. The broadband characteristic makes them more robust against the detuning produced by the tissues influence, but the integration with the rectifier is complex. Most wearable rectenna designs for on body clothing are based on narrow band antennas [21]- [24], although a few examples operate with broadband designs [26]-[28].

For example, an UHF patch rectenna [22] was designed on a bi-layer substrate made of pile and jeans with a maximum efficiency of 50 % at 876MHz and 14 μW/cm^2. SMS285X diode with a resistive load of 1 kΩ was used.

A dual-band wearable patch rectenna over jeans substrate [23],using copper tap as a radiating element, was designed at 2.45 GHz and 5.8 GHz, getting a 20 % of efficiency at -15 dBm at both frequencies and a maximum efficiency of 60 % at -3 dBm at 5.8 GHz and 0 dBm at 2.45 GHz. Another design [24] at 4.65 GHz was tested in flat and bent positions, over the same substrate, getting a power conversion efficiency of 43 % (bent position) and 55 % (flat position) at 5 dBm.

In [25] a wearable triple-band ring-shaped patch antenna was designed to scavenge ambient energy at GSM 900, GSM 1800 and WiFi. The antenna choice gives circular polarization and reduced dimensions, important for these applications. A multilayered design with a ground plane was studied to be placed in a jacket. Transmitted power was varied from 10 to 20 dBm at 30 cm, getting from -10 to 3 dBm DC power at 900 MHz and from -13 to -1 dBm at 2450 MHz.

Nevertheless, a few examples operate with broadband designs. In [26] a 0.9 to 4 GHz circularly-polarized archimedean spiral antenna was designed using a 6-stage voltage doubler. Two different substrates were tested, felt and fleece, comparing when the antenna is folded or rolled. An HSMS2820 diode was used and a balun was employed to integrate the balanced antenna and the unbalanced rectifier. A maximum DC voltage value of 1.5 V and 0.5V was got for outdoor and indoor scenarios, where the overall efficiency was 30 %, using a power boost regulator.

In this chapter, simulations and measurements are presented for a wearable and broadband screen-printed rectenna array on a cotton T-shirt. Previous works were reported in [27] and [28], although unpublished simulations and measurements are shown here for completeness.

5.2. Wearable rectenna design

5.2.1. Simulations

A broadband 2 to 5 GHz wearable rectenna array screen printed on a cotton T-shirt (see Figure 5.2.1) has been designed and measured for harvesting a wide range of incident power densities.

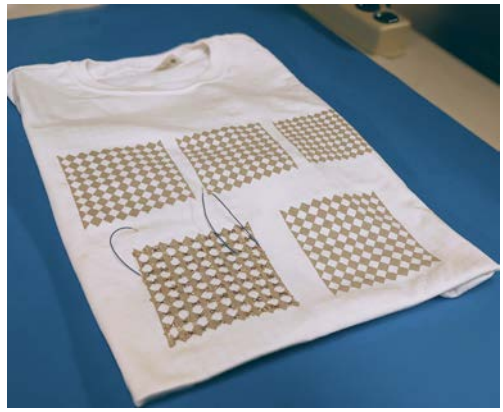

Figure 5.2.1: Photo of RF harvesting T-shirt with 81-element rectenna array. Courtesy of José Estrada.

A self-complementary tightly-coupled bow-tie array similar to the non-wearable design in [29] was chosen as the element due to its broadband characteristics and high impedance. The period of the array is 1.25 cm, which is approximately $\lambda_0/6$ at the highest frequency considered in the measurements. Zero bias Schottky diodes SMS7630 (package SC-79) were attached across the feed points (horizontal plane) using silver paint and solder and different rectenna array sizes have been studied (4×4 and 9×9). This wearable design is inexpensive, with an estimated low-quantity price of 70 \$. The special screen printing costs 20 \$ approximately and the conductive ink costs 50 \$. This means that the wearable antenna can be an option to power wearable sensors and be integrated into different applications.

The rectenna array is analyzed over a saltwater solution, which acts as a human body phantom, and over a real human torso. A variable air-gap between the T-shirt and body (or phantom) is also taken into account for realistic simulations. Some important facts when working with human tissues are coupling and detuning. Human electrical characteristics affect the antenna performance. Therefore, placing it on the outermost layer of clothing can be beneficial. Moreover, the air layer also reduces the coupling influence of the substrate (body or phantom) with the antenna, improving its performance. In order to design the rectenna, both diode and antenna simulations are performed.

The diode exhibits a non-linear performance, which must be taken into account across the entire bandwidth for the integration. Thus, the diode characterization is realized in NI/AWR through source-pull and harmonic balance simulations. The source-pull method is important for non-linear devices where the operating point may change with power level, frequency and loading conditions, as it happens with a diode. It is used to find the source reflection coefficient at different frequencies, input power levels and DC loads, that results in a specific DC output power. Source-pull simulations are performed from 2 to 5 GHz over a diode connected to a 2 kΩ load. This load value was obtained from previous studies [28]. Once the source-pull contours are plotted over the Smith chart, it is possible to design the antenna.

Full-wave simulations for the antenna have been performed in CST considering the diode complex impedance at each feed point, using lumped elements, loading all the array elements except one in the center, which acts as the driven port. For a good characterization, the electrical characteristics and thicknesses for specific tissue layers such as muscle, fat and skin for the torso, and a saltwater solution for the water-filled phantom, are taken into account. Different rectenna array sizes are analyzed when the antenna is screen printed over a cotton T-shirt.

The work shown in this chapter is summarized in the following points:
Source-pull simulations:
The diode impedance as a function of DC load, power level, and frequency is analyzed using source-pull harmonic-balance simulations in AWR, to integrate antenna and rectifier.

Single antenna element:
A single antenna element is simulated and the results are shown as follows:

1. Comparison of the input impedance of a single element and different finite arrays (9×9 and 20×20) when all elements are loaded with the diode complex impedance from 2 to 5 GHz over the human torso (H=2 mm). 2-D directivity patterns for the copolar component for phi=0° and phi=90° at 3.5 GHz.

2. Input impedance, over a water-filled phantom and human torso from 2 to 5 GHz, varying the air-gap (between the T-shirt and the body) from H=0 to 2 mm for the single antenna element. 2-D directivity patterns for the copolar component for phi=0° and phi=90° at 2, 3.5 and 5 GHz.

Rectenna array design:
Two array sizes are compared (4×4 and 9×9) to investigate limitations of array size. The antenna arrays are analyzed in the following cases:

1. Comparison of the input impedance and radiation patterns for a 4×4 and 9×9 rectenna array (with all elements loaded with the diode complex impedance, using a driven port at the center of the array) over the human body phantom and the real torso, from 2 to 5 GHz, varying the air-gap from 0 to 2 mm.

2. Different muscle, fat and skin thicknesses are used in order to analyze the antenna performance for the 9×9 rectenna array, to check the variation under different body compositions (overweight people, athletes with fibrous tissues or thin people). Bending conditions are included to see the performance under different circumstances.

5.2.2. Measurements

Measurements of DC output power versus frequency, and RF to DC power conversion efficiency versus different power density values, ranging from 4 to 130 μW/cm^2, are shown for vertical and horizontal polarization, due to the array design. A comparison is established for different rectenna array sizes (4×4 and 9 ×9). Measurements are performed over free space, the water-filled phantom and the human body, in an anechoic chamber.

5.3. Source-pull simulations in AWR

Source-pull simulations are performed in AWR [30] to know in which region of the Smith Chart the antenna should be designed. Simulations are carried out from 2 to 5 GHz over the diode (zero bias Schottky SMS7630) connected to a 2 kΩ load and different input power levels. The source-pull contours show, with step increments, the amount of DC power that can be rectified, and the impedance that the antenna must present to get that specific DC power value for a fixed value of frequency and input power. Different contours can be obtained varying these parameters (see Figure 5.3.1).

At 2.9 GHz and 100 μW RF power (see Figure 5.3.1 (a)), a maximum of 49.15 μW DC power can be extracted, at just one point. Lower powers can be achieved as long as we move away from the maximum. 10 μW step contours of DC power are illustrated as an example, although smaller steps can be used. In Figure 5.3.1 (b) different contours are plotted when the frequency is varied to 2, 3.5 and 5 GHz at 100 μW RF power. Circles are moved following the arrow as long as the frequency is increased, in a counter-clock direction.

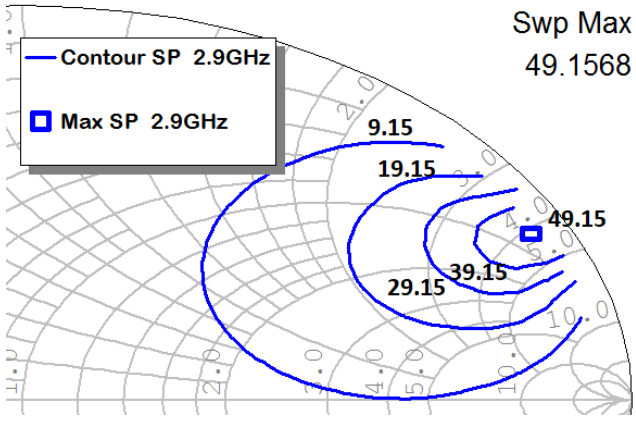

(a)

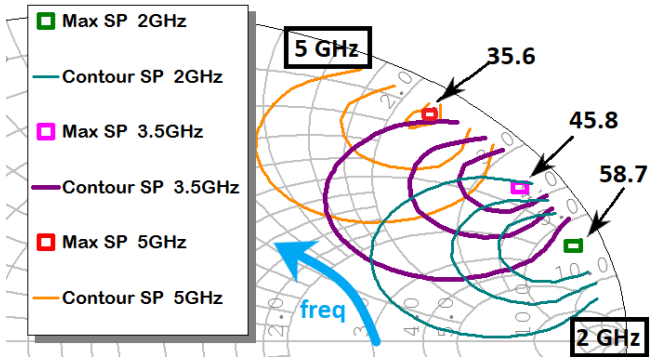

(b)

Figure 5.3.1: Simulated source-pull contours of constant rectified DC power with 10 μW steps at 100 μW input power and 2 kΩ load. a) At 2.9 GHz. b) At 2, 3.5 and 5 GHz.

5.4. Electrical characteristics of tissues and materials

The wearable rectenna over a cotton T-shirt is simulated in two different scenarios, a water-filled human phantom, and a standarized human torso.

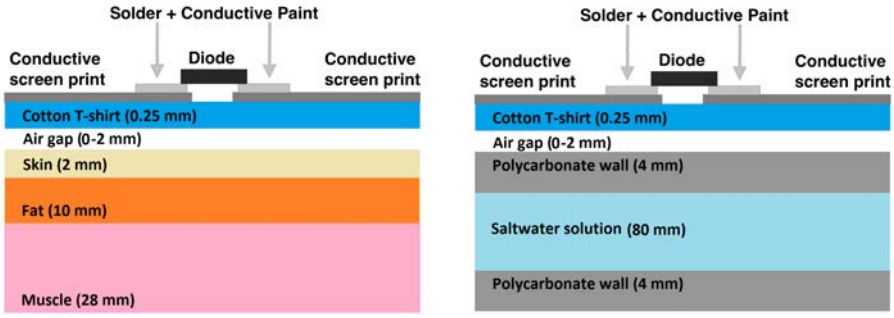

(a) (b)

Figure 5.4.1: Cross-section setup with rectenna on T-shirt. a) Placed over a torso. b) Placed over a body phantom made of saline solution in a polycarbonate container.

Complex permittivity values from [31] are used in the full-wave models implemented in CST, as a stack-up simulation with standarized thicknesses for each layer is performed (see Figure 5.4.1). In Table 5.1, electrical parameters and tissue thicknesses for the different layers are summarized [32]. To design the body phantom, human body electrical properties were averaged and synthesized with a saltwater solution [33], achieving a specific conductivity of 2 S/m. This solution was placed inside a plastic container. Two polycarbonate walls were included to model the container (see Figure 5.6.1 (b)).

Metallic ink (NovaCentrix Metalon HPS-FG57B) with a resistivity of 0.007 Ω/Sq was screen printed on the cotton T-shirt [34]. The diode suffered from problems when attaching to the conductive ink using solder or conductive epoxy. Nevertheless, silver paint with 0.01 Ω/sq showed better

Layer	Thickness (mm)	ϵ_r	tan δ
Cotton T-shirt	0.25	1.60	0.040
Torso skin	2	39.75	0.335
Torso fat	10	5.20	0.154
Torso muscle	28	54.50	0.270
Polycarbonate wall	4	2.90	0.010
Saltwater solution	80	74.00	0.154

Table 5.1: Tissues electrical parameters for the stack-up simulation model.

results in terms of repeatability and resistance due to the lower viscosity of the paint compared to epoxy. In Figure 5.4.2 a single element with a diode attached with solder and silver paint is presented, showing its dimensions.

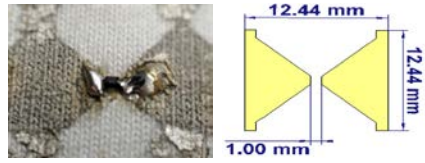

(a) (b)

Figure 5.4.2: Single element of the rectenna array. a) Attached with solder and silver paint. b) Dimensions of the simulated single bow-tie element.

5.5. Bow-tie rectenna array simulations

A single antenna element and different array sizes are analyzed over the human torso stack-up model (9×9 and 20×20). The input impedance and the radiation pattern (directivity) at the center frequency of the band are shown. Lumped elements with the diode complex impedance are added at each feed point. As long as the array size increases, the input impedance becomes higher and is focused in the right upper side of the Smith Chart,

in the same position where source-pull contours are plotted (Figure 5.5.1 (a)). This is due to the tight coupling between elements, which derives in a high impedance (close to the bow-tie impedance, 188 Ω) but over the torso as substrate. Nevertheless, the single element shows a capacitive impedance, consistent with that of a electrically small antenna. The phi=0° and phi=90° directivity cuts for different array sizes are shown at 3.5 GHz for the horizontal polarization (copolar), where the body is in the lower half-plane. As it can be seen, the shape is not affected although the back radiation towards the tissues is reduced when the array size is increased (see Figure 5.5.1 (b)). This is due to the fact that the substrate size becomes larger as long as the number of elements is increased.

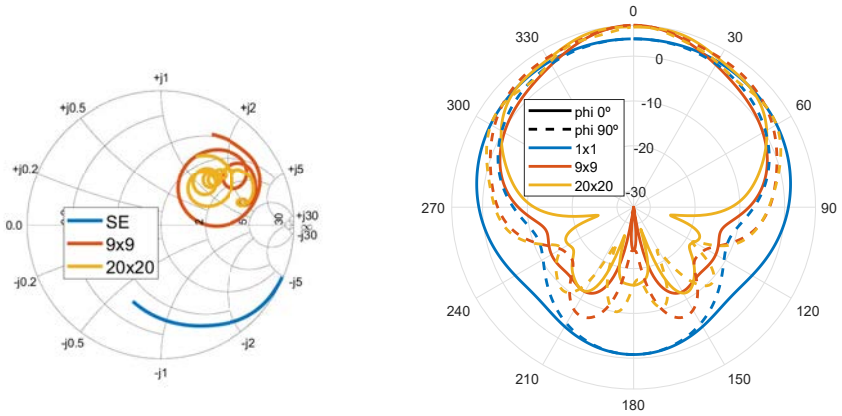

(a) (b)

Figure 5.5.1: Simulation of the antenna for different array sizes. Single element (1x1), 9x9 and 20x20. a) Input impedance from 2 to 5 GHz. b) Directivity patterns for different array sizes at 3.5 GHz at copolar component.

It is important to remind that in a common antenna array, the directivity increases (narrow beam) with the number of elements. Nevertheless, in this case a rectenna array is employed, which is different as a directive antenna is not desired (see Chapter 4). But with a rectenna array, the

rectified DC output power is increased, improving the performance. Also, the gain is improved a bit, but the beamwidth is not reduced.

Measurements are performed over a human phantom and a real torso, so the single antenna element is compared also in simulations when placed over them, showing similar impedance performance (capacitive), as a single element is electrically small. An air-gap is introduced between the T-shirt and the skin. This gap is real (it occurs in a realistic situation) as the T-shirt is not body tight. Indeed this fact improves the performance as it reduces the loading effect from the layered substrate especially with the body torso. In Figure 5.5.2 the input impedance of the antenna is plotted when the air-gap is varied from 0 to 2 mm.

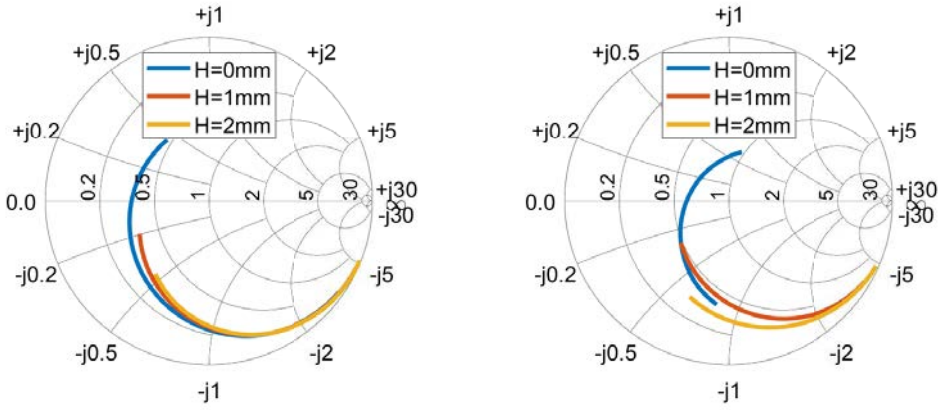

Figure 5.5.2: Simulated single element input impedance from 2 to 5 GHz. a) Over a phantom and b) over a human body.

In Figure 5.5.3 the radiation patterns (directivity) at 2, 3.5 and 5 GHz are plotted when H=2 mm, showing a slight variation on the shape versus frequency. For the phantom, the variation is lower as the substrate does not interact too much with the antenna due to the very high permittivity of the saltwater solution. The loading effects are small as the electric field lines are constrained to the upper part, above the stack-up model.

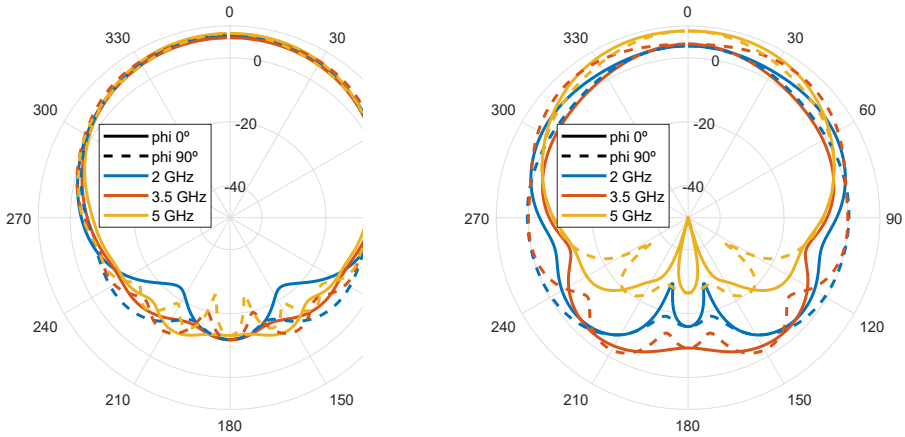

Figure 5.5.3: Simulated single element directivity pattern for the copolar component at 2, 3.5 and 5 GHz. a) Over a phantom and b) over a human body.

Nevertheless, the electrical characteristics of human tissues vary significantly over frequency when compared with the phantom, producing a significantly change. The back radiation is reduced as long as the electrical dimensions of the substrate is bigger but, as the body torso stack is composed of three different layers while the body phantom is homogeneous, a more noticeable change is experimented in the torso. This affects, as multiple reflections occur between the interfaces of the different media producing large changes in the diagrams in the back radiation, but not at boresight. In the human torso a higher gain is obtained at 5 GHz.

For a rectenna array implementation, diodes are placed over the T-shirt forming a 4×4 and 9×9 array. The 4×4 array is indeed an asymmetric subarray where the rest of the elements are open-ended forming a 9×9 square of elements. The reason for this is that fabrication was only carried out for the 9×9 square array, and testing with a small number of elements involves leaving elements in open circuit (see Figure 5.2.1). This subarray (highlighted in yellow lines) and the complete rectenna array of 9×9 elements are shown in Figure 5.5.4 (b), where diodes are placed in feeds along the direction referred to as horizontal, indicated by the $\vec{E}_H$ incident electric field vector. For the full-wave simulation in CST, the diode impedance is modeled at -20 dBm from 2 to 5 GHz as a series RLC network where R=0.1 Ω, L=0.423 nH, and C=0.27 pF, using a lumped element (see Figure 5.5.4 (a)).

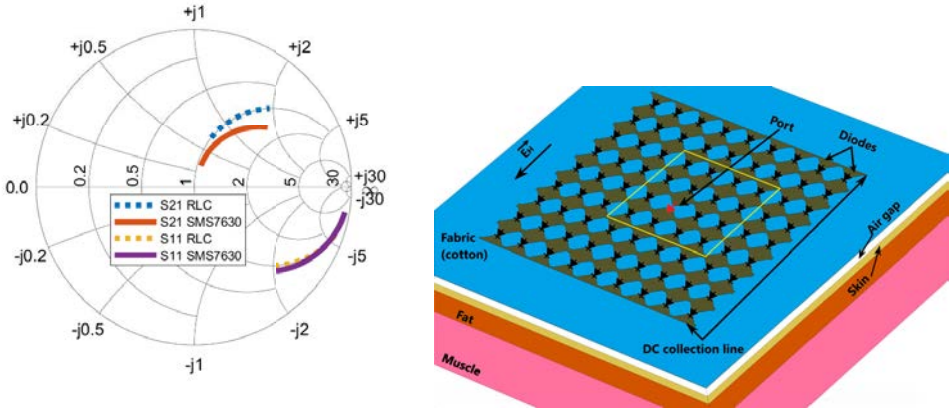

(a) (b)

Figure 5.5.4: a) Simulated S-parameters of the SMS-7630 diode and its corresponding RLC network. b) Torso stack-up prototype over a T-shirt with 81-element rectenna array.

The impedance for both array sizes over the phantom and the body torso are shown in Figure 5.5.5 when the air-gap is varied from 0 to 2 mm. The body torso produces higher loading effects than the phantom when no air-gap is introduced. The phantom shows a higher permitivity so the isolation is higher. When an air-gap is included, the performance is similar and, in the right upper side of the Smith Chart, close to the source-pull contours. As the body acts as a lossy substrate, the impedance variations are not very remarkable.

Radiation patterns (realized gain) are shown in Figure 5.5.6 at 3.5 GHz (center of the frequency band), showing variations of the air-gap between 0 to 2 mm. The 4×4 sub-array presents an asymmetry in the pattern that does not appear in the bigger array. This is because the sub-array is not symmetric. The driven port is not centered in a 4×4 squared design. Moreover, the rest of the elements are open ended since the complete antenna size is 9×9. Thus, an asymmetry in the pattern is not strange. Also, a null appears in the phi=0 ° plane for the 16-element design over the phantom at H=2 mm. It is probably due to the destructive reflections from all the layers. If the air-gap thickness is increased, the null may move to another angle. For the 9×9 design, the radiation pattern is not distorted as no asymmetries happen. The gain is increased when the air-gap is larger, as the influence of the body tissues is reduced.

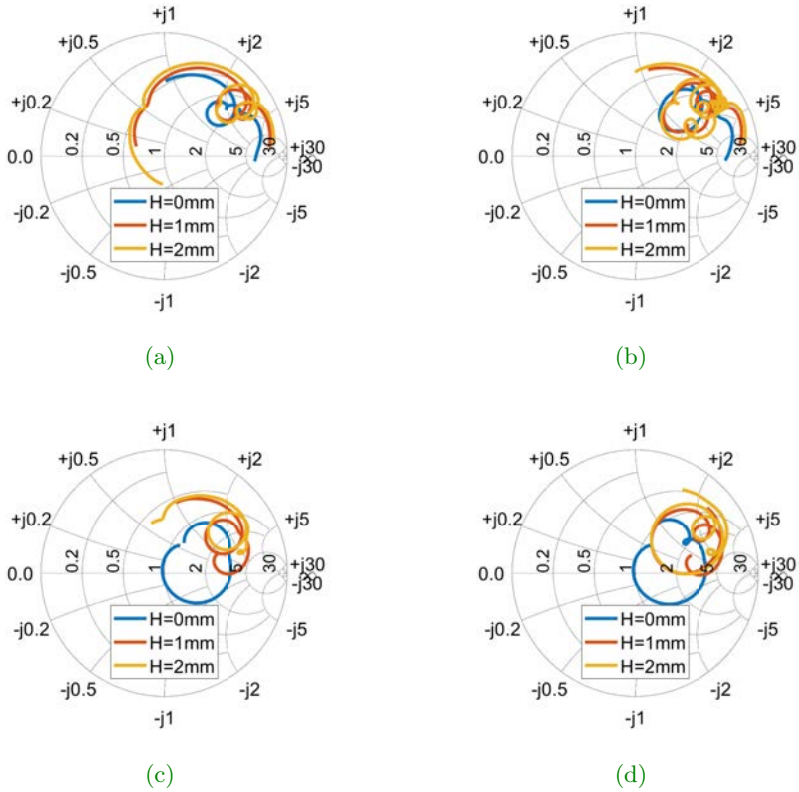

Figure 5.5.5: Simulated antenna input impedance from 2 to 5 GHz over the human phantom for a) 4×4 and b) 9×9 array. Over the human torso for c) 4×4 and d) 9×9 array.

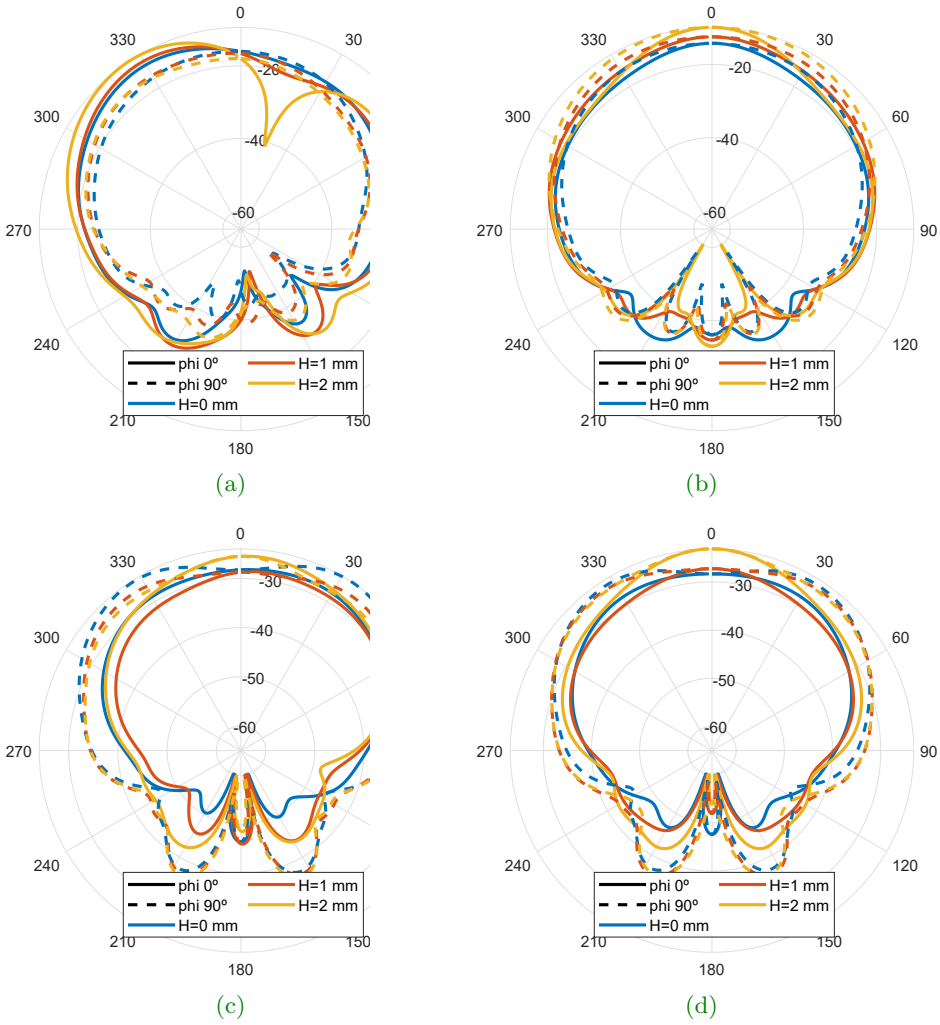

Figure 5.5.6: Simulated realized gain pattern for the copolar component over the human phantom for a) 4×4 and b) 9×9 array. Over a human torso for c) 4×4 and d) 9×9 array.

An important fact to study is the influence of the body composition. From an electromagnetic point of view, it is not the same to have a sustrate thickness of 10 cm than 2 cm as the effective permitivity will vary affecting to the radiation and the fields will be more constrained if the permitivity is high. The same happens with the body composition. Each human body has different characteristics imposed by the different composition (percentage of muscle versus fat). Also the skin varies from one part of the body to other and from one person to another. Therefore, the influence of each layer is studied. For the fat layer, simulations are carried out from 6 to 30 mm, showing a no significant difference in the input impedance (see Figure 5.5.7). Nevertheless, increasing the fat over muscle thickness is like moving an antenna away from a ground plane, so the gain will improve for some distances. This means that the wearable rectenna can be globally used because its performance will not be degraded due to possible anatomical differences between users.

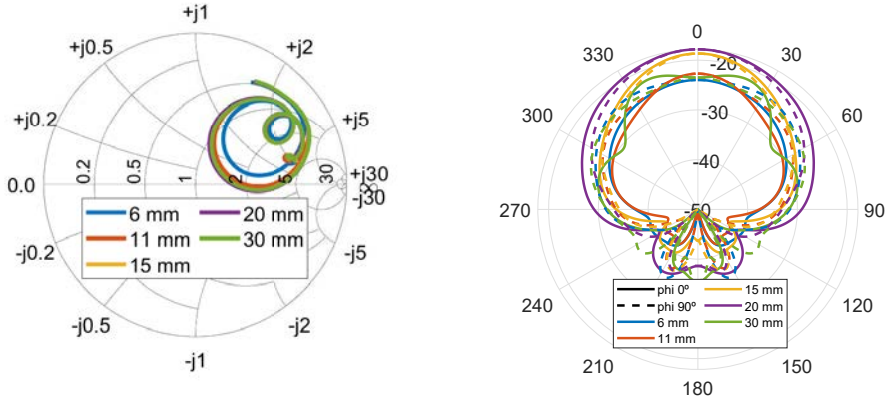

(a) (b)

Figure 5.5.7: Simulations of a 9×9 element antenna over a human torso under different fat thicknesses. a) Impedance and b) realized gain.

For variations in the thickness of the skin and muscle layers, the antenna input impedance for the 9×9 array is plotted in Figure 5.5.8 and Figure 5.5.9. It can be seen that no differences are appreciated in the antenna impedance, because the influence of the tissues is controlled by introducing a cotton layer (and air-gap) between the antenna and the body. Nevertheless, again the gain is improved when the skin thickness is increased. For the muscle, no significant variations are appreciated. This is the inner layer, so its variation does not influence the performance too much. This stack-up works as a multilayered media where an incident plane wave is reflected in each interface, producing a different reflection response when the characteristics of each media are varied. This means that the skin and the fat are the layers which more influence the performance.

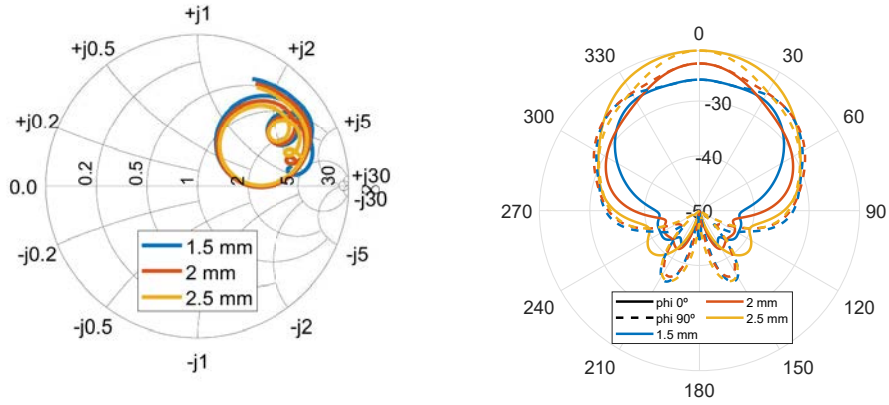

(a) (b)

Figure 5.5.8: Simulations of a 9×9 element antenna over a human torso under different skin thicknesses. a) Impedance and b) realized gain.

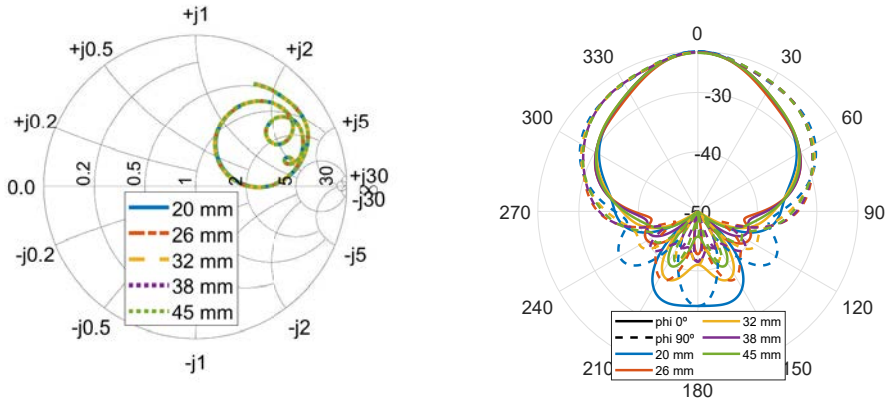

(a) (b)

Figure 5.5.9: Simulations of a 9×9 element antenna over a human torso under different muscle thicknesses. a) Impedance and b) realized gain.

To conclude, the effect of the curvature of the body torso is analyzed in this section. A simulation of the rectenna folded with different curvature angles is compared to a flat situation (see Figure 5.5.10). This has been simulated for the 9×9 array with 1 mm air-gap, when all elements except the driven port are loaded with the diode complex impedance. A cylindrical bend is performed orthogonal to the diodes orientation with a curvature angle of 30°, 60° and 90°. Just a slight difference can be noticed after bending the array, with a small reduction in the main lobe maximum. The back radiation is increased from the sides, as the curvature is more pronounced. The antenna input impedance and radiation pattern (realized gain) are shown for comparing all cases in Figure 5.5.11.

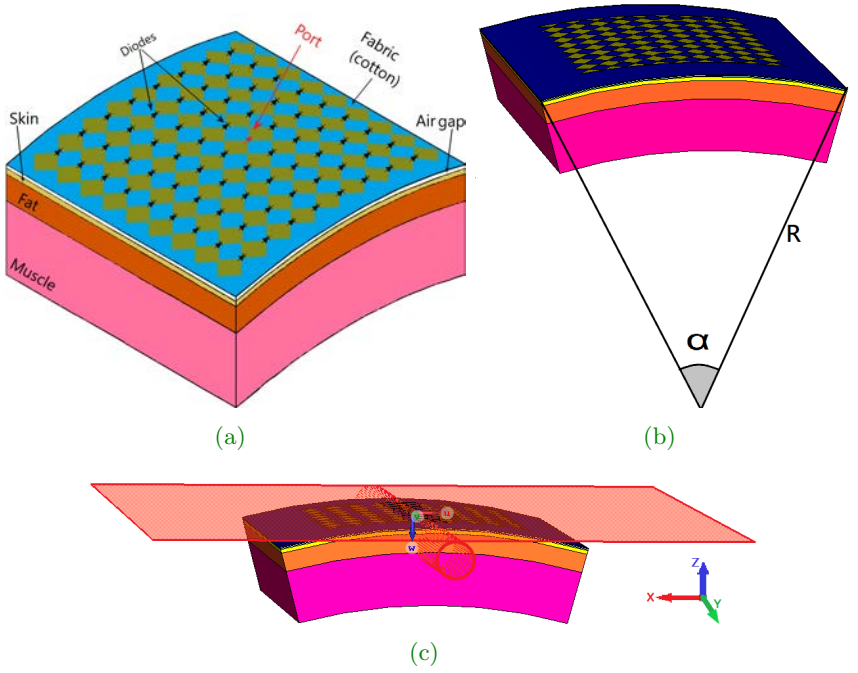

(a) (b)

(c)

Figure 5.5.10: Bent T-shirt with 81-element rectenna array where a) shows the complete scheme, b) the curvature angle and the radius and c) shows the cylindrical bend.

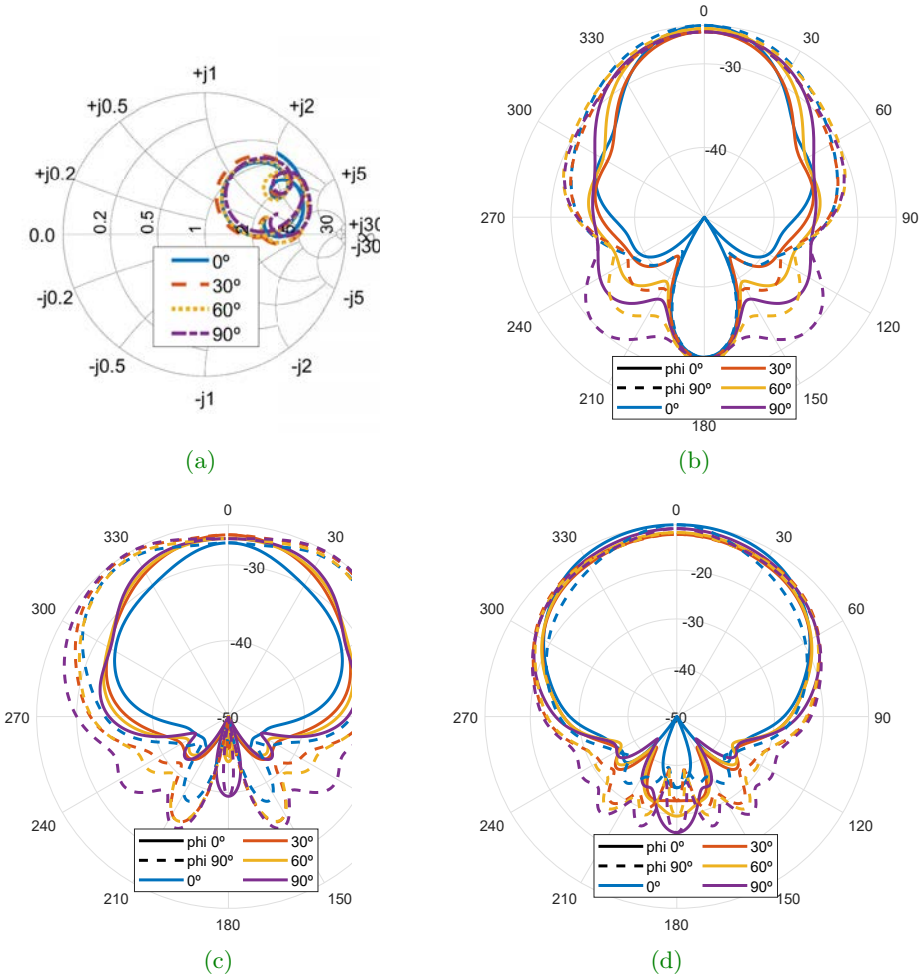

Figure 5.5.11: Folded T-shirt with 81-element rectenna array and different curvature angles (0 °, 30 °, 60 ° and 90 °). Antenna impedance. b) Realized gain at 2 GHz. c) At 3.5 GHz d) At 5 GHz.

5.6. Bow-tie rectenna array measurements

In Figure 5.6.1 a representation of the measurement setup is shown. Measurements are performed over free space, a body phantom and over a real torso and a comparison has been established. The wearable rectenna is placed inside an RF anechoic chamber, mounted on the phantom (or over the body). A load ($R_{LOAD} = 2\,k\Omega$) is attached to it to monitor the DC voltage.

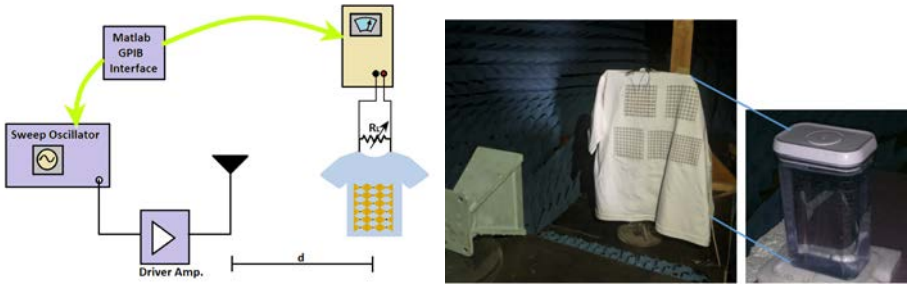

Figure 5.6.1: a) Measurement setup for the wearable rectenna over a cotton T-shirt, d = 69 cm. b) Photo of the wearable rectenna with the body phantom.

The incident power density on the T-shirt is controlled through a Matlab GPIB interface that controls a transmitter (with a power amplifier). A well-characterized transmitting antenna (a horn) is used taking into account the Friis line of sight equation. The distance is 69 cm, and the far-field is considered at $\frac{2D^2}{\lambda}$ =26 cm for the transmitting horn, where D is the maximum aperture of the antenna. Power density incident to the rectenna is varied from 4 to 130 μW/cm^2 while frequency is varied using a 100 MHz step from 2 to 5 GHz. DC power versus frequency is measured for both polarizations for the 4×4 and 9×9 arrays.

5.6.1. On-body phantom measurements

Over a 9× 9 elements antenna array, a 4×4 square subarray is populated with diodes and measured in free space and then over the human body phantom (see Figure 5.6.2). The rest of the elements are open ended.

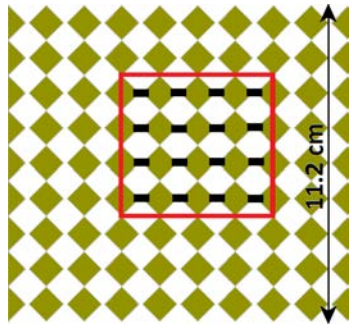

Figure 5.6.2: 4×4 subarray over the complete 9×9 antenna array.

Later, this subarray array is completely expanded, using the full array with 81 diodes. Measurements are done for both array sizes to compare their performance. In Figure 5.6.1, the measurement setup for the phantom in the RF anechoic chamber is shown. The T-shirt is placed covering the water saline solution container, and it is connected to the 2 kΩ load.

The incident power density at $d = 69$ cm is then varied from 4 μW/cm^2 to 130 μW/cm^2, while the frequency is swept from 2 to 5 GHz in 100 MHz steps.

Power conversion efficiency is defined as:

$$\eta = \frac{P_{DC}}{S(0°, 0°) \cdot A_g} \tag{5.6.1}$$

where $S(0°, 0°)$ is the power density and A_g is the geometric area of the antennas, which results in a conservative efficiency estimate [35]. Measurements for the DC power versus frequency are shown in Figure 5.6.3 for different power densities for the 4×4 and 9×9 arrays, at free space and over human phantom, for the horizontal and vertical polarization. As expected, horizontal polarization provides higher results as the diodes are placed in that direction. It is in agreement with the radiation pattern, comparing the copolar and crosspolar components. Due to the antenna design, it is also possible to scavenge power from the vertical component, although it is lower. This value can be increased if diodes are also placed in the vertical direction, increasing the conversion efficiency. When compared the rectified DC power, both array sizes provide nearly the same values and trends, although its geometric area is different. Therefore, the power conversion efficiency yields larger values for the smaller array because its geometric area is lower.

It is noticeable that the 4×4 array provides a better performance than the bigger array. This is due to the fairly large resistance of the conductive ink and silver paint employed in the design, which reduces the efficiency in larger arrays. As the array is bigger, losses increase, also with the frequency. In free space, the degradation in the performance is more significant than over the human phantom. The phantom does not affect the rectified power, indeed the performance is improved as the input impedance of the antenna is moved closer to the source-pull contours where maximum power can be achieved, while in free space is far from that region and therefore, the rectified DC power is lower, as it can be seen in Figure 5.6.4. This is as expected, as the wearable rectenna has been designed to be placed over a torso (or phantom). In conclusion, in this specific design it is better to work with five 4×4 rectenna arrays, as more power will be rectified, than with a 9×9 rectenna array.

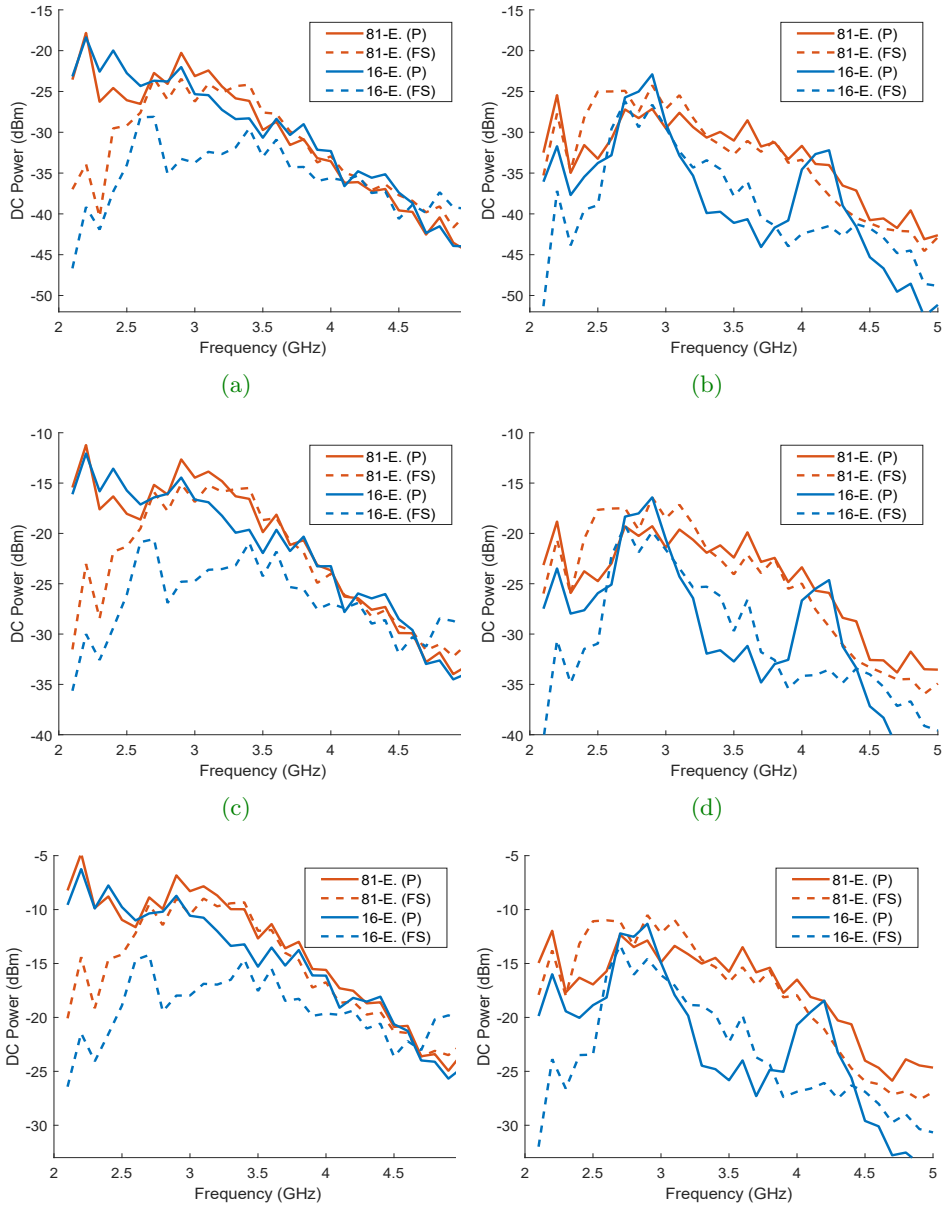

Figure 5.6.3: DC power versus frequency for 4×4 and 9×9 array in free space (FS) and phantom (P). Horizontal (left) and vertical (right) polarization. a, b) 4 μW/cm^2. c, d) 10 μW/cm^2. e, f) 25 μW/cm^2.

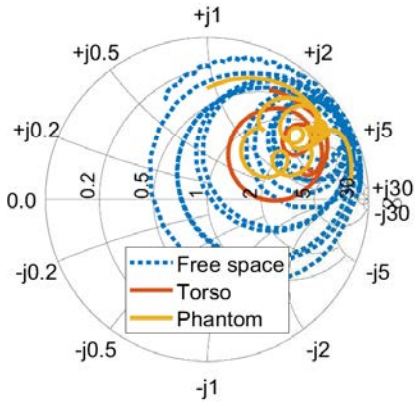

Figure 5.6.4: 9×9 antenna input impedance over free space, phantom and human torso.

RF to DC power conversion efficiency measurements for different power densities over the human phantom are shown in Figure 5.6.5 at 2.2 and 2.9 GHz, for the 4×4 and 9×9 designs at both polarizations. The highest efficiencies are obtained for 4×4 array. At the horizontal polarization the maximum is around 2.2 GHz, where a 62 % and 20 % of conversion efficiency is obtained at 72 μW/cm^2, for the 4×4 and 9×9. For the vertical polarization the maximum is shifted at 2.9 GHz, getting a 16 % and a 4 % of efficiency at 86 μW/cm^2. At lower power densities, 13 μW/cm^2, an efficiency of 25 % at 2.2 GHz is achieved for the horizontal polarization. For the vertical polarization the value is reduced to 11 % at 19 μW/cm^2 (2.9 GHz) for the smallest design. It corresponds to -5 and -3 dBm RF input power. In Figure 5.6.6, the plot is extended from 2 to 5 GHz, where is easier to appreciate the difference in the conversion efficiency between the 4×4 (a, b) and the 9×9 design (c, d). Also, between (a, c) and (b, d) it is possible to observe that the maximum is shifted from 2.2 GHz for the horizontal polarization to 2.9 GHz for the vertical polarization.

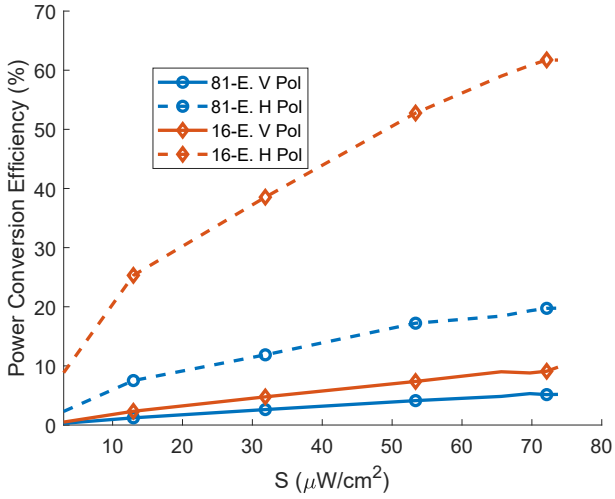

(a)

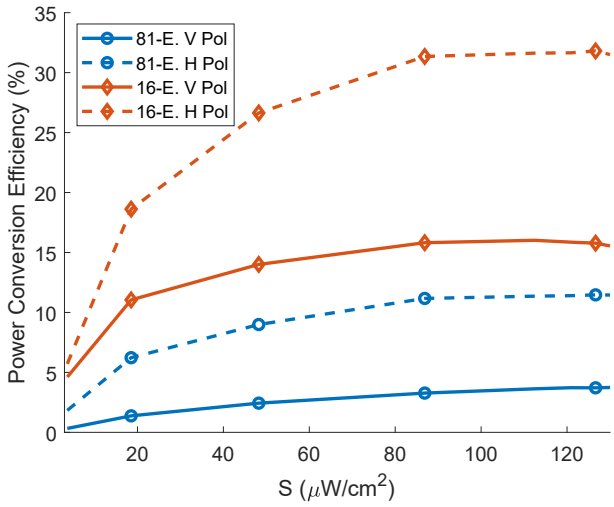

(b)

Figure 5.6.5: RF to DC power conversion efficiency for the 16 and 81-element arrays over the body phantom a) at 2.2 GHz. b) at 2.9 GHz.

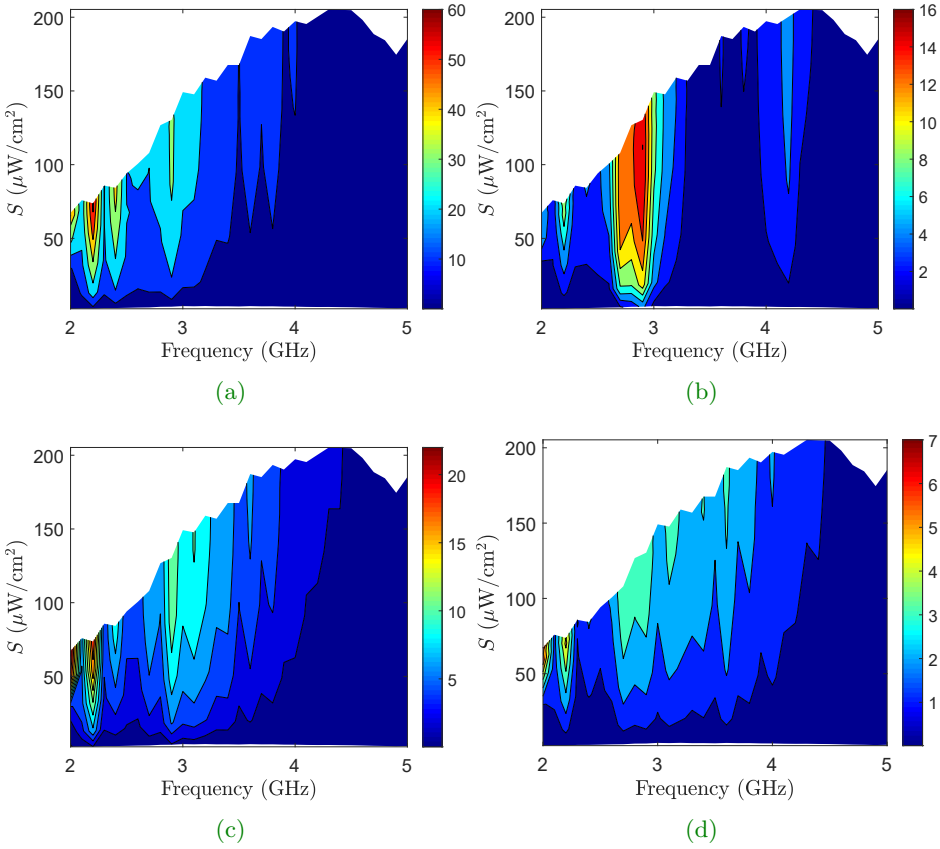

Figure 5.6.6: Power conversion efficiency versus frequency and density power for the 16 and 81-element array over the human phantom. a) Horizontal polarization 4×4. b) Vertical polarization 4×4. c) Horizontal polarization 9×9. d) Vertical polarization 9×9.

5.6.2. On real human body measurements

Figure 5.6.7: Photo of RF harvesting T-shirt with an 81-element rectenna array. Courtesy of José Estrada.

The array has been also tested over a real human torso (see Figure 5.6.7), but just over the 9x9 array, as all diodes had already been attached to the T-shirt. In Figure 5.6.8 a comparison of the DC power vs frequency for the 9×9 array over the human phantom and the real torso is shown where where different power densities are used (4, 10 and 25 μW/cm^2). The RF to DC power conversion efficiency is summarized in Figure 5.6.9 for 2.2, 2.4 and 2.6 GHz, and in Figure 5.6.10 the conversion efficiency is plotted over frequency, from 2 to 5 GHz at different power densities, for both polarizations. It can be seen that similar results are obtained, for both polarizations.

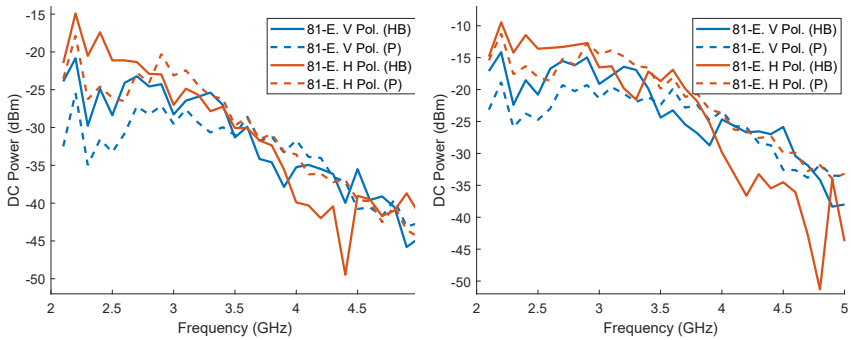

(a) (b)

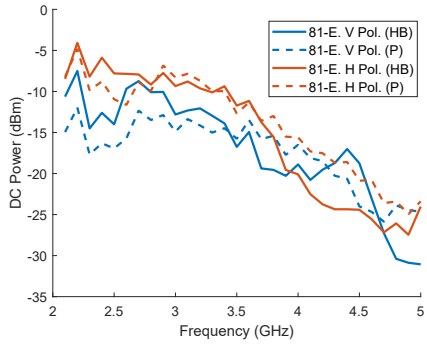

(c)

Figure 5.6.8: DC power vs frequency with a DC load of 2 kΩ. On-body (HB) and on-phantom (P) measurement comparison at different power densities for the 9×9 rectenna array at a) 4 μW/cm^2. b) 10 μW/cm^2. c) 25 μW/cm^2.

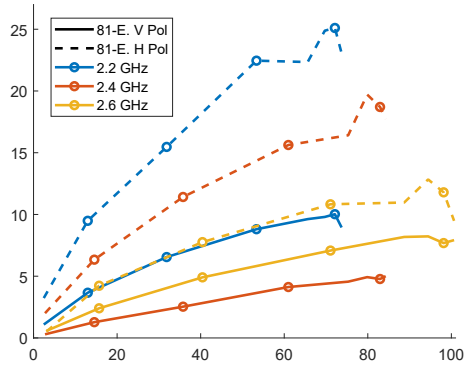

Figure 5.6.9: RF to DC power conversion efficiency for the 16 and 81-element arrays over the body torso at 2.2, 2.4 and 2.6 GHz.

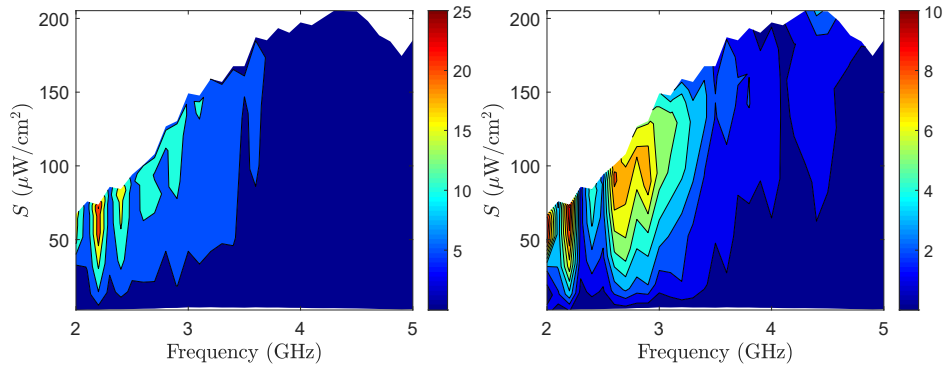

Figure 5.6.10: Power conversion efficiency versus frequency and density power for the 81-element array over the human phantom. a) Horizontal polarization. b) Vertical polarization.

5.7. Conclusions and future work

A broadband wearable rectenna array over a cotton T-shirt has been designed from 2 to 5 GHz. Two different rectenna array sizes are measured, showing a maximum efficiency of 62 % at 72 μW/cm^2 for the 16-element rectenna at 2.2 GHz. Less power is obtained at the vertical polarization (16 % at 2.9 GHz and 86 μW/cm^2) as diodes are just placed in the rows of the array. The rectenna integration is done using source-pull simulations, checking in which region the rectified DC power could be maximized. Then, the antenna is designed to show an input impedance as close as possible to that region. The 4×4 array provides a better performance than the larger array. This is due to the fairly large resistance of the conductive ink and silver paint, employed in the design, which reduces the efficiency in larger arrays, although it is a reliable method for connecting the diodes to the conductive ink. Moreover, the antenna is not designed to be used in free space but rather on a human torso or body phantom. For that reason, in free space the degradation in performance is more significant than on the human phantom. Over the phantom the input impedance of the antenna is moved closer to the source-pull contours, where maximum power can be achieved. Nevertheless, in free space, it is far from that region and, therefore, the rectified DC power is lower.

In Table 5.2, a comparison with the state-of-the-art designs is done, showing the most significant results. Not all data were found to properly compare all designs. Different frequency bands were employed although a comparison can be established. This design provides a wider bandwidth to scavenge energy if we compare to other designs, with different power densities ranging from 4 to 130 μW/cm^2. [23] and [25] provide a larger efficiencies but the design works over just a few specific frequencies. In [22], a high-efficiency value was achieved over a very low power density, although the antenna size at that frequency is big, so a trade-off is established.

Reference	Frequency (GHz)	Efficiency (%) or DC power
[This work]	(2-5) 2.2	62 % (H) 9% (V) @ 72 μW/cm^2 (2.5 dBm)
[This work]	(2-5) 2.9	31 % (H) 16 % (V) @ 86 μW/cm^2 (3 dBm)
[This work]	(2-5) 2.2	25 % (H) 2 % (V) @ 13 μW/cm^2 (-5 dBm)
[18]	2.45	28.7 % @ -7 dBm
[21]	2.45	100 μW (DC) @ 15 cm (100 mW EIRP)
[22]	0.86-0.918	50 % @ 876 MHz & 14 μW/cm^2
[23]	2.45 & 5.8	60 % @ 0 dBm & -3 dBm
[24]	4.65	55 % @ 5 dBm
[25]	2.45	-13 dBm (DC)@ 10 dBm (Tx power)

Table 5.2: Efficiency comparison with state-of-the-art designs.

Another important fact is the manufacturing expenses. This wearable design is cheap (around 70 $) therefore, the wearable antenna can be an option to power wearable sensors and be integrated into different applications. Future improvement will study the placement of the diodes in the vertical plane to benefit from the dual polarization scenario, and designing wearable rectennas over different parts of the body. Finally, a multiple-tone analysis would be interesting for the complete bandwidth, to characterize the power conversion efficiency improvement.

This design was presented in the Wireless Power Transfer Conference (WPTC 2019) in London and a deeper study was submitted to IEEE Transaction on Microwave Theory and Techniques. This chapter shows unpublished analyses performed for the design, such as the study of the influence of the body fat on the antenna performance, although skin and muscle variations are also included. A joined collaboration was established between University Charles III of Madrid (Spain) and University of Boulder, Colorado (United States). All simulations and spectrum measurements were done in Madrid while wearable rectenna measurements were performed in the facilities at the University of Boulder.

Conference contribution:
J. A. Estrada, E. Kwiatkowski, **A. López-Yela**, M. Borgoñós-García, D. Segovia Vargas, T. Barton, Z. Popovic, "*An Octave Bandwidth RF Harvesting Tee-Shirt*," 2019 IEEE Wireless Power Transfer Conference (WPTC), London, United Kingdom, 2019, pp. 232-235,
doi: 10.1109/WPTC45513.2019.9055642.

Journal article:
J. A. Estrada, E. Kwiatkowski, **A. López-Yela**, M. Borgoñós-García, D. Segovia Vargas, T. Barton, Z. Popovic," *RF-Harvesting Tightly Coupled Rectenna Array Tee-Shirt With Greater Than Octave Bandwidth*," in IEEE Transactions on Microwave Theory and Techniques,
doi: 10.1109/TMTT.2020.2988688.
This paper was awarded with "the Best Reading Paper of the Issue September 2020".

References

[1] J. A. Hagerty, F. B. Helmbrecht, W. H. McCalpin, R. Zane and Z. B. Popovic, "Recycling ambient microwave energy with broad-band rectenna arrays," in IEEE Transactions on Microwave Theory and Techniques, vol. 52, no. 3, pp. 1014-1024, March 2004.

[2] M. Piñuela, P. D. Mitcheson and S. Lucyszyn, "Ambient RF Energy Harvesting in Urban and Semi-Urban Environments," in IEEE Transactions on Microwave Theory and Techniques, vol. 61, no. 7, pp. 2715-2726, July 2013.

[3] Z. Popović, E. A. Falkenstein, D. Costinett and R. Zane, "Low-Power Far-Field Wireless Powering for Wireless Sensors," in Proceedings of the IEEE, vol. 101, no. 6, pp. 1397-1409, June 2013.

[4] C. R. Valenta and G. D. Durgin, "Harvesting Wireless Power: Survey of Energy-Harvester Conversion Efficiency in Far-Field, Wireless Power Transfer Systems," in IEEE Microwave Magazine, vol. 15, no. 4, pp. 108-120, June 2014.

[5] T. Paing, E. Falkenstein, R. Zane and Z. Popovic, "Custom IC for Ultra-low Power RF Energy Harvesting," 2009 Twenty-Fourth Annual IEEE Applied Power Electronics Conference and Exposition, Washington, DC, 2009, pp. 1239-1245.

[6] R. Scheeler, S. Korhummel and Z. Popovic, "A Dual-Frequency Ultralow-Power Efficient 0.5-g Rectenna," in IEEE Microwave Magazine, vol. 15, no. 1, pp. 109-114, Jan.-Feb. 2014.

[7] I. Ramos and Z. Popović, "A compact 2.45 GHz, low power wireless energy harvester with a reflector-backed folded dipole rectenna," 2015 IEEE Wireless Power Transfer Conference (WPTC), Boulder, CO, 2015, pp. 1-3.

[8] E. Falkenstein, M. Roberg and Z. Popovic, "Low-Power Wireless Power Delivery," in IEEE Transactions on Microwave Theory and Techniques, vol. 60, no. 7, pp. 2277-2286, July 2012.

[9] J. Wang, M. Leach, E. G. Lim, Z. Wang, R. Pei and Y. Huang, "An Implantable and Conformal Antenna for Wireless Capsule Endoscopy," in IEEE Antennas and Wireless Propagation Letters, vol. 17, no. 7, pp. 1153-1157, July 2018

[10] A. Cihangir, F. Gianesello and C. Luxey, "Dual-Antenna Concept With Complementary Radiation Patterns for Eyewear Applications," in IEEE Transactions on Antennas and Propagation, vol. 66, no. 6, pp. 3056-3063, June 2018.

[11] R. Salvado, C. Loss, R. Gonalves, and P. Pinho, "Textile materials for the design of wearable antennas: A survey," Sensors, vol. 12, no. 11, pp. 15 841–15 857, 2012. [Online]. Available: https://www.mdpi.com/1424-8220/12/11/15841

[12] J. C. G. Matthews and G. Pettitt, "Development of flexible, wearable antennas," 2009 3rd European Conference on Antennas and Propagation, Berlin, 2009, pp. 273-277.

[13] S. J. Chen, T. Kaufmann, D. C. Ranasinghe and C. Fumeaux, "A Modular Textile Antenna Design Using Snap-on Buttons for Wearable Applications," in IEEE Transactions on Antennas and Propagation, vol. 64, no. 3, pp. 894-903, March 2016.

[14] S. Li and J. Li, "Smart patch wearable antenna on Jeans textile for body wireless communication," 2018 12th International Symposium on Antennas, Propagation and EM Theory (ISAPE), Hangzhou, China, 2018, pp. 1-4.

[15] M. F. Ismail, M. K. A. Rahim, M. R. Hamid and H. A. Majid, "Circularly polarized textile antenna with bending analysis," 2013 IEEE International RF and Microwave Conference (RFM), Penang, 2013, pp. 460-462.

[16] H. Lee, J. Tak and J. Choi, "Wearable Antenna Integrated into Military Berets for Indoor/Outdoor Positioning System," in IEEE Antennas and Wireless Propagation Letters, vol. 16, pp. 1919-1922, 2017.

[17] D. Gaetano et al., "Insole Antenna for On-Body Telemetry," in IEEE Transactions on Antennas and Propagation, vol. 63, no. 8, pp. 3354-3361, Aug. 2015.

[18] S. Adami et al., "A Flexible 2.45-GHz Power Harvesting Wristband With Net System Output From -24.3 dBm of RF Power," in IEEE Transactions on Microwave Theory and Techniques, vol. 66, no. 1, pp. 380-395, Jan. 2018.

[19] L. Zhu, H. Hwang, E. Ren and G. Yang, "High performance MIMO antenna for 5G wearable devices," 2017 IEEE International Symposium on Antennas and Propagation and USNC/URSI National Radio Science Meeting, San Diego, CA, 2017, pp. 1869-1870.

[20] X. Chen, H. He, Y. Lu, H. Lam, L. Ukkonen and J. Virkki, "Fabrication and reliability evaluation of passive UHF RFID T-shirts," 2018 International Workshop on Antenna Technology (iWAT), Nanjing, 2018, pp. 1-4.

[21] S. Adami, D. Zhu, Yi Li, E. Mellios, B. H. Stark and S. Beeby, "A 2.45 GHz rectenna screen-printed on polycotton for on-body RF power transfer and harvesting," 2015 IEEE Wireless Power Transfer Conference (WPTC), Boulder, CO, 2015, pp. 1-4.

[22] G. Monti, L. Corchia and L. Tarricone, "UHF Wearable Rectenna on Textile Materials," in IEEE Transactions on Antennas and Propagation, vol. 61, no. 7, pp. 3869-3873, July 2013.

[23] Naresh B., V. K. Singh and V. Bhargavi, "Dual band RF energy harvester for wearable electronic technology," 2017 Third International Conference on Advances in Electrical, Electronics, Information, Communication and Bio-Informatics (AEEICB), Chennai, 2017, pp. 274-277.

[24] B. Naresh, V. K. Singh and V. Bhargavi, "4.65 GHz wearable rectenna for low power wireless applications," 2017 Second International Conference on Electrical, Computer and Communication Technologies (ICECCT), Coimbatore, 2017, pp. 1-5.

[25] D. Masotti, A. Costanzo and S. Adami, "Design and realization of a wearable multi-frequency RF energy harvesting system," Proceedings of the 5th European Conference on Antennas and Propagation (EUCAP), Rome, 2011, pp. 517-520.

[26] R. M. E. Khosht et al., "A foldable textile-based broadband archimedean spiral rectenna for RF energy harvesting," 2016 16th Mediterranean Microwave Symposium (MMS), Abu Dhabi, 2016, pp. 1-4.

[27] J. A. Estrada, E. Kwiatkowski, A. López-Yela, M. Borgoñós-García, D. Segovia Vargas, T. Barton, Z. Popovic, "An Octave Bandwidth RF Harvesting Tee-Shirt,"2019 IEEE Wireless Power Transfer Conference (WPTC), London, United Kingdom, 2019, pp. 232-235.
doi: 10.1109/WPTC45513.2019.9055642.

[28] J. A. Estrada, E. Kwiatkowski, A. López-Yela, M. Borgoñós-García, D. Segovia Vargas, T. Barton, Z. Popovic, " An RF-Harvesting Tightly-Coupled Rectenna Array Tee-Shirt with Greater than Octave Bandwidth," IEEE Transaction on Microwave Theory and Techniques.
doi: 10.1109/TMTT.2020.2988688.

[29] N. P. Basta, E. A. Falkenstein and Z. Popovic, "Bow-tie rectenna arrays," 2015 IEEE Wireless Power Transfer Conference (WPTC), Boulder, CO, 2015, pp. 1-4.

[30] User guide for source-pull in NI/AWR. https://awrcorp.com/download/faq/english/docs/Users_Guide/load_pull_wiz2.html

[31] C Gabriel, S Gabriel, and E Corthout. "The dielectric properties of biological tissues: I. Literature survey". In:Physics in Medicineand Biology41.11 (Nov. 1996), pp. 2231–2249.

[32] H. Vladimír, "Planar antenna in proximity of human body models," 2013 7th European Conference on Antennas and Propagation (EuCAP), Gothenburg, 2013, pp. 3309-3311.

[33] A. T. Mobashsher and A. M. Abbosh, "Artificial Human Phantoms: Human Proxy in Testing Microwave Apparatuses That Have Electromagnetic Interaction with the Human Body," in IEEE Microwave Magazine, vol. 16, no. 6, pp. 42-62, July 2015. doi: 10.1109/MMM.2015.2419772

[34] Jim morris environmental t-shirts. https://www.jimmorris.com/

[35] Z. Popović, E. A. Falkenstein, D. Costinett and R. Zane, "Low-Power Far-Field Wireless Powering for Wireless Sensors," in Proceedings of the IEEE, vol. 101, no. 6, pp. 1397-1409, June 2013.

6

Conclusions and further work

A summary of the conclusions from this thesis is given in this chapter. Chapter 1 shows an overview of the historical development of the wireless power transfer concept. It is interesting to notice that this technology is quite old, with the most relevant milestones made by famous scientists in the 18th and 19th centuries. Nowadays, the vast majority of contributions are related to the idea of scavenging the ambient otherwise wasted electromagnetic energy. This idea is related to the green-energy concept, which tries to reduce batteries. Indeed, the mail goal of this thesis is to improve the RF-DC conversion efficiency to autonomously power sensors and eliminate batteries.

To this end, Chapter 2 tries to explore some alternatives to improve the conversion efficiency focusing on the diode performance under multiple-tone scenarios, where its non-linear characteristics are used to help increase the DC rectified power. Previous studies were limited to a very simplified model where $R_s = 0$ (the series resistance of the diode in its equivalent circuit). This assumption is not correct as that parameter affects the IV

curve slope, especially in the exponential region where the non-linear rectifying process happens. Therefore, this thesis tries to give a comprehensive answer to that problem. Two different approaches to estimate the I_{DC} contribution are shown, one that can be used only for low input voltage and other that can be used to any voltage. In the first approach, the Wright Omega function and its finite derivatives are used to approximate the IV curve using a Taylor series. This approach is good, being the error less than 6 % in its convergence region (estimated empirically below 0.1 V). Nevertheless, for higher input voltages the error is high. The other approach is implemented for working with low and high voltage excitations when Legendre polynomials are used. The Legendre polynomials approximation has the advantage that they converge in the orthogonality region, in our case, $[V_0, V_1]$. The disadvantage of this approximation is that the convergence is weaker since it converges in L2-norm although it is pretty good, as observed in the experiements. Both theoretical models have been tested over the Spice parameters published in the datasheet for the SMS7630 zero-bias Schottky diode. A general four-tone scenario (varying the input amplitude and the number of tones) where tones are not equally spaced and a non-general scenario with harmonic-spaced tones have been studied. The DC current component is increased as the harmonic relation between tones contributes to more DC current, but both cases outperform a CW excitation at low voltages. As long as the voltage level is increased, the efficiency improvement is reduced. This is from the point of view of an ideal diode.

Future studies could extend the treatment to the influence of the non-linear junction capacitance and the parasitic influence of the diode package. Although the last theoretical model using Legendre polynomials shows good accuracy over low and high voltage levels and for four tones, the accuracy can be improved at the expense of increased complexity. However, this would lead to a better understanding of the non-linear process.

Chapter 3 deals with the multiple-tone simulations and measurements of a rectifier, analyzing the real performance. For that purpose, an accurate simulation and experimental setup is designed. Moreover, the diode Spice model was analyzed, showing poor agreement between simulation and measurements. Therefore, a new Spice and parasitics model has been pre-

sented along this chapter, where a very good characterization of the diode is shown from -10 to -25 dBm and from 0.9 to 4 GHz. In this way, it is possible to verify the RF-DC efficiency improvement under a multiple-tone scenario. Multiple-tone simulations and measurements were carried out in the rectifier although measurements could not be performed at high power levels due to some limitations of the available sources. The results show that the power conversion efficiency improvement can be understood as a non-linear process, respect to the frequency and input power. Some frequency tones produce a higher efficiency than others. And also, low input power levels make the diode to work in the exponential region, where the threshold limit can be overpassed more efficiently, getting higher current peaks, under multiple-tone excitations. Nevertheless, at higher power levels this efficiency improvement disappears, as the diode starts working in a linear region.

In Chapter 4 indoor and outdoor measurements were carried out using a single broadband rectenna element. Enough RF power was scavenged to turn on the diode, although a small amount of rectified DC power was obtained (-40 dBm). Ambient power density values were analyzed through measurements (recording data every 30 seconds for 3 hours during two weeks in a different environments). The study showed very low power density values. Therefore, the main conclusion is that the harvested power is limited due to the low power density values.

Future work will include working with a dual linear polarized antenna, to scavenge power from both polarizations, and adding a DC-DC boost converter to produce a steady DC output. Different number of elements can be included to increase the rectified DC power. Indeed, in Chapter 5 some of the above aspects are shown. Also, different studies can be performed comparing multiband and broadband designs, and its integration with the rectifier and efficiencies.

In Chapter 5 a broadband wearable rectenna array screen-printed over a cotton T-shirt is designed and measured from 2-5 GHz. Two different rectena array sizes are measured (4×4 and 9×9), showing a maximum efficiency of 62 % at 72 μW/cm^2 for the 16-element rectenna at 2.2 GHz. Less power is obtained in the vertical polarization (16 % at 2.9 GHz and

$86\,\mu W/cm^2$) as diodes are just placed in the rows of the array. The rectenna integration is done using source-pull simulations, checking in which region the rectified DC power can be maximized. Then, the antenna is designed to show an input impedance as close as possible to that region. The 4×4 array provides a better performance than the larger array. This is due to the fairly large resistance of the conductive ink and silver paint, employed in the design, which reduces the efficiency in larger arrays. The antenna was not designed to be used in free space but rather on a human torso or body phantom. So, in free space the degradation in performance is more significant than on the human phantom. Over the phantom the input impedance of the antenna is moved closer to the source-pull contours, where maximum power can be obtained.

A comparison with the state-of-the-art designs is done, showing the most significant results. This design provides a wider bandwidth to scavenge energy if we compare to other designs, with different power densities ranging from 4 to $130\,\mu W/cm^2$. Although other designs provide a larger efficiency, they just work over a few specific frequencies. Another important fact is the manufacturing expenses. This wearable design is cheap (around 70 \$) therefore, the wearable antenna can be an option to power wearable sensors and be integrated into different applications.

Future improvements will include the placement of the diodes in the vertical plane to benefit from the dual polarization scenario and designing wearable rectennas over different parts of the body. Moreover, it would be interesting to test the multi-tone approach for this design, to analyze the efficiency improvement.

6.1. About the author

Ana was born in Madrid (Spain) on July 12, in 1991. She received the B.S degree in Electrical Engineering at the Technical University of Madrid (UPM) in 2013 and got the best academic record prize for the first year and the complete degree (COITT prize). In 2015 she finished a M.S degree in Telecommunications Engineering and a M.S in Multimedia and Communications at University Carlos III of Madrid (UC3M), where she got the best academic record prize. From 2015 to 2016, she worked for one and a half years in MANA project, for miniaturizing antennas for military aircrafts (in collaboration with Airbus Defense and Space). The project was based on electrically small antennas in the VHF and UHF bands. In 2016, she got a Scholarship from the Spanish Ministry of Education for pursuing the PhD studies (FPU). During these years, she has authored and co-authored 9 conference papers (national and international) and 2 journal articles. She has collaborated with the University of Liverpool (where she has been a visiting researcher for three months) and with the University of Colorado Boulder (with professor Zoya Popović).

Her work is divided into two different research lines: on electrically small antennas for aircraft communications and in the analysis of multiple-tone receivers for energy harvesting applications.

7

Appendix

The appendix section includes a list of tables, for a better understanding, with all the data from the simulations and measurements published throughout the thesis, in Chapters 2 and 3. The origin of the data is explained in each foot of the table. To this end, transparency is given to the work, to facilitate possible implementations (or improvements) in future projects.

7.1. Published data from Chapter 2

This appendix includes an extended version of Table 2.6 for the diode characterization in a multiple-tone scenario.

N	Tone Amplitude (mV)	Average Power (dBm)	Predicted I_{DC} (μA)	Simulated I_{DC} (μA)	Maximum Relative Error (%)
4	2.50	-36.0	$4.21{\cdot}10^{-2}$	$4.26{\cdot}10^{-2}$	1.19
1	5.00	-36.0	$4.20{\cdot}10^{-2}$	$4.25{\cdot}10^{-2}$	1.18
4	5.00	-30.0	$17.02{\cdot}10^{-2}$	$17.22{\cdot}10^{-2}$	1.17
1	10.00	-30.0	$16.92{\cdot}10^{-2}$	$17.10{\cdot}10^{-2}$	1.05
4	7.50	-26.5	$38.97{\cdot}10^{-2}$	$39.47{\cdot}10^{-2}$	1.25
1	15.00	-26.5	$38.45{\cdot}10^{-2}$	$38.92{\cdot}10^{-2}$	1.21
4	36.25	-12.8	18.03	18.01	0.10
1	72.50	-12.8	13.20	13.42	1.65
4	38.75	-12.2	22.63	22.36	1.20
1	77.50	-12.2	15.91	16.19	1.74
4	41.25	-11.7	28.27	27.51	2.75
1	82.50	-11.7	19.06	19.40	1.75
4	43.75	-11.2	35.17	33.54	4.85
1	87.50	-11.2	22.71	23.13	1.80
4	45.00	-11.0	39.17	36.91	6.12
1	90.00	-11.0	24.75	25.21	1.82

Table 7.1: Extended version of Table 2.6 (1/2).

N	Tone Amplitude (mV)	Average Power (dBm)	Predicted I_{DC} (μA)	Simulated I_{DC} (μA)	Maximum Relative Error (%)
4	47.50	-10.5	48.46	44.40	9.13
1	95.00	-10.5	29.29	29.85	1.90
4	50.00	-10.0	59.74	52.89	12.95
1	100.00	-10.0	34.50	35.18	1.93

Table 7.2: Extended version of Table 2.6 (2/2).

7.2. Published data from Chapter 3

This appendix includes all the data from simulations and measurements of the complete setup for the multiple-tone and single-tone comparison in Chapter 3. Data from Section 3.2.5 are summarized in Table 7.3 and Table 7.4. In Section 3.2, entitled "Development of the parasitical and intrinsic circuit diode model", a CW excitation was used to characterize the non-linear performance of the diode (Spice model). For simplicity, just the most relevant frequencies are shown (see Table 7.5 to Table 7.7), as those measurements were done from 0.1 to 2.9 GHz. In this case, the input power corresponds to the generator output. In Section 3.4, entitled "Rectifier performance in a multiple-tone scenario", the DC rectified power data and RF power (at coupled port) data in the rectifier are summarized in different tables for the three circuits analyzed in Chapter 3. The two-tone, three-tone and a four-tone scenario are compared using the same average power (see from Table 7.8 to Table 7.53).

7.2.1. Validation of the theoretical approach with the designed Spice model

N	Tone Amplitude (mV)	Input Power (dBm)	Predicted I_{DC} (μA)	Simulated I_{DC} (μA)	Maximum Relative Error (%)
4	5.00	-30.0	$13.15{\cdot}10^{-2}$	$13.31{\cdot}10^{-2}$	1.20
2	7.07	-30.0	$13.12{\cdot}10^{-2}$	$13.28{\cdot}10^{-2}$	1.20
1	10.00	-30.0	$13.08{\cdot}10^{-2}$	$13.23{\cdot}10^{-2}$	1.11
4	10.00	-24.0	$54.60{\cdot}10^{-2}$	$55.20{\cdot}10^{-2}$	1.09
2	14.14	-24.0	$54.15{\cdot}10^{-2}$	$54.85{\cdot}10^{-2}$	1.27
1	20.00	-24.0	$53.43{\cdot}10^{-2}$	$54.09{\cdot}10^{-2}$	1.23
4	15.00	-20.5	$13.05{\cdot}10^{-1}$	$13.19{\cdot}10^{-1}$	1.06
2	21.21	-20.5	$12.82{\cdot}10^{-1}$	$12.99{\cdot}10^{-1}$	1.32
1	30.00	-20.5	$12.40{\cdot}10^{-1}$	$12.59{\cdot}10^{-1}$	1.51
4	20.00	-18.0	$25.13{\cdot}10^{-1}$	$25.00{\cdot}10^{-1}$	0.52
2	28.28	-18.0	$24.38{\cdot}10^{-1}$	$24.75{\cdot}10^{-1}$	1.52
1	40.00	-18.0	$23.17{\cdot}10^{-1}$	$23.48{\cdot}10^{-1}$	1.32
4	25.00	-16.0	$43.07{\cdot}10^{-1}$	$43.43{\cdot}10^{-1}$	0.82
2	35.35	-16.0	$41.31{\cdot}10^{-1}$	$42.03{\cdot}10^{-1}$	1.70
1	50.00	-16.0	$38.34{\cdot}10^{-1}$	$38.87{\cdot}10^{-1}$	1.36
4	30.00	-14.5	$68.35{\cdot}10^{-1}$	$68.90{\cdot}10^{-1}$	0.80
2	42.42	-14.5	$65.08{\cdot}10^{-1}$	$66.33{\cdot}10^{-1}$	1.88
1	60.00	-14.5	$58.99{\cdot}10^{-1}$	$59.84{\cdot}10^{-1}$	1.42
4	35.00	-13.0	10.22	10.34	1.15
2	49.49	-13.0	$97.26{\cdot}10^{-1}$	$99.76{\cdot}10^{-1}$	2.51
1	70.00	-13.0	$86.37{\cdot}10^{-1}$	$87.66{\cdot}10^{-1}$	1.47

N	Tone Amplitude (mV)	Input Power (dBm)	Predicted I_{DC} (μA)	Simulated I_{DC} (μA)	Maximum Relative Error (%)
4	40.00	-12.0	14.54	14.77	1.56
2	56.56	-12.0	13.93	14.35	2.94
1	80.00	-12.0	12.18	12.37	1.51
4	45.00	-11.0	19.85	20.27	2.05
2	63.63	-11.0	19.22	19.89	3.37
1	90.00	-11.0	16.67	16.93	1.54
4	50.00	-10.0	26.15	26.83	2.53
2	70.71	-10.0	25.68	26.67	3.71
1	100.00	-10.0	22.23	22.58	1.55
4	55.00	-9.2	33.44	34.49	3.06
2	77.78	-9.2	33.31	34.68	3.97
1	110.00	-9.2	28.96	29.40	1.50
4	60.00	-8.5	41.69	43.23	3.56
2	84.85	-8.5	42.07	43.87	4.10
1	120.00	-8.5	36.92	37.47	1.48
4	65.00	-7.7	50.87	52.99	4.00
2	91.92	-7.7	51.95	54.29	4.31
1	130.00	-7.7	46.13	46.81	1.45
4	70.00	-7.0	60.96	63.80	4.45
2	98.99	-7.0	62.86	65.71	4.34
1	140.00	-7.0	56.59	57.39	1.38
4	75.00	-6.5	71.89	75.36	4.61
2	106.06	-6.5	74.75	78.10	4.29
1	150.00	-6.5	68.27	69.19	1.33

N	Tone Amplitude (mV)	Input Power (dBm)	Predicted I_{DC} (μA)	Simulated I_{DC} (μA)	Maximum Relative Error (%)
4	80.00	-6.0	83.64	87.90	4.85
2	113.13	-6.0	87.54	91.39	4.21
1	160.00	-6.0	81.12	82.14	1.24
4	85.00	-5.4	96.15	101.16	4.95
2	120.20	-5.4	101.17	105.50	4.10
1	170.00	-5.4	95.07	96.26	1.24
4	90.00	-5	109.40	115.26	5.08
2	127.27	-5	115.57	120.35	3.97
1	180.00	-5	110.05	111.36	1.18
4	95.00	-4.4	123.30	130.00	5.15
2	134.35	-4.4	130.70	135.90	3.83
1	190.00	-4.4	125.98	127.40	1.11

Table 7.3 Relative error vs input voltage for a 4-tone, 2-tone and single tone excitation with the same average power. SMS7630 final verification. Small signal excitation.

N	Tone Amplitude (V)	Input Power (dBm)	Predicted I_{DC} (mA)	Simulated I_{DC} (mA)	Maximum Relative Error (%)
4	0.1000	-4.0	$13.78{\cdot}10^{-2}$	$14.54{\cdot}10^{-2}$	5.23
2	0.1414	-4.0	$14.64{\cdot}10^{-2}$	$15.19{\cdot}10^{-2}$	3.68
1	0.2000	-4.0	$14.28{\cdot}10^{-2}$	$14.42{\cdot}10^{-2}$	0.97
4	0.2000	2.0	$51.86{\cdot}10^{-2}$	$53.97{\cdot}10^{-2}$	3.91
2	0.2828	2.0	$54.69{\cdot}10^{-2}$	$55.45{\cdot}10^{-2}$	1.36
1	0.4000	2.0	$59.11{\cdot}10^{-2}$	$59.36{\cdot}10^{-2}$	0.42
4	0.3000	5.5	$98.53{\cdot}10^{-2}$	$10.13{\cdot}10^{-1}$	2.73
2	0.4242	5.5	$10.25{\cdot}10^{-1}$	$10.32{\cdot}10^{-1}$	0.62
1	0.6000	5.5	$11.32{\cdot}10^{-1}$	$11.36{\cdot}10^{-1}$	0.38

N	Tone Amplitude (V)	Input Power (dBm)	Predicted I_{DC} (mA)	Simulated I_{DC} (mA)	Maximum Relative Error (%)
4	0.4000	8.0	$14.87{\cdot}10^{-1}$	$15.19{\cdot}10^{-1}$	2.06
2	0.5656	8.0	$15.36{\cdot}10^{-1}$	$15.43{\cdot}10^{-1}$	0.46
1	0.8000	8.0	$17.05{\cdot}10^{-1}$	$17.12{\cdot}10^{-1}$	0.37
4	0.5000	10.0	$20.08{\cdot}10^{-1}$	$20.42{\cdot}10^{-1}$	1.65
2	0.7071	10.0	$20.64{\cdot}10^{-1}$	$20.73{\cdot}10^{-1}$	0.43
1	1.0000	10.0	$22.95{\cdot}10^{-1}$	$23.02{\cdot}10^{-1}$	0.30
4	0.6000	11.5	$25.41{\cdot}10^{-1}$	$25.67{\cdot}10^{-1}$	1.01
2	0.8485	11.5	$26.03{\cdot}10^{-1}$	$26.14{\cdot}10^{-1}$	0.43
1	1.2000	11.5	$28.94{\cdot}10^{-1}$	$29.01{\cdot}10^{-1}$	0.22
4	0.7000	13.0	$30.80{\cdot}10^{-1}$	$30.65{\cdot}10^{-1}$	0.50
2	0.9899	13.0	$31.47{\cdot}10^{-1}$	$31.61{\cdot}10^{-1}$	0.456
1	1.4000	13.0	$35.00{\cdot}10^{-1}$	$35.05{\cdot}10^{-1}$	0.15
4	0.8000	14.0	$36.25{\cdot}10^{-1}$	$35.27{\cdot}10^{-1}$	2.78
2	1.1313	14.0	$36.98{\cdot}10^{-1}$	$36.51{\cdot}10^{-1}$	1.27
1	1.6000	14.0	$41.11{\cdot}10^{-1}$	$41.14{\cdot}10^{-1}$	0.08
4	0.9000	15.0	$41.74{\cdot}10^{-1}$	$39.51{\cdot}10^{-1}$	5.63
2	1.2727	15.0	$42.51{\cdot}10^{-1}$	$40.39{\cdot}10^{-1}$	5.25
1	1.8000	15.0	$47.24{\cdot}10^{-1}$	$47.26{\cdot}10^{-1}$	0.03
4	0.9500	15.5	$44.49{\cdot}10^{-1}$	$41.47{\cdot}10^{-1}$	7.30
2	1.3435	15.5	$45.29{\cdot}10^{-1}$	$42.09{\cdot}10^{-1}$	7.59
1	1.9000	15.5	$50.32{\cdot}10^{-1}$	$50.32{\cdot}10^{-1}$	0.00

Table 7.4 Relative error vs input voltage for a 4-tone, 2-tone and single tone excitation with the same average power. SMS7630 final verification. Large signal excitation.

7.2.2. CW measurements

Measurements for a CW excitation at different frequencies for the three rectifiers under test are shown.

Input Power (dBm)	Tone 1 0.9 GHz (mV)	Tone 1 1.5 GHz (mV)	Tone 1 1.7 GHz (mV)	Tone 1 1.9 GHz (mV)	Tone 1 2.1 GHz (mV)	Tone 1 2.3 GHz (mV)
-10	139.4	152.7	164.4	195.0	247.4	144.3
-15	50.9	55.1	64.3	75.4	109.4	54.0
-20	16.6	17.8	22.0	26.7	42.1	18.1
-25	5.3	5.8	7.2	8.9	15.0	6.0
-30	1.8	2.0	2.5	3.1	5.1	2.1

Table 7.5: Measured DC voltage for a CW excitation for circuit 1.

Input Power (dBm)	Tone 1 0.9 GHz (mV)	Tone 1 1.5 GHz (mV)	Tone 1 1.7 GHz (mV)	Tone 1 1.9 GHz (mV)	Tone 1 2.1 GHz (mV)	Tone 1 2.3 GHz (mV)
-10	39.1	214.8	334.2	351.1	253.5	170.3
-15	12.2	88.3	151.0	157.4	104.2	61.2
-20	3.9	32.1	61.2	63.0	37.1	20.7
-25	1.3	10.7	21.9	22.4	12.4	6.9
-30	0.6	3.7	7.7	7.8	4.2	2.4

Table 7.6: Measured DC voltage for a CW excitation for circuit 2.

Power (dBm)	0.9 GHz (mV)	1.5 GHz (mV)	1.7 GHz (mV)	1.9 GHz (mV)	2.1 GHz (mV)	2.3 GHz (mV)
-10	173.0	254.7	255.7	216.4	177.8	132.8
-15	64.0	102.1	105.9	83.9	64.9	47.1
-20	21.2	35.1	37.8	28.9	21.1	15.8
-25	6.9	11.7	12.6	9.7	6.9	5.4
-30	2.3	3.7	4.2	3.4	2.5	2.1

Table 7.7: Measured DC voltage for a CW excitation for circuit 3.

7.2.3. Multiple-tone simulations and measurements

Multiple-tone simulations and measurements for the three rectifiers under test are shown (up to four tones).

Average Input Power (dBm)	All (dBm)	Tone 1 0.9 GHz (dBm)	Tone 2 1.85 GHz (dBm)	Tone 3 2.1 GHz (dBm)	Tone 4 2.45 GHz (dBm)
26	-3.55	-3.39	-3.44	-3.44	-3.53
20	-3.84	-3.45	-3.69	-3.62	-3.91
15	-4.44	-3.67	-4.14	-4.09	-4.26
10	-6.02	-5.34	-5.24	-5.88	-7.00
5	-9.28	-11.39	-8.81	-7.98	-10.28
0	-15.17	-18.25	-15.05	-13.6	-17.71
-5	-22.26	-26.21	-22.15	-20.47	-26.12
-10	-30.52	-35.41	-30.43	-28.38	-35.54
-15	-40.08	-45.32	-39.75	-37.28	-45.37

Table 7.8: Simulated rectified DC power for a CW (Tone X) and for a four-tone excitation (all) for circuit 1 (1/3).

Average Input Power (dBm)	All (dBm)	Tone 1 1.85 GHz (dBm)	Tone 2 2.10 GHz (dBm)	Tone 3 2.25 GHz (dBm)	Tone 4 3.25 GHz (dBm)
26	-3.60	-3.44	-3.44	-3.48	-5.85
20	-3.92	-3.69	-3.62	-3.83	-7.38
15	-4.33	-4.14	-4.09	-4.39	-8.34
10	-5.23	-5.24	-5.88	-6.70	-9.07
5	-8.12	-8.81	-7.98	-8.65	-10.03
0	-13.59	-15.05	-13.6	-11.42	-15.82
-5	-20.25	-22.15	-20.47	-18.09	-23.17
-10	-27.84	-30.43	-28.38	-25.73	-31.74
-25	-36.66	-39.75	-37.28	-34.36	-41.11

Table 7.9: Simulated rectified DC power for a CW (Tone X) and for a four-tone excitation (all) for circuit 1 (2/3).

Average Input Power (dBm)	All (dBm)	Tone 1 2.15 GHz (dBm)	Tone 2 2.20 GHz (dBm)	Tone 3 2.25 GHz (dBm)	Tone 4 2.30 GHz (dBm)
26	-3.59	-3.45	-3.45	-3.48	-3.48
20	-3.97	-3.69	-3.77	-3.83	-3.88
15	-4.63	-4.16	-4.31	-4.39	-4.43
10	-6.47	-6.18	-6.46	-6.70	-6.93
5	-8.80	-8.15	-8.35	-8.65	-9.10
0	-12.26	-13.11	-12.17	-11.42	-11.85
-5	-18.81	-19.79	-18.67	-18.09	-19.23
-10	-26.17	-27.44	-26.09	-25.73	-27.63
-15	-34.56	-36.08	-34.49	-34.36	-36.82

Table 7.10: Simulated rectified DC power for a CW (Tone X) and for a four-tone excitation (all) for circuit 1 (3/3)].

Average Input Power (dBm)	All (dBm)	Tone 1 0.90 GHz (dBm)	Tone 2 1.85 GHz (dBm)	Tone 3 2.10 GHz (dBm)	Tone 4 2.45 GHz (dBm)
26	-3.63	-3.44	-3.46	-3.48	-3.54
20	-3.99	-3.62	-3.62	-3.79	-3.84
15	-4.53	-5.61	-3.92	-4.25	-4.16
10	-6.03	-11.66	-4.55	-6.20	-7.04
5	-8.92	-18.49	-6.18	-8.06	-12.04
0	-14.80	-26.43	-10.67	-14.48	-19.02
-5	-21.75	-35.63	-17.07	-22.37	-27.06
-10	-29.76	-45.54	-24.32	-31.35	-36.18
-15	-39.06	-55.58	-32.65	-41.00	-45.82

Table 7.11: Simulated rectified DC power for a CW (Tone X) and for a four-tone excitation (all) for circuit 2 (1/3).

Average Input Power (dBm)	All (dBm)	Tone 1 1.70 GHz (dBm)	Tone 2 1.90 GHz (dBm)	Tone 3 2.00 GHz (dBm)	Tone 4 2.10 GHz (dBm)
26	-3.59	-3.46	-3.46	-3.45	-3.48
20	-3.86	-3.64	-3.65	-3.67	-3.79
15	-4.29	-3.98	-3.93	-4.05	-4.25
10	-5.32	-4.60	-4.73	-5.43	-6.20
5	-7.25	-6.07	-6.32	-6.86	-8.06
0	-11.97	-11.00	-10.54	-11.26	-14.48
-5	-18.42	-17.17	-16.96	-18.23	-22.37
-10	-25.61	-24.11	-24.22	-26.15	-31.35
-15	-33.85	-32.11	-32.55	-35.16	-41.00

Table 7.12: Simulated rectified DC power for a CW (Tone X) and for a four-tone excitation (all) for circuit 2 (2/3).

Average Input Power (dBm)	All (dBm)	Tone 1 1.70 GHz (dBm)	Tone 2 1.75 GHz (dBm)	Tone 3 1.80 GHz (dBm)	Tone 4 1.85 GHz (dBm)
26	-3.58	-3.46	-3.46	-3.46	-3.46
20	-3.82	-3.64	-3.67	-3.66	-3.62
15	-4.17	-3.98	-4.03	-3.96	-3.92
10	-4.9	-4.60	-4.56	-4.50	-4.55
5	-6.53	-6.07	-5.99	-6.05	-6.18
0	-11.1	-11.00	-10.58	-10.61	-10.67
-5	-17.2	-17.17	-16.84	-16.98	-17.07
-10	-24.1	-24.11	-23.89	-24.17	-24.32
-15	-31.99	-32.11	-31.99	-32.45	-32.65

Table 7.13: Simulated rectified DC power for a CW (Tone X) and for a four-tone excitation (all) for circuit 2 (3/3).

Average Input Power (dBm)	All (dBm)	Tone 1 0.90 GHz (dBm)	Tone 2 1.85 GHz (dBm)	Tone 3 2.10 GHz (dBm)	Tone 4 2.45 GHz (dBm)
26	-3.59	-3.39	-3.42	-3.50	-6.38
20	-3.91	-3.46	-3.52	-3.68	-8.36
15	-4.35	-3.68	-3.83	-3.87	-9.40
10	-5.15	-4.62	-5.68	-4.12	-10.17
5	-7.75	-9.49	-8.48	-6.76	-11.92
0	-13.75	-15.92	-12.41	-13.01	-19.06
-5	-20.67	-23.25	-19.59	-19.97	-27.15
-10	-28.69	-31.77	-27.72	-28.00	-36.02
-15	-38.08	-41.30	-36.65	-37.16	-45.23

Table 7.14: Simulated rectified DC power for a CW (Tone X) and for a four-tone excitation (all) for circuit 3 (1/3).

Average Input Power (dBm)	All (dBm)	Tone 1 1.40 GHz (dBm)	Tone 2 1.55 GHz (dBm)	Tone 3 1.75 GHz (dBm)	Tone 4 2.10 GHz (dBm)
26	-3.53	-3.43	-3.44	-3.44	-3.50
20	-3.74	-3.56	-3.59	-3.53	-3.68
15	-4.06	-3.92	-3.89	-3.81	-3.87
10	-4.76	-4.35	-4.44	-4.92	-4.12
5	-6.97	-6.28	-6.33	-7.41	-6.76
0	-12.00	-11.97	-11.26	-12.14	-13.01
-5	-18.51	-18.60	-17.86	-19.03	-19.97
-10	-25.90	-26.21	-25.40	-26.92	-28.00
-15	-34.51	-34.99	-34.07	-35.80	-37.16

Table 7.15: Simulated rectified DC power for a CW (Tone X) and for a four-tone excitation (all) for circuit 3 (2/3).

Average Input Power (dBm)	All (dBm)	Tone 1 1.50 GHz (dBm)	Tone 2 1.55 GHz (dBm)	Tone 3 1.60 GHz (dBm)	Tone 4 1.65 GHz (dBm)
26	-3.53	-3.43	-3.44	-3.44	-3.44
20	-3.75	-3.58	-3.59	-3.57	-3.58
15	-4.10	-3.91	-3.89	-3.89	-3.90
10	-4.86	-4.40	-4.44	-4.51	-4.63
5	-6.87	-6.23	-6.33	-6.57	-6.88
0	-11.51	-11.36	-11.26	-11.52	-11.96
-5	-17.98	-17.92	-17.86	-18.25	-18.83
-10	-25.30	-25.41	-25.40	-25.95	-26.70
-15	-33.79	-34.04	-34.07	-34.77	-35.66

Table 7.16: Simulated Rectified DC power for a CW (Tone X) and for a four-tone excitation (all) for circuit 3 (3/3).

Average Input Power (dBm)	Tone 1 0.90 GHz (dBm)	Tone 2 1.85 GHz (dBm)	Tone 3 2.10 GHz (dBm)	Tone 4 2.45 GHz (dBm)
26	13.41	13.34	15.02	14.81
20	7.09	7.59	8.85	8.68
15	1.78	2.85	3.50	3.64
10	-3.26	-1.94	-2.39	-1.18
5	-7.95	-6.86	-8.76	-5.74
0	-12.79	-11.94	-14.40	-10.58
-5	-17.68	-17.02	-19.23	-15.50
-10	-22.57	-22.07	-24.36	-20.40
-15	-27.46	-27.09	-29.43	-25.31

Table 7.17: Simulated RF input power (in the rectifier) for a four-tone excitation for circuit 1 (1/3).

Average Input Power (dBm)	Tone 1 1.85 GHz (dBm)	Tone 2 2.10 GHz (dBm)	Tone 3 2.25 GHz (dBm)	Tone 4 3.25 GHz (dBm)
26	13.42	14.99	14.22	5.34
20	7.70	8.79	8.11	0.89
15	2.98	3.37	2.92	-2.26
10	-1.79	-2.48	-2.43	-5.45
5	-6.76	-8.60	-7.70	-10.38
0	-11.86	-13.97	-12.63	-15.35
-5	-16.96	-19.10	-17.63	-20.11
-10	-22.03	-24.26	-22.65	-24.77
-15	-27.08	-29.39	-27.70	-29.45

Table 7.18: Simulated RF input power (in the rectifier) for a four-tone excitation for circuit 1 (2/3).

Average Input Power (dBm)	Tone 1 2.15 GHz (dBm)	Tone 2 2.20 GHz (dBm)	Tone 3 2.25 GHz (dBm)	Tone 4 2.30 GHz (dBm)
26	14.70	14.39	14.23	14.29
20	8.52	8.24	8.12	8.22
15	3.20	2.98	2.94	3.10
10	-2.46	-2.56	-2.43	-2.14
5	-8.38	-8.13	-7.74	-7.41
0	-13.92	-13.19	-12.65	-12.63
-5	-18.81	-17.93	-17.60	-17.61
-10	-23.66	-22.71	-22.62	-22.57
-15	-28.47	-27.53	-27.67	-27.54

Table 7.19: Simulated RF input power (in the rectifier) for a four-tone excitation for circuit 1 (3/3).

Average Input Power (dBm)	Tone 1 0.90 GHz (dBm)	Tone 2 1.85 GHz (dBm)	Tone 3 2.10 GHz (dBm)	Tone 4 2.45 GHz (dBm)
26	11.53	15.40	13.89	14.42
20	6.03	9.09	7.75	8.25
15	1.50	3.66	2.52	3.18
10	-3.06	-2.01	-2.97	-1.61
5	-7.75	-7.62	-8.83	-6.22
0	-12.64	-12.64	-14.08	-11.13
-5	-17.59	-17.59	-19.27	-16.08
-10	-22.53	-22.48	-24.52	-21.01
-15	-27.48	-27.34	-29.74	-25.93

Table 7.20: Simulated RF input power (in the rectifier) for a four-tone excitation for circuit 2 (1/3).

Average Input Power (dBm)	Tone 1 1.70 GHz (dBm)	Tone 2 1.90 GHz (dBm)	Tone 3 2.00 GHz (dBm)	Tone 4 2.10 GHz (dBm)
26	14.40	15.09	14.03	13.90
20	8.42	8.83	7.87	7.78
15	3.48	3.46	2.64	2.57
10	-1.55	-2.09	-2.69	-2.83
5	-6.57	-7.51	-8.00	-8.63
0	-11.82	-12.51	-13.18	-14.08
-5	-17.05	-17.48	-18.38	-19.20
-10	-22.32	-22.42	-23.60	-24.38
-15	-27.65	-27.31	-28.88	-29.60

Table 7.21: Simulated RF input power (in the rectifier) for a four-tone excitation for circuit 2 (2/3).

Average Input Power (dBm)	Tone 1 1.70 GHz (dBm)	Tone 2 1.75 GHz (dBm)	Tone 3 1.80 GHz (dBm)	Tone 4 1.85 GHz (dBm)
26	14.39	14.92	15.38	15.47
20	8.38	8.82	9.18	9.21
15	3.39	3.69	3.89	3.83
10	-1.58	-1.50	-1.57	-1.76
5	-6.66	-6.89	-7.22	-7.43
0	-11.87	-12.23	-12.54	-12.59
-5	-17.07	-17.43	-17.63	-17.59
-10	-22.30	-22.62	-22.70	-22.56
-15	-27.59	-27.83	-27.72	-27.48

Table 7.22: Simulated RF input power (in the rectifier) for a four-tone excitation for circuit 2 (3/3).

Average Input Power (dBm)	Tone 1 0.90 GHz (dBm)	Tone 2 1.85 GHz (dBm)	Tone 3 2.10 GHz (dBm)	Tone 4 2.45 GHz (dBm)
26	14.12	13.42	13.2	13.48
20	7.70	7.38	7.19	7.47
15	2.11	2.49	2.30	2.31
10	-4.00	-2.20	-2.33	-3.42
5	-10.24	-6.64	-7.09	-9.10
0	-15.36	-11.38	-11.94	-13.93
-5	-20.51	-16.17	-16.72	-18.82
-10	-25.69	-20.93	-21.46	-23.75
-15	-30.78	-25.71	-26.21	-28.69

Table 7.23: Simulated RF input power (in the rectifier) for a four-tone excitation for circuit 3 (1/3).

Average Input Power (dBm)	Tone 1 1.40 GHz (dBm)	Tone 2 1.55 GHz (dBm)	Tone 3 1.75 GHz (dBm)	Tone 4 2.10 GHz (dBm)
26	13.98	13.72	14.05	13.29
20	7.71	7.56	7.88	7.21
15	2.44	2.44	2.74	2.42
10	-2.52	-2.43	-2.33	-2.09
5	-6.79	-7.01	-7.57	-7.05
0	-11.40	-11.95	-12.75	-12.07
-5	-16.22	-17.02	-17.69	-16.84
-10	-20.96	-22.03	-22.67	-21.58
-15	-25.66	-27.01	-27.66	-26.32

Table 7.24: Simulated RF input power (in the rectifier) for a four-tone excitation for circuit 3 (2/3).

Average Input Power (dBm)	Tone 1 1.50 GHz (dBm)	Tone 2 1.55 GHz (dBm)	Tone 3 1.60 GHz (dBm)	Tone 4 1.65 GHz (dBm)
26	13.76	13.69	13.73	13.88
20	7.53	7.50	7.55	7.68
15	2.37	2.38	2.44	2.54
10	-2.47	-2.46	-2.48	-2.48
5	-6.85	-7.04	-7.42	-7.81
0	-11.56	-11.94	-12.63	-13.31
-5	-16.50	-17.00	-17.84	-18.59
-10	-21.37	-22.02	-23.08	-23.97
-15	-26.19	-27.00	-28.34	-29.49

Table 7.25: Simulated RF input power (in the rectifier) for a four-tone excitation for circuit 3 (3/3).

Average Input Power (dBm)	Tone 1 0.9 GHz (dBm)	Tone 1 1.85 GHz (dBm)	Tone 1 2.1 GHz (dBm)	Tone 1 2.15 GHz (dBm)	Tone 1 2.2 GHz (dBm)
26	19.42	19.43	21.01	20.72	20.38
20	13.07	13.72	14.87	14.54	14.21
15	7.82	8.97	9.58	9.24	8.93
10	3.12	4.15	3.65	3.39	3.336
5	-1.77	-0.75	-3.27	-2.94	-2.27
0	-6.66	-5.87	-8.73	-8.16	-7.17
-5	-11.54	-10.97	-13.72	-12.85	-11.82
-10	-16.44	-16.03	-18.67	-17.56	-16.56
-15	-21.39	-21.07	-23.59	-22.33	-21.39

Table 7.26: Simulated RF input power (rectifier) for a CW excitation for circuit 1 (1/2).

Average Input Power (dBm)	Tone 1 2.25 GHz (dBm)	Tone 1 2.30 GHz (dBm)	Tone 1 2.45 GHz (dBm)	Tone 1 3.25 GHz (dBm)
26	20.20	20.26	20.82	12.33
20	14.07	14.16	14.74	7.68
15	8.85	9.02	9.74	4.03
10	3.45	3.71	4.92	0.49
5	-1.81	-1.54	0.60	-3.08
0	-6.54	-6.79	-4.34	-7.94
-5	-11.49	-11.87	-9.28	-12.97
-10	-16.56	-16.80	-14.24	-17.99
-15	-21.68	-21.66	-19.22	-23.02

Table 7.27: Simulated RF input power (rectifier) for a CW excitation for circuit 1 (2/2).

Average Input Power (dBm)	Tone 1 0.90 GHz (dBm)	Tone 1 1.70 GHz (dBm)	Tone 1 1.75 GHz (dBm)	Tone 1 1.80 GHz (dBm)
26	17.90	20.39	20.90	21.36
20	12.80	14.37	14.78	15.15
15	8.35	9.38	9.61	9.84
10	3.40	4.39	4.39	4.36
5	-1.55	-0.79	-1.12	-1.43
0	-6.50	-6.06	-6.52	-6.80
-5	-11.47	-11.31	-11.71	-11.82
-10	-16.45	-16.58	-16.88	-16.80
-15	-21.44	-21.87	-22.02	-21.73

Table 7.28: Simulated RF input power (rectifier) for a CW excitation for circuit 2 (1/2).

Average Input Power (dBm)	Tone 1 1.85 GHz (dBm)	Tone 1 1.90 GHz (dBm)	Tone 1 2.00 GHz (dBm)	Tone 1 2.10 GHz (dBm)	Tone 1 2.45 GHz (dBm)
26	21.45	21.09	20.00	19.86	20.47
20	15.18	14.81	13.83	13.72	14.33
15	9.77	9.43	8.59	8.51	9.21
10	4.15	3.87	3.26	2.96	4.51
5	-1.60	-1.56	-1.91	-3.28	0.09
0	-6.72	-6.46	-7.02	-8.76	-4.90
-5	-11.62	-11.36	-12.37	-13.90	-9.88
-10	-16.50	-16.27	-17.76	-18.96	-14.86
-15	-21.36	-21.17	-23.14	-23.96	-19.85

Table 7.29: Simulated RF input power (rectifier) for a CW excitation for circuit 2 (2/2).

Average Input Power (dBm)	Tone 1 0.90 GHz (dBm)	Tone 1 1.40 GHz (dBm)	Tone 1 1.50 GHz (dBm)	Tone 1 1.55 GHz (dBm)	Tone 1 1.60 GHz (dBm)
26	20.23	19.93	19.72	19.65	19.71
20	13.74	13.93	13.48	13.45	13.51
15	7.85	8.43	8.37	8.37	8.42
10	0.65	3.72	3.69	3.67	3.61
5	-5.30	-0.17	-0.45	-0.78	-1.34
0	-10.15	-4.95	-5.20	-5.66	-6.56
-5	-15.02	-9.81	-10.17	-10.78	-11.87
-10	-19.90	-14.62	-15.10	-15.86	-17.19
-15	-24.82	-19.44	-20.01	-20.91	-22.49

Table 7.30: Simulated RF input power (rectifier) for a CW excitation for circuit 3 (1/2).

Average Input Power (dBm)	Tone 1 1.65 GHz (dBm)	Tone 1 1.75 GHz (dBm)	Tone 1 1.85 GHz (dBm)	Tone 1 2.10 GHz (dBm)	Tone 1 2.45 GHz (dBm)
26	19.86	20.00	19.37	19.20	19.48
20	13.64	13.73	13.71	13.17	13.47
15	8.49	8.48	8.01	8.26	8.32
10	3.55	3.50	3.35	3.64	2.57
5	-1.95	-1.92	-0.82	-1.13	-3.96
0	-7.60	-7.35	-5.09	-5.81	-8.47
-5	-13.05	-12.16	-9.83	-10.52	-13.10
-10	-18.57	-16.95	-14.62	-15.27	-17.86
-15	-24.06	-21.75	-19.50	-20.09	-22.73

Table 7.31: Simulated RF input power (rectifier) for a CW excitation for circuit 3 (2/2).

Average Input Power (dBm)	Tone 1+2 (1.85+2.10) GHz (dBm)	Tone 1+2 (2.25+3.25) GHz (dBm)	Tone 1+2 (2.15+2.30) GHz (dBm)
26	-3.62	-3.73	-3.67
20	-3.93	-4.08	-4.01
15	-4.37	-4.32	-4.51
10	-5.52	-4.82	-6.44
5	-7.98	-7.39	-8.86
0	-13.70	-13.23	-12.36
-5	-20.50	-19.98	-19.10
-10	-28.40	-27.68	-26.75
-15	-37.57	-36.48	-35.53

Table 7.32: Simulated rectified DC power for a two-tone excitation for circuit 1.

Average Input Power (dBm)	Tone 1+2 (0.90+2.45) GHz (dBm)	Tone 1+2 (1.70+2.00) GHz (dBm)	Tone 1+2 1.75+1.85 GHz (dBm)
26	-3.87	-3.68	-3.65
20	-4.29	-3.94	-3.88
15	-5.04	-4.31	-4.16
10	-8.50	-5.14	-4.79
5	-14.01	-6.93	-6.40
0	-21.15	-11.41	-10.71
-5	-29.45	-17.73	-16.94
-10	-38.97	-24.79	-23.90
-15	-49.02	-32.96	-31.93

Table 7.33: Simulated rectified DC power for a two-tone excitation for circuit 2.

Average Input Power (dBm)	Tone 1+2 (0.90+2.45) GHz (dBm)	Tone 1+2 (1.40+1.75) GHz (dBm)	Tone 1+2 (1.55+1.65) GHz (dBm)
26	-3.52	-3.59	-3.59
20	-3.82	-3.87	-3.86
15	-4.51	-4.15	-4.12
10	-6.25	-4.88	-4.77
5	-9.52	-7.12	-6.84
0	-16.05	-11.69	-11.37
-5	-23.51	-18.24	-17.92
-10	-32.29	-25.73	-25.37
-15	-42.20	-34.51	-34.07

Table 7.34: Simulated rectified DC power for a two-tone excitation for circuit 3.

Average Power (dBm)	Tone 1 1.85 GHz (dBm)	Tone 2 2.10 GHz (dBm)	Tone 1 2.25 GHz (dBm)	Tone 2 3.25 GHz (dBm)
26	16.35	18.03	17.15	8.31
20	10.63	11.88	10.96	4.01
15	5.93	6.53	5.68	0.91
10	1.16	0.61	0.31	-2.42
5	-3.83	-6.00	-4.73	-7.09
0	-8.90	-11.26	-9.61	-12.03
-5	-13.98	-16.31	-14.60	-16.85
-10	-19.04	-21.41	-19.65	-21.60
-15	-24.07	-26.47	-24.73	-26.36

Table 7.36: Simulated RF input power (in the rectifier) for a two-tone excitation for circuit 1 (1/2).

Average Power (dBm)	Tone 1 2.15 GHz (dBm)	Tone 2 2.30 GHz (dBm)
26	17.67	17.30
20	11.45	11.26
15	6.12	6.16
10	0.46	0.91
5	-5.39	-4.42
0	-10.94	-9.69
-5	-15.82	-14.67
-10	-20.64	-19.63
-15	-25.42	-24.58

Table 7.36: Simulated RF input power (in the rectifier) for a two-tone excitation for circuit 1 (2/2).

Average Input Power (dBm)	Tone 1 0.90 GHz (dBm)	Tone 2 2.45 GHz (dBm)	Tone 1 1.70 GHz (dBm)	Tone 2 2.00 GHz (dBm)
26	14.57	17.41	17.40	17.03
20	9.04	11.28	11.43	10.86
15	4.66	6.29	6.49	5.63
10	0.21	1.77	1.53	0.30
5	-4.60	-2.94	-3.62	-5.03
0	-9.56	-7.92	-8.87	-10.20
-5	-14.51	-12.90	-14.11	-15.37
-10	-19.47	-17.87	-19.38	-20.59
-15	-24.45	-22.86	-24.71	-25.87

Table 7.38: Simulated RF input power (in the rectifier) for a two-tone excitation for circuit 2 (1/2).

Average Input Power (dBm)	Tone 1 1.75 GHz (dBm)	Tone 2 1.85 GHz (dBm)
26	17.93	18.45
20	11.84	12.18
15	6.74	6.80
10	1.57	1.21
5	-3.84	-4.45
0	-9.22	-9.61
-5	-14.44	-14.59
-10	-19.67	-19.56
-15	-24.88	-24.46

Table 7.38: Simulated RF input power (in the rectifier) for a two-tone excitation for circuit 2 (2/2).

Average Input Power (dBm)	Tone 1 0.90 GHz (dBm)	Tone 2 2.45 GHz (dBm)	Tone 1 1.40 GHz (dBm)	Tone 2 1.75 GHz (dBm)
26	17.17	16.49	16.99	16.97
20	10.68	10.48	10.69	10.77
15	4.78	5.34	5.39	5.63
10	-1.66	-0.35	0.46	0.64
5	-7.90	-6.57	-3.79	-4.52
0	-12.89	-11.26	-8.31	-9.83
-5	-17.89	-16.01	-13.12	-14.77
-10	-22.86	-20.83	-17.87	-19.75
-15	-27.81	-25.72	-22.59	-24.71

Table 7.40: Simulated RF input power (in the rectifier) for a two-tone excitation for circuit 3 (1/2).

Average Input Power (dBm)	Tone 1 1.55 GHz (dBm)	Tone 2 1.65 GHz (dBm)
26	16.69	16.87
20	10.51	10.68
15	5.36	5.54
10	0.54	0.52
5	-4.00	-4.80
0	-8.85	-10.32
-5	-13.92	-15.63
-10	-18.95	-21.06
-15	-23.96	-26.61

Table 7.40: Simulated RF input power (in the rectifier) for a two-tone excitation for circuit 3 (2/2).

Average Input Power (dBm)	$V_{DC}(V)$	Tone 1 2.25 GHz (dBm)	Tone 2 3.25 GHz (dBm)
5	0.606	-26.77	-34.06
0	0.291	-31.87	-39.16
-5	0.127	-36.81	-44.58
-10	0.049	-41.92	-49.28
-15	0.017	-47.11	-54.05
-18	0.009	-50.11	-57.19
-21	0.005	-53.14	-60.19

Table 7.41: Measured rectified DC voltage for a two-tone excitation for circuit 1. RF power at the coupled port for each tone (1/3).

Average Input Power (dBm)	$V_{DC}(V)$	Tone 1 1.85 GHz (dBm)	Tone 2 2.10 GHz (dBm)
5	0.707	-31.62	-28.17
0	0.354	-36.69	-32.70
-5	0.153	-42.56	-37.17
-10	0.061	-48.08	-41.52
-15	0.021	-53.50	-46.14
-18	0.011	-56.33	-48.92
-21	0.006	-59.64	-51.92

Table 7.42: Measured rectified DC voltage for a two-tone excitation for circuit 1. RF power at the coupled port for each tone (2/3).

Average Input Power (dBm)	$V_{DC}(V)$	Tone 1 2.15 GHz (dBm)	Tone 2 2.30 GHz (dBm)
5	0.698	-29.6	-28.71
0	0.352	-33.47	-34.00
-5	0.157	-37.78	-39.88
-10	0.065	-41.75	-44.84
-15	0.023	-46.13	-50.31
-18	0.013	-48.52	-53.48
-21	0.006	-51.72	-56.72

Table 7.43: Measured rectified DC voltage for a two-tone excitation for circuit 1. RF power at the coupled port for each tone (3/3).

Average Input Power (dBm)	$V_{DC}(V)$	Tone 1 0.90 GHz (dBm)	Tone 2 2.45 GHz (dBm)
5	0.435	-25.16	-24.75
0	0.189	-29.93	-29.52
-5	0.068	-35.36	-34.31
-10	0.022	-40.39	-39.22
-15	0.007	-45.28	-44.19
-18	0.003	-49.77	-47.30
-21	0.002	-50.69	-50.20

Table 7.44: Measured rectified DC voltage for a two-tone excitation for circuit 2. RF power at the coupled port for each tone (1/3).

Average Input Power (dBm)	$V_{DC}(V)$	Tone 1 1.70 GHz (dBm)	Tone 2 2.00 GHz (dBm)
5	0.882	-27.88	-26.34
0	0.462	-31.83	-31.43
-5	0.208	-36.31	-37.27
-10	0.092	-40.45	-42.70
-15	0.036	-44.70	-48.16
-18	0.019	-47.19	-51.28
-21	0.010	-49.83	-54.45

Table 7.45: Measured rectified DC voltage for a two-tone excitation for circuit 2. RF power at the coupled port for each tone (2/3).

Average Input Power (dBm)	$V_{DC}(V)$	Tone 1 1.75 GHz (dBm)	Tone 2 1.85 GHz (dBm)
5	0.907	-28.41	-26.34
0	0.479	-32.48	-31.59
-5	0.235	-37.16	-36.58
-10	0.106	-41.25	-41.72
-15	0.043	-45.52	-46.77
-18	0.020	-49.69	-49.64
-21	0.013	-50.52	-52.66

Table 7.46: Measured rectified DC voltage for a two-tone excitation for circuit 2. RF power at the coupled port for each tone (3/3).

Average Input Power (dBm)	$V_{DC}(V)$	Tone 1 1.85 GHz (dBm)	Tone 2 2.25 GHz (dBm)	Tone 3 3.25 GHz (dBm)
5	0.600	-32.00	-29.59	-35.45
0	0.289	-37.51	-34.16	-41.16
-5	0.127	-42.70	-38.91	-46.75
-10	0.049	-47.64	-42.67	-52.58
-15	0.013	-52.72	-46.78	-58.19
-18	0.008	-54.47	-49.23	-59.39
-21	0.004	-55.73	-52.63	-65.25

Table 7.47: Measured rectified DC voltage for a three-tone excitation for circuit 1. RF power at the coupled port for each tone (1/2).

Average Input Power (dBm)	$V_{DC}(V)$	Tone 1 2.15 GHz (dBm)	Tone 2 2.20 GHz (dBm)	Tone 3 2.25 GHz (dBm)
5	0.623	-31.16	-29.32	-29.02
0	0.304	-35.05	-33.20	-33.72
-5	0.139	-39.33	-38.00	-38.50
-10	0.055	-44.09	-42.53	-42.02
-15	0.019	-48.22	-46.73	-46.78
-18	0.010	-50.64	-50.56	-49.75
-21	0.005	-53.36	-51.89	-52.00

Table 7.48: Measured rectified DC voltage for a three-tone excitation for circuit 1. RF power at the coupled port for each tone (2/2).

Average Input Power (dBm)	$V_{DC}(V)$	Tone 1 0.90 GHz (dBm)	Tone 2 1.85 GHz (dBm)	Tone 3 2.45 GHz (dBm)
5	0.725	-27.02	-27.98	-26.45
0	0.361	-32.13	-33.17	-31.09
-5	0.169	-37.64	-38.09	-35.70
-10	0.070	-42.23	-43.17	-40.42
-15	0.025	-47.09	-47.39	-45.17
-18	0.013	-50.20	-50.52	-47.90
-21	0.007	-53.19	-52.78	-50.91

Table 7.49: Measured rectified DC voltage for a three-tone excitation for circuit 2. RF power at the coupled port for each tone (1/2).

Average Input Power (dBm)	$V_{DC}(V)$	Tone 1 1.70 GHz (dBm)	Tone 2 1.90 GHz (dBm)	Tone 3 2.00 GHz (dBm)
5	0.885	-29.46	-28.52	-27.78
0	0.453	-33.92	-34.39	-32.88
-5	0.214	-38.30	-39.94	-37.63
-10	0.095	-42.11	-45.19	-42.50
-15	0.037	-46.13	-50.19	-47.77
-18	0.020	-48.08	-53.30	-50.53
-21	0.010	-50.73	-58.05	-53.23

Table 7.50: Measured rectified DC voltage for a three-tone excitation for circuit 2. RF power at the coupled port for each tone (2/2).

Average Input Power (dBm)	$V_{DC}(V)$	Tone 1 1.85 GHz (dBm)	Tone 2 2.10 GHz (dBm)	Tone 3 2.25 GHz (dBm)	Tone 4 3.25 GHz (dBm)
0	0.282	-38.06	-37.41	-34.95	-41.17
5	0.584	-32.97	-33.30	-29.91	-36.17
9	1.012	-28.98	-29.51	-26.13	-32.95

Table 7.51: Measured rectified DC voltage for a four-tone excitation for circuit 1. RF power at the coupled port for each tone (1/2).

Average Input Power (dBm)	$V_{DC}(V)$	Tone 1 2.15 GHz (dBm)	Tone 2 2.20 GHz (dBm)	Tone 3 2.25 GHz (dBm)	Tone 4 2.30 GHz (dBm)
0	0.377	-35.63	-33.64	-30.37	-35.92
5	0.627	-32.08	-29.70	-30.34	-30.63
9	1.038	-27.15	-26.16	-28.39	-26.32

Table 7.52: Measured rectified DC voltage for a four-tone excitation for circuit 1. RF power at the coupled port for each tone (2/2).

Average Input Power (dBm)	$V_{DC}(V)$	Tone 1 1.70 GHz (dBm)	Tone 2 1.90 GHz (dBm)	Tone 3 2.00 GHz (dBm)	Tone 4 2.10 GHz (dBm)
0	0.407	-34.70	-34.92	-33.69	-33.92
5	0.812	-30.53	-29.06	-29.03	-29.71
9	1.303	-28.35	-24.67	-24.76	-25.85

Table 7.53: Measured rectified DC voltage for a four-tone excitation for circuit 2. RF power at the coupled port for each tone.